Spectroscopische studies van de dynamica van onzuiverheidsionen in de tokamaks JET en TEXTOR

Spectroscopic Studies of Impurity Ion Dynamics on the JET and TEXTOR Tokamaks

Kristel Crombé

Promotoren: prof. dr. ir. G. Van Oost, dr. J. Ongena
Proefschrift ingediend tot het behalen van de graad van
Doctor in de Toegepaste Wetenschappen: Natuurkunde

Vakgroep Toegepaste Fysica
Voorzitter: prof. dr. W. Wieme
Faculteit Ingenieurswetenschappen
Academiejaar 2004 - 2005

UNIVERSITEIT
GENT

ISBN 90-8578-033-0
NUR 926, 961
Wettelijk depot: D/2005/10.500/33

Promotoren

prof. dr. ir. G. Van Oost	Universiteit Gent
dr. J. Ongena	Koninklijke Militaire School Brussel

Examencommissie

dr. Y. Andrew	UKAEA Fusion
ereprof. dr. E. Desoppere	Universiteit Gent
prof. dr. ir. C. Leys	Universiteit Gent
prof. dr. ir. J.-M. Noterdaeme	Universiteit Gent
prof. dr. ir. R. Verhoeven	Universiteit Gent
prof. dr. ir. R. Weynants	Koninklijke Militaire School Brussel
prof. dr. W. Wieme	Universiteit Gent

Universiteit Gent
Faculteit Ingenieurswetenschappen

Vakgroep Toegepaste Fysica
Rozier 44
9000 Gent
Belgium

e-mail: Kristel.Crombe@UGent.be

Enkele woorden van dank . . .

. . . zijn hier op hun plaats, nu het ' verslag van mijn onderzoek ' is geschreven. Van de velen die mij hebben geholpen wil ik graag enkele mensen vermelden die sterk betrokken zijn geweest bij dit werk.

De eerste cursus plasmafysica kreeg ik van Guido Van Oost. Hij heeft daardoor niet alleen mijn interesse in kernfusie aangewakkerd, maar bovendien heeft hij ervoor gezorgd dat ik met dit onderzoek van start kon gaan. Regelmatige discussies gedurende de voorbije vier jaar vermeden dat ik te sterk zou afdwalen van het uiteindelijke doel, het afleveren van dit proefschrift, en daarom dank ik hem ook in het bijzonder voor de steun om het werk aan JET te blijven voortzetten.

De eigenlijke introductie tot de JET tokamak en de onderzoeksgroepen in Culham werd me gegeven door de immer enthousiaste Jef Ongena.

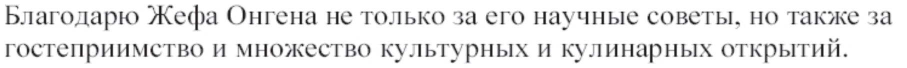

Благодарю Жефа Онгена не только за его научные советы, но также за гостеприимство и множество культурных и кулинарных открытий.

Yasmin Andrew successfully guided me through the complex process of a PhD thesis. It has been a true pleasure to work with her and I learned a lot from her enthusiasm for science and research. I appreciate the continuous and patient advice on writing good (English) texts and giving clear presentations, and I look forward to our future collaboration.

The charge exchange diagnostic that I used, was built by Nick Hawkes. He always had a clear view on the results and his concerns and questions largely improved the analysis.

I want to express my gratitude also to the other members of the Core Spectroscopy Group, who all helped, in one way or the other, to make my many stays at JET fruitful and most enjoyable.

L'interesse di Andrea Murari per il progresso del mio lavoro è stato un grande sostengo, senza il quale questi risultati non sarebbero stati possibili. Lo ringrazio per tutte le discussioni, spesso brevi, ma sempre efficaci, e per difendere l'importanza di questo diagnostico.

Von den Kollegen des Forschungszentrums Jülich will ich hier vor allem Herr Schwarz erwähnen. Durch seine Findlichkeit und Kreativität werden alle technische Probleme schnell gelösst. Ohne ihn war es nie möglich gewesen die Diagnostik am TEXTOR zu installieren. Ich hoffe dass er seine Erfahrung noch lange benutzen kann um die Messungen zu verfeinern und junge Studenten zu begleiten.

Hoewel ik slechts uitzonderlijk in Gent was, wil ik toch de leden (en sympathisanten) van de Vakgroep Toegepaste Fysica niet vergeten, de weinige uren die ik met hen heb doorgebracht waren mij steeds aangenaam. Hetzelfde geldt voor alle collega's et tous les collègues du Laboratoire de Physique des Plasmas van de Koninklijke Militaire School.

Tot slot ben ik ook de leden van de lees- en examencommissies dankbaar voor de waardevolle commentaren, correcties en suggesties die zonder meer de kwaliteit van het proefschrift hebben verbeterd.

Kristel Crombé

Gent, september 2005

Contents

List of Tables

List of Figures

Hoofdstuk 1

Samenvatting

Plura qui ambit, male adstringit
Desiderius Erasmus

1.1 Inleiding

1.1.1 Kernfusie als mogelijke oplossing voor het energieprobleem

Het grootste deel van de nodige energie is momenteel afkomstig van de verbranding van fossiele brandstoffen, waarvan de voorraden lang niet onuitputtelijk zijn. Uit de prognose voor het energieverbruik in de komende paar honderd jaar, voorgesteld in figuur 1.1, blijkt dat we niet ver meer zijn van het punt waarop de beschikbare reserves niet meer zullen voldoen aan de behoeften en een energietekort aanbreekt. De CO_2 uitstoot die gepaard gaat met de verbranding van deze fossiele brandstoffen, heeft bovendien ernstige gevolgen voor het klimaat op aarde, het afsmelten van de poolkappen is reeds een duidelijk teken dat de aarde opwarmt. Als illustratie van de invloed van de grootschalige verbranding van fossiele brandstoffen is in figuur 1.2 de CO_2 concentratie in de atmosfeer getoond gedurende de laatste 1000 jaar, een exponentiële toename is zichtbaar die begint rond 1750 met de industriële revolutie. De energiebehoeften zullen in de komende jaren nog sterk toenemen door de bevolkingsexplosie op aarde en de groei van de levensstandaard in ontwikkelingslanden. In figuur 1.3 is een voorspelling gemaakt van de totale hoeveelheid energie die nodig zal zijn per jaar uitgaande van de gekende energietoename in de vorige eeuw en volgens drie verschillende modellen. Scenario (A) houdt rekening met een sterke bevolkingsgroei en belangrijke technologische en economische ontwikkelingen, en voorspelt dat de totale energiebehoefte zal toenemen met een factor vijf in de komende 100 jaar. Het middelste scenario (B), met een matige groei en ontwikkeling, is misschien het meest realistisch en voorspelt een toename met een factor 3. Zelfs in het meest optimistische scenario (C), dat strenge internationale afspraken rond milieu en ontwikkeling vereist, wordt nog een verdubbeling van de energiebehoefte verwacht. Gelijkaardige conclusies kunnen getrokken worden uit figuur 1.4 waarin voor verschillende landen van de wereld de totale bevolking is voorgesteld, alsook het gemiddeld energieverbruik per inwoner en het totale energieverbruik. In landen zoals China en India die nog in ontwikkeling zijn is het energieverbruik per inwoner aanzienlijk lager dan in landen met een hoge levensstandaard. Verwacht wordt dat met de groeiende ontwikkeling de inwoners van deze landen, met een enorme bevolking, ook veel meer energie zullen nodig hebben.

De mogelijke opties om aan deze groeiende vraag naar energie te kunnen voldoen op lange termijn zijn beperkt. De veelbesproken hernieuwbare energiebronnen zijn een goed alternatief, maar hebben een veel te lage energiedichtheid en rendement om de volledige basis energiebehoefte te dekken. Daarnaast is ook de noodzakelijke stockage van deze energie een niet evidente factor die de prijs doet stijgen. Een andere optie is het aanwenden van kernenergie. Een belangrijk voordeel hierbij is dat slechts zeer weinig brandstof nodig is, omdat uit kernreacties een miljoen keer meer energie vrijkomt dan uit verbrandingsreacties. Met de huidige vorm, de kernsplijting, is nog voor aanzienlijk lange tijd (3000 jaar) brandstof voorradig. Met het langlevend en hoogradioactief afval dat hierbij wordt geproduceerd, moet echter voorzichtig worden omgesprongen, en ook de reactoren zelf waarin de fissiereacties doorgaan vereisen strenge veiligheidsmaatregelen. Een derde mogelijkheid is kernfusie. Het samensmelten van waterstofisotopen (momenteel concentreert men zich op de deuterium – tritium reactie) tot helium wordt reeds gecontroleerd uitgevoerd in fusielaboratoria over heel de wereld. Er werd al aangetoond dat het fysisch mogelijk is om hierbij break-even te bereiken, dit wil zeggen dat de energie die vrijkomt uit de fusiereacties, de vereiste energie invoer compenseert. Verder onderzoek en ontwikkeling moet nu aantonen dat kernfusie ook technisch haalbaar en economisch rendabel is. De voorraden deuterium en lithium (waaruit

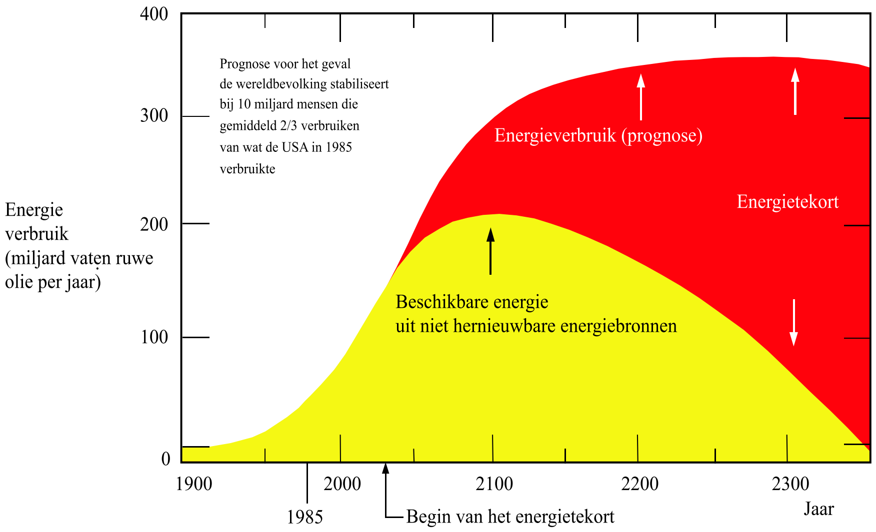

Figuur 1.1: Voorspelling van het energieverbruik tot 2350 en de beschikbare energie uit niet-hernieuwbare bronnen.

tritium wordt geproduceerd) op aarde laten toe om voor vele duizenden jaren aan de energienoden te voldoen, gebruik makend van deze reactie. Het radioactief afval is kortlevend en wordt door dezelfde generatie verwerkt die ook de energie verbruikt. Bovendien gaan de fusiereacties door in een opgesloten plasma en vallen stil zodra de nodige hoge dichtheden en temperaturen niet meer worden bereikt, bijvoorbeeld bij contact met de wand van het vat, waardoor het proces ook intrinsiek veilig is.

De meest succesvolle manier tot hiertoe om kernfusie te laten doorgaan is door het plasma op te sluiten met behulp van magnetische velden in een zogenaamde tokamak configuratie. De grootste tokamak ter wereld is JET (Joint European Torus, in Oxfordshire, UK), waar een deel van het werk voorgesteld in deze thesis is verricht. De volgende belangrijke stap in het fusieonderzoek is de bouw en exploitatie van de ITER tokamak (International Thermonuclear Experimental Reactor), met een plasmavolume van 800 m^3, acht maal groter dan dat van JET, figuur 1.5 toont de grootte van deze machine. ITER moet de technische haalbaarheid van kernfusie demonstreren en is ontworpen om meer dan 500 MW fusie-energie te produceren.

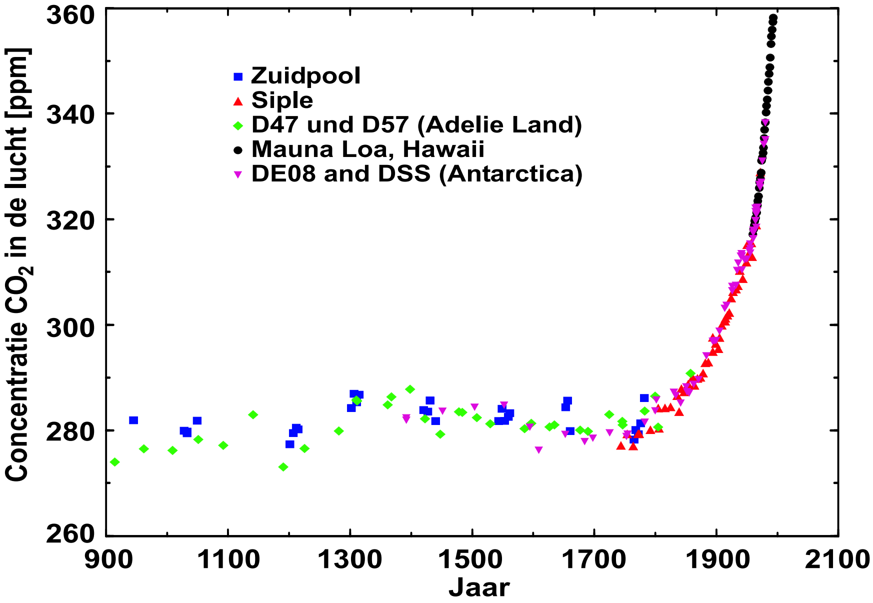

Figuur 1.2: De CO_2 concentratie in de atmosfeer van 900 tot heden.

1.2 Poloïdale rotatiesnelheden in JET ITB plasma's door middel van Charge eXchange Recombination Spectroscopy

1.2.1 Eigenschappen van plasma's met interne transportbarrières

In een tokamak zijn verschillende opsluitingsregimes mogelijk zoals geïllustreerd in figuur 1.6. De L-mode (low confinement) is de basis mode voor tokamak operatie. De H-mode (high confinement) werd voor het eerst ontdekt op de ASDEX tokamak [Wagn82]. In deze operatiemode is de energie opsluitingstijd een factor 1.5 - 2 groter dan voor de L-mode. H-mode plasma's vertonen een transportbarrière aan de rand, de Edge Transport Barrier (ETB), een zone met een grote drukgradiënt. Boven een zekere grens valt deze drukgradiënt terug naar lagere waarden waarbij energie en deeltjes uit het plasma worden gedreven. Dit zijn de zogeheten ELMs (Edge Localised Modes). De ELMy H-mode wordt uitgebreid bestudeerd op JET en zal de conventionale operatiemode zijn voor ITER. Het tweede scenario voor ITER (Advanced Tokamak Scenario) zijn plasma's met een bijkomende verhoging van de opslui-

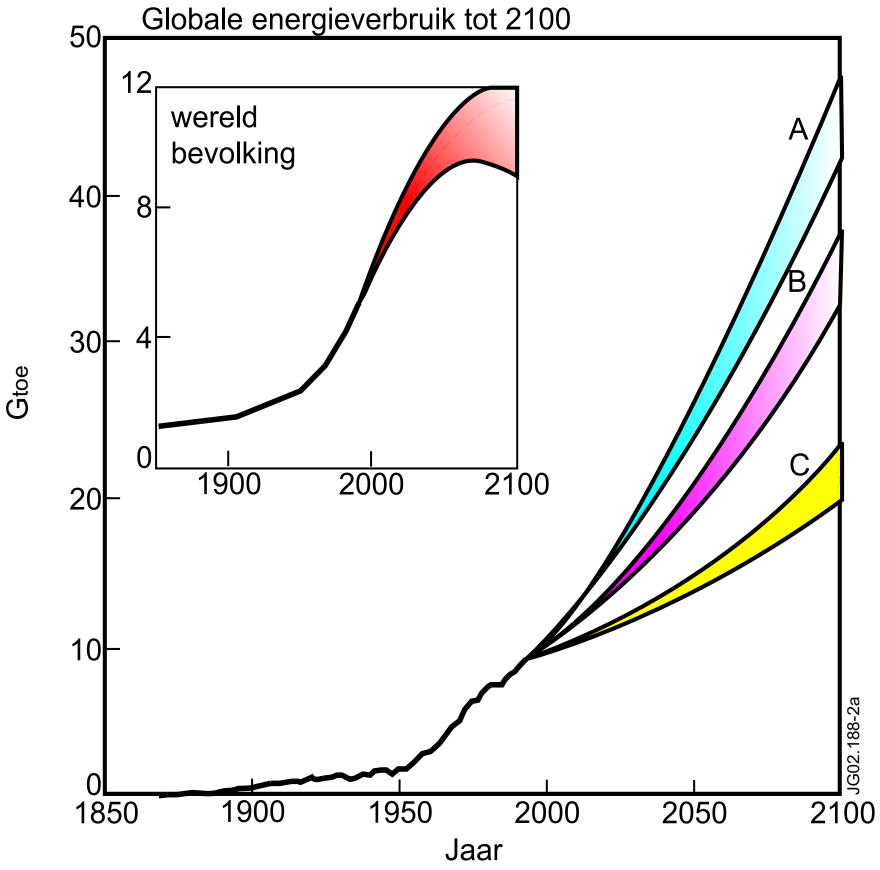

Figuur 1.3: Voorspelling van het totale energieverbruik tot 2100, uitgaande van de gekende toename en volgens drie verschillende modellen, en de verwachte bevolkingsgroei in deze periode.

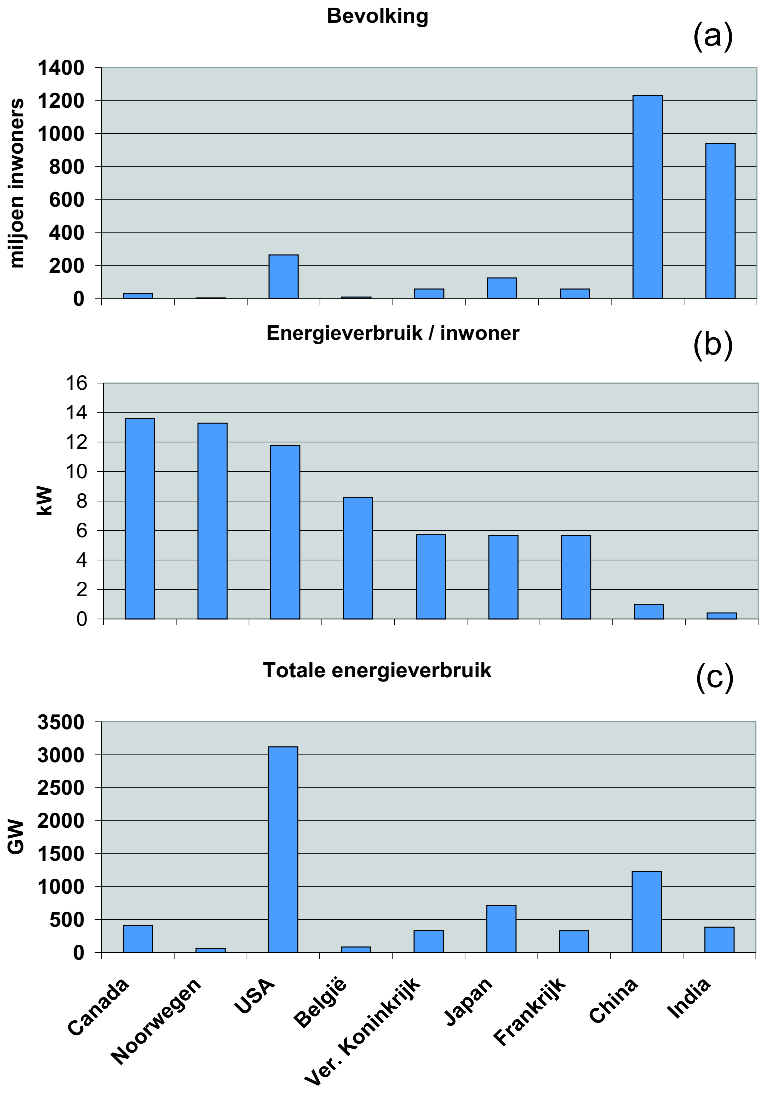

Figuur 1.4: (a) De totale bevolking, (b) het energieverbruik per inwoner en (c) het totale energieverbruik in verschillende landen van de wereld. De USA is op dit moment de grootste verbruiker, maar wat het aantal inwoners betreft zijn China en India de koplopers. Enorme energie behoeften kunnen verwacht worden in deze landen tijdens hun ontwikkeling in de komende jaren, aangezien het energieverbruik per inwoner verband houdt met de levensstandaard.

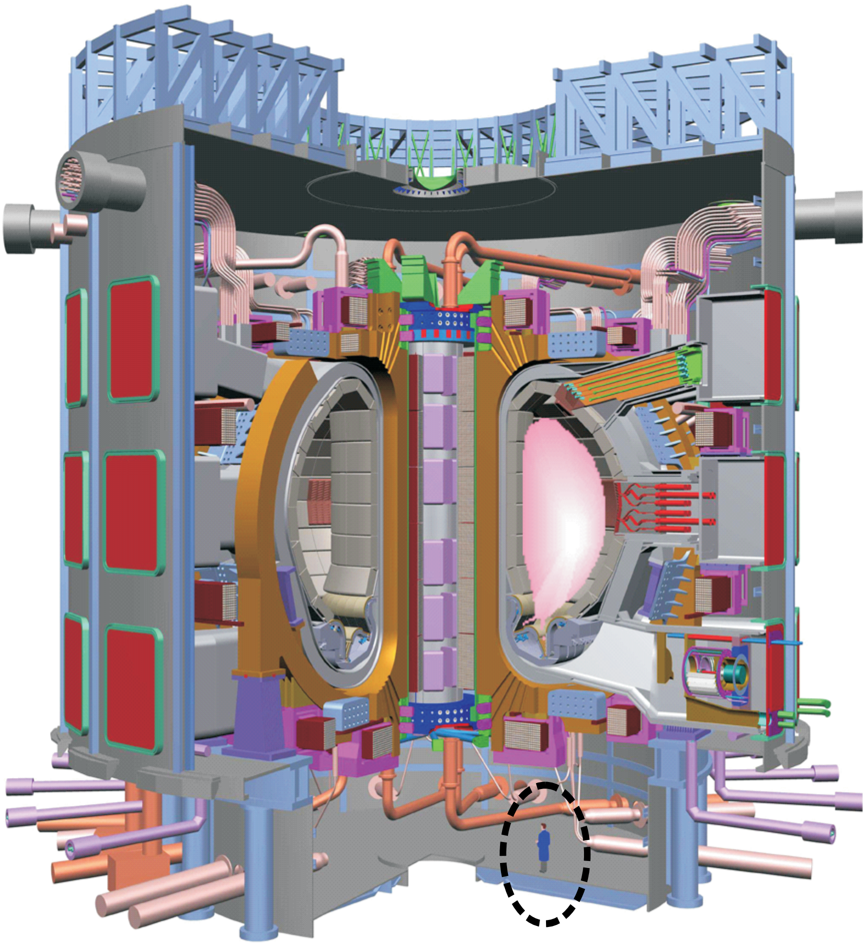

Figuur 1.5: Voorstelling van de ITER tokamak, die in een cryostaat wordt geplaatst omdat de magnetische spoelen supergeleidend zullen zijn.

tingstijd in de kern, een interne transportbarrière (ITB), voor het eerst ontdekt in de jaren 1990 [Koid94, Levi95, Stra95]. Typisch hebben deze plasma's een steile drukgradiënt in een gebied r/a = 0.3 - 0.6. De ITB kan zowel op de profielen van de ionen als van de electronen temperatuur zichtbaar zijn, alsook op de electronen dichtheid en toroïdale rotatiesnelheid. Niet noodzakelijk treedt de ITB op in al deze kanalen tegelijkertijd.

De fysische mechanismen die deze ITBs veroorzaken en laten voortbestaan in de plasma's zijn nog niet alle volledig begrepen en verklaard. Algemeen wordt aangenomen dat turbulentie wordt onderdrukt in de ITB regio door een samenspel van verschillende factoren. De belangrijkste hiervan zijn:

- een differentiële **E**x**B** stromingssnelheid van het plasma die onstabiele modes in het plasma stabiliseert door het breken van de turbulente cellen
- het q-profiel en de grootheid $s = \frac{r}{q}\frac{dq}{dr}$ (magnetic shear) die een invloed hebben op de groeisnelheid van de onstabiliteiten
- de verhouding tussen ionen en electronen temperatuur
- de electronen dichtheidsgradiënt.
- stromingen in het plasma die door de turbulentie zelf worden gegenereerd (zonal flows)

Het werk in deze thesis concentreert zich op poloïdale rotatiesnelheden (v_θ) die optreden bij de berekening van het radiaal electrisch veld E_r (en dus rechtstreeks verband houden met de **E**x**B** stromingssnelheid),

$$E_r = \frac{1}{Zen}\frac{dp}{dr} - \left(v_\theta B_\phi - v_\phi B_\theta\right), \tag{1.1}$$

met Z de lading van de deeltjes, e de elementaire lading, n is de dichtheid, p is de druk, v_θ is de poloïdale en v_ϕ de toroïdale rotatiesnelheid, en B_ϕ en B_θ zijn de toroïdale resp. poloïdale magnetische veld componenten.

Op JET en vele andere tokamaks worden rotatiesnelheden van onzuiverheidsionen gemeten via Charge eXchange Recombination Spectroscopy (CXRS) op koolstof (C^{6+}) ionen, die een ladingsuitwisselingsreactie ondergaan met de neutrale deeltjes bundel die gebruikt wordt voor de plasmaverhitting.

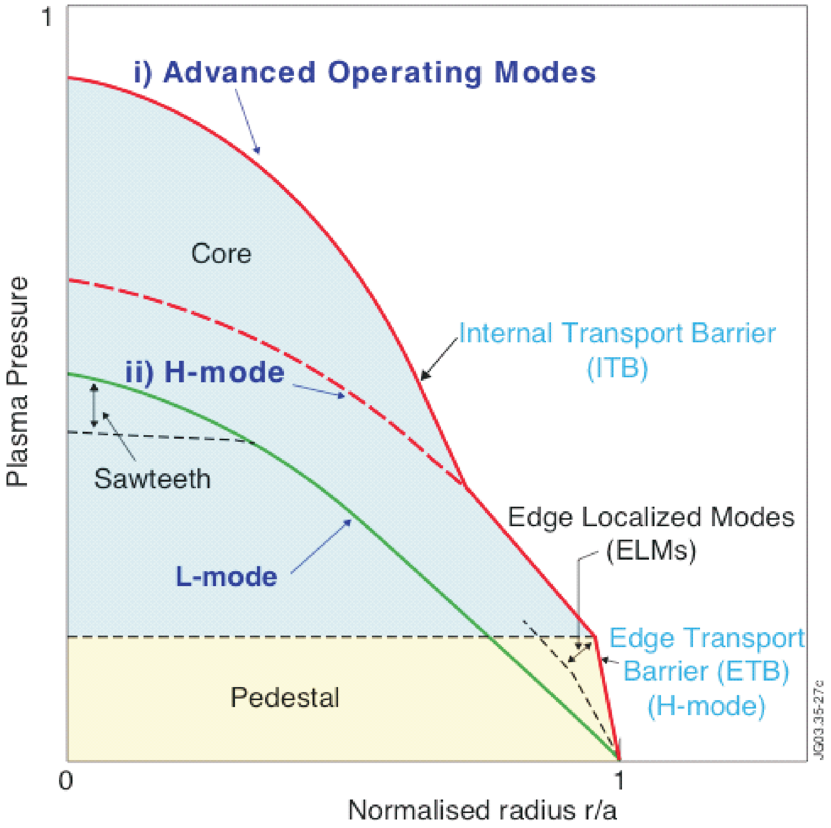

Figuur 1.6: Schematische voorstelling van de verschillende opsluitingsregimes in een tokamak.

1.2.2 Verbeteringen aan de metingen met behulp van de poloïdale CXRS diagnostiek in het centrale gedeelte van JET plasma's

Twee verschillende calibratie methodes worden gebruikt om de centrale positie van de C VI spectrale lijn (met golflengte $\lambda = 529.05$ nm) te bepalen. Bij de lamp calibratie worden de posities van vier duidelijk te onderscheiden spectrale lijnen in het golflengte gebied 527.14 – 529.82 nm geselecteerd uit een lamp spectrum, aan de hand waarvan dan de dispersie relatie van het instrument en de centrale positie van de C VI lijn kan worden bepaald. Er is echter gebleken dat de positie van deze lijnen op de CCD wijzigt met de tijd, mogelijks door kleine bewegingen van het instrument of temperatuur schommelingen, en daarom moet deze calibratie methode regelmatig worden herhaald. Ideaal zou zijn om bij elke ontlading ook het lamp spectrum op te meten als referentie. Dit was echter technisch niet mogelijk met de bestaande opstelling en daarom werd een tweede calibratie methode ontwikkeld, gebaseerd op het plasma spectrum zelf. Immers, naast de C VI lijn worden ook een Be II ($\lambda = 527.06$ nm) en een C III lijn ($\lambda = 530.47$ nm) opgemeten tijdens elke ontlading. De rotatiesnelheden van de Be^{1+} en C^{2+} ionen langs de gezichtslijnen zijn voldoende laag en relatief constant tijdens een shot, zodat ze als referentielijnen (zonder Doppler verschuiving) kunnen worden gebruikt om de dispersie relatie te berekenen bij elke ontlading afzonderlijk. Deze methode kan echter alleen gebruikt worden indien de Be II en C III lijnen voldoende intens zijn om een nauwkeurige Gaussische fit toe te laten. Daarom wordt ook de lamp calibratie nog regelmatig uitgevoerd, zo mogelijk bij elke serie van ontladingen waarbij de meting van poloïdale rotatie (v_θ) is vereist. Uiteraard komen beide methodes nauwkeurig overeen wanneer een recente lamp calibratie voor handen is. Figuur 1.7 toont twee profielen van v_θ, het ene met een lamp calibratie die is genomen enkele weken voor het eigenlijke shot, en het andere met de plasma spectrum calibratie. Het verschil is hoofdzakelijk een verschuiving van het profiel over +/- 20 km/s, wat in dit geval overeenkomt met 100 % van de totale rotatiesnelheden.

De gezichtslijnen waarlangs de poloïdale rotatie wordt gemeten aan JET bevatten een belangrijke toroïdale component. Een serie van experimenten is uitgevoerd precies om deze toroïdale component te meten en te vergelijken met de berekenende waarden. Deze berekeningen worden voor elke ontlading uitgevoerd, rekening houdend met de magnetische configuratie van de ontlading, de gebruikte injectoren van neutrale deeltjes en hun vermogen, en de design parameters van de CXRS diagnostiek. De experimenten bestonden uit een serie L-mode shots, waarbij de toroïdale rotatiesnelheid stapsgewijs werd opgevoerd door het verhogen van het totale vermogen van de meest horizontaal gerichte injectoren. De totale rotatiesnelheid, gemeten langs de gezichtlijn ($\mathrm{v_{LOS}}$) kan geschreven worden als :

$$\mathrm{v_{LOS}} = v_\phi \cos\phi + v_\theta \cos\theta, \tag{1.2}$$

met v_ϕ de toroïdale rotatie op de plaats van de meting, geïnterpoleerd uit de dataset van een onafhankelijke toroïdale CXRS diagnostiek, en ϕ en θ de hoeken tussen de gezichtslijn en de toroïdale respectievelijk poloïdale magnetische veld component. In figuur 1.8 is een dataset weergegeven voor één van de posities waarlangs v_θ wordt gemeten, die overeenkomt met $\mathrm{R_{mid}} = 3.34$ m. De helling van de rechte gefit door deze data punten komt dan overeen met de $\cos\phi$ voor deze gezichtslijn, en is in dit geval +/- 0.18, dit betekent dat 18 % van de toroïdale rotatiesnelheid op deze positie wordt opgepikt door de poloïdale CXRS diagnostiek. Deze component moet dan afgetrokken worden van de totale gemeten snelheid ($\mathrm{v_{LOS}}$) om de poloïdale rotatie te kennen. Een vergelijking tussen deze experimentele waarden voor $\cos\phi$ en de berekeningen is voorgesteld in fig. 1.9. De gemeten waarden liggen +/- 15 % lager dan de berekende resultaten en dit komt overeen met +/- 5 km/s in de poloïdale rotatiesnelheden zoals te zien op fig. 1.10 waar v_θ profielen zijn voorgesteld, met zowel de experimentele als berekende $\cos\phi$.

De snelheidsmeting met behulp van CX wordt bemoeilijkt door Doppler shifts van de spectrale lijn die niet het gevolg zijn van een effectieve rotatiesnelheid van de ionen, maar te wijten zijn aan (i) de energie afhankelijkheid van de werkzame doorsnede van de CX reactie en aan (ii) de beweging op de gyro-orbit tijdens de eindige levensduur van de geëxciteerde C^{5+} ionen na ladingsuitwisseling. Hoe hoger de temperatuur hoe belangrijker deze effecten [vH95, Bell00, Meis01, Solo04b]. Correcties op de JET CX spectra werden toegepast om deze schijnbare rotatiesnelheid te elimineren. De impact op de gemeten snelheid is geïllustreerd in fig. 1.11. De tijdsevolutie van v_θ is voorgesteld, in een plasma met $T_i \approx 20$ keV op de plaats van de meting, (i) zonder enige correcties, met (ii) alleen de energie afhankelijkheid van de werkzame doorsnede (τ_{eff} = 0.0 ns), en (iii) met verschillende waarden voor de eindige levensduur van de geëxciteerd C^{5+} ionen (τ_{eff} = 0.7 ns – 1.7 ns). De effectieve rotatiesnelheid blijkt aanzienlijk lager te zijn dan de rotatiesnelheid die volgt uit de totale Doppler verschuiving. Het verschil bedraagt in dit geval tot +/- 15 km/s.

Uit de CX spectra van de poloïdale diagnostiek wordt ook de ionen temperatuur afgeleid. Hiervoor wordt de breedte van de spectrale lijn gebruikt. Dit levert een vergelijking op met twee andere diagnostieken die T_i kunnen meten: de toroïdale CXRS diagnostiek die eveneens C VI spectra opmeet, en een x-ray crystal spectrometer die Ni^{26+} ionen detecteert. De drie onafhankelijke diagnostieken tonen goede overeenkomsten tussen de gemeten T_i waarden, zoals ook blijkt uit figuur 1.12.

1.2.3 Experimentele resultaten in ITB plasma's

Het eerste voorbeeld is een typische ontlading met interne transportbarrière (ITB) met een omgekeerd q-profiel [Mail04]. Hierbij werden 13 MW Neutrale Beam Injectie (NBI), 4 MW Ion Cyclotron Resonant Heating (ICRH) en 2MW Lower Hybrid (LH) heating gebruikt. In figuur 1.13(a) zijn T_i profielen getoond tijdens de vorming en radiale expansie van de ITB. Het ITB criterion voor deze ontlading is in figuur 1.14(a) en toont verder de tijds- en ruimtelijke evolutie van de transportbarrière. Dit ITB criterion is gedefinieerd als wanneer de lokale dimensieloze Larmor straal ρ^*_T, met $\rho^*_T = \rho_S/L_T$ (de verhouding van de Larmor straal van de ionen bij de geluidssnelheid, ρ_S, en de typische lengte van de temperatuursgradiënt, L_T), een bepaalde kritische waarde overschrijdt, namelijk 0.014 zoals beschreven in [Tres02]. De ruimtelijke lokatie van drie van de CXRS gezichtslijnen zijn aangeduid in de figuren 1.13(a) en 1.14(a). De overeenkomstige v_θ waarden (fig. 1.14(b)) langs de gezichtslijn bij R$_{\text{mid}}$ = 3.33 m nemen toe in de positieve (electronen diamagnetische) richting, van 7 tot 20 km/s tijdens het tijdsinterval dat dit kanaal het centrale gedeelte van de T_i gradiënt ziet (t $\sim$ 4.2s – 5.1s). Bij de verbreding van de barrière naar het buitenste deel van het plasma toe (t > 5.1 s) verandert de positie van de CXRS gezichtlijn t.o.v. de T_i gradiënt, en een sterke positieve stijging wordt nu gemeten langs de aangrenzende gezichtslijn (R$_{\text{mid}}$ = 3.40 m), de poloïdale rotatie hier neemt toe van 7 tot 40 km/s. Het

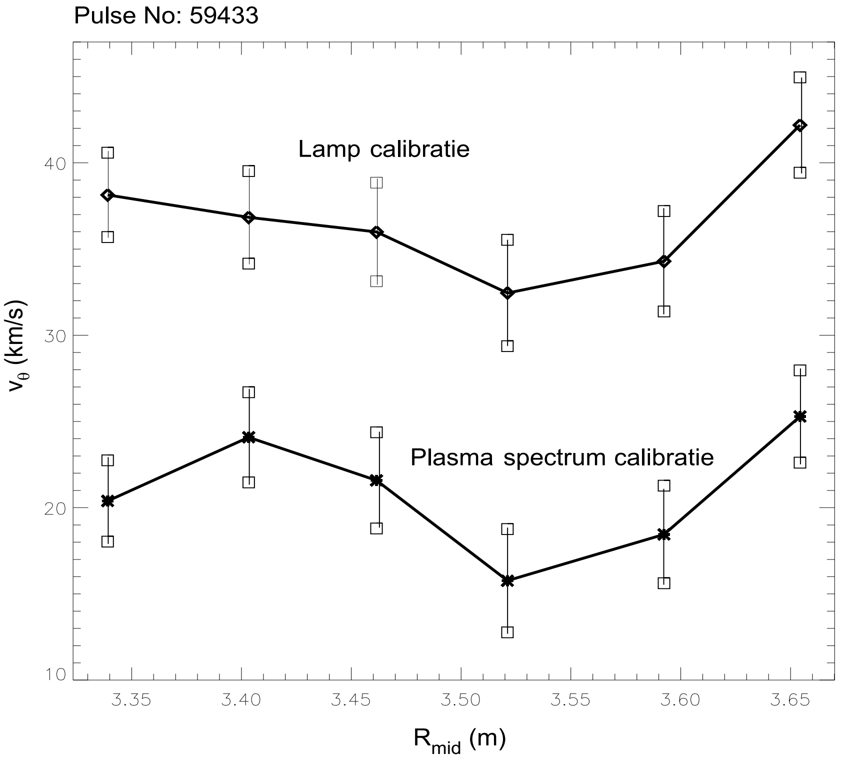

Figuur 1.7: Profiel van de poloïdale rotatiesnelheden gebruik makend van een lamp calibratie van enkele weken voor het eigenlijke shot, en gebruik makend van de calibratie methode gebaseerd op het plasma spectrum. Het verschil in absolute waarde is aanzienlijk, en bedraagt in dit geval tot 20 km/s.

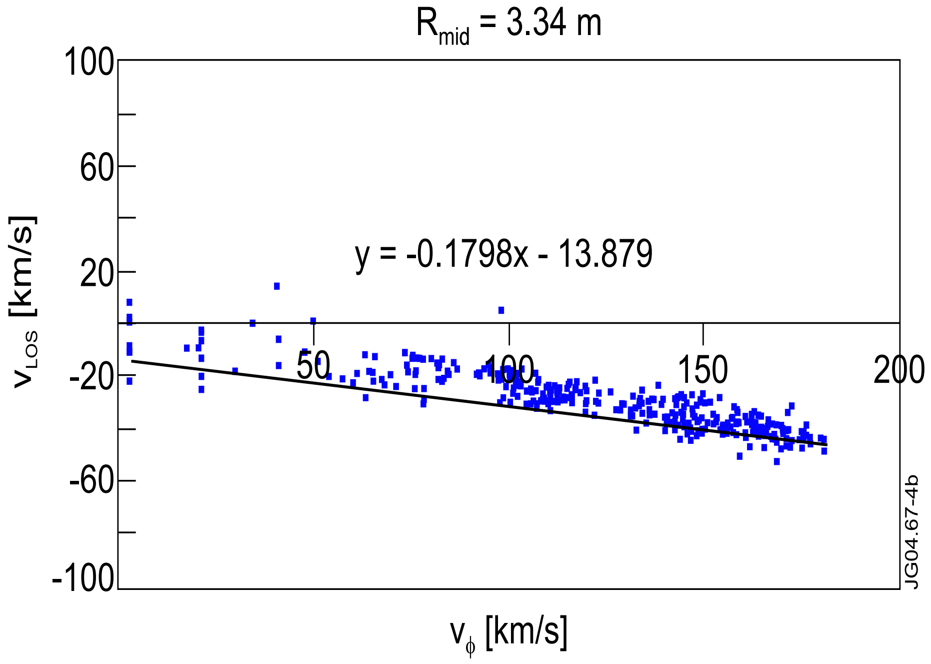

Figuur 1.8: De totale snelheid langs één van de gezichtslijnen van de poloïdale CXRS diagnostiek, gemeten tijdens de *L*-mode shots met toenemende neutrale beam injectie, als functie van de toroïdale snelheid op deze positie. De helling van de rechte die door deze datapunten is gefit, geeft de experimentele waarde voor de toroïdale component langs deze gezichtslijn en bedraagt in dit geval 0.1798.

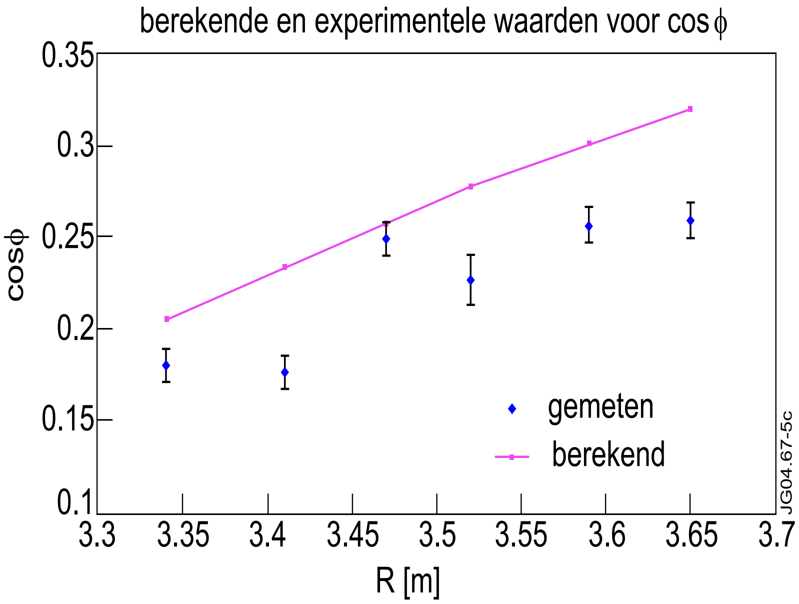

Figuur 1.9: Vergelijking van de gemeten en berekende waarden voor $\cos\phi$ langs de zes verschillende gezichtslijnen van de poloïdale CXRS diagnostiek.

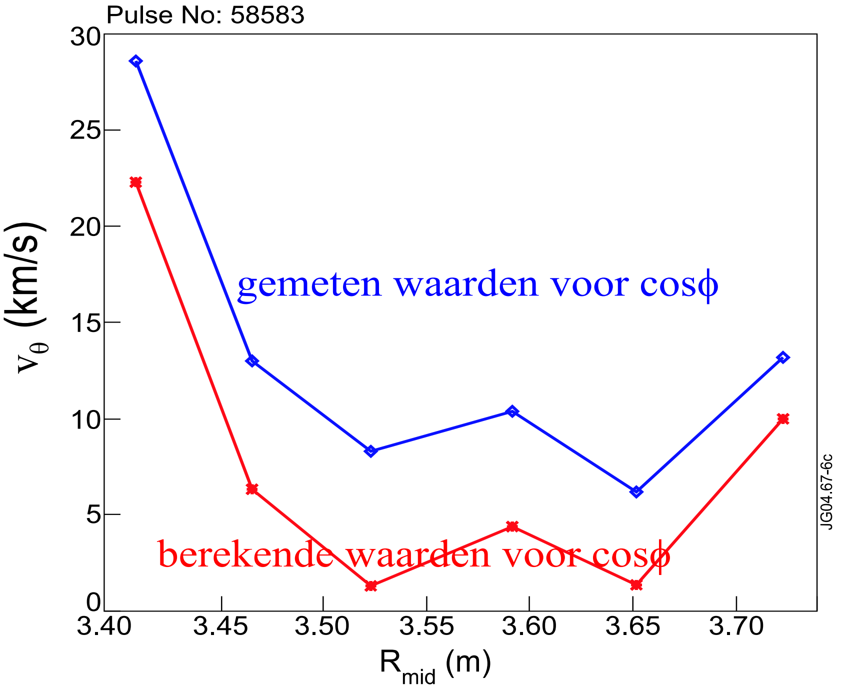

Figuur 1.10: Poloïdale rotatieprofielen waarbij zowel de experimentele als de berekende $\cos\phi$ worden gebruikt.

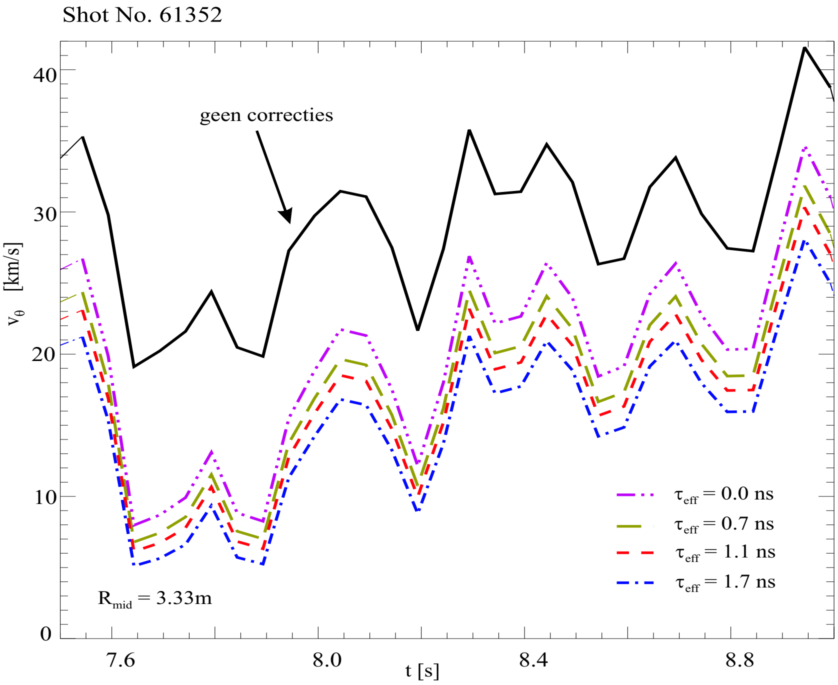

Figuur 1.11: Tijdsevolutie van v_θ, zonder temperatuurcorrecties, en met verschillende waarden voor τ_{eff} (de levensduur van de geëxciteerde toestand van het C^{5+} ion na ladingsuitwisseling). Hoe groter τ_{eff}, hoe belangrijker deze temperatuur correcties worden.

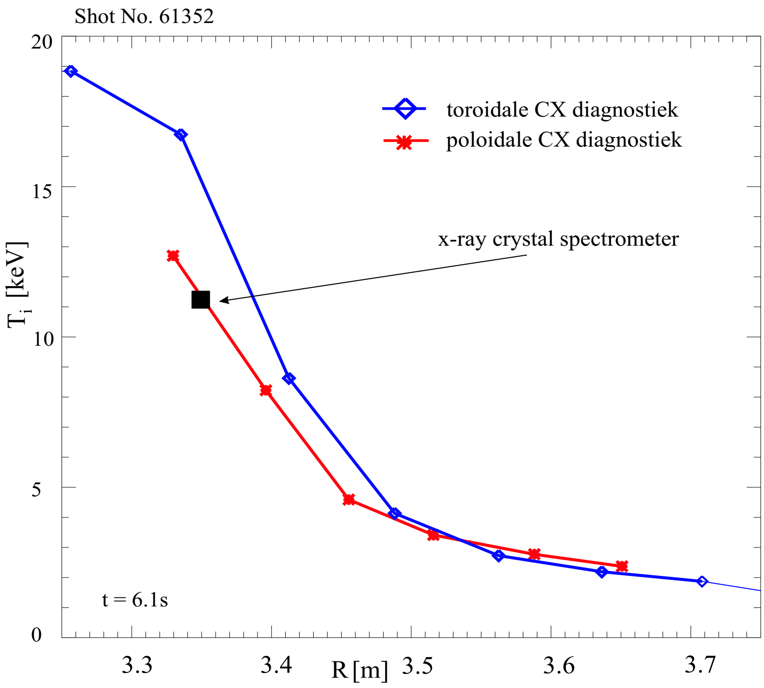

Figuur 1.12: Vergelijking van T_i metingen met drie onafhankelijke diagnostieken.

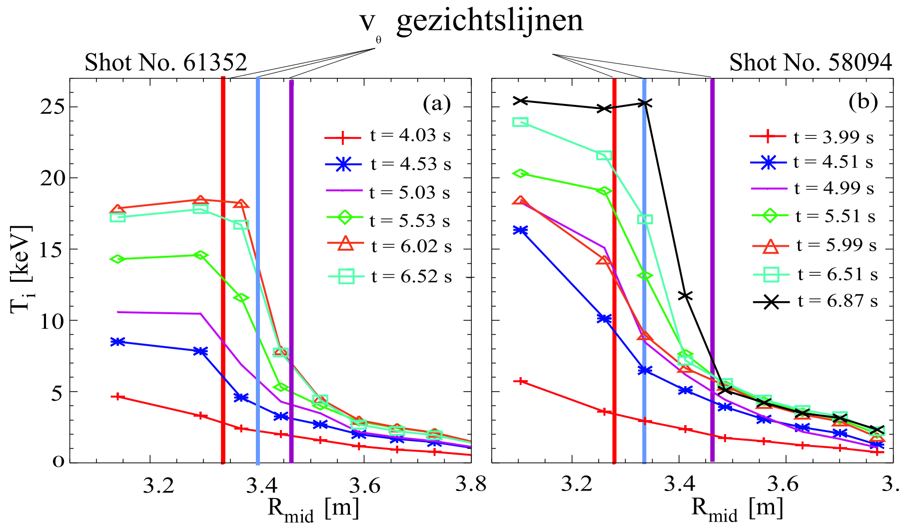

Figuur 1.13: T_i profielen tijdens de evolutie van de ITB voor (a) shot no. 61352 en (b) 58094. De verticale lijnen tonen de posities van de CXRS gezichtslijnen voor de v_θ metingen.

meest centraal gelegen kanaal (R_{mid} = 3.33 m) meet nu een v_θ in de tegengestelde richting tot -25 km/s. De v_θ waarden langs de gezichtslijn bij R_{mid} = 3.47 m, gelegen buiten de ITB zone, blijft constant bij 7 km/s. In de eindfase van de ITB evolutie, komt de sterke T_i gradiënt weer meer naar binnen te liggen, en de poloïdale rotatie langs R_{mid} = 3.40 m neemt terug haar oorspronkelijke waarde aan van 7 km/s, terwijl de snelheid langs R_{mid} = 3.33 m opnieuw toeneemt in positieve richting tot 25 km/s.

Experimentele v_θ data worden ook voorgesteld voor een tweede ontlading (shot no. 58094) in figuur 1.15, waarbij een meer centraal bereik was gekozen voor de meting van v_θ, zoals aangeduid in fig. 1.13(b). Bij deze ontlading was de centrale T_i tot 24 keV. De evolutie van de ITB en de poloïdale rotatie langs drie van de gezichtslijnen van de CXRS diagnostiek zijn voorgesteld in de figuren 1.15 (a) en (b). Deze meting toont dat v_θ zeer sterk toeneemt tot -75 km/s langs de gezichtslijn bij R_{mid} = 3.34 m. Dit kanaal ziet dan de binnenste zijde van de steile T_i gradiënt. De R_{mid} = 3.28 m gezichtslijn is gelegen in een minder

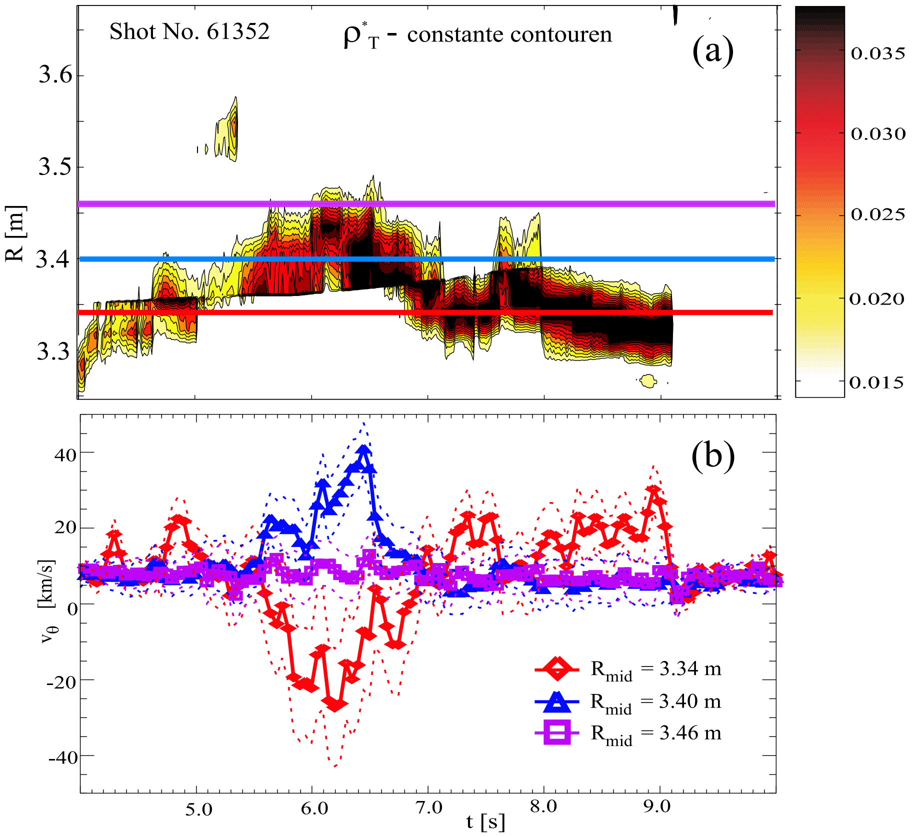

Figuur 1.14: (a) Het ITB criterium en de lokaties van drie van de v_θ kanalen in het gebied met de steile temperatuursgradiënt. (b) De tijdsevolutie van v_θ bij deze drie verschillende CXRS radii.

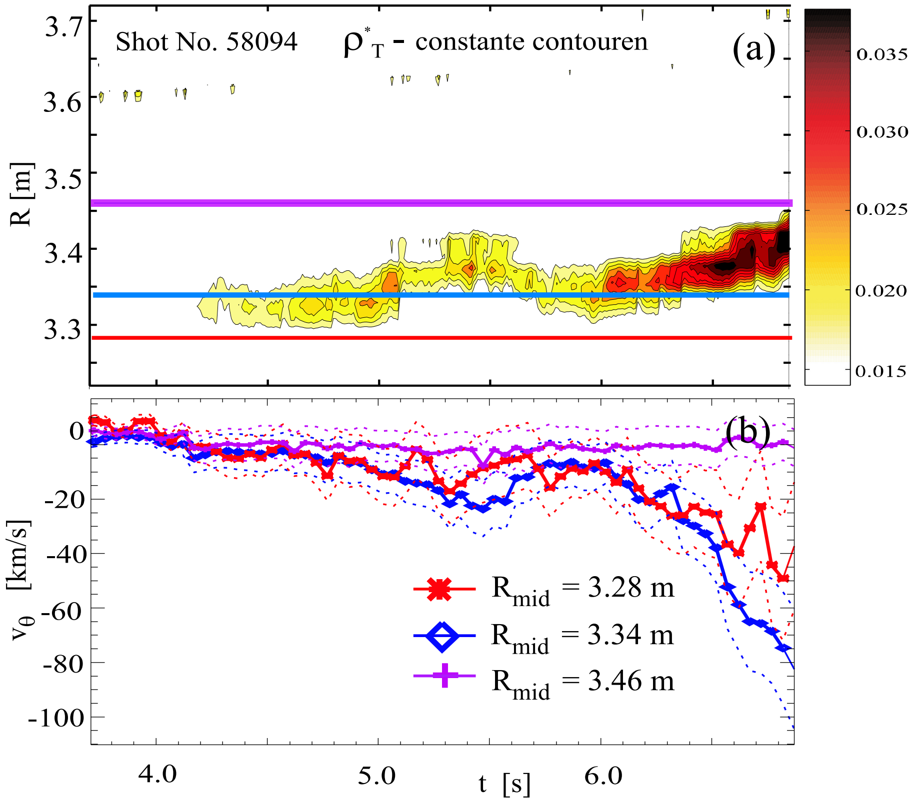

Figuur 1.15: (a) Het ITB criterium voor shot no. 58094 en de posities van de CXRS kanalen voor de v_θ metingen. (b) De v_θ evolutie in de tijd gemeten bij deze drie verschillende radii die getoond zijn in fig. 1.13(b).

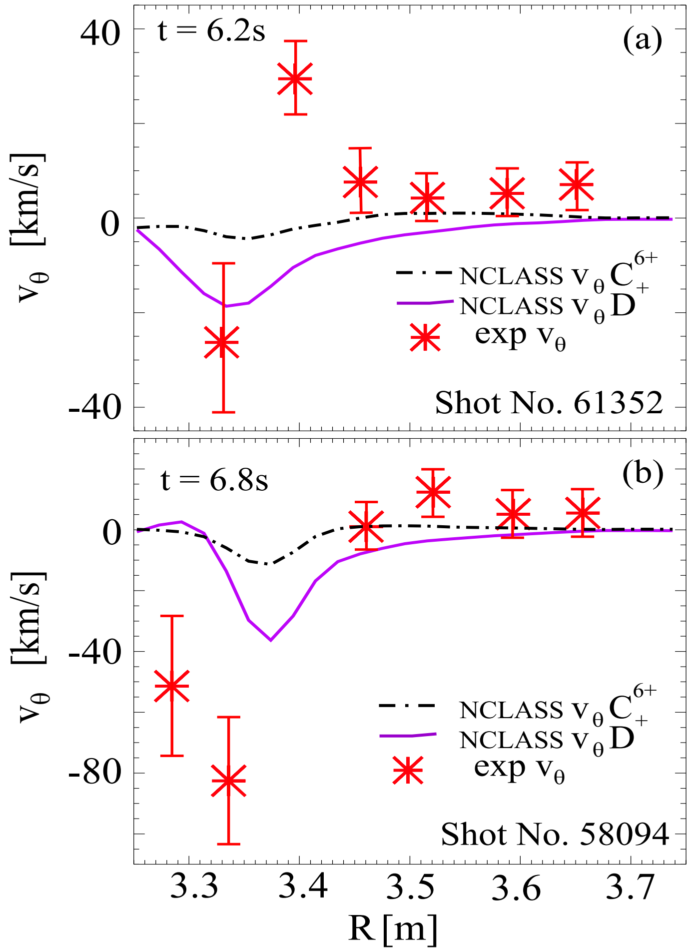

Figuur 1.16: Vergelijking tussen de gemeten v_θ profielen (aangeduid met een ster) en de neoklassieke voorspellingen door NCLASS voor C^{6+} (stippellijn) en voor D^+ (volle lijn) tijdens de ITB voor de twee ontladingen. De gemeten waarden zijn een grootteorde hoger dan de voorspellingen voor de C^{6+} ionen. De excursies in negatieve richting zijn van dezelfde orde als de NCLASS voorspellingen voor de gewone plasma ionen.

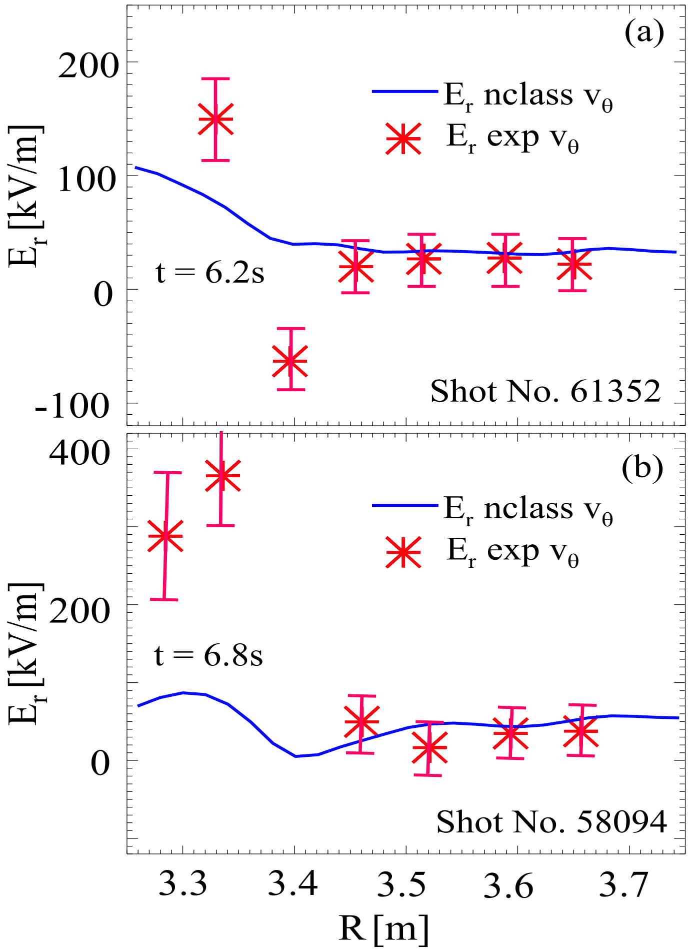

Figuur 1.17: E_r profielen voor de ontladingen shot no. 61352 en 58094 tijdens de ITBs, berekend m.b.v. vgl. 1.1, met de gemeten v_θ waarden (aangeduid met sterren) en de NCLASS voorspellingen voor v_θ (volle lijn). In beide gevallen werden de experimentele toroïdale rotatiesnelheden, temperaturen en dichtheden gebruikt.

steil gedeelte van het T_i-profiel en stijgt tot -40 km/s. Het kanaal bij $\mathrm{R}_{\mathrm{mid}} = 3.47$ m dat de voet van de barrière ziet, toont geen duidelijke verandering in v_θ.

Deze twee voorbeelden tonen aan dat er een verband is tussen het bestaan van een ITB en sterke, lokale excursies in v_θ. De relatieve toename in v_θ en de rotatierichting hangen af van de plaats van de meting op de T_i gradiënt, en houden dus verband met de sterkte van de barrière. Door het beperkt ruimtelijk bereik van de v_θ meting en de tijdsresolutie van slechts 50 ms, was het niet mogelijk om de causaliteit te onderzoeken tussen de v_θ excursies en de vorming van de ITB [Stae99, Bell98].

De gemeten v_θ profielen werden vergeleken met neoklassieke voorspellingen gemaakt met behulp van de NCLASS module in de JETTO transport code. Het resultaat is geïllustreerd in figuur 1.16 voor deze twee ontladingen. Op de plaats van de negatieve dip in de neoklassieke voorspellingen van v_θ wordt ook de meest negatieve v_θ gemeten. Er blijkt echter een groot verschil te zijn in absolute waarde tussen de neoklassieke berekeningen en de experimentele data, bijna een grootteorde. De positieve toename zoals gemeten in het voorbeeld shot no. 61352 bij $\mathrm{R}_{\mathrm{mid}} = 3.40$ m, wordt niet voorspeld door NCLASS. Er is een relatief goede overeenkomst tussen de gemeten negatieve excursie en de NCLASS berekeningen voor de poloïdale rotatiesnelheid van de deuteriumionen, waarvoor de snelheden een grootteorde hoger liggen dan voor de onzuiverheidsionen. De oorzaak voor dit verschil tussen gemeten en berekende v_θ is op dit moment niet duidelijk. Mogelijks heeft de NBI een invloed op de rotatiesnelheden via de injectie van snelle ionen, hoewel er geen rechtstreeks verband kon worden vastgesteld in deze voorbeelden.

Bij het gebruik van de experimentele v_θ profielen voor de berekening van het radiaal elektrisch veld E_r via vergelijking 1.1 blijkt er een goede overeenkomst te zijn tussen de gemeten en berekende waarden in het gebied buiten de barrière, maar in het gebied met de sterke T_i gradiënt is er echter een groot verschil zoals te zien op fig. 1.17. De E_r gradiënt is veel groter als de experimentele v_θ wordt gebruikt in plaats van de NCLASS berekeningen. Dit suggereert dan dat de stabilisatie van turbulentie door middel van een differentiële **ExB** stromingssnelheid sterker is dan de berekeningen voorspellen.

1.2.4 Conclusies

Dankzij de verbeteringen aangebracht aan de poloïdale CXRS diagnostiek op JET inzake calibratie, toroïdale component van de gezichtslijnen en de temperatuurafhankelijke effecten, kunnen de poloïdale rotatie en ionen temperatuur standaard opgemeten worden. Deze verbeterde meettechniek werd in het bijzonder gebruikt om v_θ in ITB plasma's te bekijken. Voor het eerst werden aan JET belangrijke wijzigingen in poloïdale rotatiesnelheden gekoppeld aan ITBs opgemeten. Afhankelijk van de relatieve lokatie van de meting t.o.v. het temperatuursprofiel van de barrière kunnen de v_θ excursies in de diamagnetische richting van de ionen of electronen zijn. De tijdsintervallen met een verhoogde poloïdale rotatiesnelheid komen overeen met de intervallen waarbij reflectometrie een vermindering van de turbulente fluctuaties vaststelt. Hoewel de oorsprong van deze v_θ excursies nog niet duidelijk is, zouden ze kunnen verband houden met het standhouden van de barrière, aangezien ze blijven bestaan gedurende de volledige tijd dat de ITB binnen het bereik van de gezichtslijnen ligt. De experimentele waarden werden vergeleken met neoklassieke voorspellingen voor v_θ met behulp van de NCLASS module die gekoppeld is met de JETTO transport code. Om na te gaan of deze excursies de ITB ook doen ontstaan, zijn verdere experimenten voorzien tijdens de volgende JET campagnes met een goede controle van plaats en tijd van het ontstaan van de ITB. Ook zullen een aantal CXRS kanalen uitgerust worden met snelle detectors en zullen verschillende q-profielen worden getest.

1.3 Studie van de invloed van de dynamische ergodische divertor op straling en transport van koolstof in de TEXTOR tokamak

1.3.1 Algemene eigenschappen van de dynamische ergodische divertor

Op de TEXTOR tokamak werd in de periode maart 2001 - mei 2003 een Dynamische Ergodische Divertor (DED) geïnstalleerd, bestaande uit een set van zestien helische spoelen (en twee compensatie spoelen), zoals te zien op fig. 1.18. Het magnetische veld opgewekt door deze spoelen is maximaal van dezelfde grootteorde als het poloïdale veld in de tokamak (0.1 T) en heeft een gelijkaardige helische structuur als de veldlijnen op het $q = 3$ flux oppervlak. Het verstoort daarom alleen lokaal, rond $q = 3$, de magnetische oppervlakken, terwijl de kern van het plasma opgesloten blijft.

De resulterend magnetische configuratie is voorgesteld in fig. 1.19. Rond de onverstoorde kern zit een ergodische zone die contact maakt met de wand via zogenaamde ergodische vingers. De laminaire zone bestaat uit veldlijnen met een korte reconnectielengte (i.e. de lengte vooraleer de veldlijn contact maakt met de wand), en is het dichtst bij de wand gesitueerd. De veldlijnen in de ergodische zone hebben een zeer lange reconnectielengte en op de Poincaré plots in figuren 1.19(b) en (c) is deze ergodische zone te herkennen als het donkerste gebied, met de meeste doorsnijdingen van de veldlijn met de poloïdale doorsnede. Kettingen van magnetische eilanden die niet overlappen zijn nog zichtbaar evenals de ergodische vingers. De laminaire zone is wit omdat de reconnectie lengte van de veldlijnen hier meestal kleiner is dan één toroïdale omwenteling. De gesloten magnetische oppervlakken in de kern zijn niet getekend op de Poincaré plots, maar zouden voorgesteld worden als cirkels, of rechten in de vlakke representatie van fig. 1.19(c). De basis configuratie van het storingsveld is de m/n = 12/4 mode, maar ook 3/1, 6/2 en combinaties hiervan, zijn mogelijk.

Deze nieuwe magnetische structuur heeft gevolgen voor het energie- en deeltjestransport in het plasma. Door de korte reconnectielengte van de veldlijnen in de laminaire zone worden deeltjes onmiddellijk naar de wand geleid, waar ze neutraliseren, en terug in het plasma kunnen worden gereflecteerd. In de ergodische zone, met zeer lange reconnectie lengtes, wordt het transport door diffusie van deeltjes (aangeduid door de diffusie coëfficiënt D) en energie (genoteerd als χ) sterk vergroot in vergelijking met de limiter plasma's, door het stochastische gedrag van de veldlijnen in deze zone [Toka97, Gerh04]. Het gevolg is een dicht en koel randplasma [Lehn05].

Voor de onzuiverheidsionen werd gemodelleerd [Toka97, Gerh04] dat vooral de convectie snelheid (v_I) wijzigt (omkeert van richting, dus positief wordt) onder invloed van de nieuwe magnetische configuratie. Het gevolg is een daling van de randtemperatuur, omdat onzuiverheden naar de wand worden gedreven, en daar vaker worden gerecycleerd en dus ook meer stralen. Eveneens ontstaat een transportbarrière die de onzuiverheden verhindert om door te dringen tot het kernplasma. Dit is het zogenaamde 'screening' effect (afscherming) van de onzuiverheden, en werd reeds experimenteel vastgesteld op de tokamak Tore Supra onder invloed van een statische ergodische divertor [Ghen96].

Op TEXTOR werd geopteerd voor een dynamische ergodische divertor omdat op die manier de hitte beter zou kunnen worden verspreid over de wand, en omdat een snel roterend storingsveld een plasma rotatie zou kunnen induceren [Fink99, Fink05]. Een differentiële rotatie in bepaalde zones van het plasma zou dan weer turbulente cellen kunnen breken en de opsluiting verbeteren, analoog aan het mechanisme voor de creatie van een ITB.

1.3.2 Een spectroscopische diagnostiek voor de detectie van koolstofionen

Voor de studie van het 'screening' effect op de intrinsieke onzuiverheid koolstof is een diagnostiek ontworpen en geïnstalleerd op TEXTOR. In een poloïdale doorsnede worden op verschillende lokaties C^{2+} en C^{4+} ionen gedetecteerd. De gezichtslijnen zijn schematisch voorgesteld in fig. 1.20. De fotonen in de negen kanalen in rood, gericht naar de binnenzijde van de torus, High Field Side (HFS) waar de DED spoelen zich bevinden, worden naar een spectrometer geleid via optische vezels waar de spectrale lijnen $\lambda_{C^{2+}} = 229.6$ nm (C III) en $\lambda_{C^{4+}} = 227.1$ nm

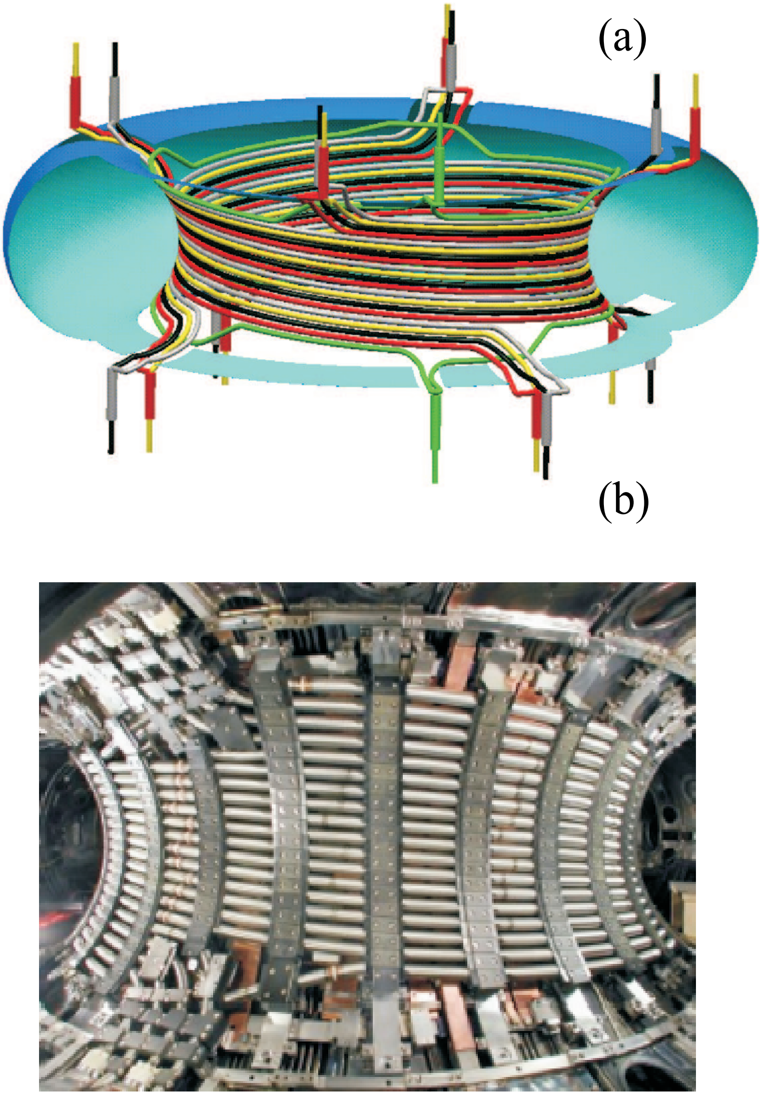

Figuur 1.18: De DED aan de binnenzijde van TEXTOR. (a) Schematische voorstelling met de 4 sets van 4 spoelen en in groen de 2 compensatie spoelen, nodig voor de stabiliteit. (b) Eigenlijke opstelling in de tokamak, de grafiet tegels die de spoelen en de wand beschermen tegen het hete plasma, zijn nog niet gemonteerd op deze foto.

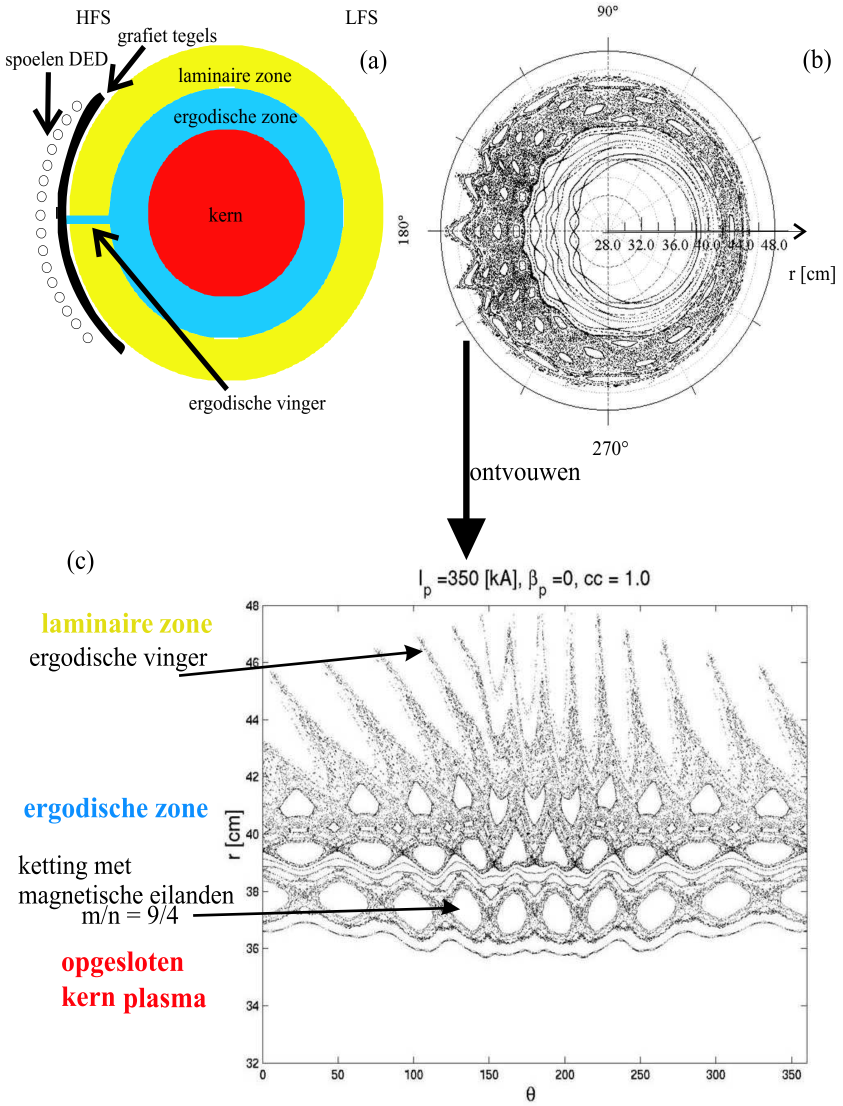

Figuur 1.19: (a) De verschillende magnetische zones die gecreëerd worden door het storingsveld van de DED: de laminaire en ergodische zone en de onverstoorde kern. (b) Een voorbeeld van een Poincaré plot in een poloïdale doorsnede en (c) de vlakke representatie, het resultaat van het openen van de circulaire plot op $\theta = 0$. Hierbij is de horizontale as de poloïdale hoek en de verticale as is de kleine straal.

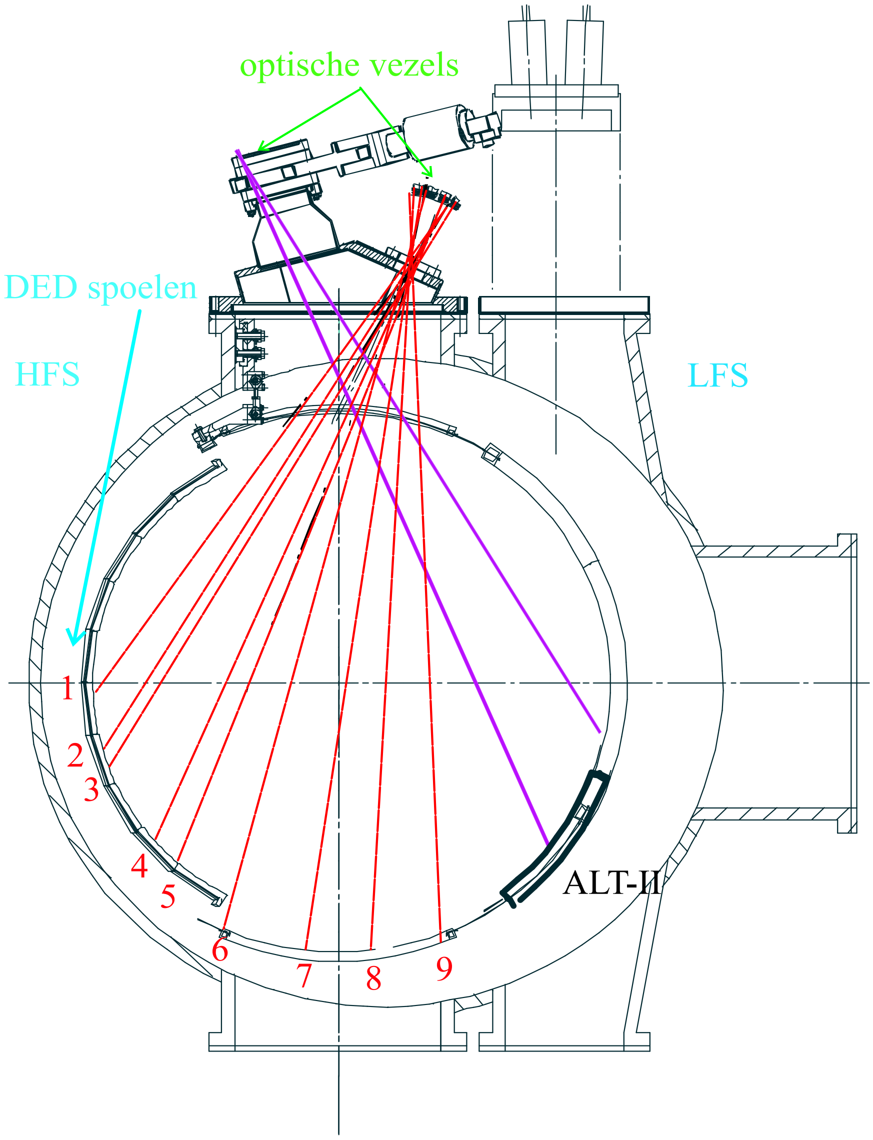

Figuur 1.20: Schematische voorstelling van de gezichtslijnen van de diagnostiek voor de detectie van koolstofionen in een poloïdale doorsnede van TEXTOR. De fotonen worden via optische vezels naar spectrometers geleid waar spectrale lijnen van de koolstofionen worden geselecteerd.

(C V), in het UV, worden gedetecteerd. De twee gezichtslijnen aan de buitenzijde van de torus, de Low Field Side (LFS) zijn verbonden met een tweede spectrometer en detecteren eveneens C^{2+} ionen, maar via een spectrale lijn in het zichtbare golflengte bereik bij 465 nm. De keuze van de spectrale lijnen in het UV vereisten optische vezels met een relatief hoge transmissie bij deze golflengtes, en ook de fotomultiplicatoren werden zodanig gekozen dat de kwantumefficiëntie maximaal is rond 230 nm.

Een nauwkeurige relatieve calibratie van de negen verschillende kanalen aan de LFS was niet mogelijk door kleine afwijkingen in de uitlijning van de verschillende optische vezels aan de in- en uitgang van de spectrometer. Tests werden gedaan met een Hg(Ar) calibratie lamp.

Het UV gedeelte van de diagnostiek kan op twee verschillende manieren worden gebruikt :

- Een scan van de negen gezichtslijnen met een herhalingstijd van ongeveer 100 ms voor de complete set. Elke gezichtslijn afzonderlijk wordt telkens gedurende ongeveer 10 ms geselecteerd en de fotonen worden gedetecteerd met de fotomultiplicatoren. Met behulp van een deconvolutie programma is het mogelijk om de tijdsevolutie van de verschillende kanalen afzonderlijk te bekijken, met een tijdsresolutie van 100 ms.
- Eén gezichtslijn kan worden geselecteerd voor de detectie met hoge tijdsresolutie (< 1 ms), hierbij gaat de informatie van de andere kanalen verloren. Een scan over de verschillende kanalen is dan slechts mogelijk met een set van identieke ontladingen.

1.3.3 Screening van koolstofionen door middel van de DED

Experimentele data van deze diagnostiek werden gebruikt om het effect van de DED op de koolstofemissie te bestuderen in zowel de 3/1 als de 12/4 configuratie. In deze laatste configuratie was echter slechts een beperkte sterkte van het storingsveld technisch haalbaar.

Het voorbeeld van fig. 1.21 is in de 3/1 mode, de DED stroom in een set van spoelen werd tijdens de ontlading opgevoerd van 0 tot -2 kA. In deze configuratie vloeit een positieve stroom in acht van de zestien spoelen en een negatieve in de andere. Bij +/- 1 kA wordt een 2/1 mode in het plasma geëxciteerd met als gevolg een verlies van deeltjes en energie uit het plasma. Op de figuur is een plotse daling van n_e te zien, die dan wordt gecompenseerd door de actie van het feedback systeem. De C III emissie reageert met een sterke toename. Dit is zowel te zien op de signalen van de UV diagnostiek, als bij de VUV diagnostiek, die één gezichtslijn heeft in het horizontale vlak en dwars door het plasma kijkt van de buiten- naar de binnenzijde van de torus. De relatieve toename is echter sterker bij de UV diagnostiek, en verschillend voor de verschillende kanalen. Tegelijkertijd daalt de C V emissie en de gemiddelde onzuiverheidsconcentratie ($\mathrm{Z_{eff}}$).

Een zoom op de verschillende kanalen van de UV diagnostiek zonder en met de ED illustreert beter het verschil in respons afhankelijk van de poloïdale oriëntatie van de gezichtslijn (fig. 1.22). De toename van de C III emissie met de ED is het sterkst in de kanalen 2 en 3. Ook de daling van C V emissie is relatief gezien het grootst in deze kanalen. De verhouding van de intensiteiten van de beide spectrale lijnen (C III / C V) kan beschouwd worden als een maat voor het 'screening effect' veroorzaakt door de ED. Een verhoging in C III intensiteit is wijten aan de creatie van een dicht en koud randplasma onder invloed van de ED en een verhoogde recycling van de koolstofionen, door een positieve convectie snelheid (i.e. uit het plasma) voor de onzuiverheidsionen. De daling in C V intensiteit gaat gepaard met een daling in C^{6+} concentratie (gemeten met CXRS) en in de centrale Z_{eff}, en wijst daarom op een vermindering in totale koolstofconcentratie van het opgesloten kernplasma. De oorzaak van deze plasma decontaminatie is het transport naar buiten toe van de onzuiverheidsionen door wrijvingskrachten met de plasma ionen, die zelf een verhoogde diffusiecoëfficiënt hebben in de stochastische zone. Zoals te zien op figuur 1.23 neemt de verhouding van de intensiteiten C III / C V toe met de stroom in de DED spoelen, en is zeer sterk uitgesproken voor kanaal 2. Een verklaring voor het verschil tussen kanalen 2 (en 3) en de andere gezichtslijnen moet gezocht worden in het onderscheid tussen een lokale en globale plasma respons op de DED. In figuur 1.24 is de magnetische structuur voorgesteld die gecreëerd wordt door de DED in 3/1 mode. Kanaal 2 (en 3 ligt zeer dicht in de buurt) doorsnijdt een ergodische vinger, waar dus een onmiddellijk

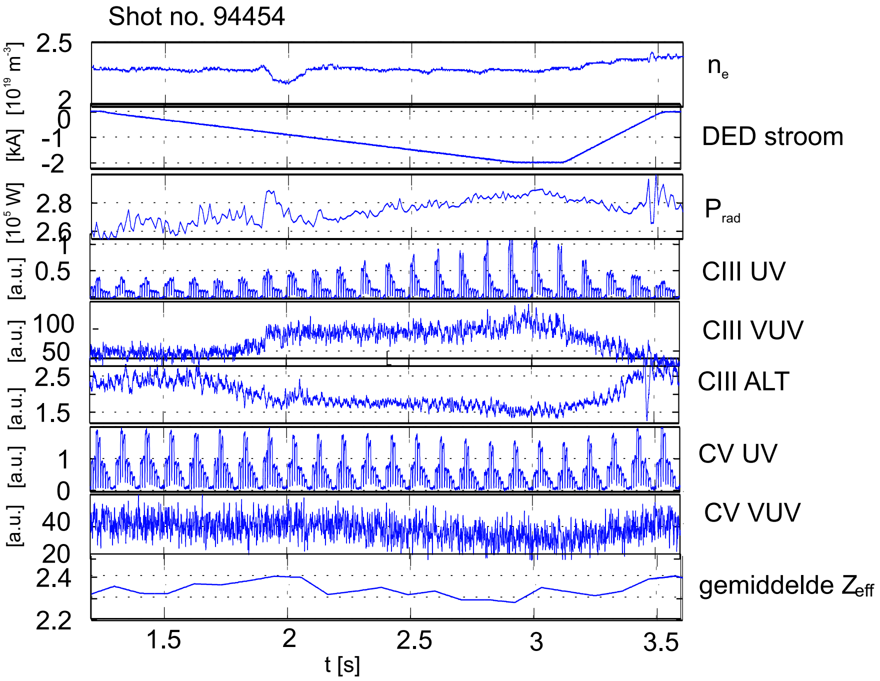

Figuur 1.21: Effect van de statische ED in 3/1 mode (met een geleidelijke toename van de DED stroom) op de plasma dichtheid (n_e), de totale straling (P_{rad}) en de onzuiverheidsconcentratie (Z_{eff}), en op de intensiteiten van de C III en C V spectrale lijnen. Het plasma had $I_p = 300kA$ en $B_t = 2.25T$.

contact is tussen de ergodische zone en de wand met een sterke plasma wand interactie tot gevolg. Dit is dus een lokaal fenomeen. De toename in kanaal 8 daarentegen is representatief voor de globale respons van het plasma.

Anders is de situatie in de 12/4 mode, zoals geïllustreerd in figuur 1.25 voor een ontlading met DED stroom (statisch) van 7 kA (dit was de maximaal toegelaten stroom in de voorbije TEXTOR operatie). Bij het aanschakelen van de DED kan een verhoging worden gezien in de intensiteit van de spectrale lijn van de laaggeïoniseerde koolstofionen van zowel de UV als VUV diagnostiek (CI VUV, CIII UV en CIII VUV). Geen verandering treedt op bij de C V intensiteit, noch bij de UV, noch bij de VUV diagnostiek.

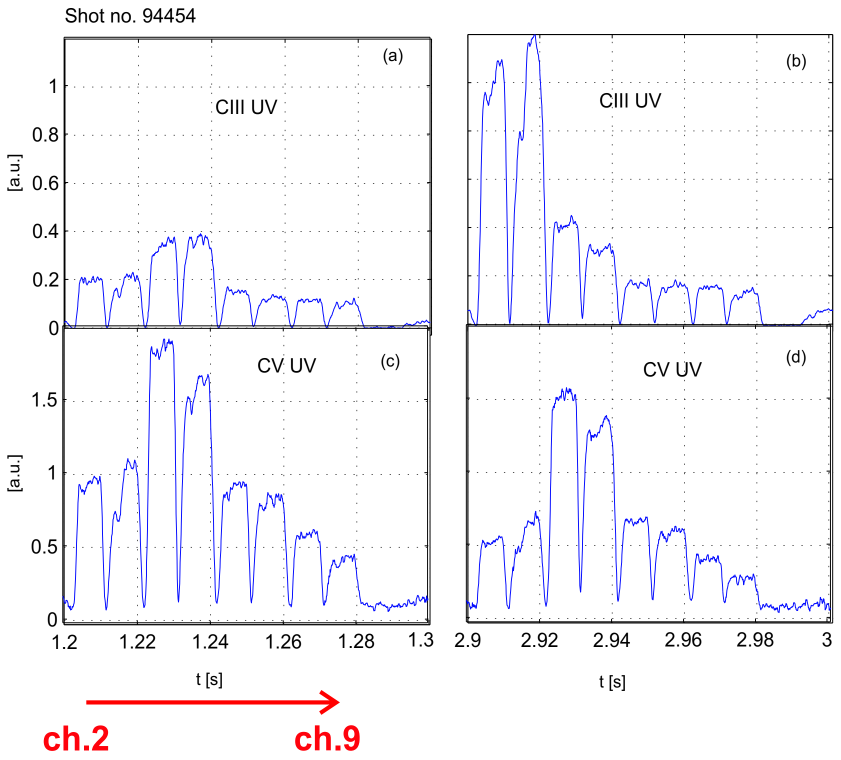

Figuur 1.22: Een zoom van fig. 1.21 met de acht (op dit moment werkende) kanalen van de UV diagnostiek voor de detectie van C III en C V. (a) C III emissie zonder ED, (c) CV emissie zonder ED, (b) C III met ED en (d) C V met ED. De C III emissie stijgt met een factor 5 in de eerste twee kanalen (nummers 2 en 3) wanneer de ED actief is, terwijl de andere kanalen slechts een matige toename vertonen. Gelijkaardig is het gedrag van de C V emissie : een daling met een factor 2 in de kanalen 2 en 3, en met een matige 30 % in de andere kanalen.

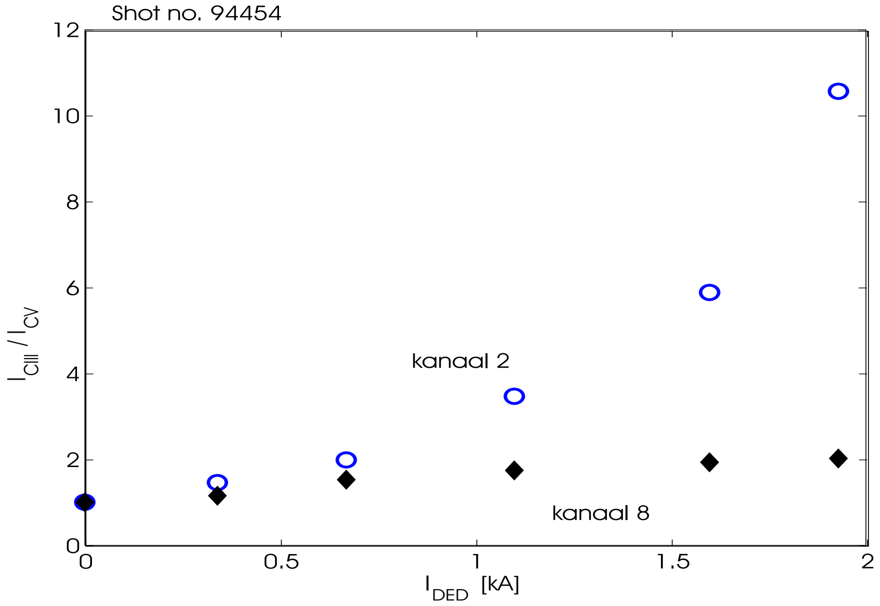

Figuur 1.23: De verhouding in C III en C V intensiteiten voor de kanalen 2 en 8 als een functie van de ED stroom. Kanaal 2 stijgt veel sterker dan kanaal 8.

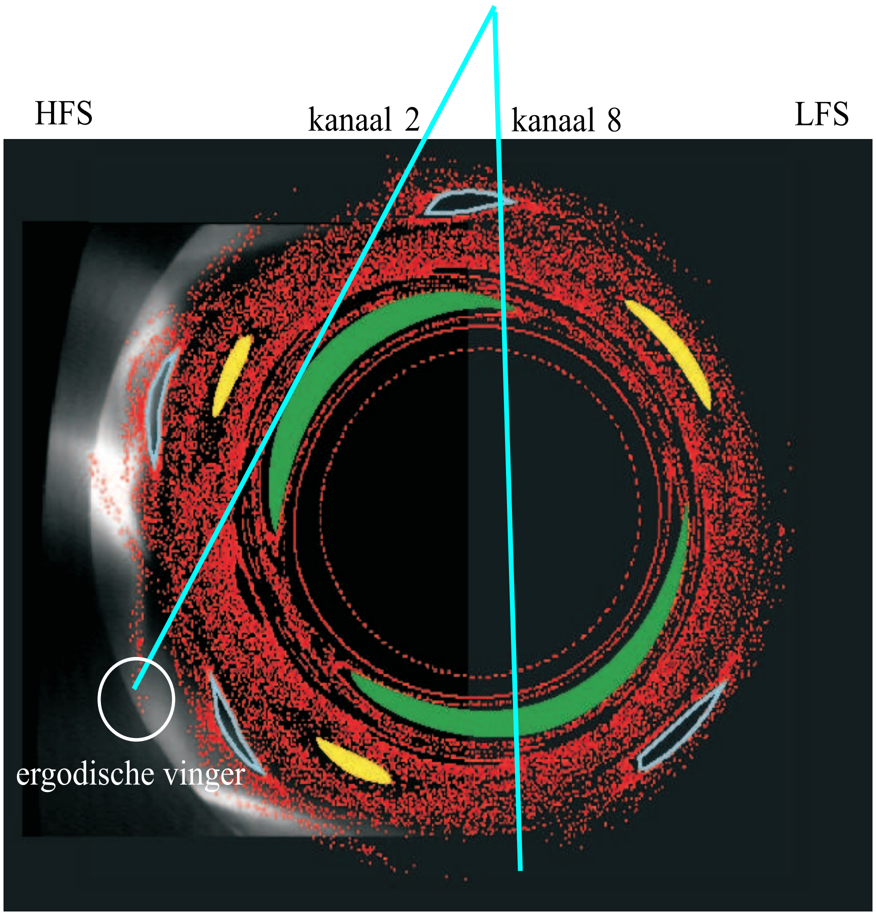

Figuur 1.24: Oriëntatie van twee kanalen op een Poincaré plot van de magnetische veldstructuur. Kanaal 2 doorsnijdt een ergodische vinger, en de emissie in dit kanaal stelt dus een lokaal fenomeel voor, terwijl de emissie van kanaal 8 de globale respons van het plasma op de DED voorstelt.

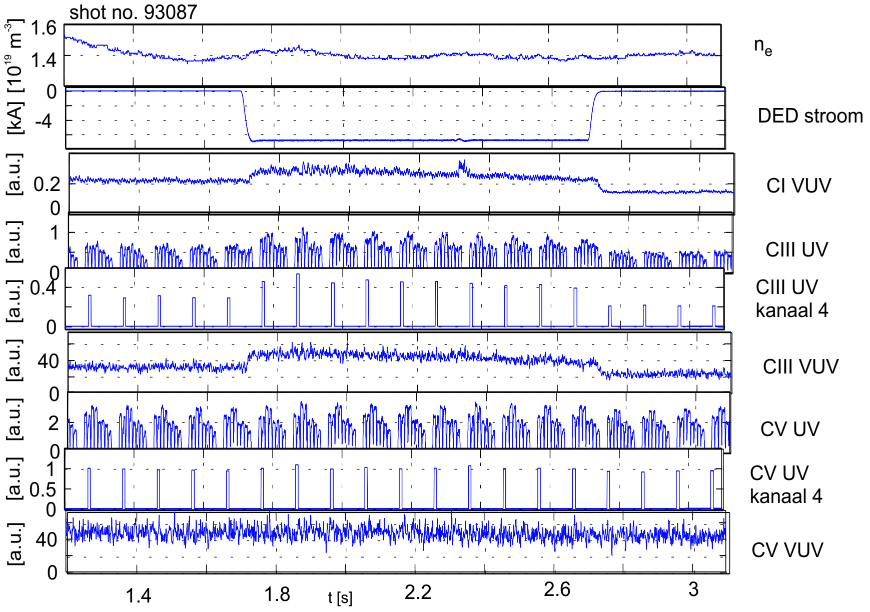

Figuur 1.25: Lijn gemiddelde centrale electronen dichtheid en ED stroom in de statische 12/4 mode ($I_p = 380$kA, $B_t = 1.9$T). Koolstofemissie van de VUV en de UV diagnostiek voor verschillende ionisatie graden van de onzuiverheid. Er is een matige toename van de emissie van de laaggeïoniseerde koolstof met de ED, maar geen verandering in de C V emissie.

1.3.4 Conclusies

In [Toka97] werd het screening effect van onzuiverheden in een ED plasma verklaard door een sterke positieve convectie (naar de wand) tengevolge van een wrijvingskracht tussen de onzuiverheden en de plasma ionen. Deze plasma ionen hebben dan weer een verhoogde diffusie coëfficiënt (ook naar buiten gericht) tengevolge van de diffusie van de veldlijnen in de ergodische zone. Aangezien de sterkte van de wrijvingskracht tussen onzuiverheden en plasma ionen afhangt van de ionisatiegraad van de onzuiverheden, worden hooggeïoniseerde onzuiverheden preferentieel naar buiten gedreven, met een vermindering van de totale onzuiverheidsconcentratie (Z_{eff}) tot gevolg. Tegelijkertijd stijgt de stralingsefficiëntie van de onzuiverheden omdat een randplasma met hoge dichtheid en lage temperatuur wordt gecreëerd door de ED. Deze effecten werden in 3/1 mode ook vastgesteld aan de hand van de verhouding tussen C III en C V emissies, opgemeten langs verschillende kanalen in een poloïdale doorsnede. In 12/4 mode werd wel een verhoging van de C III emissie geobserveerd, maar geen vermindering van C V of Z_{eff} en daarom kan hier niet echt gesproken worden van een screening effect. Dit kan te wijten zijn aan de minder diepe penetratie van het storingsveld in de 12/4 configuratie, of de beperkte amplitude, omdat slechts 50% van de maximale stroom in de DED spoelen toegelaten was. Verdere studies in 12/4 met hogere stroom zijn voorzien in de toekomst, als ook in de 6/2 configuratie.

Aan de diagnostiek zelf zijn volgende verbeteringen mogelijk :

- Een betere relatieve calibratie is mogelijk door de installatie van nieuwe ingangs- en uitgangsslits met een nauwkeuriger positionering van de optische vezels. Bovendien is de flux van de fotonen voldoende groot om een vernauwing van de ingangsslit toe te laten waardoor de resolutie vergroot. Er kan geopteerd worden voor uitgangsvezels met een grotere kerndiameter waardoor een groter gedeelte van de spectrale lijn wordt gedetecteerd, en de gevoeligheid voor uitlijningsfouten verkleint.

- Een hogere tijdsresolutie voor alle kanalen is aangewezen tijdens de DED operatie met hoge rotatiefrequenties van het storingsveld, zodat ook overgangsverschijnselen kunnen worden bestudeerd. Hiervoor werd een set van 2×9 fotomultiplicatoren aangekocht, waardoor de C III en C V intensiteiten langs de negen kanalen alle afzonderlijk kunnen worden opgemeten. De tijdsresolutie zal hierdoor van de orde van 1 ms worden.

- Om een uitgebreidere studie van het transport van de koolstofionen mogelijk te maken werd een bijkomende set van spectrometers geïnstalleerd voor de detectie van C^{1+} ionen langs gezichtslijnen met ongeveer dezelfde oriëntatie als de UV diagnostiek.

Chapter 2

Introduction

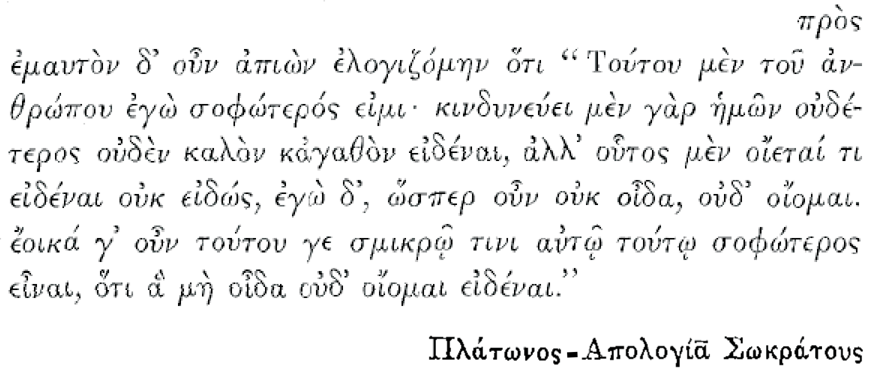

> πρὸς ἐμαυτὸν δ᾽ οὖν ἀπιὼν ἐλογιζόμην ὅτι “Τούτου μὲν τοῦ ἀνθρώπου ἐγὼ σοφώτερός εἰμι· κινδυνεύει μὲν γὰρ ἡμῶν οὐδέτερος οὐδὲν καλὸν κἀγαθὸν εἰδέναι, ἀλλ᾽ οὗτος μὲν οἴεταί τι εἰδέναι οὐκ εἰδώς, ἐγὼ δ᾽, ὥσπερ οὖν οὐκ οἶδα, οὐδ᾽ οἴομαι. ἔοικά γ᾽ οὖν τούτου γε σμικρῷ τινι αὐτῷ τούτῳ σοφώτερος εἶναι, ὅτι ἃ μὴ οἶδα οὐδ᾽ οἴομαι εἰδέναι.”
>
> **Πλάτωνος - Ἀπολογίᾱ Σωκράτους**

2.1 Fusion energy on earth

The need for sources of clean and sustainable energy is growing with the increasingly urgent global energy demand situation. The evolution of the global energy consumption during the period 1850 – 1990 is illustrated by the graph in figure 2.1. During the last century the total amount of energy used each year has increased by a factor of ten and the primary source has been fossil fuels. The environmental and political consequences of the large scale use of fossil fuels are well documented. Intrinsically, the energy released by a chemical reaction such as burning is much lower (about a factor of 10^6) than the energy released by a nuclear reaction (fission or fusion). The electromagnetic

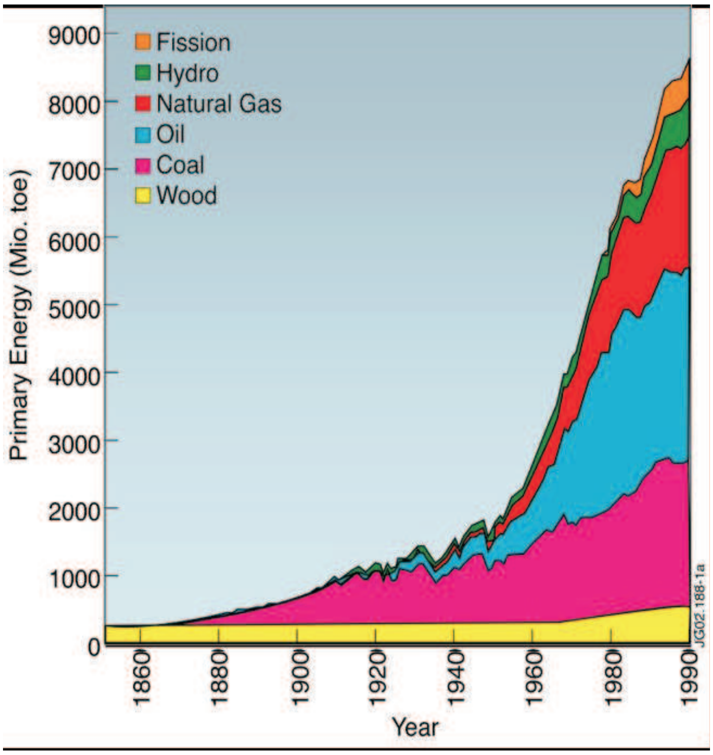

Figure 2.1: Amount of energy produced each year from different primary energy sources.

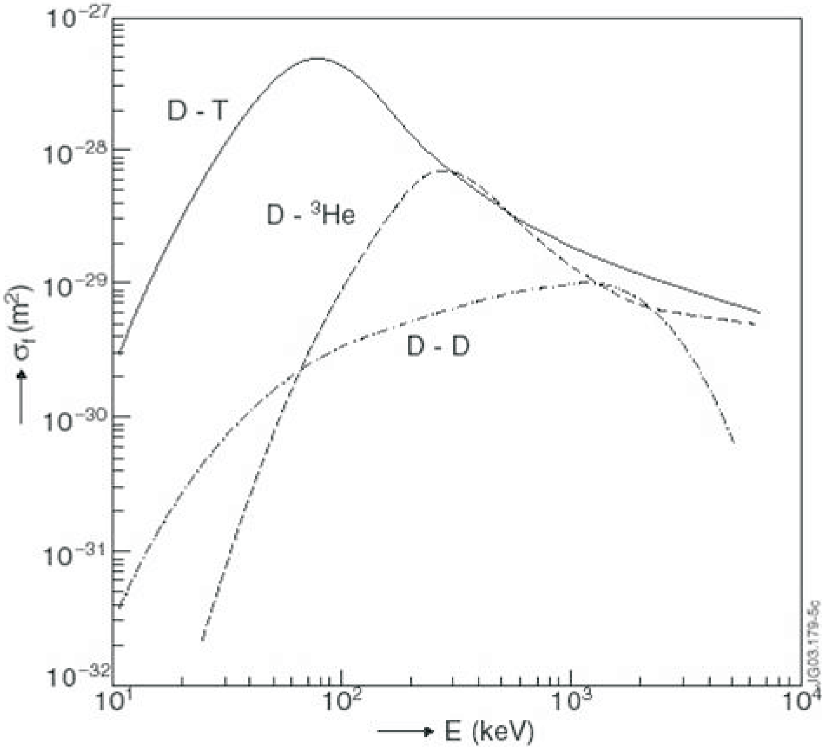

Figure 2.2: Cross-sections of the fusion reactions between D-T, D-D and D-^{3}He.

force that holds the atoms together in molecules is much weaker than the strong nuclear force that binds the protons and neutrons into an atomic nucleus. Therefore, the amount of fuel that is required for nuclear energy production is only a small fraction of the many tons of coal and gas, which are burned daily for the present electricity supply base-load. The roles of both nuclear power and renewable energy have become more important as the need to restrict the burning of fossil fuels due to the greenhouse effect. The use of renewable energy sources in place of fossil fuels can substantially reduce the greenhouse gases and other pollutants. While it is presently impossible for renewable energy sources to meet base-load requirements due to their fluctuations in time and space, they can provide a valuable contribution to the total energy mix. Most renewable energies use indigenous resources and enhance a country's independence from external supplies of primary fuels. Fusion is a potential alternative to nuclear power from fission. While it is arguably one of the major research challenges of the 21^{st} century, it would produce energy with no troublesome emissions and would run on fuel readily available to all nations. It could be operated safely, and would create no long-lived waste. Fusion is an option to provide environmentally benign energy for the future without depleting natural resources for next generations [Onge02].

In stars such as our sun, mainly hydrogen nuclei (protons) fuse to helium, but this reaction has too low probability to be used for energy production on earth, because of the very limited size of the laboratory plasmas, as compared to the enormous volume of the sun. For the same reason artificial means, such as magnetic fields [1], have to be used instead of gravitational force to control the plasma dimensions, and thus to confine the particles during a sufficiently long time (at the required high densities and temperatures) to allow a certain number of fusion reactions to happen. So far, the most promising way towards a fusion reactor based on magnetic confinement is the tokamak configuration (section 2.2). The fusion reaction that is used is between the hydrogen isotopes deuterium (D) and tritium (T), producing helium-4 (^{4}He) and a neutron (n) with a total energy of 17.6 MeV and can be written as :

$$\mathrm{D} + \mathrm{T} \rightarrow^4 \mathrm{He}(3.56\mathrm{MeV}) + \mathrm{n}(14.03\mathrm{MeV}). \tag{2.1}$$

---

[1] An alternative direction of the nuclear fusion research is inertial confinement, in which laser or particle beams are used to strongly compress a fuel pellet and start the fusion reaction.

The reaction probability as a function of energy for this and two other reactions (D + D and D + ^{3}He) that naturally happen in a deuterium tritium plasma, are shown in figure 2.2. It can be seen that the required energies for a reasonable reaction probability are of the order of 10 keV, which corresponds to temperatures of more than 100 million degrees, much hotter than the center of the sun. At such high temperatures the deuterium and tritium atoms split into positive ions and negative electrons to form a plasma, and the movements of these charged particles can be controlled by magnetic fields.

In eq.(2.1) the partition of the total energy of 17.6 MeV into the neutron (80 %) and the α-particle (20 %) is given. Ideally a future fusion reactor will be self-sustained by the energy of the α-particles, which are charged and thus confined by the magnetic field. In terms of Q, the fusion performance parameter, defined as the ratio between fusion power and the total input power

$$Q = \frac{P_{\text{fusion}}}{P_{\text{input}}}, \tag{2.2}$$

this situation corresponds to $Q = \infty$ and is called ignition. As already described above, the ion density (n_i) and temperature (T_i) are two crucial parameters for the total achievable fusion power in a reactor. A third important factor is the energy confinement time (τ_E), defined as

$$\tau_E = \frac{W}{P_{\text{loss}}} \tag{2.3}$$

with W the energy of the plasma, and P_{loss} the power lost by thermal conduction and convection (and radiation, depending on the exact definition of τ_E). It is a measure for the quality of the magnetic confinement. For a given value of Q the three parameters n_i, T_i and τ_E are related, as first stated by Lawson [Laws57].

2.2 The tokamak

No material can withstand the high temperatures involved in fusion, and therefore the plasma cannot make contact with the walls of the vessel in which it is contained. In figure 2.3a the example of a cylindrical plasma is given with its random thermal particle motion. Applying a constant magnetic field parallel to the axis of the cylinder forces the charged particles to follow the field lines (figure 2.3b), and holds the plasma into limited boundaries controlled by the external field. The

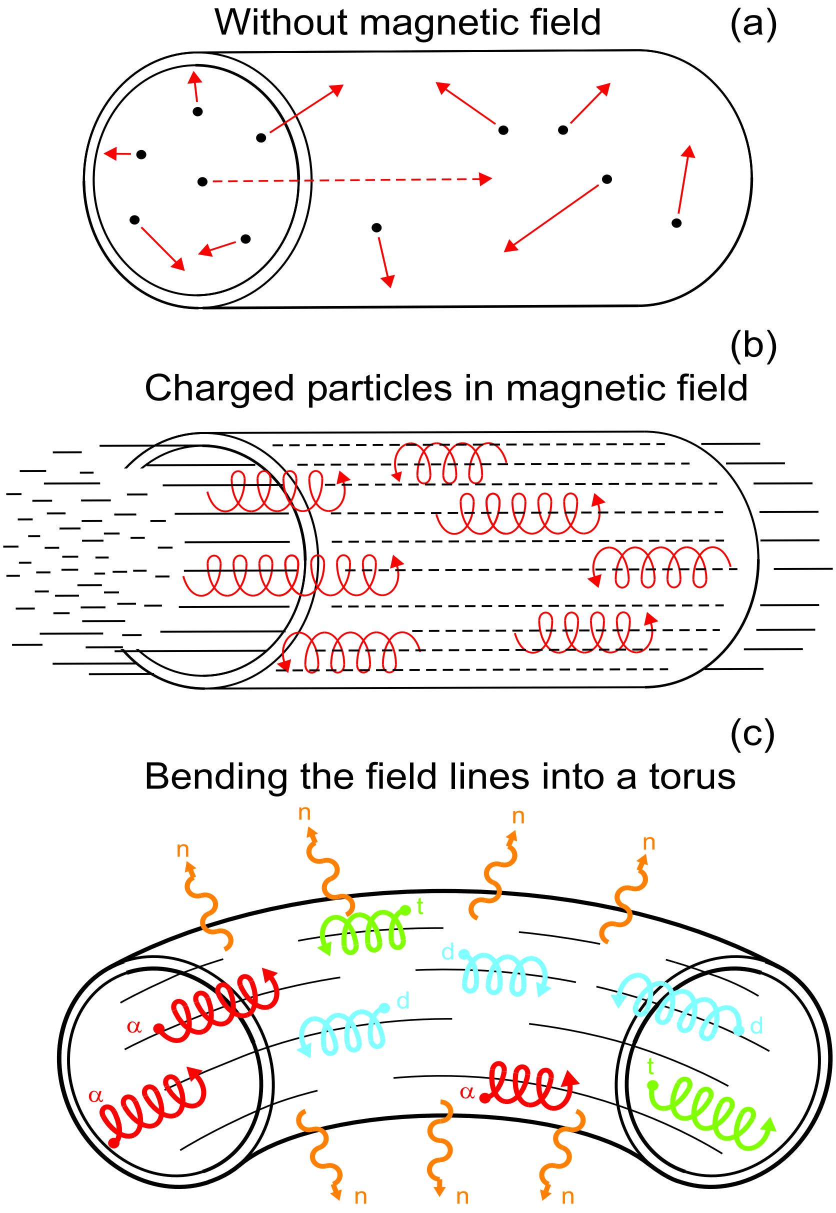

Figure 2.3: (a) Random movement of particles in a cylinder without magnetic field. (b) The charged particles move in a spiral around the magnetic field lines by the Lorentz force. (c) A toroidal trap for the particles is created by bending the edges of the cylinder together into a torus.

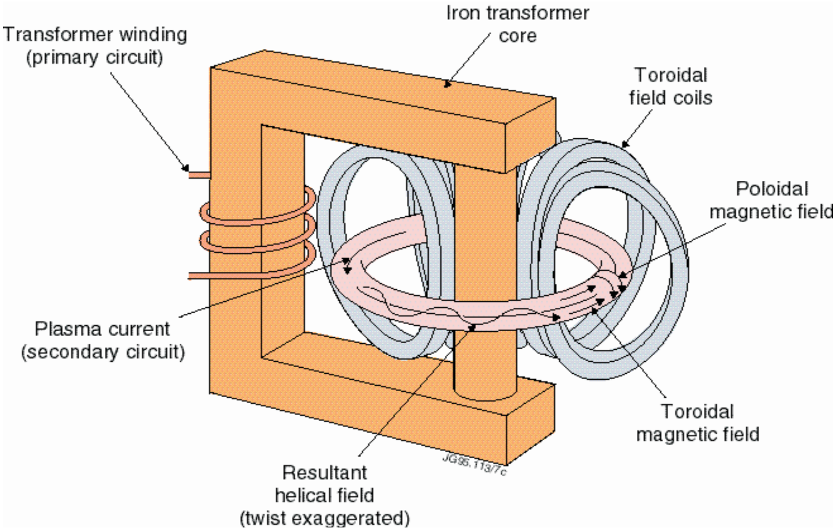

Figure 2.4: Magnetic fields and currents in a tokamak. The transformer induces the plasma current, and this toroidal current generates the poloidal magnetic field (B_θ). The toroidal magnetic field (B_ϕ) is created by the toroidal field coils. The resulting combination of the toroidal and poloidal field components is the helical field.

particles spiral around the field lines under the influence of the Lorentz force. Bending the field lines into a torus deals with the end losses (figure 2.3c) of a cylinder, but creates additional losses due to the curvature of the magnetic field and its gradient. The toroidal magnetic field (B_ϕ), that is created by a current flowing in coils poloidally wound around the torus, indeed decreases from the center of the torus towards the outside (Ampère's law for a toroidal configuration). These particle losses can be avoided by adding a poloidal field component (B_θ). Since the poloidal field generates a circulation of the charged particles around the magnetic axis, it short circuits any vertical electric field that would build up from the charge separation of ions and electrons caused by the vertical motion due to curvature and gradient drifts.

In a stellarator configuration complicated structures of coils are wrapped around the torus to create the desired helical magnetic field, whereas in a tokamak only B_ϕ is created by the 'toroidal field coils', wound poloidally around the torus, and B_θ is generated by a toroidal current induced in the plasma that acts as the second circuit of a transformer. A summary of the currents and magnetic fields in and around a tokamak is given in figure 2.4. Because of the transformer action that induces the plasma current a tokamak is pulsed and the discharges have a strongly limited duration. However, in view of a continuous reactor operation, methods are being studied to sustain the plasma current via other means.

An additional vertical magnetic field is used to provide horizontal stabilization of the plasma and is generated by coils wound around the torus in toroidal direction (not shown in figure 2.4). In tokamaks B_ϕ is typically 10 times larger than B_θ, which also increases the plasma stability. Nevertheless the operating conditions of a tokamak must be carefully selected as the plasma becomes unstable above a certain plasma current, density and β. β is the ratio of the kinetic or plasma pressure (p) and the magnetic pressure ($B^2/2\mu_0$),

$$\beta = \frac{p}{B^2/2\mu_0}. \tag{2.4}$$

The plasma pressure is the sum of electron and ion pressures ($p = n_e kT_e + \sum n_i kT_i$), k is Boltzmann's constant and μ_0 is the permeability of the vacuum. The total fusion power in a reactor scales with the square of the density (more precisely $n_i^2/4$ for a pure mixture of 50 % deuterium and 50 % tritium) and thus with $\beta^2 B^4$. Therefore, high values of β and magnetic field are desired, but the achievable range is determined by the operating limits.

Table 2.1: Typical JET, TEXTOR and ITER tokamak parameters.

Parameter	JET	TEXTOR	ITER
Major Radius R_0 [m]	3.00	1.75	6.21
Minor Radius a [m]	1.25	0.50	2.00
Vertical elongation κ	1.6	≈ 1.0 (circular)	1.8
Plasma volume [m^3]	80 - 100	7	837
Magnetic field B_ϕ [T]	3.4	3.0	5.3
Plasma current I_p [MA]	5 - 7	0.8	15 (upto 17)
Duration pulse [s]	10 - 60	< 10	≥ 400
Fusion power [MW]	16		500 (upto 700)
Performance Q	0.7		10

Typical parameters of two tokamaks, JET and TEXTOR, on which the work for this thesis was performed, are given in table 2.1.

JET

The Joint European Torus (JET) is located in Oxfordshire, UK, and is presently the largest tokamak in the world. An inside view both with and without the plasma is shown in figure 2.5. During experiments in 1997 with 50 % D – 50 % T plasmas Q values close to break-even ($P_{\text{fusion}} = P_{\text{input}}$) were reached.

TEXTOR

The Tokamak EXperiment for Technology Oriented Research (TEXTOR) in Jülich, Germany, is a medium sized tokamak, specially suited for studies of plasma wall interaction (figure 2.6). It is a limiter (section 2.3.2) tokamak with circular plasma cross-section, as can be seen in figure 2.7.

ITER

The fusion world is now eagerly waiting for the International Thermonuclear Experimental Reactor (ITER), a 500 MW (thermal power) experimental plant, which is a collaboration between China, Europe, Japan,

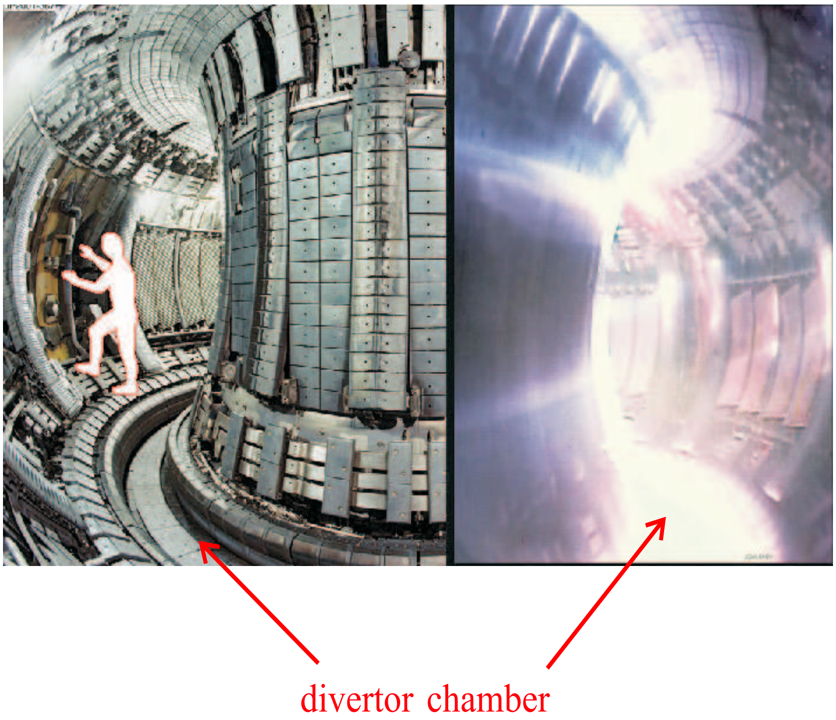

Figure 2.5: Inside view of the JET tokamak. Left part is without plasma, the right is during a discharge. The visible light is Balmer D_α radiation. The divertor chamber is indicated (section 2.3.2). In this cooler region, the intensity of the visible Balmer D_α radiation is much higher than in the hot central parts of the plasma.

Figure 2.6: View of TEXTOR, the tokamak can be split in two halves to allow good access to the machine.

Russia, South-Korea and the United States. In June this year was decided to build ITER in Cadarache (France). ITER will have about double the size of JET and have plasmas of eight times the JET plasma volume. A comparison on the same scale of the present JET and future ITER is in figure 2.8. Numerical values of the typical parameters for ITER are also shown in table 2.1. Although further research and development needs to be done on materials for ITER, it is expected to be the last major step between today's experiments and a demonstration power plant.

2.3 Topics studied in the thesis and their relation to the current fusion research

2.3.1 High confinement in plasmas with internal transport barriers

In order to reach a high fusion power the hot and dense plasma must be confined for a sufficiently long time. In a tokamak plasma several physical mechanisms lead to cross field transport of energy and particles, limiting their confinement times. Therefore understanding these

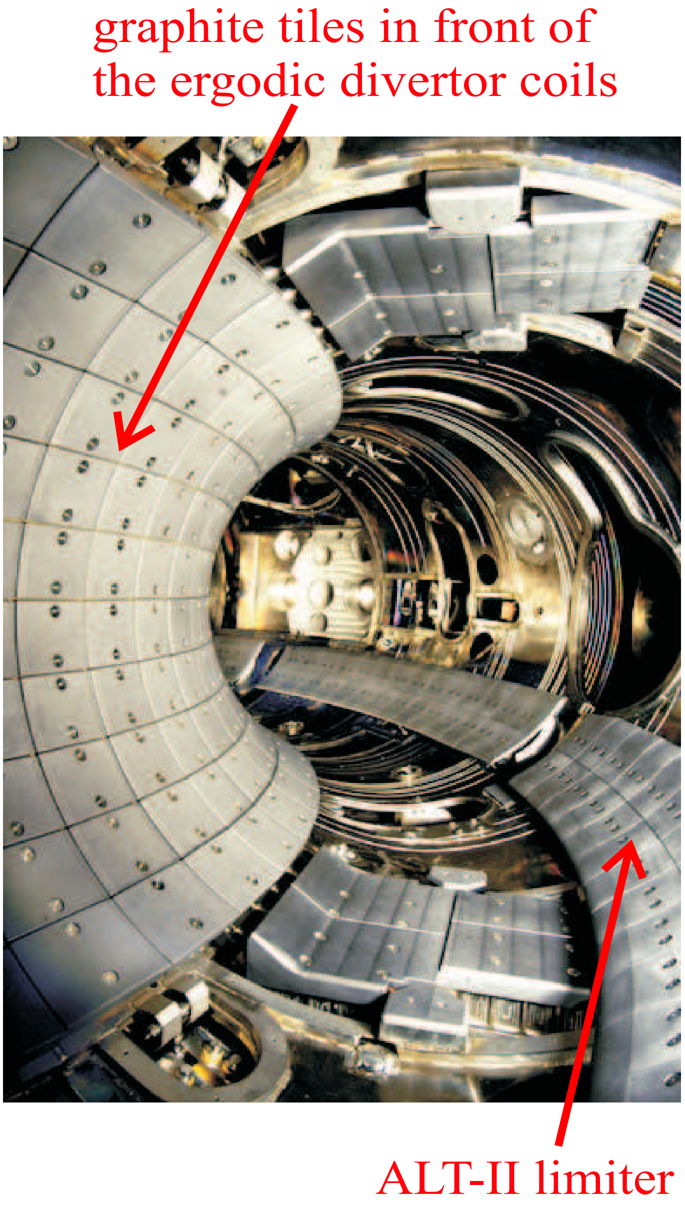

Figure 2.7: Interior of TEXTOR, the circular cross-section is clearly visible, as well as the graphite tiles covering the coils of the ergodic divertor at the high field side, and the ALT-II limiter at the low field side (section 2.3.2).

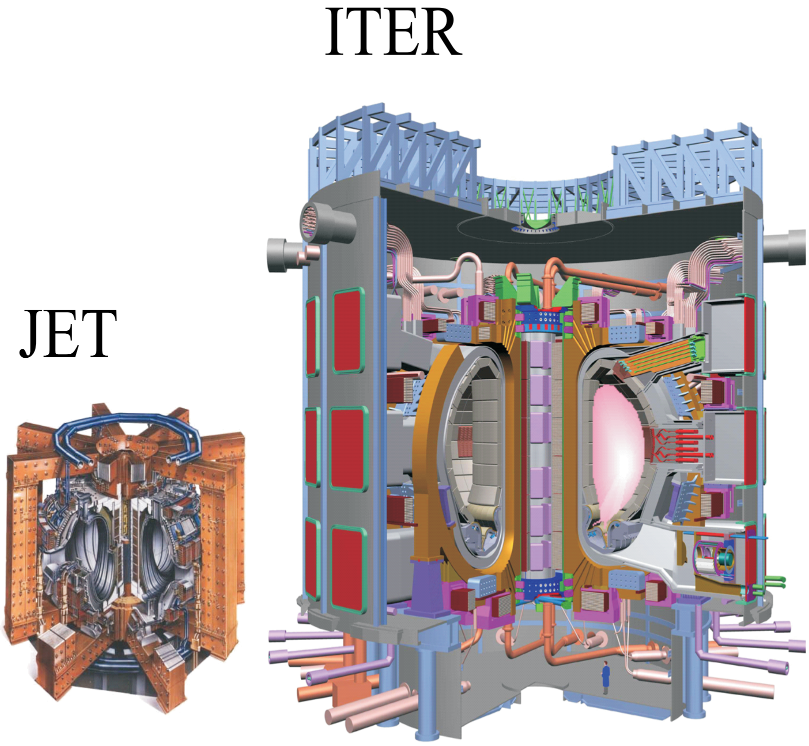

Figure 2.8: Comparison of the JET and ITER tokamak dimensions.

processes is a crucial aspect of fusion research. One of the biggest discoveries during tokamak development has been tokamak scenarios with high confinement. (i) The H-mode, which was identified for the first time in the ASDEX tokamak (Garching, Germany) [Wagn82]. (ii) The 'Advanced Modes', which rely on the presence of an Internal Transport Barrier (ITB). It is generally believed that a modification of the plasma current profile leads to a strong reduction of the turbulent transport in certain regions of these plasmas, although the conditions are not yet completely understood or controlled. Most likely a radially sheared plasma flow tears apart turbulent eddies. With the measurement of the poloidal rotation velocity on JET, presented in this thesis, an important contribution to the radial electric field and $\mathbf{E} \times \mathbf{B}$ shearing rate has been identified. Another reason why the ITB operating regime is interesting for a reactor is because of its potential for long pulse operation; the strong pressure gradient, associated with the transport barrier, drives a toroidal current (the 'boot-strap' current).

2.3.2 Hot central and cool edge plasmas

Three different methods are used to obtain the high temperatures necessary for fusion. The first one is the ohmic (joule) heating, which increases with the plasma current ($\mathrm{P_{ohmic}} \sim \eta \mathrm{I_p^2}$, where η is the resistivity), but the current limit sets a maximum value unless the B-field is also increased. The highest possible magnetic fields are technologically constrained to about 6 Tesla. Moreover the plasma resistivity decreases with increasing temperature, reducing the capability of the current to heat the plasma. Therefore two additional heating methods are used : the injection of fast neutral particles, deuterium or tritium atoms can be used on JET, and the injection of electromagnetic waves, resonant to certain characteristic frequencies of the plasma. By controlling the power deposition profile of these additional heating methods a non-inductive current can also be driven, for example in order to create the ITB plasmas mentioned in 2.3.1, and with a view to continuous operation.

While the centre of the plasma in this way easily reaches temperatures of more than 100 million degrees, the heat fluxes to the wall elements must remain below 10 MW/m^2, considered to be the technological limit. An important part of fusion research is oriented to plasma wall interactions and efficient heat and particle exhaust. The neutrons carry 80 % of the fusion power produced and immediately escape from the magnetically confined plasma. In a reactor this heat flux would be dissipated in a blanket around the torus and is not expected to pose major problems. The α-particles carry the remaining 20 % of the fusion energy and usually remain in the central region of the plasma long enough to be able to keep the temperature high (ignition of the reactor). On the other hand, after thermalisation with the D and T ions, the helium ash needs to be efficiently removed to avoid dilution of the DT fuel. A good control of both heat and particle exhaust is thus required and the two are to a certain extent related. The energy contained in the plasma is partly radiated (by Bremsstrahlung, electron cyclotron radiation, impurity line radiation, ...). The related heat loads are quite homogeneously spread over the total plasma surface and remain below the 10 MW/m^2 limit. The thermal flux from the particles following the field lines that intersect the wall is a more serious issue. These heat loads can easily locally exceed the tolerable limit and cause severe damage to the wall elements. Sputtering releases impurities and can cause physical or chemical erosion of the walls. The role of impurities in the plasmas is somehow ambiguous. They must be avoided in the core plasma, since they dilute the fuel and radiate part of the necessary energy for fusion. However, in the edge impurity line radiation can also help to cool down the plasma and protect the vessel walls. Several options for wall materials are being studied, as well as methods to control plasma wall interaction.

A limiter that is especially designed to sustain high heat loads and particle impacts, can be built inside the torus to act as the first contact with the plasma. In some cases the limiter can be pumped to increase the particle removal efficiency. It is placed further in from the rest of the vessel and limits the size of the plasma. The limiter creates an edge region with open magnetic field lines (i.e. connected to the limiter), the scrape-off layer (SOL), that is separated from the confined plasma. A schematic picture is given in fig. 2.9a. As soon as a particle crosses the last closed flux surface (the boundary between the confined plasma and the SOL) it is almost immediately (typically 100 μs) directed towards the limiter, by fast parallel transport. The TEXTOR tokamak has toroidal as well as poloidal limiters. In figure 2.7 the toroidal ALT-II limiter is indicated. The longer the open field lines are, the longer particles can radiate and cool down before hitting the limiter surface. The characteristic length of the open field lines is of the order of $L_c = 2\pi R q$,

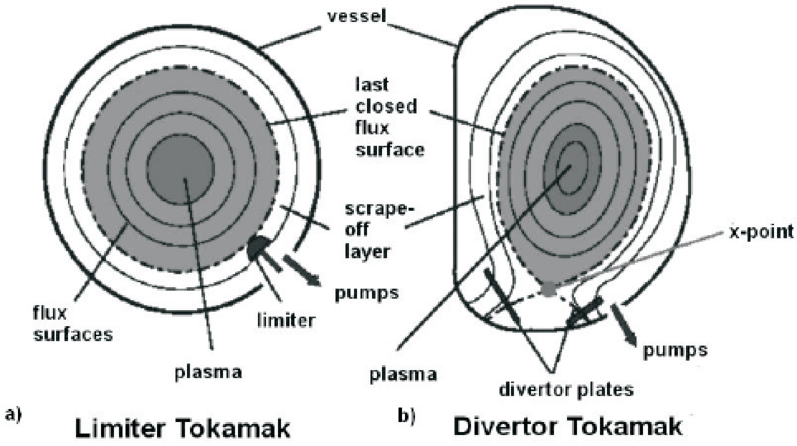

Figure 2.9: Simplified magnetic topology of (a) a limiter and (b) a divertor configuration.

with R = 1.75m (table 2.1) and $q_a \sim 3$ gives $\mathrm{L_c} \sim 30\mathrm{m}$ for TEXTOR.
The idea of a cold radiating belt around the hot plasma core has also led to the discovery of the Radiative Improved mode on TEXTOR [Mess96], a mode of operation in which injected impurities enhance the edge radiation. This scenario has also been tested on other tokamaks including JET [Onge01, MG04]. However, strong contamination of the central plasma must be avoided in a reactor, and therefore the level of impurity seeding may be limited.
Another way to enhance the edge radiation using only the intrinsic impurities while avoiding strong core contamination is to use an ergodic divertor, as has been installed on TEXTOR. The confined plasma is separated from the wall by an ergodic layer with stochastic field lines that have long connection lengths $L_c = p \cdot (2\pi R q)$, where p is the number of poloidal turns, which can be over 100 in the ergodic zone [Eich00]. The special magnetic edge configuration is achieved by introducing a small magnetic perturbation resonant to the $q = 3$ surface, as will be further discussed in chapter 7. In this thesis a contribution is made to the study of the effects of the ergodic divertor on the carbon radiation and core penetration (chapter 9). An example of the field line topology in TEXTOR with the ergodic divertor is in figure 2.10.

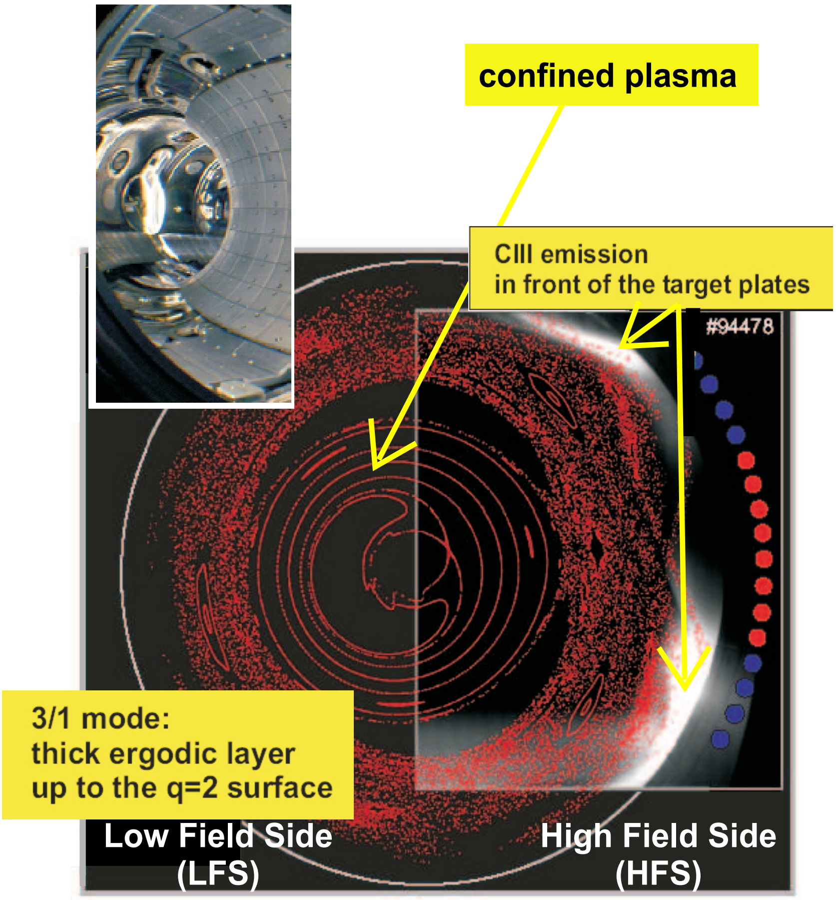

Figure 2.10: Field line mapping shows the magnetic topology in the boundary of TEXTOR with the ergodic divertor at the High Field Side (HFS). An ergodic layer forms the buffer between the confined plasma and the vessel. A cool region with enhanced radiation (here C III line radiation is shown) is created at the field line intersections with the wall, these locations can be compared to the target plates of a classic divertor. (figure has been adapted from [Lehn04])

In the axi-symmetric poloidal (classic) divertor, as installed in JET and foreseen for ITER, the magnetic field lines near the wall are diverted into a separate chamber. This is done with extra coils in which a current flows in the same toroidal direction as the plasma current. The resulting magnetic field acts against B_ϕ in the edge region, the point where the field is exactly cancelled out is the X-point, from the projection of the field line in a poloidal plane. The magnetic topology is schematically shown in fig. 2.9 (b). Particles crossing the last closed flux surfaces flow to the divertor chamber and deposit their power onto target plates. A strong pump removes a large fraction of the particles reflected from the target plates and the other part cools the divertor region, the divertor plasma temperatures are of the order of 10 eV. An important reason for the success of the divertor has been the discovery of the H-mode [Wagn82] in this type of plasma. Also, the particles released from the target plates are more likely to stay in the divertor chamber. Back streaming towards the main chamber plasma is made difficult by the dense partly-ionised gas in front of the divertor tiles, and by the flow directions in the divertor region itself. Compared to the ergodic divertor, the open field lines in the classic divertor turn around the poloidal cross-section once before connecting back to the target plates ($p = 1$).

2.3.3 Impurity radiation

Tokamak plasma parameters such as temperature, density, electric fields and flow velocities are studied using a whole range of spectroscopic techniques. For the work described in this thesis line radiation from carbon impurities has been used. On the TEXTOR tokamak the evolution of the radiation intensity of different carbon ionisation states was studied, which is related to both the temperature profile and the edge particle transport. Above a certain temperature (490 eV) carbon is fully stripped and does not emit line radiation from electron transitions, as it is the case in the central region of most tokamaks. Nevertheless a special technique allows the detection of C^{6+} ions, called Charge eXchange Recombination Spectroscopy (CXRS). Here an electron is captured from a fast neutral particle injected into the plasma (from the heating beam or from a special diagnostic beam). After the charge exchange process the now C^{5+} ion emits line radiation. This method has been used to diagnose velocities and temperatures on JET.

2.4 Outline

As already mentioned, the work described in this thesis has been performed on two different machines, JET and TEXTOR, and on two different aspects of fusion research, high confinement regimes and heat exhaust. The thesis is therefore divided in two parts. Part I, "Poloidal rotation velocity in JET ITB plasmas using charge exchange recombination spectroscopy", and Part II, "Study of the influence of the dynamic ergodic divertor on carbon radiation in the TEXTOR tokamak". In both topics spectroscopy was used to examine the impurity (carbon) ion dynamics in the plasmas.

Part *I* starts with an introduction to transport in internal transport barriers and a summary of the present understanding of this advanced tokamak scenario (chapter 3). The subsequent chapter (chapter 4) covers the improvements that have been made to the analysis of the spectra obtained with the poloidal charge exchange recombination spectroscopy diagnostic on JET. With the improved measurement technique, local increases in C^{6+} poloidal rotation velocity (v_θ) have been observed in internal transport barrier regions and are discussed in chapter 5. Comparison to neoclassical predictions for v_θ by the NCLASS code and the consequences for the total radial electric field profile are also presented in the same chapter. This part concludes with a summary and plans for future v_θ studies on JET (chapter 6).

Part *II* introduces the recently installed dynamic ergodic divertor (DED) on TEXTOR, and the radiation and transport aspects of impurities related to the novel edge magnetic geometry (chapter 7). The spectroscopic diagnostic that has been designed and installed on TEXTOR for the detection of line radiation of C^{2+} and C^{4+} ions, is described in chapter 8. It has been used to study carbon radiation in different operational configurations of the DED (chapter 9). Conclusions and prospects for further use of and improvements to the diagnostic are given in chapter 10.

2.5 Publications

The results obtained within this work have led to the following publications.

International refereed journals

1. 'Calibration of the charge exchange recombination spectroscopy diagnostic for core poloidal rotation velocity measurements on JET'; K. Crombé, Y. Andrew, C. Giroud, N.C. Hawkes, A. Murari, M. Valisa, G. Van Oost, K.-D. Zastrow and JET-EFDA Contributors; Review of Scientific Instruments, Vol. 75, No. 10 (2004) p. 3452

2. 'Preliminary study of the influence of DED on carbon radiation and transport in the TEXTOR tokamak'; G. Telesca, K. Crombé, M. Tokar, B. Unterberg, G. Verdoolaege, R. Zagorski, G. Van Oost; Journal of Nuclear Materials, 337-339 (2005) p. 361

3. 'Poloidal rotation dynamics, radial electric field and neoclassical theory in the JET ITB region'; K. Crombé, Y. Andrew, M. Brix, C. Giroud, S. Hacquin, N.C. Hawkes, A. Murari, M.F.F Nave, J. Ongena, V. Parail, G. Van Oost, I. Voitsekhovitch, K.-D. Zastrow and JET-EFDA Contributors; accepted for publication in Physical Review Letters

4. 'Impurity-seeded ELMy H-modes in JET, with high density and sustainable heat load'; P. Monier-Garbet, P. Andrew, P. Belo, G. Bonheure, Y. Corre, K. Crombé, P. Dumortier, T. Eich, R. Felton, J. Harling, J. Hogan, A. Huber, S. Jachmich, E. Joffrin, H.R. Koslowski, A. Kreter, G. Maddison, G.F. Matthews, A. Messiaen, M.F.F. Nave, J. Ongena, V. Parail, M.E. Puiatti, J. Rapp, R. Sartori, J. Stober, M.Z. Tokar, B. Unterberg, M. Valisa, I. Voitsekhovitch, M. von Hellermann and JET-EFDA Contributors; presented at the 20th IAEA Fusion Energy Conference, Vilamoura, 1-6 November 2004, (IAEA-CN-116, EX/P1-2) and accepted for publication in Nuclear Fusion

Proceedings of International Conferences

5. 'Transport, radiation and rotation properties of carbon on TEXTOR under the influence of the Dynamic Ergodic Divertor - Physical issues and design of a new diagnostic'; K. Crombé, G. Telesca, G. Van Oost, G. Van Den Berge; 29th EPS Conference on Controlled Fusion and Plasma Physics, 17-21 June 2002, Montreux, Switzerland, ECA Vol. 26B, P-2.056

6. 'Improved measurements of impurity ion poloidal rotation velocity in JET'; K. Crombé, Y. Andrew, I. Coffey, P. De Vries, C. Giroud, N.C. Hawkes, E. Joffrin, D.C. McDonald, A. Murari, J. Ongena, F. Sattin, M. Valisa, K.-D. Zastrow and EFDA-JET contributors; 30th EPS Conference on Controlled Fusion and Plasma Physics, 7-11 July 2003, St.-Petersburg, Russia, ECA Vol. 27A, P-1.55

7. 'Dual feedback controlled high performance Ar seeded ELMy H-mode discharges in JET including trace tritium experiments'; P. Dumortier, G. Bonheure, R. Felton, J. Harling, E. Joffrin, A. Messiaen, J. Ongena, P. Belo, I. Coffey, Y. Corre, K. Crombé, M. de Baar, A. Huber, D. Kalupin, A. Kreter, S. Jachmich, G. Maddison, P. Monier-Garbet, M.F.F Nave, V. Parail, M.E. Puiatti, G. Telesca, M. Tokar, B. Unterberg, M. Valisa, I. Voitsekhovitch, M. von Hellermann and contributors to the JET-EFDA work programme; 31st EPS Conference on Controlled Fusion and Plasma Physics, 28 June - 2 July 2004, London, United Kingdom, ECA Vol. 28B, P-5.170

8. 'Poloidal rotation velocity studies on JET'; K. Crombé, Y. Andrew, M. Brix, C. Giroud, N.C. Hawkes, A. Murari, M.F.F. Nave, J. Ongena, V. Parail, G. Van Oost, K.-D. Zastrow; 46th Annual Meeting of the Division of Plasma Physics of the American Physical Society, 15-19 November 2004, Savannah, Georgia, USA, FO3-9

9. 'Progress in predictive transport modelling of ITBs in JET'; T.J.J. Tala, Y. Andrew, G. Corrigan, K. Crombé, D. Heading, F. Imbeaux, V. Parail, P. Strand and J. Weiland; 32nd EPS Conference on Contr. Fusion and Plasma Physics, 27 June - 1 July 2005, Tarragona, Spain, P4-044

10. 'Screening and radiation efficiency of carbon with Dynamic Ergodic Divertor on TEXTOR', G. Telesca, G. Verdoolaege, K. Crombé, M. Lehnen, A. Pospieszcyk, B. Unterberg and G. Van Oost; 32nd EPS Conference on Contr. Fusion and Plasma Physics, 27 June - 1 July 2005, Tarragona, Spain, P1-020

11. 'Influence of toroidal field direction and plasma rotation on pedestal and ELM characteristics in JET ELMy H-modes', A. Loarte, G. Saibene, R. Sartori, M. Kempenaars, R.A. Pitts, Y. Andrew, J.S Lönnroth, V. Parail, E. de la Luna, S. Jachmich, C. Giroud, M.F.F. Nave, K. Crombé; 32nd EPS Conference on

Contr. Fusion and Plasma Physics, 27 June - 1 July 2005, Tarragona, Spain, P2-007

National Conference Proceedings

12. 'Impurity transport in the tokamak TEXTOR-94 under influence of a dynamic ergodic divertor'; K. Crombé, G. Van Oost and G. Telesca, 2nd FTW PhD Symposium, December 12, 2001, Universiteit Gent

13. 'Transport, radiation and rotation properties of carbon on TEXTOR under the influence of the Dynamic Ergodic Divertor'; K. Crombé, G. Telesca, G. Van Oost and G. Van den Berge; International Meeting of the Belgian Physical Society, June 5-6, 2002, Université de Liège

14. 'Transport, radiation and rotation properties of carbon on TEXTOR under the influence of the Dynamic Ergodic Divertor – Physical issues and design of a new diagnostic'; K. Crombé, G. Telesca and G. Van Oost, 3rd FTW PhD Symposium, December 11, 2002, Universiteit Gent, p.53

15. 'On the measurement of poloidal rotation of ions in JET ITB plasmas'; K. Crombé, Y. Andrew, C. Giroud, N.C. Hawkes, F. Sattin, M. Valisa, K.-D. Zastrow and contributors to the EFDA-JET workprogramme; International Meeting of the Belgian Physical Society, May 27-28, 2003, Universiteit Gent, GP16

16. 'First results of the effect of the dynamic ergodic divertor on carbon ions and their radiation properties'; K. Crombé, G. Telesca and G. Van Oost, 4th FTW PhD Symposium, December 3, 2003, Universiteit Gent, p.57

17. 'Improvements in the charge exchange measurements of core poloidal rotation velocity and ion temperature profiles of carbon ions on JET'; K. Crombé, Y. Andrew, C. Giroud, N.C. Hawkes, A. Murari, M. Valisa, G. Van Oost, K.-D. Zastrow and JET-EFDA Contributors; International Meeting of the Belgian Physical Society, May 25-26, 2004, Université de Mons, GP20

18. 'Dual feedback controlled high performance Ar seeded ELMy H-Mode discharges in JET including trace tritium experiments'; P.

Dumortier, G. Bonheure, R. Felton J. Harling, E. Joffrin, A. Messiaen, J. Ongena, P. Belo, I. Coffey, Y. Corre, K. Crombé, M. de Baar, A. Huber, D. Kalupin, A. Kreter, S. Jachmich, G. Maddison, P. Monier-Garbet, M.F.F. Nave, V. Parail, M.E. Puiatti, G. Telesca, M. Tokar, B. Unterberg, M. Valisa, I. Voitsekhovitch, M. von Hellermann and contributors to the EFDA-JET workprogramme; International Meeting of the Belgian Physical Society, May 25-26, 2004, Université de Mons, GP19

19. 'Experimental impurity ion poloidal rotation velocities on JET versus neoclassical calculations'; K. Crombé, Y. Andrew, J. Ongena, G. Van Oost and EFDA-JET contributors, 5th FTW PhD Symposium, December 1, 2004, Universiteit Gent, p.27

> Je me suis rencontré entre deux siècles, comme au confluent de deux fleuves ; j'ai plongé dans leurs eaux troublées m'éloignant à regret du vieux rivage où je suis né, nageant avec espérance vers une rive inconnue
>
> Chateaubriand – Mémoires d'outre-tombe

Part I

Poloidal rotation velocity in JET ITB plasmas using charge exchange recombination spectroscopy

Chapter 3

Transport properties of plasmas with internal transport barriers

A brief introduction is given to transport in tokamak plasmas and the forces involved, to derive an expression for the neoclassical poloidal rotation velocity (v_θ). The neoclassical predictions of v_θ will be the reference in the rest of this thesis to compare the experimental profiles with. The difficulties involved in the measurement of poloidal rotation velocity has meant that in many studies the neoclassical v_θ predictions are used due to lack of good experimental data.

Internal Transport Barrier (ITB) plasmas are introduced as one of the possible advanced operational scenarios foreseen for ITER, the possible factors involved in the formation and sustainment of ITBs are discussed, as well as the changing transport properties in the barrier region.

3.1 Transport and neoclassical poloidal rotation

3.1.1 Basic equations

The collective motion of a particle species α (with charge q_α and mass m_α) by electromagnetic forces, can be described by the Vlasov equation with Fokker-Planck collisional operator $C_\alpha(f)$:

$$\frac{\delta f_\alpha}{\delta t} + \overline{v} \cdot \nabla_r f_\alpha + \frac{q_\alpha}{m_\alpha} \left(\overline{E} + \overline{v} \times \overline{B} \right) \cdot \nabla_v f_\alpha = C_\alpha(f), \tag{3.1}$$

where $f_\alpha = f_\alpha(\overline{r}, \overline{v}, t)$ is the distribution function of the α particles. The collisional operator $C_\alpha(f) = \sum_\beta C_{\alpha\beta}$ gives the change per unit time in

the distribution function for the α particles due to Coulomb collisions with the β particle species.
The zero order velocity momentum of eq. (3.1) is the particle continuity equation

$$\begin{aligned}\frac{\delta n_\alpha}{\delta t} \quad &+ \quad \nabla \cdot n_\alpha \overline{u}_\alpha \quad = \quad \left(\frac{\delta n}{\delta t}\right)_{col} \\ \frac{\delta n_\alpha}{\delta t} \quad &+ \quad \nabla \cdot \overline{\Gamma}_\alpha \quad = \quad \left(\frac{\delta n}{\delta t}\right)_{col}\end{aligned} \tag{3.2}$$

where n_α is the fluid density, $\overline{u}_\alpha$ the flow velocity and $\overline{\Gamma}_\alpha$ the particle flux.
The first order velocity momentum is the momentum balance equation, given by:

$$n_\alpha m_\alpha \frac{d\overline{u}_\alpha}{dt} = n_\alpha q_\alpha \left(\overline{E} + \overline{u}_\alpha \times \overline{B}\right) - \nabla p_\alpha - \nabla \cdot \overline{\overline{\overline{\Pi}}}_\alpha + \overline{R}_\alpha + \overline{F}_\alpha \tag{3.3}$$

where p_α is the scalar pressure and $\overline{\overline{\overline{\Pi}}}_\alpha$ is the viscous stress tensor,
$\overline{R}_\alpha = \sum_\beta \int m_\alpha \overline{v} C_{\alpha\beta} d^3v$ is the collisional friction, and $\overline{F}_\alpha$ is the external force acting on the α particles (for instance from unbalanced neutral beam injection) and $\overline{u}_\alpha$ the flow velocity.
Combining the radial and poloidal components of eq.(3.3) leads to the following expression for the particle flux from eq.(3.2)

$$\overline{\Gamma}_\alpha = -D\nabla n_\alpha + n_\alpha \overline{V} \tag{3.4}$$

where D is the diffusion coefficient and V is the convective velocity.

3.1.2 Classical, neoclassical and anomalous transport

In the simpliest picture for transport a cylindrical geometry is considered with a homogenous and stationary magnetic field, this is called classical transport [Balea]. In general the charged particles follow the field lines, with excursions from the flux-surfaces of the order of their Larmor radius ($\rho_L = mv_\perp/qB$), undergoing a series of small-angle collisions with other particles, and displacing the center of the gyro-orbit from one flux-surface to the other, either inward or outward. Therefore the transport can be described by a random walk diffusive process, with diffusion coefficient D_{class}

$$D_{\text{class}} = \frac{\overline{(\Delta x)^2}}{\Delta t} = (\rho_L)^2 \nu \tag{3.5}$$

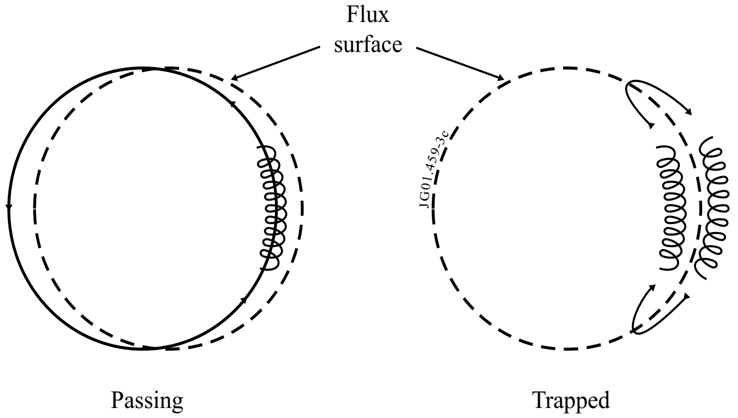

Figure 3.1: Projection in a poloidal cross-section of the orbits of trapped and untrapped (passing) particles in a tokamak.

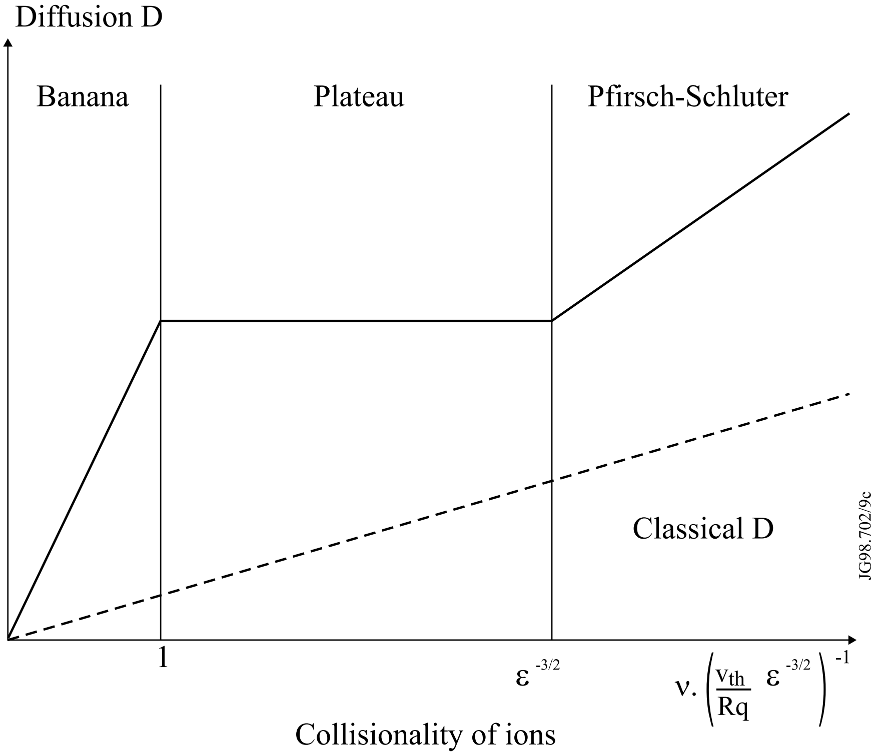

Figure 3.2: The diffusion coefficient as a function of collisionality for the three different regimes.

where ν is the collision frequency.
In a tokamak however, the magnetic field is not homogenous, and the particle guiding center that follows the curved magnetic field lines, undergoes a drift giving rise to two types of guiding center orbits, as illustrated in figure 3.1: the passing and trapped (banana) orbits. The diffusion coefficient is enhanced, and the transport is called neoclassical [Baleb]. The actual diffusion coefficient depends on the collisionality regime of the plasma, as summarised in figure 3.2. For low collision frequencies, the trapped particles follow the banana orbit several times before being scattered away. The diffusion coefficient is determined by the width of the banana orbit and the fraction of trapped particles $\epsilon^{1/2}$ (with ϵ the inverse aspect ratio). It is called the Banana regime and D_{neocl} is found to be

$$D_{\mathrm{neocl}} \sim q^2 \rho_L^2 \nu \epsilon^{-3/2}. \tag{3.6}$$

In the case of highly collisional plasmas the trapped particles do not complete their banana orbit, and transport is determined by the untrapped particles. In the so-called Pfirsch-Schlütter regime D_{neocl} is

$$D_{\mathrm{neocl}} \sim q^2 \rho_L^2 \nu. \tag{3.7}$$

In the Plateau regime, in between banana and Pfrisch-Schlütter, the diffusion coefficient is independent of the collisionality and given by

$$D_{\mathrm{neocl}} \sim \frac{q v_{th} \rho_L^2}{R}, \tag{3.8}$$

where v_{th} is the thermal velocity.
This picture is still not complete, in many experiments the transport coefficients are measured to be much larger than the neoclassical level. That is because micro-turbulence is not considered in the neoclassical theory and is believed to play a crucial role in the enhanced transport, due to fluctuations in the electric field (electrostatic turbulence), originating from density or temperature fluctuations, or due to magnetic turbulence (from fluctuations in the magnetic field).

The term 'transport' should in fact be seen in a broader context, and is not limited to particle movements. It also consists of other channels, such as the electron and ion heat transport and the transport of the toroidal current. All these different aspects are coupled and can best be described by a matrix relationship:

$$\begin{pmatrix} \Gamma/n \\ q_e/(nT_e) \\ q_i/(nT_i) \\ j \end{pmatrix} = \begin{pmatrix} D & L_{21} & L_{31} & L_{41} \\ L_{12} & \chi_e & L_{32} & L_{42} \\ L_{13} & L_{23} & \chi_i & L_{43} \\ L_{14} & L_{24} & L_{34} & \sigma \end{pmatrix} \begin{pmatrix} \nabla n/n \\ \nabla T_e/T_e \\ \nabla T_i/T_i \\ E \end{pmatrix} \tag{3.9}$$

The diagonal terms are the diffusion terms (particle diffusion D and heat diffusivity χ_e, χ_i) and the electrical conductivity (σ). The off-diagonal ones are the pinch terms, typical effects from the neoclassical theory are the current driven by the density and temperature gradients (L_{14}, L_{24} and L_{34}, i.e. the bootstrap current), and the particle flux driven by an electric field (L_{41}, called the Ware pinch).

3.1.3 Neoclassical poloidal rotation

Taking the radial component of eq.(3.3) (with the standard right handed toroidal coordinate system (r, θ, ϕ)) and neglecting the radial inertia, viscosity and collisional friction, and assuming no external forces, leads to :

$$E_r = \frac{1}{q_\alpha n_\alpha} \frac{dp_\alpha}{dr} - \left(u_{\alpha\theta} B_\phi - u_{\alpha\phi} B_\theta\right). \tag{3.10}$$

The flux-surface average of eq.(3.10) reveals different contributions to the poloidal rotation velocity (the $\mathbf{E} \times \mathbf{B}$ velocity and diamagnetic contribution) and the relationship with the flux-surface averaged toroidal rotation velocity [Rozh97] :

$$v_\theta = -\frac{E_r}{B} + \frac{1}{q_\alpha n_\alpha B} \frac{dp_\alpha}{dr} + \frac{B_\theta}{B_\phi} v_\phi, \tag{3.11}$$

which can be re-written as :

$$v_\theta = v_{\mathbf{E}\times\mathbf{B}} + v_{dia} + \frac{B_\theta}{B_\phi} v_\phi. \tag{3.12}$$

In eq.(3.10) $u_{\alpha\phi}$ and $u_{\alpha\theta}$ have been multiplied by B/B_ϕ before averaging over a flux-surface, giving

$$\begin{aligned} v_\phi &= \langle (B/B_\phi) u_{\alpha\phi} \rangle \\ v_\theta &= \langle (B/B_\phi) u_{\alpha\theta} \rangle . \end{aligned} \tag{3.13}$$

Following [Kim91] the equilibrium flux-surface averaged parallel component of the balance eq.(3.3), neglecting $\mathrm{E}_{\|}$, external forces, and the electron contributions to the viscous and friction forces, since these contributions are at most of the order of $(n_e m_e / n_C m_C)^{1/2}$ (C stands for the impurity species (mostly carbon) and e for the electrons), is

$$< \overline{B} \cdot \nabla \cdot \overline{\overline{\Pi_\alpha}} > = < \overline{B} \cdot \overline{R}_\alpha > \tag{3.14}$$

where $\overline{R}_\alpha$ is defined in [Kim91], (note that $< \overline{B} \cdot \nabla p > = 0$, since the plasma pressure is constant on a flux-surface). This means a balance exists between the viscous and friction forces. The impurity ion poloidal rotation velocity, resulting from eq.(3.14), using the Hirshman and Sigmar [Hirs81] momentum approach, is then given by

$$v_\theta^C = \frac{1}{2} v_{th,i} \rho_i \left(\left(K_1 + \frac{3K_2}{2} \right) \frac{1}{L_{T_i}} - \frac{1}{L_{p_i}} + \frac{Z_i}{Z_C} \frac{T_C}{T_i} \frac{1}{L_{p_i}} \right) \frac{B B_\phi}{< B >^2}, \tag{3.15}$$

where $v_{th,i} = \sqrt{\frac{2T_i}{m_i}}$ (i for main ions) is the main ion thermal speed, $\rho_i = m_i v_{th,i} / Z_i e B$, K_1 and K_2 are the viscosity coefficients, defined in [Kim91] as a function of the viscosity matrix elements and depending on the collisionality, and L_{T_i} is the ion temperature gradient scale length, with $\frac{1}{L_{T_i}} = \frac{d \ln T_i}{dr}$, and similarly L_{p_i} is the pressure gradient scale length. For the main ions the poloidal rotation velocity is given by

$$v_\theta^i = \frac{1}{2} v_{th,i} \rho_i \left(K_1 \frac{1}{L_{T_i}} \right) \frac{B B_\phi}{< B >^2}. \tag{3.16}$$

These results are the so-called 'neoclassical calculations' and are used in the thesis to compare the experimental poloidal rotation velocities with. No turbulence driven terms are included in the balance equations (3.15) and (3.16). From the equations can be seen that the main ion poloidal rotation velocity depends on the T_i gradient scale length, whereas for the impurity ions also the main ion pressure gradient scale length plays a role.

3.2 Internal transport barrier plasmas

3.2.1 Confinement regimes in a tokamak

In figure 3.3 the different confinement regimes in a tokamak are illustrated. The *L-mode* (the low confinement mode) is a common mode of

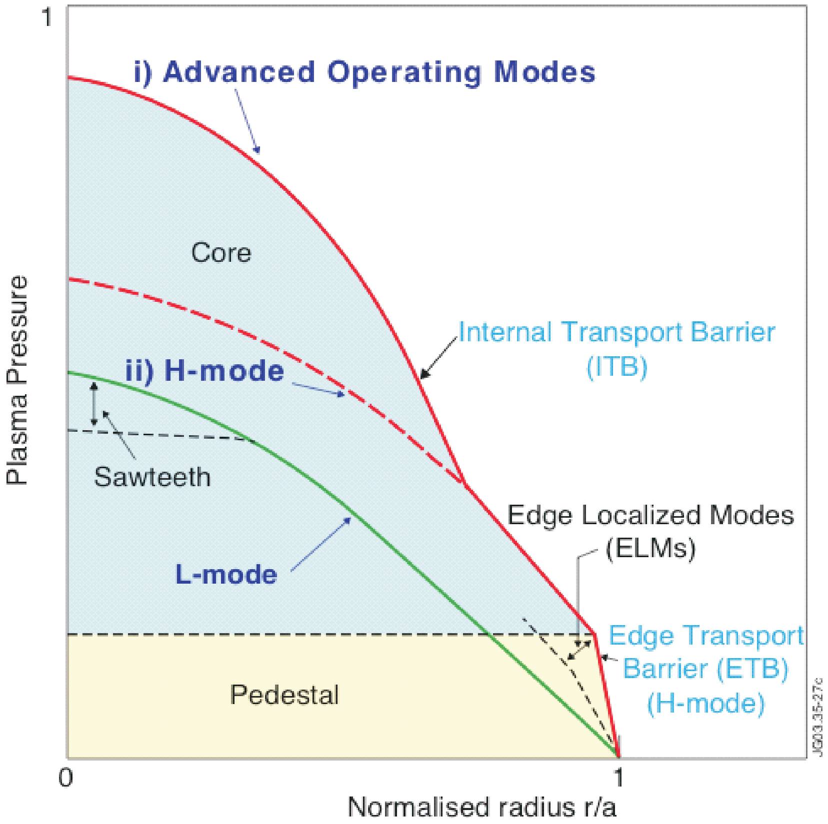

Figure 3.3: Schematic view of the different confinement regimes in a tokamak.

tokamak operation with auxiliary heating. The inner part of the plasma is affected by periodic sawtooth crashes (turbulent rearrangements of the temperature, density and current) connected with the formation of a helical m=1, n=1 mode and the flattening of the profiles inside the q=1 surfaces. The high confinement regime (*H-mode*) was first discovered on ASDEX [Wagn82]. In the H-mode the energy confinement is enhanced by a factor of 1.5 - 2 over the L-mode values. H-mode plasmas have an Edge Transport Barrier (ETB) with a large edge pressure gradient. Above a certain limit for the pressure gradient, MHD instabilities develop and so-called ELMs (Edge Localised Modes) reduce the edge pressure gradient periodically, expelling energy and particles. In this form, the ELMy H-mode is extensively studied on JET and is planned to be the Standard Tokamak Scenario for ITER [ITER01]. ELMs can be beneficial for expelling impurities and α-particles in a reactor, but they also cause large heat loads and particle impacts on the divertor targets, leading to strong erosion, evaporation or melting of the target plates. Therefore, the ELM frequency must be controlled, lower frequencies have large amplitudes and thus large energy and particle bursts onto the vessel wall.

The Advanced Tokamak Scenario is also considered as an operation regime, with a confinement enhancement in the core plasma and the potential for fully non-inductive current drive, which is important for steady-state operation of future reactors [ITER01]. First discovered in the 1990s [Koid94, Levi95, Stra95], this scenario has an Internal Transport Barrier (ITB), and is formed from either an L-mode or H-mode starting plasma, by a subtle modification of the plasma current. Sawtooth crashes are not usually present in the Advanced Tokamak Scenario, as $q > 1$ everywhere in these plasmas. The ITB confinement regime has steeper temperature, density and pressure gradients compared with the standard H-mode. The barrier can be seen in the T_i, T_e, n_e and v_ϕ profiles, although not always simultaneously on all of them. Sometimes the barrier only exists in the ion channel (ion ITB), while in other cases only the electrons are affected (electron ITB), or both. It is thought that the dominant heating of ions or electrons plays a major role in the distinction of the different types of barriers, although the phenomenon is not yet completely understood.

3.2.2 Criterion for the existence of an internal transport barrier

In [Tres02] a dimensionless criterion was empirically derived to characterise ITBs in JET plasmas, and this method is now commonly used to clearly visualise the spatial and temporal evolution of the barrier. The criterion is based on the fundamental characteristic length of possible unstable modes, such as Ion Temperature Gradient (ITG) mode or Trapped Electron Mode (TEM), namely the ion Larmor radius at the sound speed $\rho_S = c_S/\omega_{ci}$, where c_S is the ion sound speed and ω_{ci} is the ion cyclotron frequency [Copp67, Erns04]. Because of the very short gradient scale lengths that are typical for transport barriers (much shorter than the plasma size), a local dimensionless Larmor radius ρ_T^* is defined as

$$\rho_T^* = \frac{\rho_S}{L_T} = -\frac{1}{T_\alpha}\frac{\delta T_\alpha}{\delta R}\rho_S \tag{3.17}$$

where α can stand for electrons or ions, depending on the transport channel in which the ITB occurs. The simpliest dimensionless criterion for the existence of an ITB at location R and time t is

$$\rho_T^*(R,t) \geq \rho_{crit}^*. \tag{3.18}$$

In principle the critical value ρ_{crit}^* depends on a few parameters, such as the magnetic shear and Mach number, but it was shown that a constant value of 0.014 can be used for the plasmas in the JET ITB database. As discussed in [Tres02], the criterion is related to the stabilisation criterion expressed by the Waltz rule (eq.(3.20)) [Walt95].

An illustration of the evolution of a barrier is given in figure 3.4(a) by the typical contour plots of ρ_T^*. The ITB criterion is fulfilled ($\rho_T^* > 0.014$) wherever a coloured line appears, the different colours correspond to different values for ρ_T^* (all larger than 0.014) and thus are related to the steepness of the temperature profile. The barrier in this example was created around $\mathrm{R_{mid}} = 3.25$m and moves radially outwards with time. From about t=5.3s till t=5.7s a second - more outer - barrier forms. The ion temperature profiles for the different time slices corresponding to the dashed vertical lines in fig. 3.4(a) are plotted in fig. 3.4(b), the region on each of the profiles where the criterion is fulfilled is indicated with a double arrow. It does correspond to the steep part of the profile, and a stronger gradient indeed has a higher ρ_T^* value. As in typical JET plasmas the ITB in this example is located radially between $\mathrm{R_{mid}} = 3.25$m and $\mathrm{R_{mid}} = 3.60$m. In general the location of the barrier corresponds to the region with normalised radius (r/a) between 0.3 and 0.8. Therefore the radial view of the poloidal rotation diagnostic, described in chapter 4, is appropriate for the study in ITB plasmas. In most cases the region [$\mathrm{R_{mid}} = 3.35\mathrm{m} - \mathrm{R_{mid}} = 3.65\mathrm{m}$] could be used for a good analysis of the spectra. An upgrade is in progress to change the present top view (looking downwards to the magnetic midplane) to upwards looking channels, in order to extent the view more centrally, possibly upto about $\mathrm{R_{mid}} = 3.18\mathrm{m}$. This would eliminate spectral lines emitted from the divertor plasma, in the vicinity of the carbon line at 529.054 nm. The new diagnostic set-up will also be especially favourable to study the barrier formation, which was often found to be around $\mathrm{R_{mid}} = 3.20 - 3.25\mathrm{m}$.

3.2.3 Mechanisms controlling the ITB

Different mechanisms may play a role in the triggering and sustainment of ITBs, the most important are:

- Flow shear and magnetic shear
  A great deal of progress has been made in recent years in the theoretical modelling [Para99, Tala01, Tala02b, Tala04, Bara04] and experimental control [Chal01, Chal02, Hawk02] of ITBs. However the underlying mechanisms for ITB formation and sustainment are not yet fully understood. Generally large similarities between ITBs and ETBs (Edge Transport Barriers) exist, and in both cases a sheared **E**x**B** flow is believed to be an important factor in reducing the turbulent transport [Burr97, Conn04, Wolf03]. The Hahm-Burrell shearing rate ($\omega_{\mathbf{E}\mathrm{x}\mathbf{B}}$) as defined in [Hahm95], can be written as:
  $$\omega_{\mathbf{E}\mathrm{x}\mathbf{B}} \approx \left| \frac{RB_\theta}{B_\phi} \frac{\delta}{\delta r} \left(\frac{E_r}{RB_\theta} \right) \right| \tag{3.19}$$
  where R is the major radius, r is the minor radius and E_r is the radial electric field (eq. 3.10). This approximation is based on experimentally obtainable variables [Zhu99].
  The two theoretical points of view for this mechanism are (i) the picture of a sheared flow breaking up the turbulent eddies by a non-linear phase decorrelation and decrease of the amplitude of the turbulent cells [Bigl90], or (ii) a linear stabilisation by a coupling of the unstable modes, such as Ion Temperature Gradient/Electron Temperature Gradient (ITG/ETG) and Trapped Electron Modes (TEM), to nearby lying stable modes [Walt95, Burr97]. Accord-

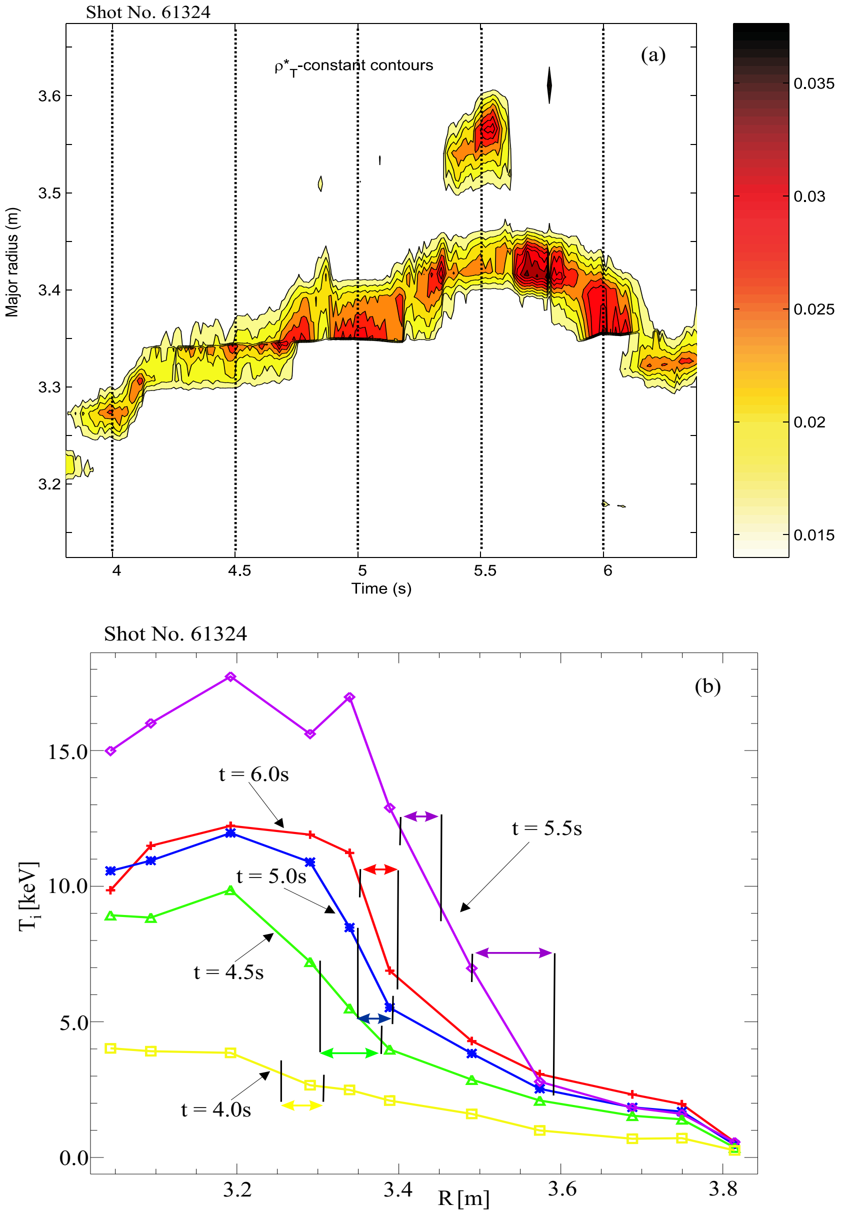

Figure 3.4: (a) Constant ρ_T^*-contours for regions where the ITB criterion is fulfilled in shot no. 61324 ($\mathrm{B_t/I_p}$ = 3.2T/3.0MA). (b) Profiles of ion temperatures with the location of the transport barrier, as defined by the criterion in (a).

ingly, turbulence is suppressed if the shearing rate exceeds the linear growth rate of the most unstable mode (γ_{lin}^{max}), i.e. the global Waltz's rule

$$\omega_{\mathbf{ExB}} \geq \gamma_{lin}^{max} \sim \frac{v_{th}}{L_T} f(s) \tag{3.20}$$

where v_{th} is the thermal velocity and L_T is the temperature gradient scale length. The function $f(s)$ is the dependence of the linear growth rate of the modes on the magnetic shear s,

$$s \approx \frac{r}{q}\frac{dq}{dr}. \tag{3.21}$$

- A small or negative magnetic shear [Burr97, Chal01, Chal02].
  Different models exist for the calculation of the linear growth rate of instabilities, and the influence by the magnetic shear. In [Bara04] some of these models are compared to experimental observations, predicting a minimum growth rate in a region connected to a small s, in agreement with experiments. A negative magnetic shear [Hawk01, Hawk02], also reduces the growth rate of instabilities and can even completely stabilise them [Garb03, Conn04](and references therein). It reduces the radial extent of the convective cells and thus the associated turbulent transport [Wolf03, Conn04]. The effect of shear on the orientation of a convective cell is demonstrated in figure 3.5 (reproduced from [Anto96]) for the case of positive, zero and negative magnetic shear. For $s > 0$ (thus a higher q and stronger helix for the larger radius) the radial extent of the convective cell increases when evolving around the torus. For $s = 0$ the radial extent is reduced with its toroidal displacement, and for $s < 0$ the direction is reversed, breaking up the cell by pushing the outer radius further inwards than the inner radius.

- Rationals of the q-profile.
  Evidence exists on JET [Hawk01, Hawk02, Bara04] and other tokamaks [Koid94, Guen00] that integer and/or rational q-surfaces are connected to the triggering and possibly also to the sustainment of ITBs. Possible explanations [Garb03] are (i) MHD modes located at the integer or rational q surfaces generate a localised velocity shear, or turbulence itself could be responsible for a sheared flow generation. (ii) In the vicinity of a low order rational q number, a layer exists without resonant q-surfaces. If this gap is larger than

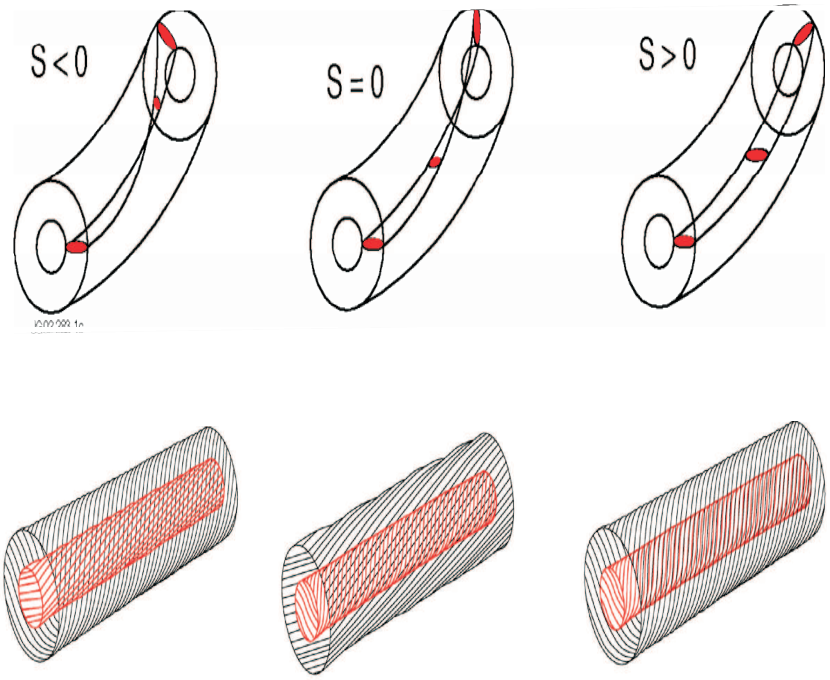

Figure 3.5: Evolution of the orientation of a convective cell in different cases of magnetic shear. A negative shear is most favorable for breaking up the turbulent eddies.

a turbulence correlation length - and assuming that the resonant modes are the most unstable - turbulent transport is reduced, and an ITB can be formed. The width is proportional to $((dq/dr)^{-1})$ or $((d^2q/dr^2)^{-1/2})$ for linear or parabolic variation of q inside the gap [Bara04], and thus weak magnetic shear increases the width of the layer and favours the ITB formation.

- Shafranov shift or α-stabilisation [Beer97, Bour03].
  The magnetic axis in a plasma differs from that in a vacuum. Due to pressure and current density profiles the magnetic axis is shifted to larger minor radii, this is called the Shafranov shift. The resulting flux-surfaces are therefore more compressed in the outer midplane as compared to the inner midplane. The effect of the Shafranov shift on the barrier dynamics is expressed through the parameter α, which is given by

  $$\alpha = -q^2 R \frac{d\beta}{dr} \tag{3.22}$$

  where β is the ratio of the plasma pressure and the magnetic pressure (eq. 2.4), and α is thus related to the pressure gradient :

  $$\alpha = -q^2 R \frac{2\mu_0}{B^2} \nabla P. \tag{3.23}$$

  In [Beer97] it is shown that a large α stabilises TEM and ETG modes as it reverses the ∇B and curvature drift motion of the electrons. It also influences the flow shear (eq.(3.19)) through $\mathrm{E_r}$. The radial electric field is higher in the outer midplane, where the flux-surfaces are more dense, since the electric potential is constant on a flux-surface. For JET plasmas the effect on the flow shear was found to be marginal [Tala01]. The α-stabilisation is immediately linked to the q-profile stabilisation mechanisms: a high q, as for example in the reversed shear plasmas, produces a high α. The positive feedback loop related to the pressure gradient is also important: a strong pressure gradient means a large α, and thus a stronger stabilisation and reduction in transport, leading to an even stronger ∇P. As α-stabilisation does not require strong rotational shear, the mechanism may be important for barriers in future reactors, without external momentum input. In [Bour03] α-stabilisation is identified as a possible triggering mechanism for ITBs in JT-60U plasmas.

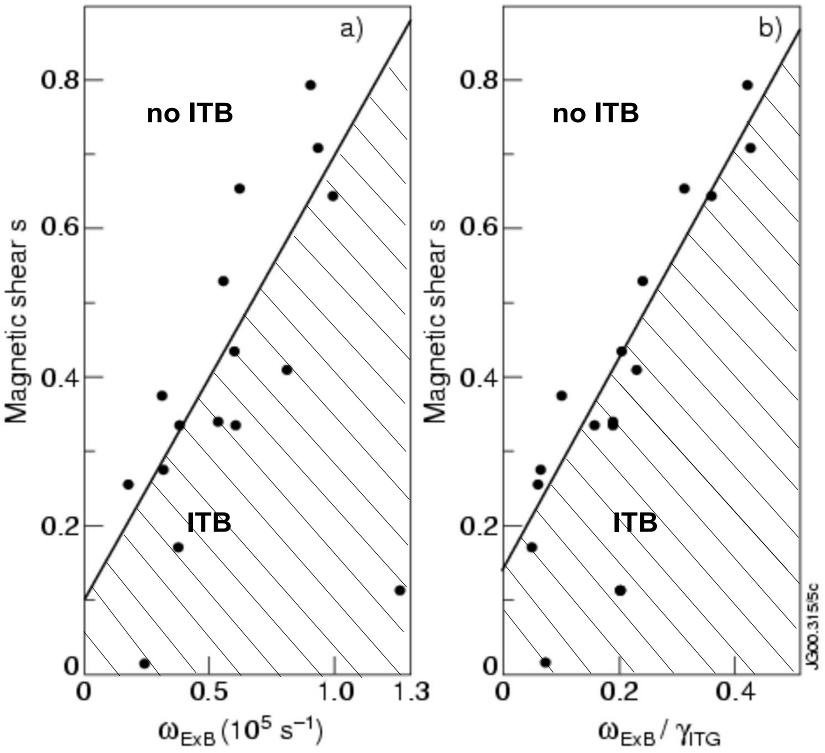

Figure 3.6: The semi-empirical relationship between magnetic shear and flow shear, as derived in [Tala01]. A high flow shear and low magnetic shear are favourable for the existence of ITBs.

The link between flow and magnetic shear has been studied in [Tala01] for JET plasmas and a linear relationship was found (figure 3.6) $s = 0.60\omega_{\mathbf{ExB}} + 0.091$. If γ_{ITG}, the growth rate of the ITG mode (often the dominant unstable mode in the JET ITB plasmas), is included, the relationship is found to be $s = 1.47\omega_{\mathbf{ExB}}/\gamma_{ITG} + 0.14$. The ITB formation from these studies seems to be favorable in regions with a high flow shear and small magnetic shear. This was interpreted by Tala as the interplay between (i) a strong flow shear that tears apart the turbulent eddies, and suppresses the long-wavelength ITG turbulence, and (ii) a small magnetic shear that disconnects the turbulent vortices (such as ballooning instabilities) that were originally linked together by toroidicity (figure 3.5). This picture can be extended to the region with negative magnetic shear, where the turbulent cell is actually reversed, strongly disconnecting the vortices.

- The density gradient [Tala02b].
  The ITG and ETG modes become unstable above a certain critical temperature gradient and this threshold depends on the density gradient [Tala02b, Stae99]. Therefore a local particle source can act as a trigger mechanism to the formation of a barrier. This principle was applied on JET in the high density ITB plasmas created by pellet injections [Frig03].

- The ratio $\mathrm{T_e/T_i}$ [Ide00, Conn04, Wolf03].
  In future reactors the fast α-particles will mainly heat the electrons, and due to the high density plasmas will have $T_i \approx T_e$. The effect of the ratio in central electron and ion temperatures was studied on JT-60U [Ide00], using an Electron Cyclotron Range of Frequencies (ECRF) system for heating and current drive and a Negative ion Neutral Beam (N-NB) to predominantly heat electrons. It was found that triangularity and poloidal β_p plays an important role in the achievable confinement improvement with respect to the central $\mathrm{T_e/T_i}$ ratio.

- Zonal flows [Lin99, Roge00, Hahm00, Diam94].
  Another possible factor triggering the transition to enhanced confinement are zonal flows driven by turbulence itself. In a turbulent

plasma the plasma flow ($\overline{u}_\alpha$) and magnetic field ($\overline{B}$) consist of an average ($\overline{u}_{ave,\alpha}$, $\overline{B}_{ave}$) and fluctuating part ($\tilde{u}_\alpha$, $\tilde{b}$), and can be written as:

$$\overline{u}_\alpha = \overline{u}_{ave,\alpha} + \tilde{u}_\alpha, \tag{3.24}$$

and

$$\overline{B} = \overline{B}_{ave} + \tilde{b}. \tag{3.25}$$

For the derivation of the momentum balance equation(3.3) no fluctuating terms were included. If the turbulent parts are taken into account and the momentum balance equation is recalculated, two additional contributions must be considered, (i) the turbulent Reynolds stress tensor, originating from

$$m_\alpha n_\alpha \nabla \cdot < \tilde{u}_\alpha \tilde{u}_\alpha > \tag{3.26}$$

and (ii) a Maxwell stress contribution, originating from

$$\begin{aligned} & n_\alpha q_\alpha \tilde{u}_\alpha \times \tilde{b} \\ = \; & \tfrac{1}{\mu_0} \left(\nabla \times \tilde{b} \right) \times \tilde{b} \end{aligned} \tag{3.27}$$

Taking the flux-surface averaging of the poloidal component of the extended momentum balance, leads to the following poloidal flow profile evolution:

$$\frac{\delta(V_\theta - V_\theta^{\mathrm{neo}})}{\delta t} = -\frac{\delta}{\delta r}\left(< \tilde{v}_r \tilde{v}_\theta > - \frac{1}{\mu_0 \rho_\alpha} < \tilde{b}_r \tilde{b}_\theta > \right) - \mu(V_\theta - V_\theta^{\mathrm{neo}}), \tag{3.28}$$

where $\rho_\alpha = m_\alpha n_\alpha$ is the mass density, μ_0 is the permeability of the vacuum, V_θ is the average poloidal flow velocity and V_θ^{neo} is the neoclassical poloidal flow.

The first two terms at the right hand side are the electrostatic (Reynolds stress) and magnetic contributions (Maxwell stress - sometimes also called magnetic Reynolds stress [Xu00, Yu00]); $< \tilde{v}_r \tilde{v}_\theta >$ is the average value of the correlation between radial and poloidal velocity fluctuations over a flux-surface, and $\tilde{b}_r$ and $\tilde{b}_\theta$ are the radial and poloidal magnetic field fluctuations. The last term in the right hand side is the damping caused by magnetic pumping [Diam94] and μ is the damping rate. This shows that turbulent fluctuations can drive a poloidal flow, and possibly stabilise the turbulence itself via $\omega_{\mathbf{E}\times\mathbf{B}}$ flow shear [Xu00, Yu00].

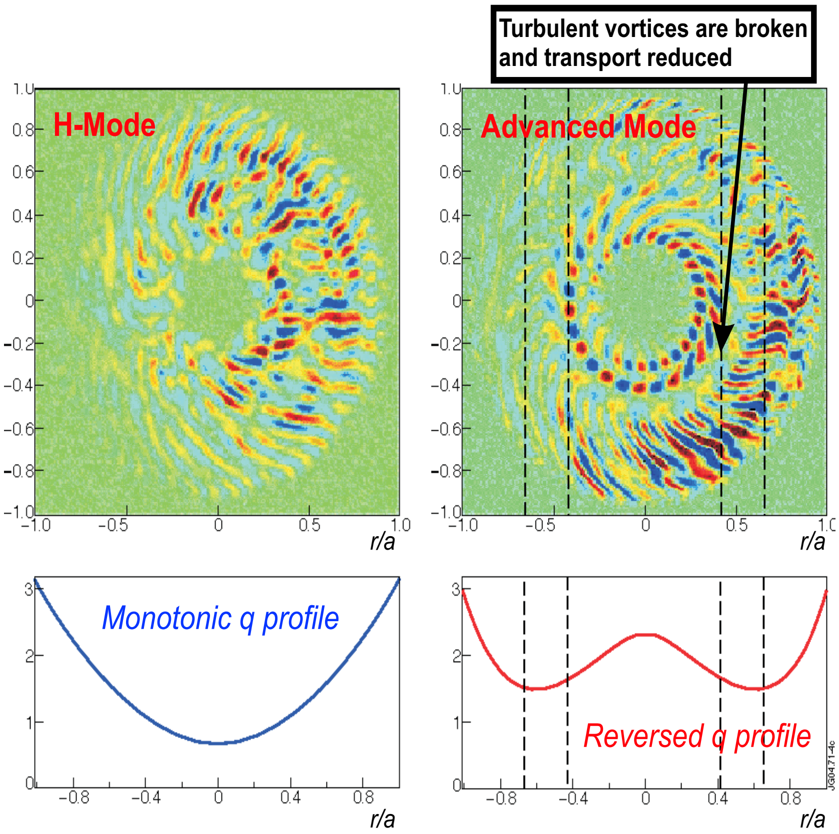

Figure 3.7: Simulation of the turbulent eddies in an H-mode and an ITB plasma, and the q-profiles, monotonic and reversed.

Most likely the ITB dynamics is controlled by a combination of two or more of the mechanisms described above, and are not necessarily the same in different tokamaks. In the following chapter experimental results for carbon ion poloidal rotation velocities in JET ITB plasmas are presented. As poloidal rotation enters the radial electric field (eq.(3.10)) it can play an important role in the calculation of the flow shearing rate and its link to turbulence stabilisation.

3.2.4 Shaping the q-profile for the creation of ITB plasmas

To control the ITB formation in JET plasmas, the q-profile is shaped in the desired way during the preheating phase. A strongly reversed q-

profile is created by a current ramp up combined with a strong electron heating to slow down the current diffusion, and the use of Lower Hybrid heating and Current Drive (LHCD) [Mail02, Chal01]. A weakly reversed q-profile is obtained by off-axis NBI or Ion Cyclotron Resonant Heating (ICRH) during the preheating phase. In the reversed shear discharges the minimum of the q-profile is located around the middle of the minor radius, in the region r/a = 0.3 - 0.6. It is mostly in this region, where later, during the main heating phase, the ITB is formed. On-axis NBI or ICRH preheating produce a monotonic q-profile [Tala02a].

To illustrate the role of the q-profile on turbulent eddies, figure 3.7 shows a simulation of the turbulent structures in H-mode and ITB plasmas. In the H-mode plasma (left) the q-profile is monotonically decreasing from the edge towards the center, and turbulent cells exist pratically everwhere in the simulated region (r/a $\approx 0 - 0.8$). For the ITB plasma on the right, the q-profile is reversed and the simulations show a reduction of the turbulent fluctuations in the region with minimal magnetic shear (r/a $\approx 0.4 - 0.65$), corresponding to the region of the transport barrier in this simulation.

The coupling between the current and pressure profile in ITB plasmas is illustrated in fig. 3.8. During the pre-heating phase a reversed q-profile is created using LHCD. An ITB is formed in the region of minimal q and the steep pressure gradient linked to the barrier region drives an off-axis bootstrap current, which adds to the total current. In this way the shape of the current (and q) profile is sustained, with a peaked current (and minimum q) profile in the barrier region.

3.3 Transport in the barrier region

In the last trace tritium campaign on JET in 2003, the diffusion coefficient (D_T) and the convective velocity (v_T) of the tritium could be measured seperately by evaluating the time evolution of the 14 MeV neutron profiles (from the DT reaction) with an impurity transport code. In the barrier region a strong reduction of both D_T and v_T was observed [Zast04, Mail04], as illustrated in figure 3.9 for shot no. 61352 ($\mathrm{B_t/I_p} = 3.2\mathrm{T}/3.0\mathrm{MA}$) with the transport barrier around $r/a = 0.5$. The neoclassical values - calculated by NCLASS - for D_T and v_T are also plotted. D_T in the ITB region reaches this neoclassical level. There

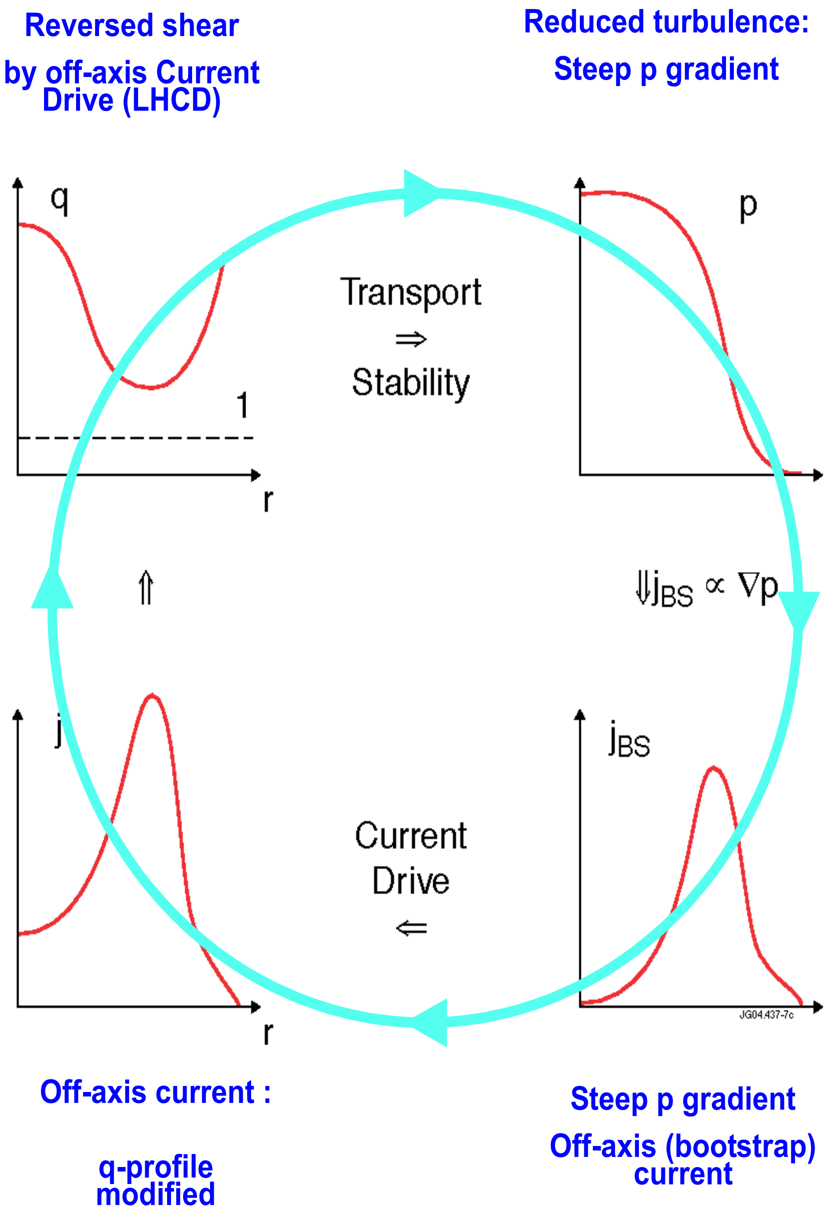

Figure 3.8: Coupling of current and pressure profile, control of the q-profile.

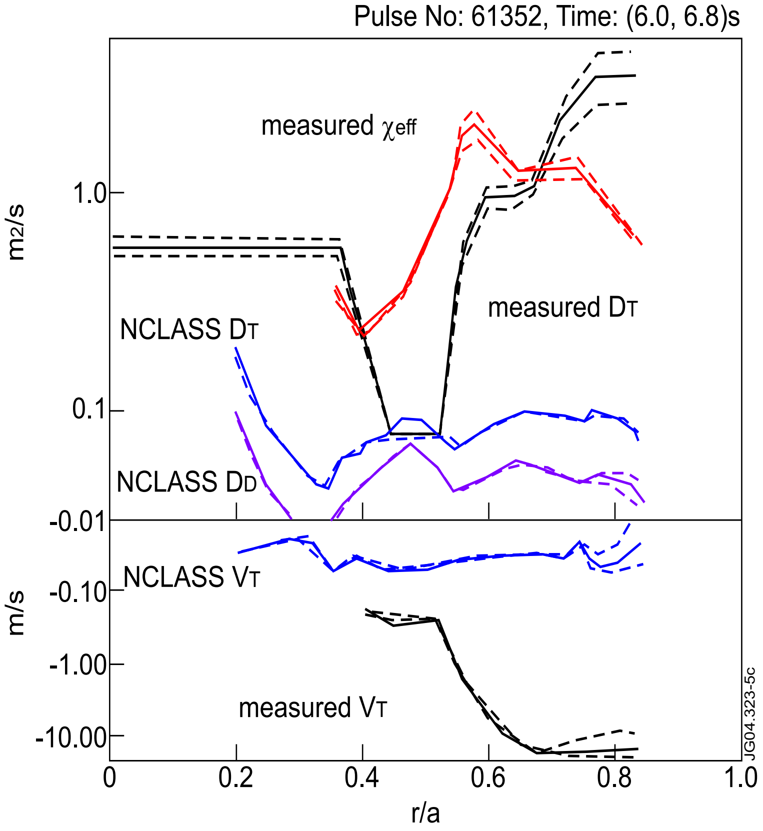

Figure 3.9: Measured diffusion coefficient and convective velocity for tritium in an ITB plasma and the neoclassical predictions by the NCLASS code. A strong reduction of the experimental values is observed in the barrier region (figure taken from [Mail04]).

is also a reduction in measured inward velocity v_T, although not to the neoclassical values. Also shown is the neo-classical prediction D_D for the major fuel ion species deuterium that differs from the prediction for the trace quantity of tritium. The difference between D_D and D_T exceeds the difference due to the mass ratio and this demonstrates that neoclassical effects are qualitatively and quantitatively different for minority and majority fuel ion species. The reason is that a deuterium and a tritium ion can exchange places after a Coulomb collision, which is important for the minority species, but much less for the majority species. This transport can be either diffusive or convective, but since v_D and v_T are both very small, only the diffusion coefficients D_D and D_T differ considerably [Zast04]. Furthermore an increase of D_T to large values is observed in the region enclosed by the barrier.

Transport in the ITB region is not only reduced in the particle channel, also the energy transport is affected, expressed by the effective thermal diffusivity χ_{eff} (accurate separation into χ_i and χ_e was not possible in these discharges), as shown in fig 3.9. The minimal value for χ_{eff} is also reached in the barrier region.

This reduction in heat and particle transport goes together with a peaking of density and temperature, and thus pressure profiles. For the same discharge profiles for different transport channels are shown in figure 3.10. On the ion temperature (a) and toroidal rotation velocity (b) the foot of the barrier appears to be at about $\text{R}_{\text{mid}} = 3.45$m, whereas for the electron density (c) the foot of the barrier is more outside at around $\text{R}_{\text{mid}} = 3.60$m. The electron temperature (d) does not show a clear sign of an internal barrier.

3.4 Simulation codes

The experimental profiles are compared to neoclassical calculations, performed by the NCLASS module [Houl01]. This module is embedded in the one and a half dimensional transport code JETTO [Gena88] that simulates the plasmas. The JETTO code solves the time-dependent plasma diffusion equations, as expressed in eq.(3.9), averaged over the magnetic flux-surfaces. In addition it has an equilibrium solver, and packages for the heating and current drive simulations, the fusion power calculation, etc. For the comparison with the experimental results JETTO has been run in an interpretative way, this means using the time dependent experimental ion and electron temperature and den-

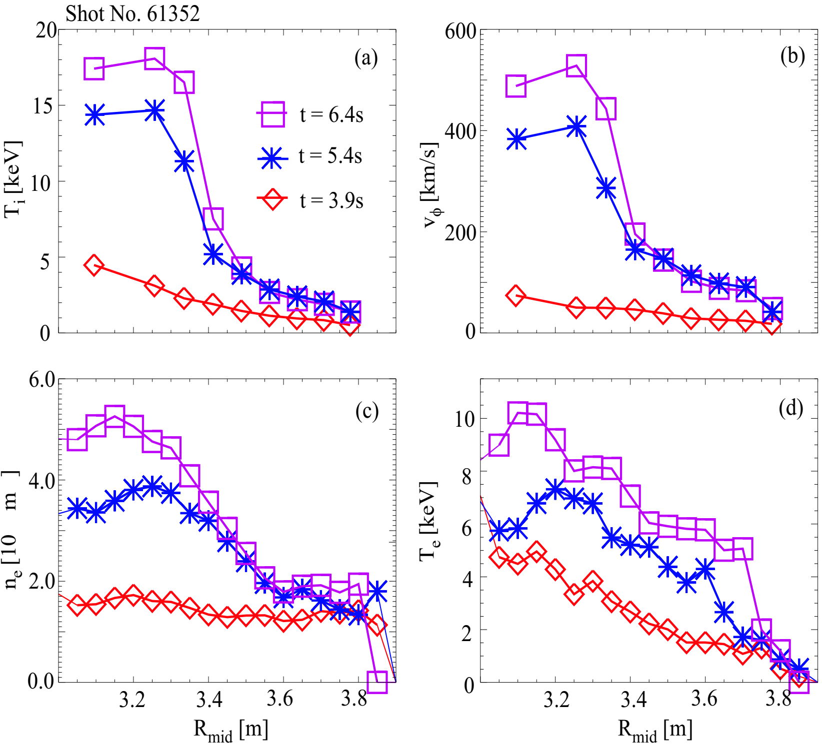

Figure 3.10: Profiles before (t=3.9s) and during the transport barrier (t=5.4s and t=6.4s) of (a) ion temperature, (b) toroidal rotation velocity, (c) electron density and (d) electron temperature.

sity profiles as input throughout the simulations, while the current is predicted by solving its diffusion equation. During the simulation of JETTO the NCLASS module was called for the prediction of the impurity and main ion poloidal rotation velocities. More theoretical studies of the ITB dynamics with the JETTO code, also performing predictive simulations for temperatures and densities (and using NCLASS predictions for v_θ) were performed in [Tala01, Tala02b, Tala04].
NCLASS is based on the approach of Hirshman and Sigmar [Hirs81], as is the analytic model of Kim [Kim91]. However, NCLASS solves a matrix for plasma flows within and across surfaces derived from the parallel and radial force balances for a multiple species plasma [Houl01], whereas the Kim model assumes only one impurity species. The flux surface averaged parallel force balance equation that is used in NCLASS to calculate the neoclassical poloidal rotation velocity, takes also the $E_{||}$ term into account, and is given by:

$$< \overline{B} \cdot \nabla \cdot \overline{\overline{\Pi_\alpha}} >=< \overline{B} \cdot \overline{R}_\alpha > + n_\alpha q_\alpha < \overline{E} \cdot \overline{B} >, \tag{3.29}$$

instead of eq.(3.14) for the Kim model.
In the simulations that were performed for this thesis only C^{6+} impurity ions were assumed.

Work is currently in progress to include the effect of the parallel flow driven by the fast beam ions in NCLASS, as it might play a crucial role in plasmas with strong NBI heating [Houl04, Solo04a]. The role of an unbalanced neutral beam injection in the calculation can be included in eq.(3.29), now adding an additional term to account for the friction force between the fast beam particles and the thermal ions, leading to the equation:

$$< \overline{B} \cdot \nabla \cdot \overline{\overline{\Pi_\alpha}} >=< \overline{B} \cdot \overline{R}_\alpha > + < \overline{B} \cdot \overline{R}_{beam} > + n_\alpha q_\alpha < \overline{E} \cdot \overline{B} > . \tag{3.30}$$

The JETTO code is presently also being upgraded to enable the use of experimental impurity v_θ profiles as input instead of the neoclassical NCLASS predictions. The effect on the barrier dynamics, through the radial electric field and flow shear could be considerable, as discussed above. The first test of this implementation is being performed and preliminary results are reported in [Tala05].

Chapter 4

Improvements to the core plasma charge exchange recombination spectroscopy measurements on JET

> Misurare ciò che può esserlo e sforzarsi di rendere misurabile ciò che non lo è
> Galileo Galilei

In this chapter the improvements that have been made to the analysis of the Charge eXchange Recombination Spectroscopy (CXRS) spectra, for the measurement of impurity ion poloidal rotation velocity (v_θ) and temperature (T_i) are described [Crom04].

4.1 Description of the diagnostic

The CXRS diagnostic makes use of the charge exchange reaction between injected neutral deuterium atoms from the heating beam (D^0_{beam}) and fully stripped impurity ions (A^{Z+}) [Koid01],

$$D^0_{beam} + A^{Z+} \rightarrow D^+_{\mathtt{beam}} + A^{(Z-1)+*}. \qquad (4.1)$$

The excited impurity ion, $A^{(Z-1)+*}$, subsequently decays emitting several emission lines, which provide information about the origi-

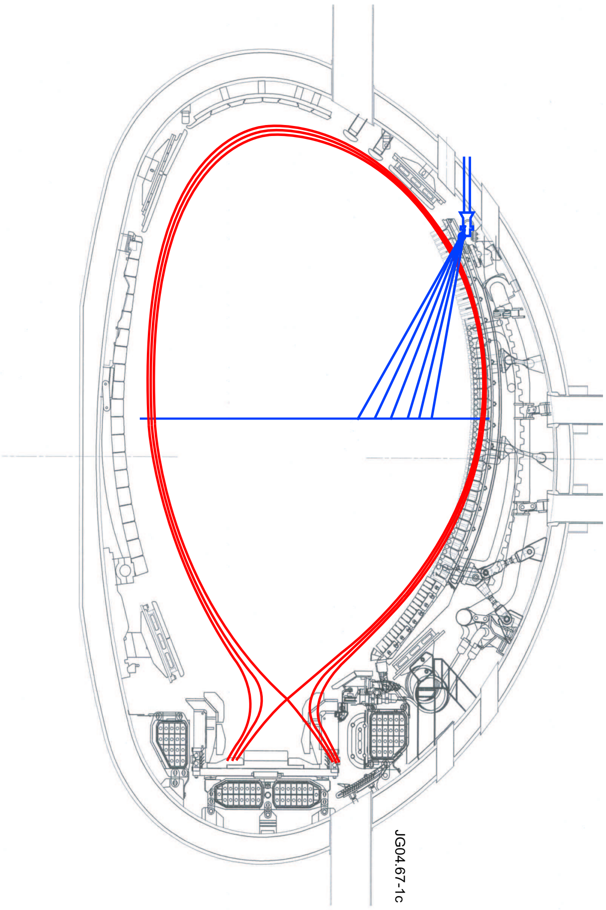

Figure 4.1: Schematic view of the core poloidal CXRS diagnostic on JET.

nal, fully stripped, impurity ion. On JET, as on many other tokamaks [Koid01, Solo04b, Meis01], the most commonly used fully ionised impurity ion is C^{6+}, since carbon is the main intrinsic plasma impurity due to the carbon tiles covering the inside of the vacuum vessel. The detected spectral line is the 529.05 nm transition of C^{5+} $n = 8 \rightarrow 7$. The emission line is actually composed of several transitions amongst different l-states, but this fine structure is not distinguishable, and the measured spectral line is a mean of the wavelengths of all the fine structure components.

A schematic picture of the core viewing CXRS diagnostic is shown in figure 4.1. A set of 20 lines of sight (LOS) intersect a Neutral Beam Injection system (NBI) on JET (the NBI4 system, located on octant four), consisting of 8 different Positive Ion Neutral Injectors (PINIs). On a shot to shot basis 6 out of the 20 viewing chords are chosen for the measurement, mostly in the mid-plane radial range $R_{mid} = 3.30m - 3.70m$, as they are indicated in fig. 4.1. The LOS view from the top of the vessel down to the midplane, and the intersection with the path of the heating beam defines their measurement volume. Optical fibres capture the photons from the plasma, and direct them to a 1.33 m Czerny-Turner spectrometer in the laboratory. The six 529.05 nm spectral lines are monitored simultaneously on a CCD camera. The spatial resolution of the LOS varies from 2 to 10 cm, depending on the number and type of neutral injectors that were used in the discharge and the magnetic geometry of the shot. Indeed, the number of flux surfaces crossed by the LOS depend on their radial location and the plasma magnetic configuration; the power deposition profile of the beams depend moreover on the total NBI power and its distribution amongst the different PINIs. The spectra are recorded with a minimum exposure time of 50 ms.

The present diagnostic for poloidal rotation velocity measurements on JET was developed by N.C. Hawkes from the original octant 4 CXRS system [Hawk95, Hawk97]. In this thesis only the central viewing system is described, used mainly for the study of internal transport barriers associated with high confinement regimes.

4.2 Line calibration for poloidal rotation measurements

The temperature and velocity of the impurity ions are deduced from the Doppler broadening and shift of the spectral line respectively, which requires an accurate wavelength calibration for the CCD camera. A double Gaussian line is fitted to the datapoints of the line profile (for the active and passive component of the charge exchange reaction), using a least-squares technique, from which the full width half maximum (FWHM) and central line position are determined, as a function of wavelength. Two independent techniques for the calculation of the dispersion relationship of the CCD have been developed.

4.2.1 Lamp calibration method

For the first calibration method [Satt01, Hawk95], the spectrum from a Perkin-Elmer type 303-306 samarium hollow cathode discharge lamp is used. The lamp spectrum has clearly identifiable lines in the neighbourhood of the C VI line at 529.05 nm. In the original analysis method [Satt01] the dispersion of the CCD was calculated using the locations on the chip of six spectral lines from the calibration lamp in the wavelength region 523.403 nm – 533.240 nm (figure 4.2), a relatively wide spectral band of about 10 nm. A linear dispersion relationship was assumed across the CCD camera tracks and calculated as the best straight line fit through the six datapoints, giving an estimate for the position of the unshifted carbon line at 529.05 nm. However, it was found that in some cases the resulting unshifted position of the 529.05 nm line was incorrect, probably because the linear approximation of the dispersion relationship across the tracks is insufficiently accurate and thus provides an additional apparent velocity to the measured line of sight velocity (v_{LOS}). This is illustrated in figure 4.3(a), where the time trace of the line of sight velocity for one of the chords, at $R_{mid} = 3.39$m, appears to be 40 km/s lower than the others. Therefore, the interval for calibration was reduced to about 3.5 nm around the C VI line, [527.139 nm - 530.476 nm] which has four clearly identifiable lines in the lamp spectrum. The dispersion of the chip was recalculated using again a linear fit, resulting in the line of sight velocities shown in figure 4.3(b). The spurious time trace from the original example (figure 4.3(a)) now has absolute values similar to the other chords.

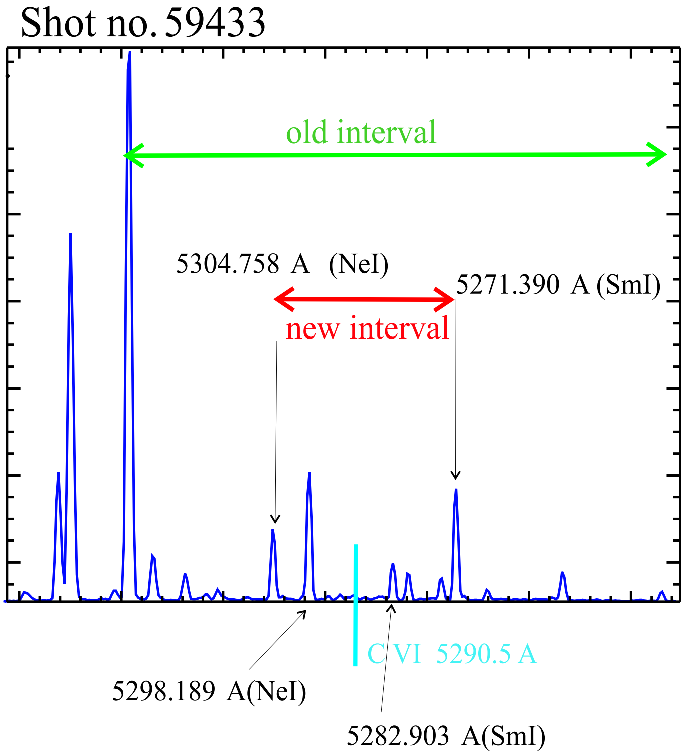

Figure 4.2: The calibration lamp spectrum. The four marker lines that are annotated are used for the calculation of the dispersion relationship of the CCD. In previous analysis a wider interval was used.

It has also been found that the lamp calibration needs to be repeated regularly to correct for errors in the reference position of C VI line, probably due to mechanical movements of the system or temperature variations. In practice, a calibration shot is done each time a new series of measurements is taken. Ideally the lamp spectrum would be monitored on top of the plasma spectrum for every discharge [Gohi99], but this was technically not possible. In figure 4.3(c) the difference in v_{LOS} is illustrated, using the data from a recent line calibration instead of one some months before the actual shot (as is the case for figures 4.3(a) and 4.3(b)). In this example an apparent offset of -30 km/s occurs (in all chords) when the older calibration data are used, highlighting the necessity to regularly repeat the lamp calibrations.

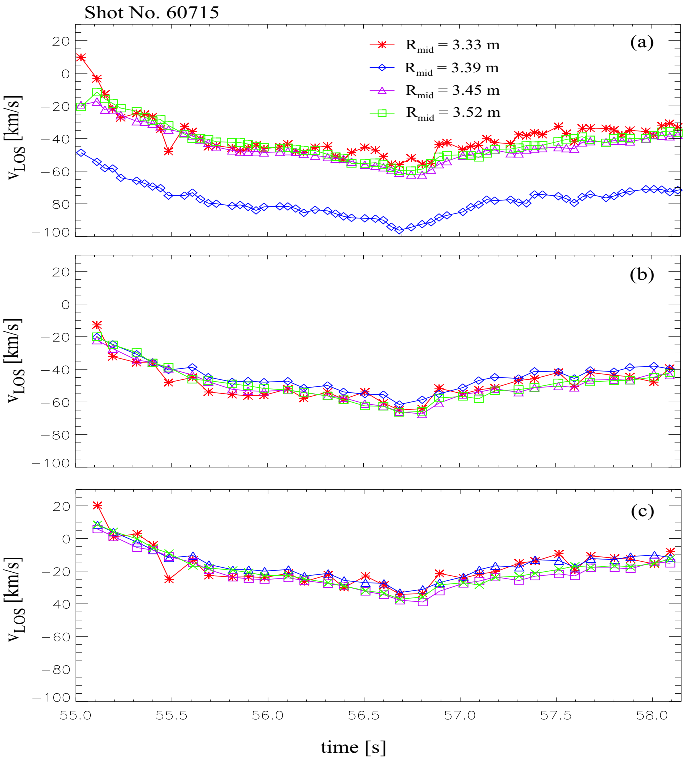

Figure 4.3: (a)Time traces of the line of sight velocities for different viewing chords for shot no. 60715 ($B_t/I_p = 2.7T/2.5MA$), using the original six line method of lamp calibration. The calibration was taken months before the actual shot. (b)Time traces for the same shot and the same lamp calibration spectrum, with the dispersion relationship calculated as a linear fit through only four spectral lines of the SmI/Ne lamp spectrum in a narrow wavelength region of 3.5 nm. (c) v_{LOS} time traces using a lamp calibration that was taken on the same day as the shot.

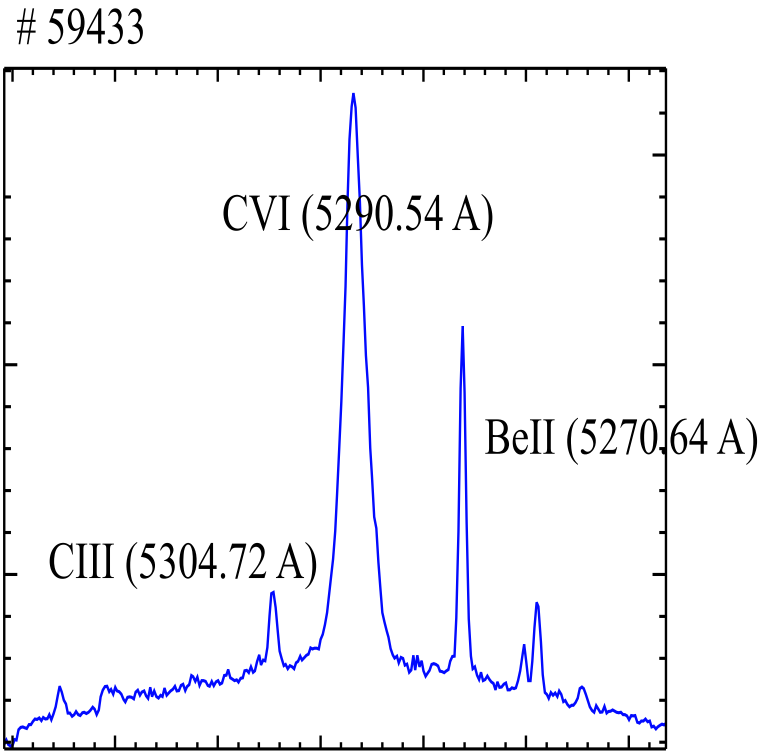

Figure 4.4: An example of a plasma spectrum: the charge exchange C VI spectral line with the two marker lines of Be II and C III on either side.

4.2.2 Plasma spectrum calibration method

Technical constraints prevented the use of the reference lamp for every discharge separately. The solution to this problem was to use the plasma spectrum itself. On the CCD two additional spectral lines of the plasma are monitored in the vicinity of the charge exchange C VI line: a Be II line at 527.06 nm and a C III line at 530.47 nm (as shown in figure 4.4). The light from the low ionisation states of the impurity ions Be and C was emitted in the scrape off layer, where plasma flows are relatively low. The flow velocities of the Be^{1+} and C^{2+} ions using a recent lamp calibration gave for a wide range of discharges an average line of sight velocities of less than 5 km/s for these ions as shown in fig. 4.5. Therefore the Be II and C III lines can be assumed stationary. Their positions, on either side of the charge exchange line, can therefore be used as markers

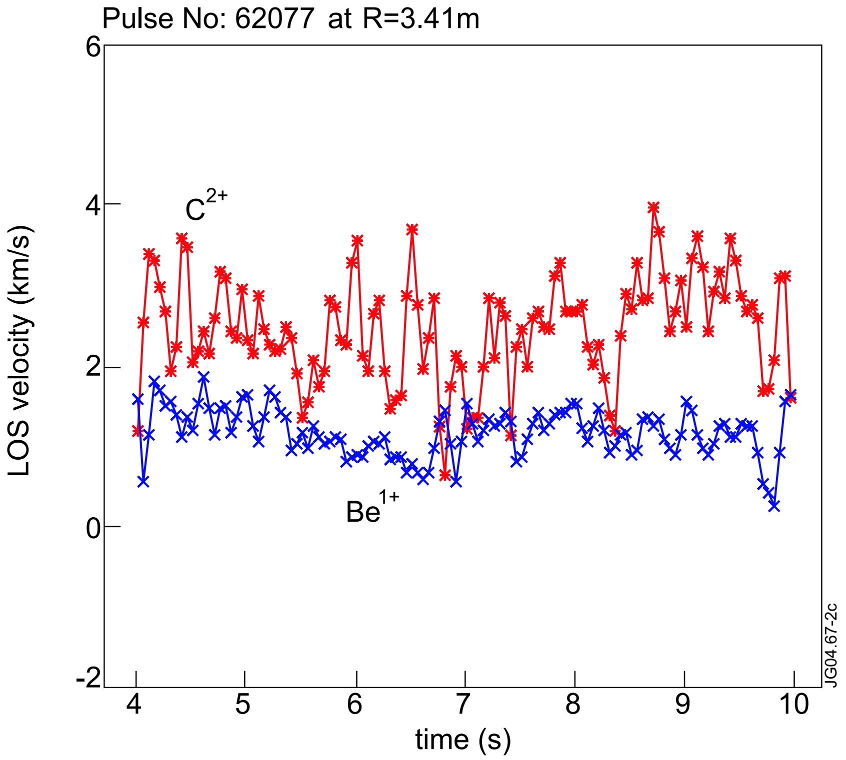

Figure 4.5: The v_{LOS} along the viewing chords for the Be^{1+} and C^{2+} ions for an ITB discharge with $I_p = 2.6$ MA and $B_\phi = 3.25$ T.

for an additional calculation of the dispersion relationship, on a shot to shot basis. Results from both calibration methods agree closely when a recent lamp calibration is used. The major constraint for using this plasma calibration method exclusively is the sometimes weak intensity of the Be II and C III emission lines, resulting in difficulties to obtain a good Gaussian curve fit to the datapoints.

The inaccurate wavelength calibration has a serious impact on the absolute values of the $\mathrm{v_{LOS}}$, as it introduces an apparent shift in the spectral line that is not related to the real impurity ion velocity as demonstrated in figs. 4.6(a) and (b). The relative error in the resulting v_θ is even larger, shown in fig. 4.7, since the additional wavelength shift is interpreted to be completely in the poloidal direction. Whenever possible, the plasma calibration method is now used on JET for the core CXRS diagnostic.

4.3 Impact of the viewing geometry

The viewing chords of the diagnostic are not completely vertical. The tilt in toroidal and poloidal components are given by the angles $\phi^{\mathrm{i}}_{\mathrm{LOS}}$ and $\theta^{\mathrm{i}}_{\mathrm{LOS}}$ and are slightly different for each chord. In the figures 4.8 and 4.9 these angles are illustrated ; here an average direction is assumed both for (A) the neutral beam injection and for (B) the viewing chord. The total line of sight velocity for chord i ($\mathrm{v^i_{LOS}}$) is then given by:

$$v^i_{LOS} = c\frac{(\Delta\lambda)^i}{\lambda_0} = v^i_\phi \cos(\phi^i_{LOS}) + v^i_\theta \cos(\theta^i_{LOS}), \tag{4.2}$$

where c is the speed of light, $(\Delta\lambda)^i$ is the wavelength shift, λ_0 is the unshifted wavelength, and v^i_ϕ and v^i_θ are the toroidal and poloidal rotation velocities at the intersection between the line of sight and the beam injection. The angles ϕ^i_{LOS} and θ^i_{LOS} change with the magnetic geometry, and are therefore recalculated for each requested time slice of the shot, giving for $\cos(\theta^i_{LOS}) \approx 0.94$ - 0.98 and for $\cos(\phi^i_{LOS}) \approx 0.20$ - 0.30.

(A) To take the finite spatial extent of the neutral beam injection into account, an effective observation radius is calculated for each of the viewing chords, using the actual magnetic equilibrium and the beam geometry [Hawk95]. Therefore the total beam density profile summed

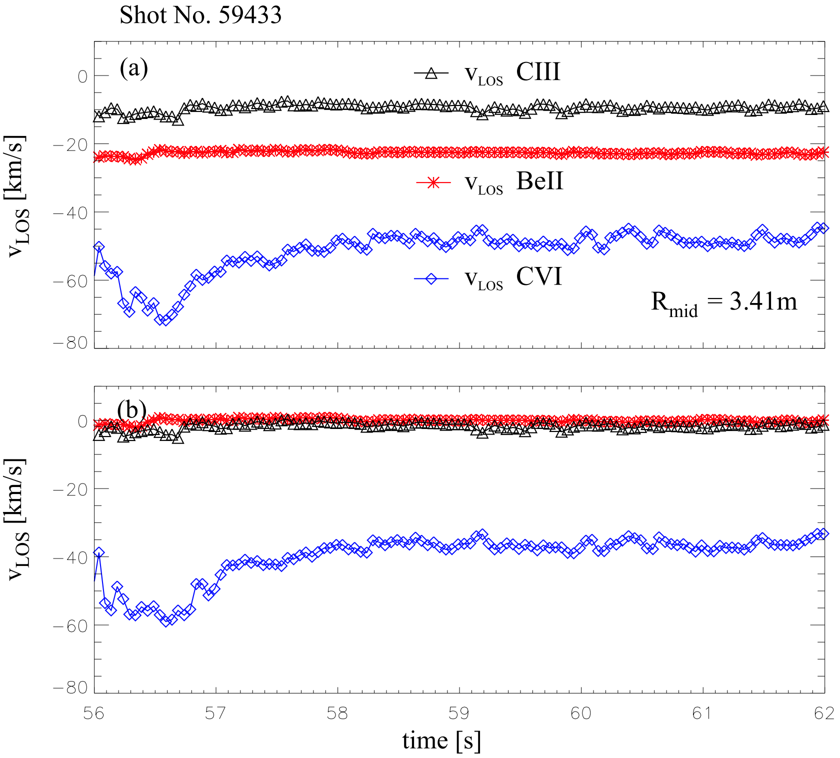

Figure 4.6: Illustration of the difference obtained in line of sight velocity using (a) an old lamp calibration and (b) the plasma spectrum for the wavelength calibration (I_p = 2.5 MA and B_ϕ = 2.4 T).

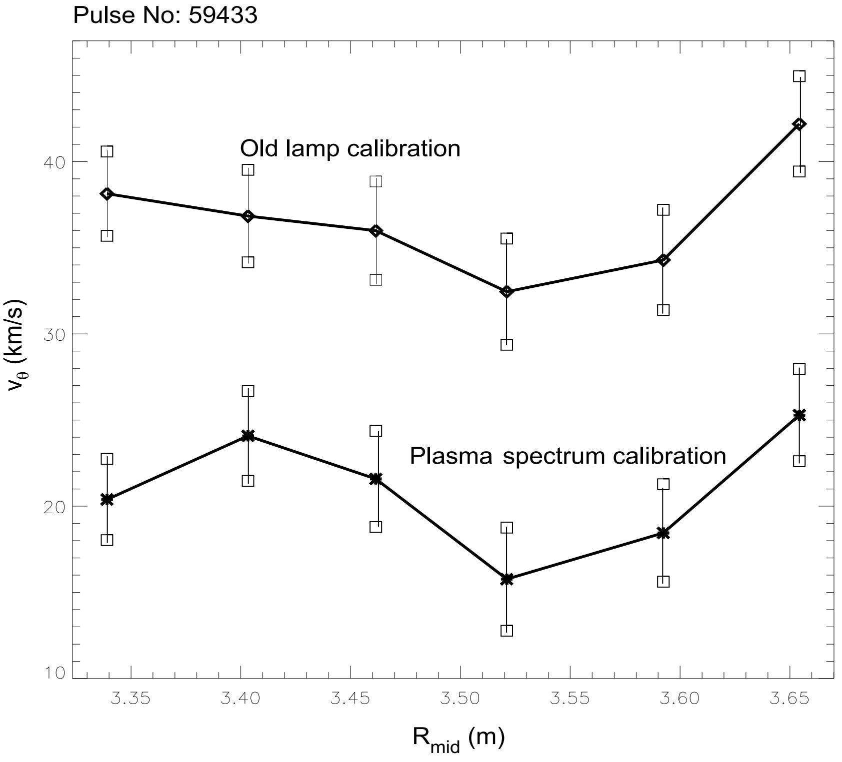

Figure 4.7: Illustration of the difference obtained in poloidal velocity using an old lamp calibration, or using the plasma spectrum itself for the calibration ($I_p = 2.5$ MA and $B_\phi = 2.4$ T). The absolute values of the poloidal rotation velocity are about 20 km/s less if the plasma spectrum is used for the wavelength calibration.

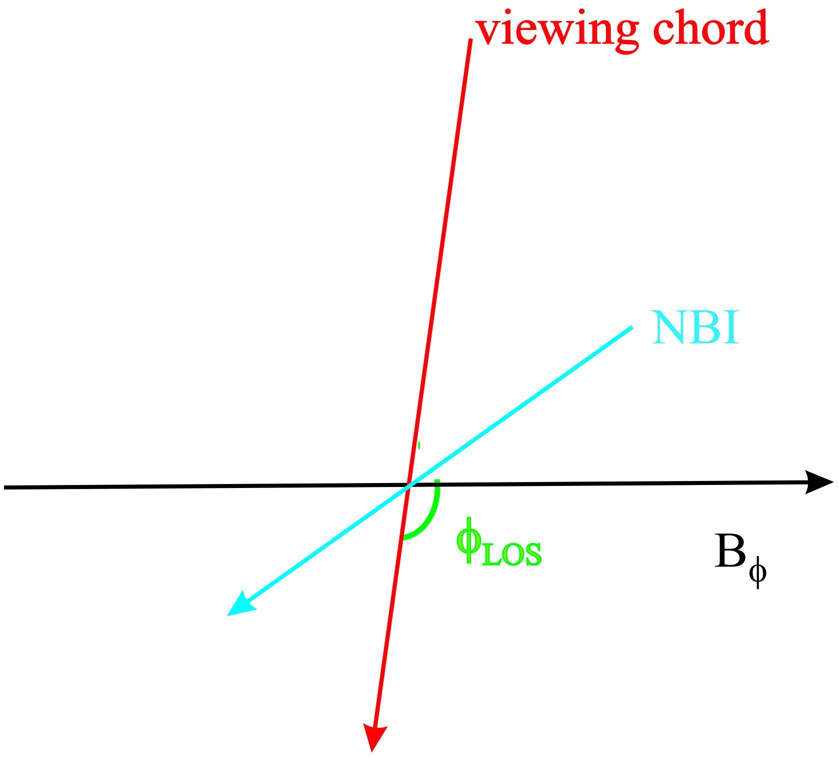

Figure 4.8: Definition of ϕ_{LOS}, the angle between the viewing chord and the toroidal direction at the intersection with the neutral beam injection. The spatial extent of the beam line and the observation chord are neglected here.

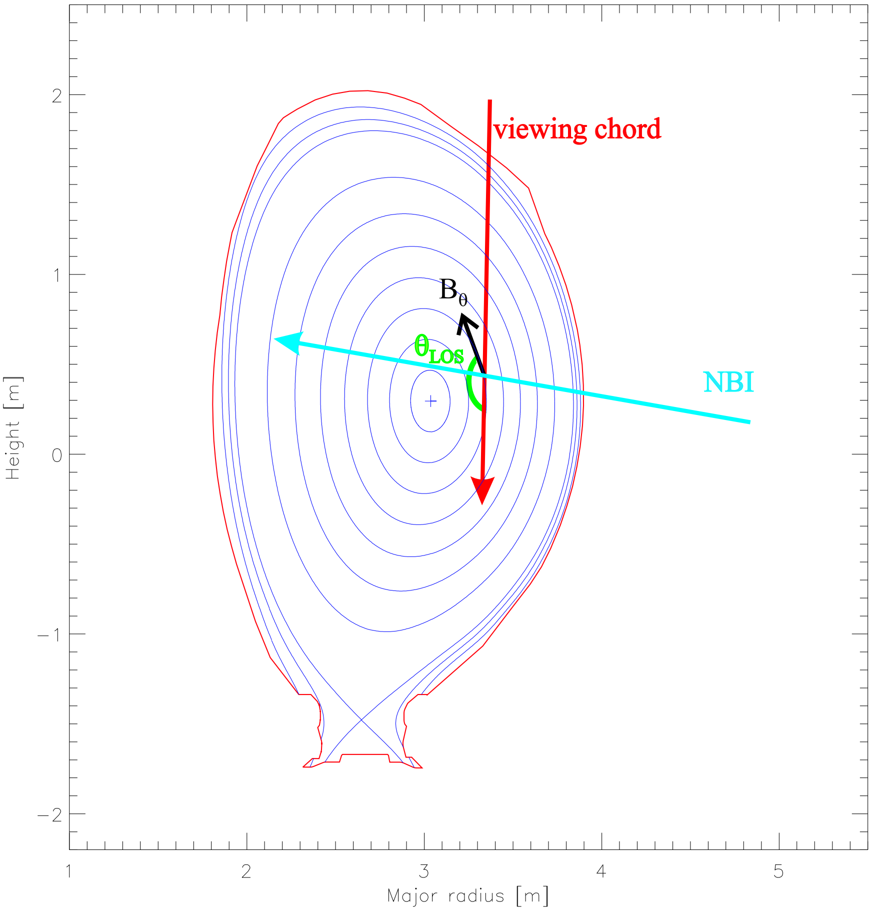

Figure 4.9: Definition of θ_{LOS}, the angle between the viewing chord and the poloidal direction, neglecting the finite intersection volume between beam injection and line of sight.

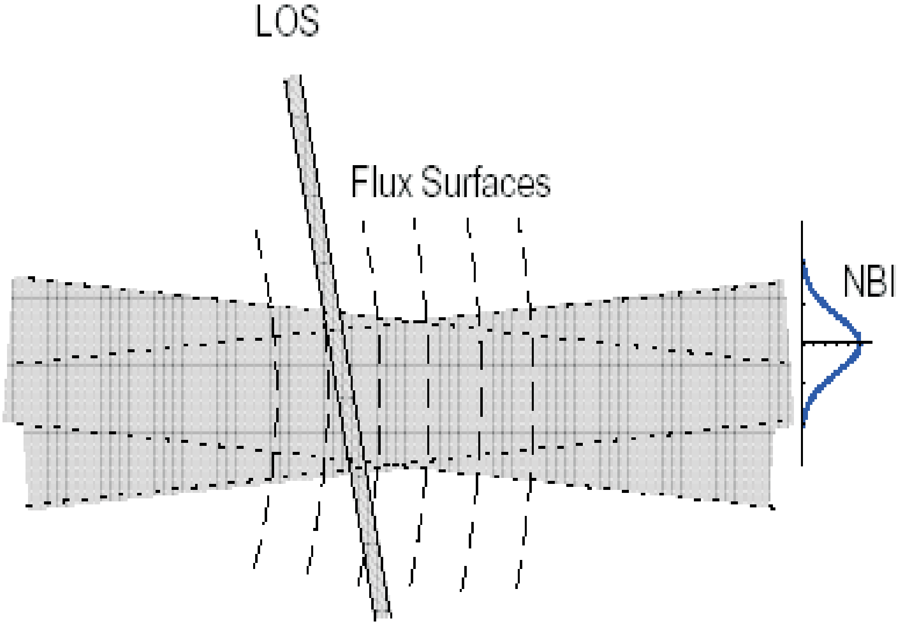

Figure 4.10: Schematic view of the intersection of a line of sight with the beam volume, when two PINIs are used [Hawk95].

over the different neutral injectors that were used in the discharge, is calculated in magnetic flux coordinates (beam attenuation is not taken into account). The paths of the lines of sight through the plasma cross different flux surfaces in their way through the beam injection volume (figure 4.10). The more tangential the line of sight to the flux surface, the more important the beam density contribution from that flux surface to the total signal, resulting in a weighted beam density function. The center of gravity of this function is the *true radius* for the line of sight; it is expressed as the major radius at the magnetic midplane after mapping up to the flux surfaces. The *resolution* is defined as the difference between the inner and outer true radius where the area under the weighted density function exceeds 20% of the total integrated density, again expressed in major radii after mapping onto the magnetic midplane.

(B) The lines of sight have a finite spatial dimension as well, and therefore an extra radial extent of about 5 cm has to be added to the resolution to determine the *real spatial extent* of the intersection volume between NBI and viewing chord. The real spatial extent varies from about 6 to 10 cm, from the outer to the inner chords, depending on the equilibrium and PINIs that were used.

4.3.1 Experimental determination of the toroidal angle

The toroidal contribution to the total line of sight velocity largely affects the poloidal rotation velocity, as in most cases the toroidal rotation velocity at JET is about 10 times larger than the poloidal one. Therefore experiments were carried out to measure the toroidal angle contributions to the LOS [Crom03]. The plasmas were run in L-mode to minimise the core poloidal rotation, according to neoclassical theory. To avoid a transition to H-mode (and possibly a strong change in v_θ) a minimal level of additional heating was used: no ICRF and only the amount of NBI power that was needed for the CXRS measurements and for the gradual increase in toroidal rotation velocity. The measurements did show low (< 5 km/s) and – more importantly – constant poloidal rotation time traces for these discharges. To allow a direct measurement of the toroidal contribution to $\mathrm{v}_{\mathrm{LOS}}$, the toroidal rotation was increased in a stepwise manner during the shot, by gradually increasing the number of tangential PINIs. The neutral beam injectors on JET are located in two opposite octants, octant 4 and octant 8. Four of the PINIs on each

bank are called tangential injectors as they launch the neutral particles mainly in toroidal direction, in contrast to the normal bank of injectors, which have a larger normal trajectory. Note that injection from neither the normal or tangential bank is completely poloidal or toroidal. The set-up of the NBI heating and the direction of toroidal magnetic field and plasma current for the standard operation are illustrated in figure 4.11. The path of injection, projected onto a poloidal cross-section, is given in more detail in figure 4.12 for all eight PINIs of one octant. During the dedicated shots the stepwise increase in toroidal rotation velocity was achieved by switching on more tangential PINIs (numbers 1,2,7 and 8 of figure 4.12). In order to minimise any possible input of poloidal momentum, this was done in pairs on opposite sites of the magnetic midplane (for example 2 and 7 start to fire at the same time).
Time traces for one of the spin-up shots are shown in figure 4.13: (a) the stepwise increase in total NBI power and (b) in toroidal rotation velocity, measured by a second, independent charge exchange diagnostic (with a purely tangential view). (c) No sign of an H-mode is seen on the D_α light from the outer divertor, and (d) the poloidal rotation velocity remains constant and < 5 km/s during the increasing toroidal rotation.
To estimate the toroidal contribution to the poloidal viewing chord geometry, the measured toroidal velocities with the toroidal CXRS diagnostic [vH90], were interpolated using a spline fit through the complete dataset to the locations of the poloidal CXRS lines of sight, as illustrated in figure 4.14.
Rewriting equation 4.2 as the equation of a straight line:

$$\overbrace{v^i_{LOS}}^{y} = \underbrace{\cos(\phi^i_{LOS})}_{A}\ \overbrace{v^i_\phi}^{x} + \underbrace{v^i_\theta \cos(\theta^i_{LOS})}_{B}, \tag{4.3}$$

and plotting $\mathrm{v^i_{LOS}}$ as a function of $\mathrm{v^i_\phi}$ for the scan of toroidal velocities, makes it possible to experimentally estimate the cosine of the toroidal angle ϕ^i from the results of the spin-up pulses. Fixed angles are assumed during the toroidal velocity scan (changes in the cosine values due to variation in the magnetic geometry are calculated to be less than 1%) and a constant $\mathrm{v^i_\theta}$, as shown by figure 4.13 (d). Therefore the coefficients A and B from eq. 4.3 can be taken to be constant and the result of the straight line fit through the datapoints is illustrated in figure 4.15 for the viewing chord at $\mathrm{R_{mid}} = 3.34$m. The slope of the fitted line ($\mathrm{A} = cos(\phi^i_{LOS})$) is then the experimental value for the cosine of the toroidal angle, and thus the fraction of the total toroidal velocity that is picked up by the poloidal charge exchange diagnostic.

The experimental values of $\cos(\phi_{LOS})$ are lower than the calculated values by about 15%, as shown in figure 4.16, indicating that the toroidal contribution to $\mathrm{v_{LOS}}$ is lower than the calculations suggest. The v_θ values are $\sim$ 5 km/s higher if the experimentally derived angles are used instead of the calculated ones, as illustrated in figure 4.17. To account for this difference in toroidal angle an uncertainty of +/-0.05 on the absolute value of $\cos(\phi^i_{LOS})$ is included in the total error bar on v_θ. In this way the 15% difference is largely covered, as typical values for $\cos(\phi^i_{LOS})$ are 0.20 - 0.30. The magnitude of the possible error in v_θ due to an uncertainty in the toroidal contribution to the total $\mathrm{v_{LOS}}$ has been quantified by the L-mode spin-up experiments. However, before using the measured $\cos(\phi^i_{LOS})$ values in the routine v_θ calculations a more complete study of the effect of magnetic geometry is recommended, since the angles ϕ^i_{LOS} and θ^i_{LOS} change with the magnetic equilibrium, and all the pulses in the study presented here, were performed with the same B_ϕ and I_p.

4.4 Atomic physics effects

The CXRS velocity measurement is complicated by atomic physics effects due to (i) the energy dependence of the cross-section and (ii) the gyro-orbit motion, and the importance of these effects increases with higher $\mathrm{T_i}$. The physical background of the distortions to the spectral lines caused by these temperature effects, was developed by Von Hellermann and Bell [vH95, Bell00]. Corrections to the CXRS spectra have been applied on ASDEX-U by Meister [Meis01], and more recently on DIII-D by Solomon [Solo04b]. The principles of these temperature effects are summarised here and the corrections that need to be applied to the CXRS spectra of JET are described. The implications for the v_θ measurements for ion temperatures up to more than 20 keV are also calculated for typical ITB plasmas.

4.4.1 Energy dependence of the CX cross-section

The spectral lineshape originates from an ensemble of particles, with velocities described by a three-dimensional velocity distribution function. The shape of the observed spectral line is determined by the velocity

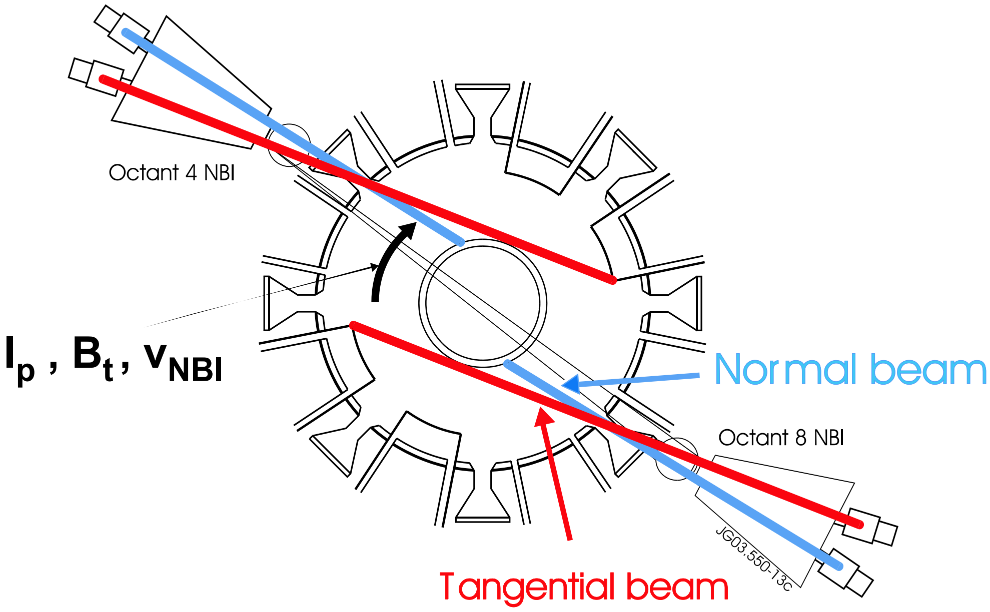

Figure 4.11: The tangential and normal neutral beam injectors on JET, and the direction of the beam induced toroidal rotation (v_{NBI}), plasma current (I_p) and toroidal magnetic field (B_t) in standard operation.

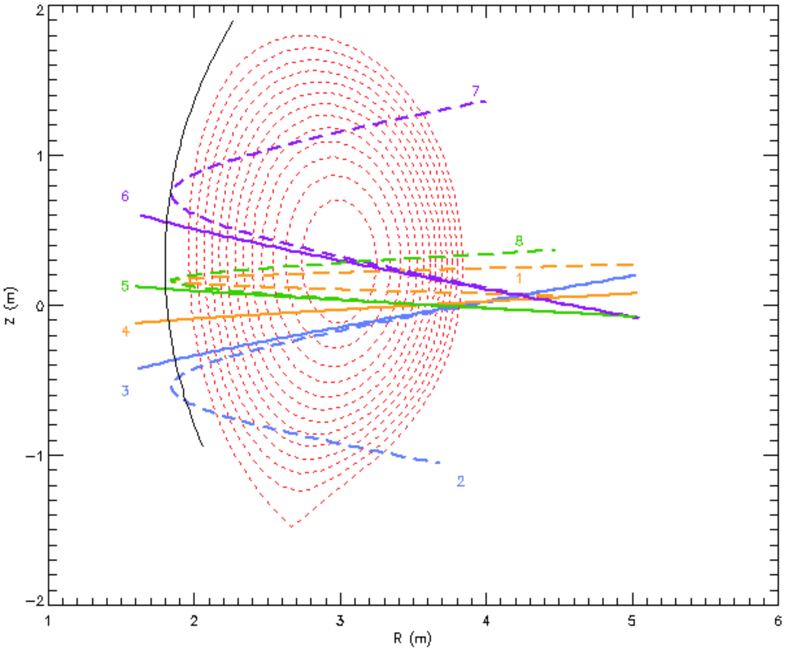

Figure 4.12: Trajectories of the different neutral injectors projected on the JET poloidal plasma cross-section : the normal bank in solid lines (numbers 3, 4, 5 and 6) and the tangential bank in dashed lines (1, 2, 7 and 8).

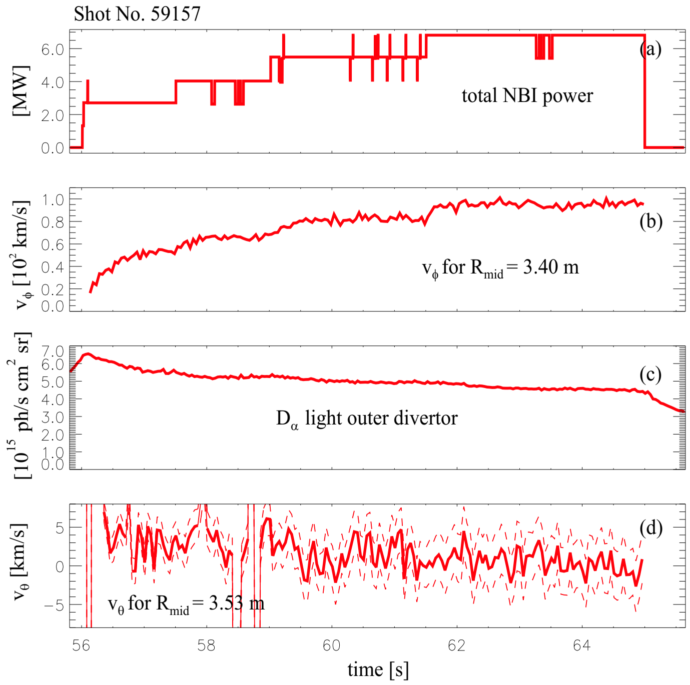

Figure 4.13: General parameters of the L-mode spin-up shots: (a) beam power, (b) toroidal velocity, (c) D_α light from the outer divertor and (d) poloidal rotation.

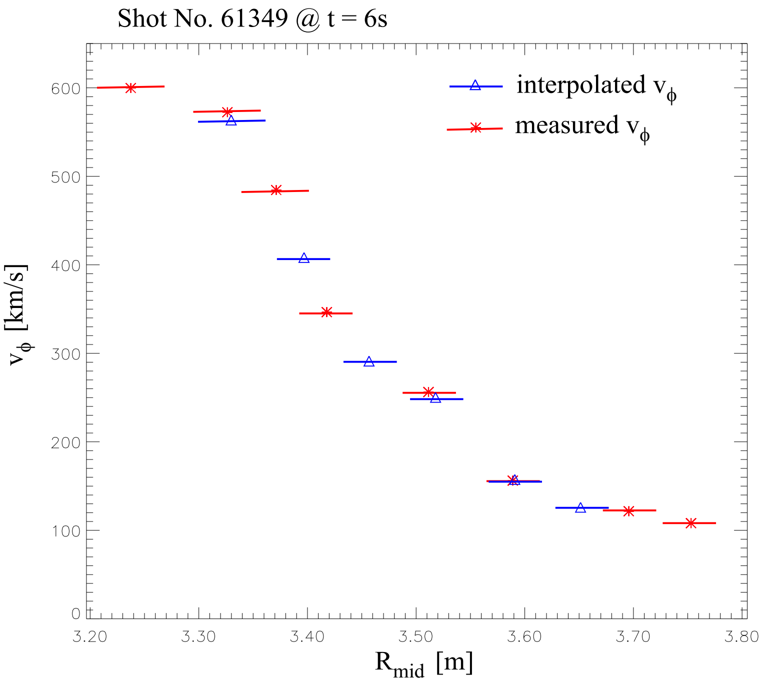

Figure 4.14: Toroidal rotation velocities measured with the horizontal CXRS diagnostic and the interpolated values at the locations of measurement of the poloidal CXRS diagnostic. The horizontal bars indicate the spatial extent (from both spot size and resolution).

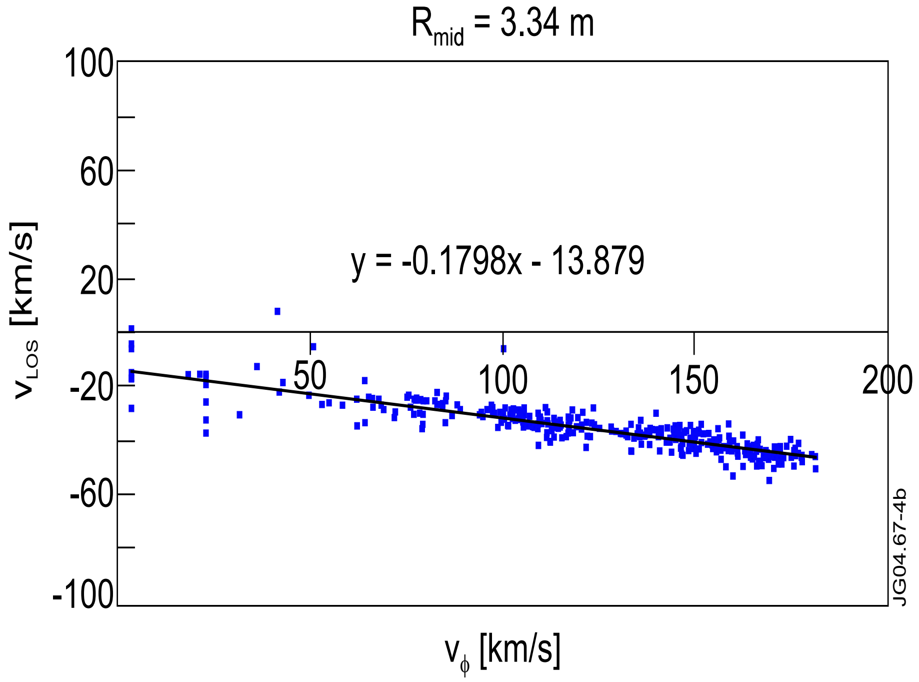

Figure 4.15: Straight line fit through the datapoints from the L-mode spin-up shots. The toroidal component of the total line of sight velocity is given by the slope of the fitted line ($\cos \phi_{\mathrm{LOS}}$).

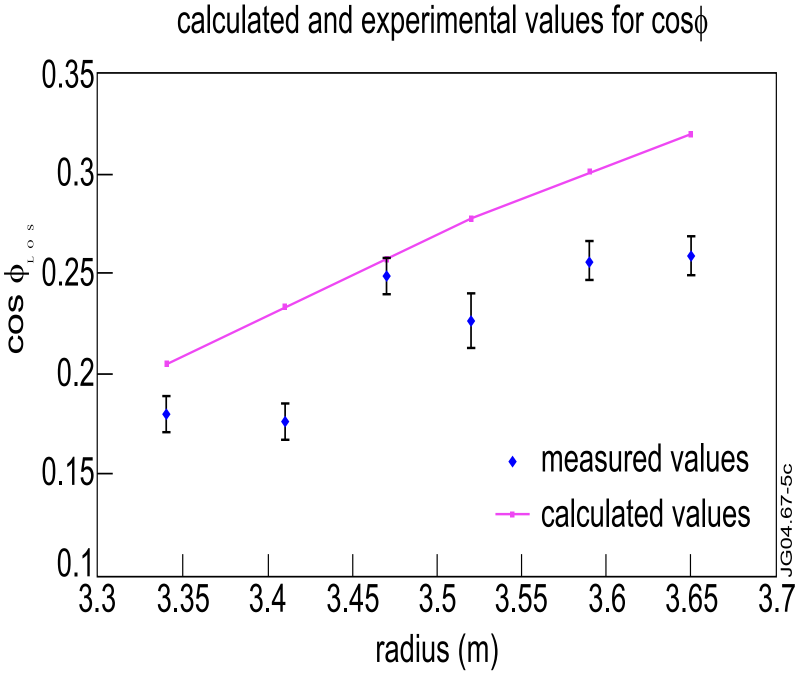

Figure 4.16: Comparison of calculated and measured values for the toroidal component of the total line of sight velocity

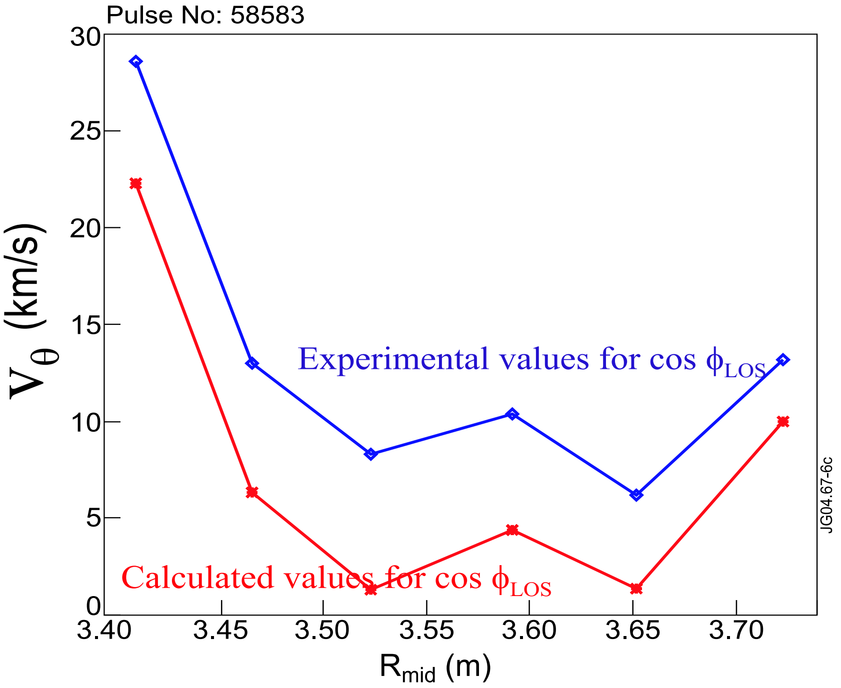

Figure 4.17: Effect of the calculated and experimentally measured $\cos \phi_{\mathrm{LOS}}$ values on the poloidal rotation velocity profiles.

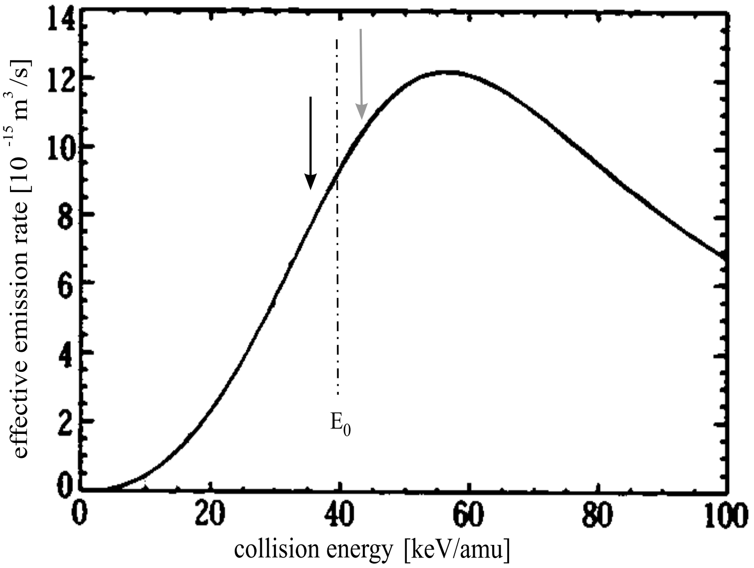

Figure 4.18: Effective emission rate for the transition $C^{5+}n = 8 \rightarrow 7$ at 529.05 nm. The full energy component of the JET deuterium beam. The C^{6+} ions moving towards the beam have a higher rate coefficient (grey arrow) than the ions moving away from the beam (black arrow).

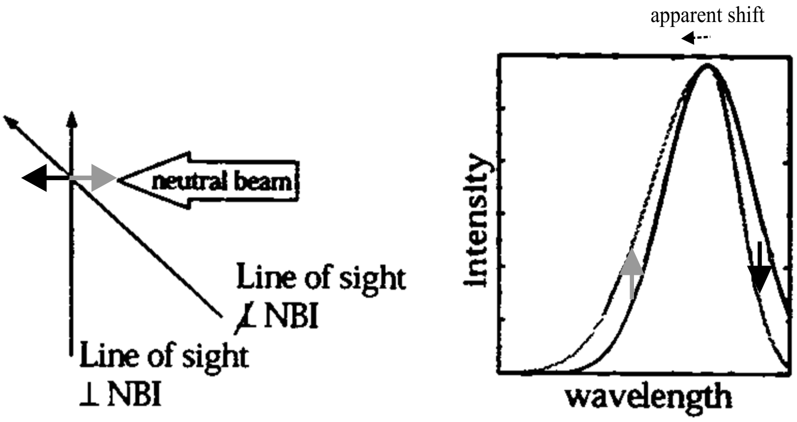

Figure 4.19: The spectral line from a viewing chord not perpendicular to the NBI injection suffers from an apparent line shift towards the observer (lower wavelengths), due to the energy dependence of the cross-section. The intensity at longer wavelengths are reduced (black), and the shorter wavelengths are enhanced (grey).

components of the emitting particles in the direction of the line of sight. The emission from a unit volume (E) is proportional to :

$$E \propto n_b n_Z < \sigma v >^{CX}, \tag{4.4}$$

where n_b is the beam neutral density, n_Z the impurity ion density and $< \sigma v >^{CX}$ the effective charge exchange rate coefficient, defined as :

$$< \sigma v >^{CX} = \int\int\int dv^3 \sigma^{CX}(|\overline{v} - \overline{v}_b|)|\overline{v} - \overline{v}_b| f(\overline{v} - \overline{v}^{rot}), \tag{4.5}$$

where $|\overline{v} - \overline{v}_b|$ is the collision velocity between impurity ion and beam neutral and $\sigma^{CX}(|\overline{v} - \overline{v}_b|)$ is the charge exchange cross-section.
$f(\overline{v} - \overline{v}^{rot})$ is the Maxwellian velocity distribution of the fully ionised impurity ion centered around its average rotation $\overline{v}^{rot}$.
Using the effective emission rate Q,

$$Q(|\overline{v} - \overline{v}_b|) = \sigma^{CX}(|\overline{v} - \overline{v}_b|)|\overline{v} - \overline{v}_b|, \tag{4.6}$$

eq.(4.5) can be re-written as:

$$< \sigma v >^{CX} = \int\int\int dv^3 Q(|\overline{v} - \overline{v}_b|) f(\overline{v} - \overline{v}^{rot}). \tag{4.7}$$

Using a right handed (x,y,z) coordinate system with the z-axis in the observation direction and the beam line in the (y,z) plane, $f(\overline{v} - \overline{v}^{rot})$ is given by:

$$\frac{1}{\pi^{3/2} v_{th}^3} \exp\left(- \frac{(v_x - v_x^{rot})^2 + (v_y - v_y^{rot})^2 + (v_z - v_z^{rot})^2}{v_{th}^2} \right), \qquad (4.8)$$

where

$$v_{th} = \sqrt{\frac{2T_i}{M_i}} \qquad (4.9)$$

is the thermal velocity.
The normalised spectral distribution in the direction of the observation is described by [vH95]:

$$\frac{f(v_z)}{< Q >} = \frac{\int\int\int dv'_x dv'_y dv'_z Q(|\overline{v} - \overline{v}_b|) \delta(\overline{v}_z - \overline{v}_{z'}) f(\overline{v}' - \overline{v}^{rot})}{\int\int\int dv'_x dv'_y dv'_z Q(|\overline{v} - \overline{v}_b|) f(\overline{v}' - \overline{v}^{rot})} \qquad (4.10)$$

Note that for simplicity the idea of one 'average' neutral beam injection direction has been used and is refered to as the beam line. In principle the specific geometry of all PINIs that contribute to the spectrum should be taken into account. In figure 4.18 the effective emission rate is plotted as a function of beam energy for the reaction (taken from [vH95]):

$$\mathrm{D}^0 + \mathrm{C}^{6+} \rightarrow \mathrm{D}^+ + \mathrm{C}^{5+(\mathrm{n}=8\rightarrow 7)}. \qquad (4.11)$$

Typical beam energies for the deuterium beam on JET are 80-130 keV, thus 40-65keV/amu for the main energy component E_0, i.e. on the left side of the maximum, so increasing for increasing collision energy. For an observation geometry with a component of the beam in the direction of observation, an apparent velocity results from the energy dependence of the cross-section. Indeed, ions moving towards the beam (and thus towards the observer) have a higher collision energy, and thus are more likely to undergo charge exchange, than the ions moving away from the beam. With the blue part of the spectrum enhanced (towards beam) and the red diminished, the net result is an apparant blue shift of the spectral line, that could wrongly be interpretated as a plasma velocity towards the observer. The higher the temperature the larger the difference of the collision energy between co- and counter (with beam) moving particles and thus the larger the apparent line shift (figure 4.19). This effect strongly depends on the component of the beam line in the observer direction, and is not present when the viewing chords are perpendicular to the direction of neutral beam injection. A simplification has been used here since in practice the partition of the beam energy in its three energy components, ($\mathrm{E}_0, \mathrm{E}_0/2$ and $\mathrm{E}_0/3$), should be considered for each individual PINI, resulting in three different cross-sections. In [vH95] the emission rate Q is assumed to be an exponential operator, and an analytic approximation is derived for the observed velocity, as a function of the angle between the direction of observation and beam injection:

$$v_{obs}^{LOS} = -\frac{\alpha \sin\delta B K T_{true}}{2G} - \frac{C v_y^{rot} - A v_z^{rot}}{G} \tag{4.12}$$

where

$$\begin{aligned} A &= 1 - KT_{true}(\epsilon \sin^2\delta + \beta \cos^2\delta) \\ B &= 1 - KT_{true}\epsilon \\ C &= \sin^2\delta \cos^2\delta K T_{true}(\epsilon - \beta) \\ G &= 1 - KT_{true}(\epsilon + \beta) + (KT_{true})^2 \epsilon\beta \end{aligned} \tag{4.13}$$

and

$$\begin{aligned} K &= 2e/m_Z \\ \epsilon &= \alpha/2v_b \\ \alpha &= \tfrac{1}{Q_0}\tfrac{dQ}{dv}|_{v=v_b} \\ \beta &= \tfrac{1}{2}[\tfrac{1}{Q_0}\tfrac{d^2Q}{dv^2}|_{v=v_b} - \alpha^2] \end{aligned} \tag{4.14}$$

and $(90^\circ - \delta)$ is the angle between the beam line and the observation direction, and $\mathrm{T}_{\mathrm{true}}$ the actual ion temperature, which may differ from the observed temperature, as described in section 4.5. An average value for δ of 16° was taken in the calculations. Furthermore v_z^{rot} and v_y^{rot} are the true rotation velocities along the z- and y-axis respectively, as defined above. In practice for typical ITB plasmas with high $\mathrm{T_i}$, the coefficient A/G is close to 1+/-0.01 and C/G is close to 0+/-0.01, therefore a good approximate relationship between the observed and real line of sight

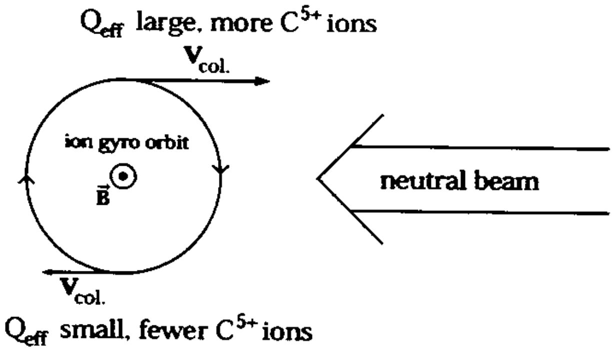

Figure 4.20: At the part of the gyro-orbit with a velocity component opposite to the direction of the injected neutral beam particles more C^{5+} ions are produced from charge exchange than at the part with a velocity component in the direction of the injected neutral beam particles, leading to a net velocity towards the neutral beam.

velocity is given by:

$$v_{obs}^{LOS} = -\frac{\alpha \sin \delta B K T_{true}}{2G} + v_{true}^{LOS} \tag{4.15}$$

The difference between the observed and real velocity is a shift in the observer's direction:

$$v_{obs}^{LOS} = v_Q^{LOS} + v_{true}^{LOS}. \tag{4.16}$$

For the beam energies on JET it will be towards the observer, i.e. $v_Q^{LOS} \leq 0$.

4.4.2 Effect of the gyro-orbit motion during the finite lifetime of the excited state

If the energy dependent cross-section was the only atomic physics effect, poloidal rotation measurements that are made almost perpendicular to the neutral beam would not have large corrections. However, for an angle δ of about 16° between observation direction and beam injection, as is the case on JET, leads to typical corrections of a few to even more than 20 km/s in v_{LOS}, and can therefore be a considerable fraction of the total v_{LOS}. More complications arise from the gyro-orbit motion during the time that the impurity ion stays in the excited state after CX before

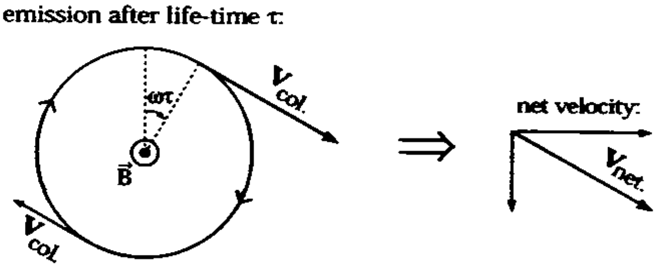

Figure 4.21: The precession of the ion in its gyro-orbit during the lifetime τ_{eff} of the excited state transforms the radial velocity from figure 4.20 into an apparent downward (poloidal) velocity.

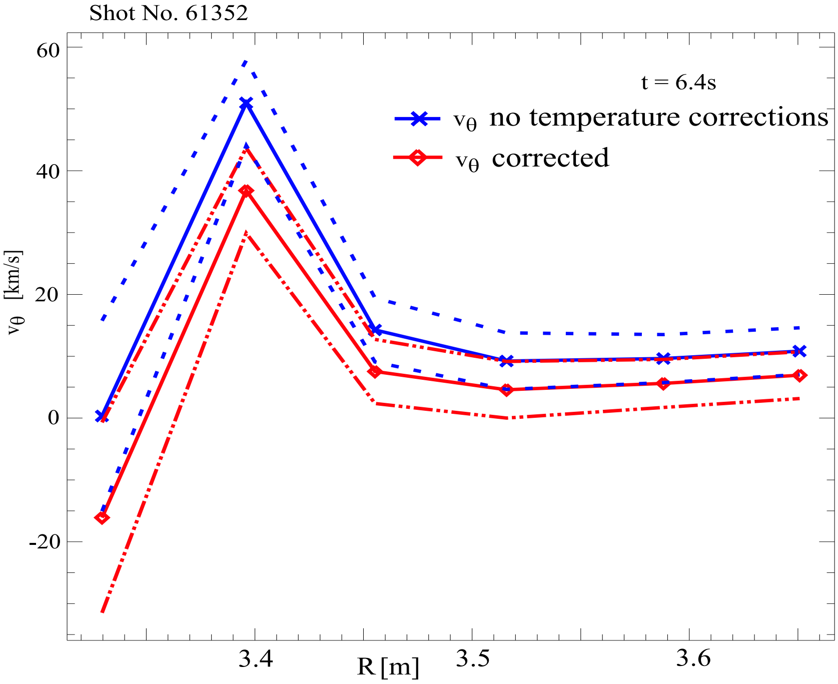

Figure 4.22: Poloidal rotation velocity profile with and without the temperature corrections.

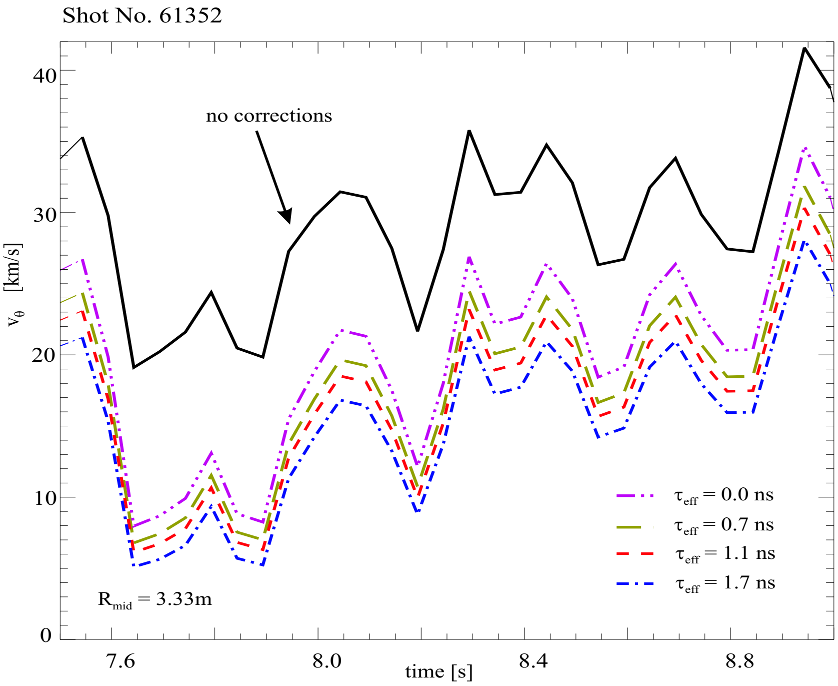

Figure 4.23: The longer the lifetime of the excited state the more important the temperature corrections become.

emitted a photon. Typical lifetimes τ for this transition for ion temperatures up to 20 keV (increasing τ with $\mathrm{T_i}$), are of the order of $10^{-9}s$. The angle on the gyro-orbit ($\omega\tau$ where ω is the cyclotron frequency), travelled between the CX reaction and relaxation from the excited level, can also significantly influence the measured velocity. For typical magnetic fields of 2-4 T, $\omega = (8-16)10^7$ and $\omega\tau = 0.08 - 0.16$. If there is a component of the neutral beam in the plane of the gyro-orbit motion (figure 4.20), the ions at the top of the gyro-orbit have a larger collision velocity and will more likely undergo CX (due to the energy dependence of the cross-section, analogous to the effects from section 4.4.1), this will lead to an apparent line shift antiparallel to the beam component of figure 4.20. After precession over angle $\omega\tau$, part of this apparent radial velocity will be redirected in poloidal direction (figure 4.21), perpendicular to the beam component. The combined implication of this gyro-orbit motion and the effect described in section 4.4.1 on the measurement, is given by eq.6 in [Solo04b] for a local measurement:

$$\overline{v}^{local}_{obs}(\overline{v}_n) = \frac{1}{1+\omega^2\tau^2}\left(\overline{v}_n + \frac{\omega\tau}{B}\left(\overline{v}_n \times \overline{B}\right) + \frac{\omega^2\tau^2}{B^2}\left(\overline{v}_n.\overline{B}\right)\overline{B}\right). \tag{4.17}$$

The observed velocity ($\overline{v}_n$) of the Z_n charge exchange ion immediately after charge exchange (including the cross-section effects of section 4.4.1) is given by :

$$\overline{v}_n = \frac{\int dv^3 Q(|\overline{v}-\overline{v}_b|)\overline{v} f_{n+1}(\overline{v}-\overline{v}^{rot})}{\int dv^3 Q(|\overline{v}-\overline{v}_b|) f_{n+1}(\overline{v}-\overline{v}^{rot})}. \tag{4.18}$$

similar to eq.(4.10), but now with a more general notation than the (x,y,z) coordinate system of eq.(4.10) and the distribution function impurity ion right before CX. The right hand side of eq.(4.17) can be seen as an operator on the observed velocity $\overline{v}_n$ describing the twist around $\overline{B}$ by the gyro-motion during the finite lifetime τ [Solo04b]. The extension of this local equation is a line integration along the viewing line of sight. The simplified treatment from section 4.4.1 is again used here, assuming an averaged beamline, and substituting $\overline{v}_n$ with $\overline{\mathrm{v}}^{\mathrm{LOS}}_{\mathrm{obs}}$ (with $\mathrm{v}^{\mathrm{LOS}}_{\mathrm{obs}}$ from eq.(4.15)), for the line integrated measurement. Eq.(4.17) then transforms into (with temperature corrections only to first order):

$$\begin{aligned} v_{obs}^{LOS*}(\overline{v}_{true}) &= \tfrac{1}{1+\omega^2\tau^2}\left(v_{true}^{LOS} + v_{Q}^{LOS}\right) \\ &+ \tfrac{\omega\tau}{1+\omega^2\tau^2}\left(\tfrac{1}{B}(\overline{v}_{true}\times\overline{B})^{LOS}\right) . \\ &+ \tfrac{\omega^2\tau^2}{1+\omega^2\tau^2}\left(\tfrac{1}{B^2}(\overline{v}_{true}.\overline{B})\overline{B}^{LOS}\right) \end{aligned} \tag{4.19}$$

The second term (v_Q^{LOS}) is the standard cross-section correction of section 4.4.1. The perpendicular and parallel flow in the third and forth term can be approximated, using the following equation :

$$\begin{aligned} U_\perp &\approx U_\theta - \tfrac{B_\theta}{B}U_\phi, \\ U_\parallel &\approx U_\phi + \tfrac{B_\theta}{B}U_\theta, \end{aligned} \tag{4.20}$$

where $U_\perp$ is the perpendicular and $U_\parallel$ the parallel flow velocity, and U_θ is the poloidal and U_ϕ the toroidal velocity component.
For the line of sight integration of the third and forth terms, the poloidal and toroidal rotation velocity components along the chords are used, resulting in:

$$\begin{aligned} v_{obs}^{LOS*}(\overline{v}_{true}) &= \tfrac{1}{1+\omega^2\tau^2}\left(v_{true}^{LOS} + v_{Q}^{LOS}\right) \\ &+ \tfrac{\omega\tau}{1+\omega^2\tau^2}\left(v_{true}^{\theta}\cos(\theta_{\mathrm{LOS}}) - \tfrac{B_\theta}{B}v_{true}^{\phi}\cos(\phi_{\mathrm{LOS}})\right) . \\ &+ \tfrac{\omega^2\tau^2}{1+\omega^2\tau^2}\left(v_{true}^{\phi}\cos(\phi_{\mathrm{LOS}}) + \tfrac{B_\theta}{B}v_{true}^{\theta}\cos(\theta_{\mathrm{LOS}})\right) \end{aligned} \tag{4.21}$$

An illustration of the impact on the poloidal rotation profile is given in figure 4.22 for $\tau_{\mathrm{eff}} = 1.1$ns. The effect of the temperature corrections on the poloidal rotation velocity is the most important for the inner channels, where $\mathrm{T_i}$ is in this example about 17 keV. The lifetime of the excited state was studied theoretically by Bell [Bell00] and measured experimentally on TFTR and DIII-D. The result from the calculations was 0.7 ns, the experiments on TFTR however gave a value of 1.1 ns, and this is now commonly used [Meis01, Solo04b]. Recent measurements on DIII-D estimated an even higher value of 1.7 ns. The effect of increasing lifetimes has been studied and the results for the time trace of the innermost chord, $\mathrm{R_{mid}} = 3.33\mathrm{m}$, are presented in figure 4.23. The trace for $\tau_{\mathrm{eff}} = 0.0\mathrm{ns}$ shows the impact of the energy dependence of the cross-section seperately, in the example the observed (uncorrected) poloidal velocities are up to 10 km/s higher than when the cross-section corrections are applied. Increasing τ_{eff} further increases the difference between real and observed velocity up to 15 km/s.

4.5 Ion temperature measurement

Assuming a Maxwellian velocity distribution for the impurity ions, the ion temperature can be calculated from the width of the Gaussian fit to the spectral line, given as a function of wavelength

$$f(\lambda) = \frac{1}{\sigma\sqrt{2\pi}} \exp\left(-\frac{(\lambda-\lambda_0)^2}{2\sigma^2}\right), \tag{4.22}$$

where

$$\sigma = \frac{\lambda_0}{c}\sqrt{\frac{2T_i}{m_C}}, \tag{4.23}$$

and $\mathrm{T_i}$ is the ion temperature in eV, λ_0 the wavelength of the central CX emission line, and $\mathrm{m_C}$ the mass of the carbon ions $\approx$ 12 amu $= 12 \times 931.494$ MeV $/\mathrm{c}^2$. The Full Width Half Maximum (FWHM) of the Gaussian function is given by:

$$\mathrm{FWHM} = 2\sqrt{2\ln 2}\sigma, \tag{4.24}$$

and thus

$$\mathrm{T_i} = 12\left(\frac{\mathrm{FWHM}}{\lambda_0}\frac{1}{7.710^{-5}}\right)^2. \tag{4.25}$$

As a consequence of the cross-section effect described in section 4.4.1, the observed temperature differs from the true temperature, following [vH95] the relationship is given by:

$$\mathrm{T_{obs}} = \mathrm{T_{true}}\frac{1-\mathrm{KT_{true}D}}{\mathrm{G}}, \tag{4.26}$$

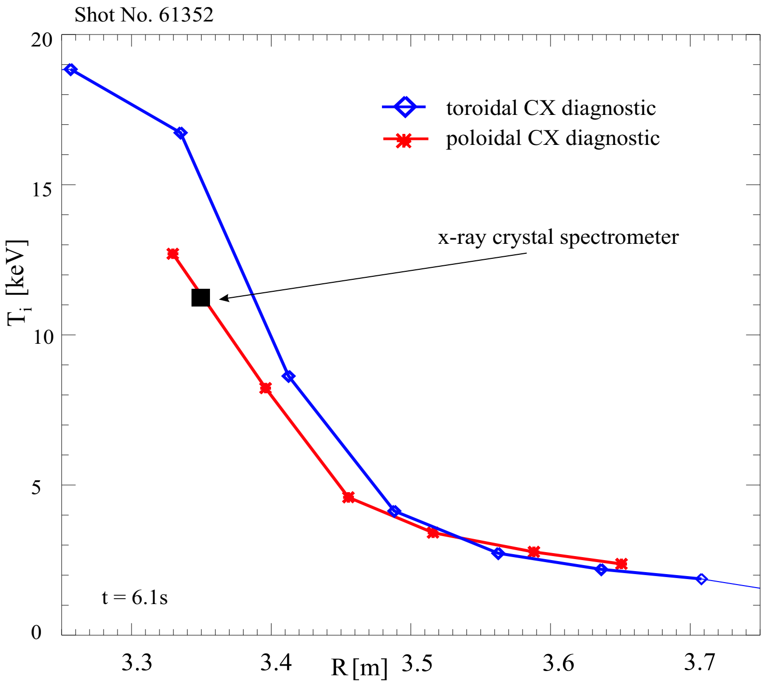

Figure 4.24: Comparison of T_i measured with three independent diagnostics.

with the same definitions for K and G as in section 4.4.1, and $D = (\epsilon \sin^2 \delta + \beta \cos^2 \delta)$.

The ion temperature is also measured by the toroidal charge exchange diagnostic (on C^{6+}) and by an X-ray crystal spectrometer observing Ni^{26+} ions. The results from the three diagnostics are in good agreement, as can be seen from the profiles in figure 4.24 and the time traces in figure 4.25. For high central temperatures the poloidal diagnostic usually gives lower results than the toroidal diagnostic, and the x-ray crystal data lies somewhere in between the two charge exchange diagnostics. The reason for this difference is at present unclear and could originate from a possible difference in parallel versus perpendicular temperature. In that case the assumption of a 3-D Maxwellian velocity distribution is not valid, and the FHWM of the Gaussian fit may differ according to the observation direction.

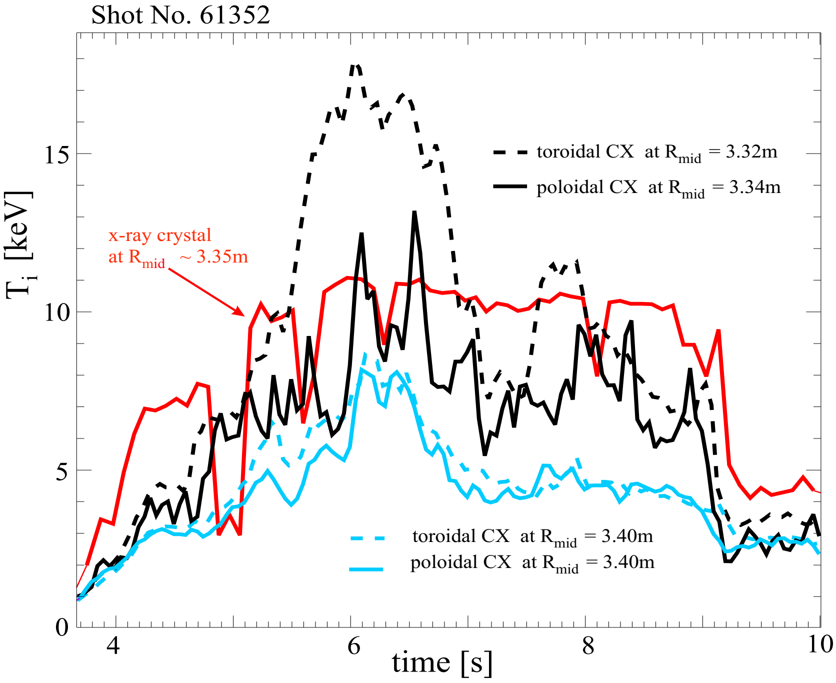

Figure 4.25: Time traces of T_i evolution during an ITB discharge, for the two innermost chords of the poloidal CXRS diagnostic. The innermost chord ($\mathrm{R_{mid}} = 3.34\mathrm{m}$) measures a lower T_i than the toroidal viewing diagnostic. The results from the x-ray crystal spectrometer lie in between both CXRS diagnostics. The ($\mathrm{R_{mid}} = 3.40\mathrm{m}$) channel of both CXRS diagnostics agree very well.

Chapter 5

Experimental results

The C^{6+} poloidal rotation velocity was measured with the core view of the poloidal CXRS diagnostic described in chapter 4 during the JET campaigns of 2002-2004. A study of spectra taken in ITB plasmas, using the improved analysis technique is presented in this chapter. A temperature correction has been included in the analysis, it comprises both a term for the energy dependence of the charge exchange cross-section [vH95], and a correction for the gyro-orbit motion during the finite lifetime of the excited state [Solo04b]. Large excursions in v_θ associated to the barrier region are observed. They appear to be an order of magnitude larger than neoclassical predictions.

5.1 General parameters of the ITB plasmas

In figure 3.10 typical density and temperature profiles have been shown for a plasma with a fully formed transport barrier. For a similar discharge (shot no. 61349, $B_t/I_p = 3.2T/3.0MA$) from the same series of ITB plasmas, the time traces of the additional heating power are shown in figure 5.1(a), together with the electron density measured by the Thomson Scattering diagnostic (b), and the ion and electron temperatures (c) at an intermediate radius ($R_{mid} = 3.4m$), respectively measured by the toroidal CXRS and the Thomson Scattering system. At this radial location the first traces of a barrier appear at about t = 5.2 s, visible in the n_e and T_i traces, and weakly in the T_e trace at $R_{mid} = 3.4$ m. This is confirmed by the contour plot of ρ_T^* (according to the ITB criterion) in figure 5.2. This figure shows that the barrier was formed more centrally and moved outwards and is viewed by the

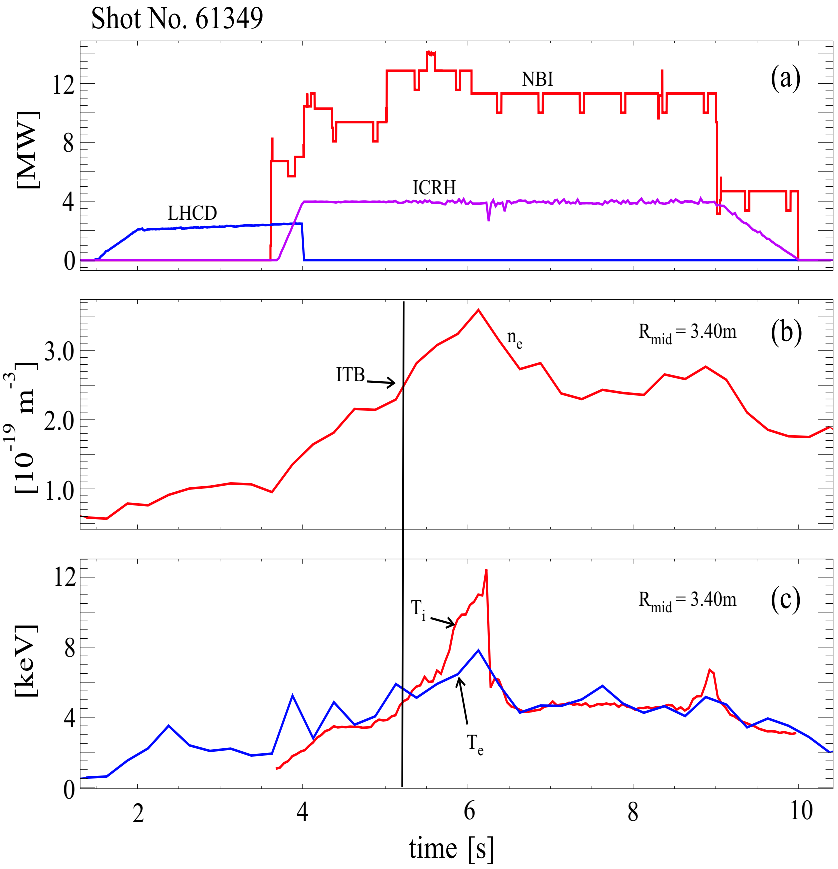

Figure 5.1: (a) Additional heating power (LHCD, ICRH and NBI), (b) the electron density (measured by the Thomson Scattering diagnostic) and (c) the ion and electron temperature (measured by respectively CXRS and Thomson Scattering) for a typical ITB shot on JET (shot no. 61349), during which tritium was also puffed.

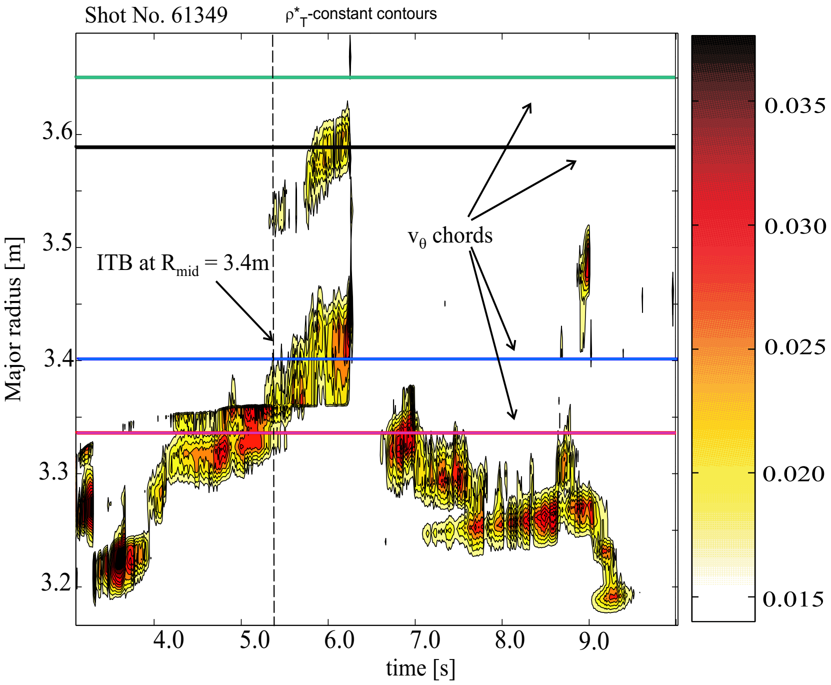

Figure 5.2: A contour plot of the regions where ρ^*_T exceeds the critical value of 0.014, defined as the criterion for the existence of an ITB on JET, for the example tritium shot no. 61349.

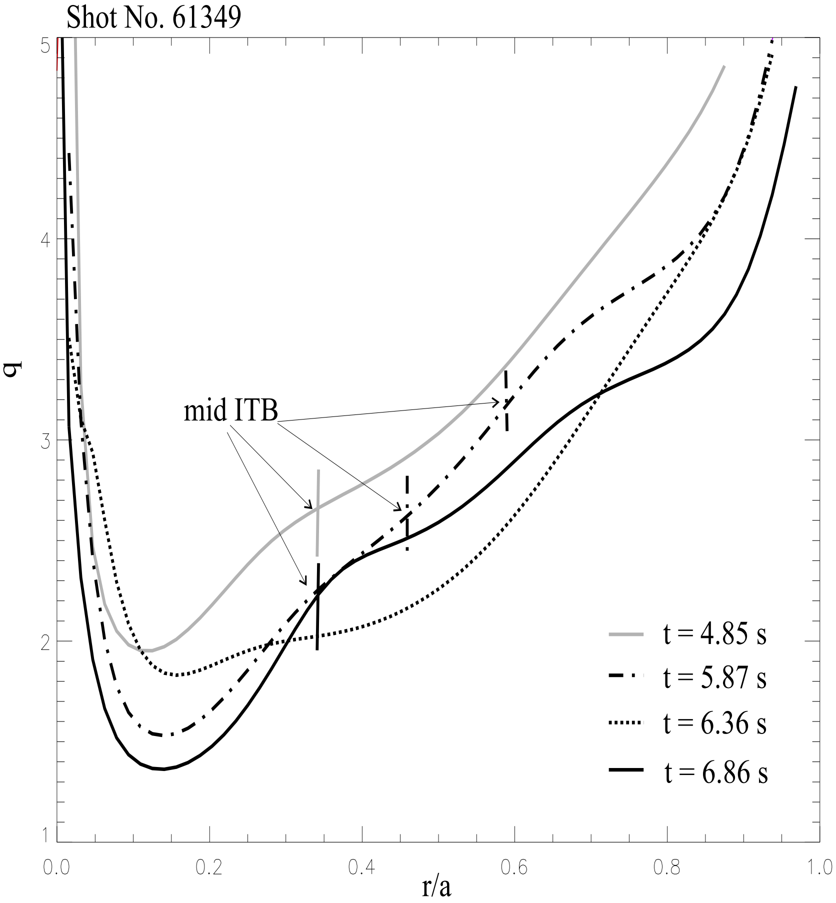

Figure 5.3: The q-profile of shot no. 61349 at different times during the existence of the barrier, with a very strong negative central shear, typical for current hole discharges.

first CXRS channel for v_θ measurements (indicated by the horizontal red line) at about t = 4.0 s. As the barrier continues to expand radially it is picked up by the second (blue line) v_θ chord at t = 5.2 s. At the same time a second, outer barrier was formed around $R_{\mathrm{mid}} = 3.52$m, which is viewed by the chord at $R_{\mathrm{mid}} = 3.59$m during t = 5.5 s – 6.3 s (in black). The outermost chord (in green) at $R_{\mathrm{mid}} = 3.65$m lies just outside the second barrier.

The q-profile is shown in fig. 5.3 for different times during this discharge with tritium injection. This was an example of a plasma with a current hole [Hawk01], for which the central q reaches very high values. The desired q-profile was obtained using off-axis lower hybrid heating and current drive (LHCD) during the current ramp up phase [Chal01, Hawk01]. The LHCD prelude can also be seen in figure 5.1(a). A strongly negative central shear is created that helps the barrier formation (section 3.2.3). The approximate location of the ITB is indicated on the q-profiles in fig. 5.3 and has been determined as the mid-radius point of the region with strong temperature gradients.

5.2 Poloidal rotation dynamics in the barrier region of ITB plasmas

For the discharge (shot no. 61349), described in the previous section, the v_θ time traces from the four chords in the region of the two ITBs are presented in fig. 5.4 for the inner and fig. 5.5 for the outer barrier. The poloidal rotation velocity of the innermost viewing channel ($R_{\mathrm{mid}} = 3.33$m) increases in positive direction (i.e. the electron diamagnetic direction) from 0 to 10 km/s during t = 4.5 s – 5.2 s, after which the direction of rotation changes to the ion diamagnetic direction and increases to -55 km/s during the interval t = 5.2 s – 6.2 s. Figure 5.2 shows that this viewing chord looks at the middle of the strong temperature gradient during t = 4.5 s – 5.2 s, and that later on the ITB moves outwards, such that the relative location of this chord with respect to the T_i gradient changes. During the second time interval, t = 5.2 s – 6.2 s, the red channel sees the inner edge of the temperature gradient and this seems to correspond to the velocity increase in ion diamagnetic direction. Over the same time interval, the adjacent chord ($R_{\mathrm{mid}} = 3.40$m) looks at the middle of the T_i gradient and v_θ increases in the positive direction from about -5 to 7 km/s.

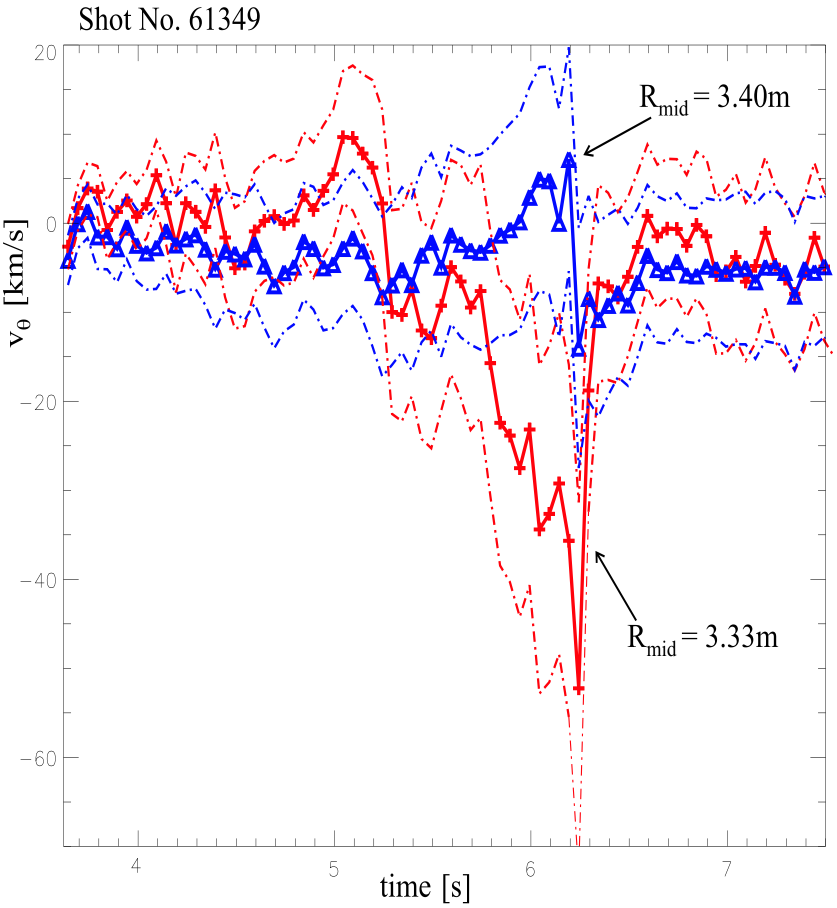

Figure 5.4: Time traces of the poloidal rotation velocity for the two chords covering the inner barrier of shot no. 61349. Positive values are in the electron diamagnetic direction.

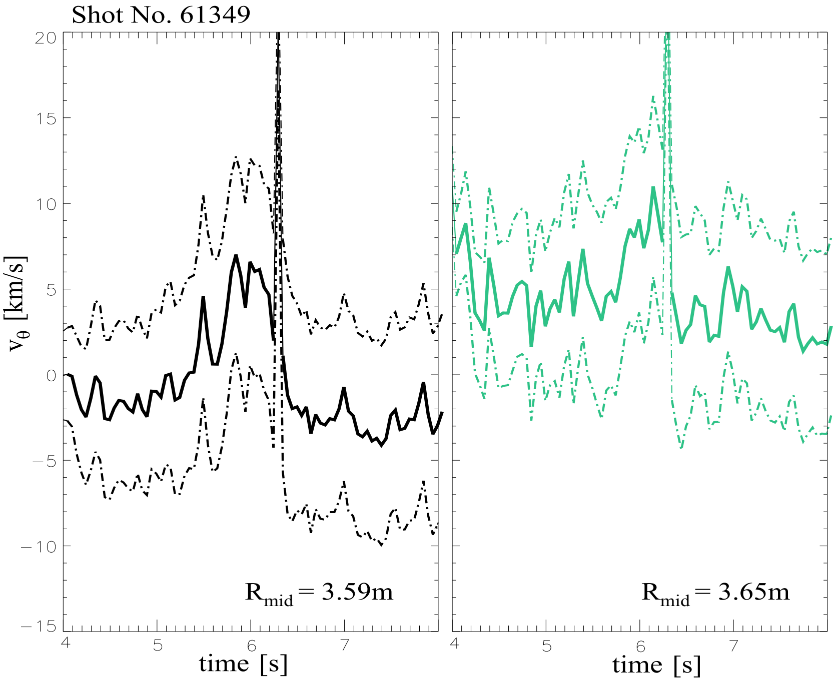

Figure 5.5: v_θ time traces for two chords covering the outer barrier in shot no. 61349.

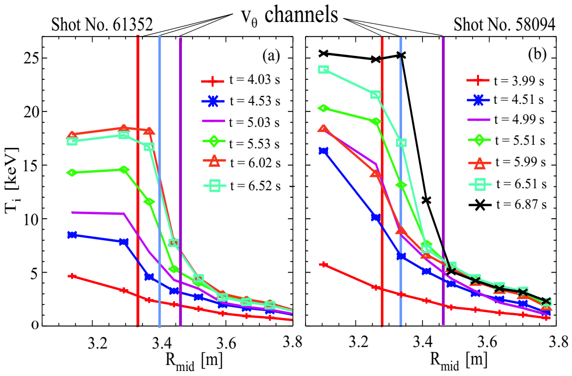

Figure 5.6: Radial T_i profiles during the evolution of the ITB for (a) shot no. 61352 and no. 58094. The vertical lines show the locations of the CXRS channels for v_θ measurements.

The chord $\mathrm{R_{mid}}$ = 3.59m viewing the outer barrier (fig. 5.5) shows an increase from -2 to 7 km/s during t = 5.4 s – 6.3 s, the interval over which the outer barrier passes this viewing chord. The time trace of $\mathrm{R_{mid}}$ = 3.65m, although it looks outside the gradient region of the second barrier according to the contour plot, also increases during t = 5.7 s – 6.3 s from about 5 to 9 km/s.

Another example from the tritium series of shots, shot no. 61352 ($\mathrm{B_t/I_p}$ = 3.2T/3.0MA), is also a current hole plasma with strong negative central shear [Mail04], and similar levels of additional heating power (13 MW of NBI, 4MW of ICRH and 2MW of LHCD). The $\mathrm{T_i, T_e, n_e}$ and v_ϕ profiles for this discharge, before and during the existence of the ITB are also shown in figure 3.10. To illustrate the link that appears to exist between the location of the v_θ measurement and the region with strong gradients, a series of T_i profiles is shown in fig. 5.6(a). At t = 4.53 s a steep T_i gradient associated with a transport barrier, can already be identified. Later on the central T_i increases strongly, up to about 20 keV at t = 6.02 s, and the profile steepens. The barrier also expands radially outwards, creating a wider central region, with high ion temperatures.

The ITB criterion for this shot is shown in figure 5.7(a) to further illustrate the temporal and spatial evolution of the barrier. The spatial location of three of the v_θ viewing chords are indicated in figures 5.6(a)

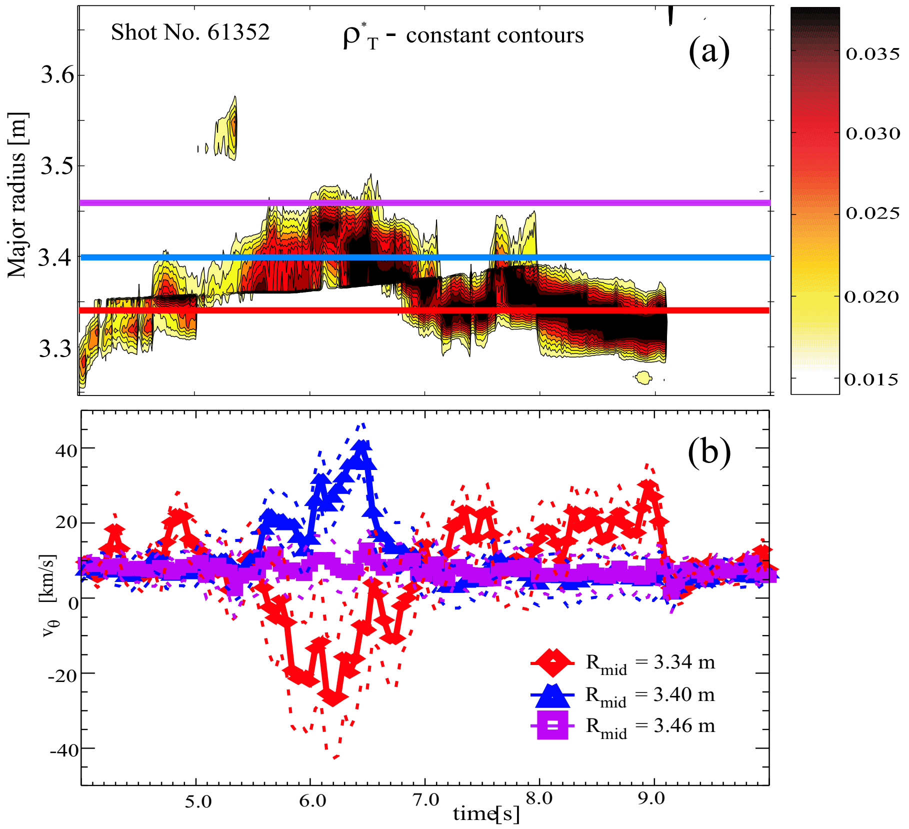

Figure 5.7: (a) The ITB criterion and the locations of three of the v_θ channels in the region of the steep temperature gradient. (b) Time traces of v_θ at the three different CXRS radii.

and 5.7(a) by colour lines. The corresponding v_θ time traces for each of these channels are shown in figure 5.7(b). The value of v_θ for the line of sight at the magnetic mid-plane $\mathrm{R_{mid}} = 3.33$ m increases in the positive (electron diamagnetic) direction, from 7 to 20 km/s during the time that the channel views the centre of the steep T_i gradient (t $\sim$ 4.0 s - 5.1 s). As the barrier moves outwards (t $>$ 5.1 s) the relative location of the v_θ measurements changes with respect to the T_i gradient, and a strong positive increase in v_θ is picked up by the adjacent CXRS channel ($\mathrm{R_{mid}} = 3.40$m), increasing from 7 to 40 km/s. The innermost channel ($\mathrm{R_{mid}} = 3.33$m) simultaneously shows v_θ to change sign and spin up to -25 km/s in the ion diamagnetic direction. The value of v_θ along the outermost channel, with a view outside the T_i gradient region ($\mathrm{R_{mid}} = 3.46$m) is constant at about 7 km/s throughout the discharge. In the final phase of the ITB evolution, the steep T_i gradient moves inwards once again at t$\sim$ 7.0 s. As this happens v_θ at $\mathrm{R_{mid}} = 3.40$m returns to its initial value of $\sim$ 7 km/s and v_θ at $\mathrm{R_{mid}} = 3.33$m increases back to 25 km/s in the electron diamagnetic direction.

An important complication arises for the measurement of v_θ in regions with strong v_ϕ gradients. The lines of sight of the poloidal CXRS diagnostic have a finite spot size of about 5 cm at their intersection with the neutral beams. The core CXRS lines of sight on JET have a toroidal component to their view, which has to be subtracted from the measured line of sight velocity to extract v_θ [Crom04]. The v_ϕ component to the CXRS lines of sight is determined by an interpolation of the v_ϕ data measured with an independent purely toroidal viewing CXRS diagnostic, to the v_θ measurement radial locations assumed to be single points. In figure 5.8(a) the measured and interpolated v_ϕ values are shown for shot no. 61352 at t = 6.0s. The finite radial extents of the lines of sight due to their spot size and line integration across the beam volume are represented by horizontal bars in figure 5.8(a). For the CXRS channels at $\mathrm{R_{mid}} = 3.40$m and $\mathrm{R_{mid}} = 3.33$m the single point approximation is reconsidered, since it introduces an underestimation of the toroidal component. Therefore v_θ has been recalculated for these chords using a finer interpolation of the v_ϕ profile at six extra points lying between the edges of the collection spots as shown in figure 5.8(a) by dotted vertical lines. The effect of taking into account the finite radial extent in the v_θ measurement is shown by the dotted lines in figure 5.8(b), where the original (single point) velocity is compared to the recalculated average velocity using the six extra points in the interpolation. For the calcu-

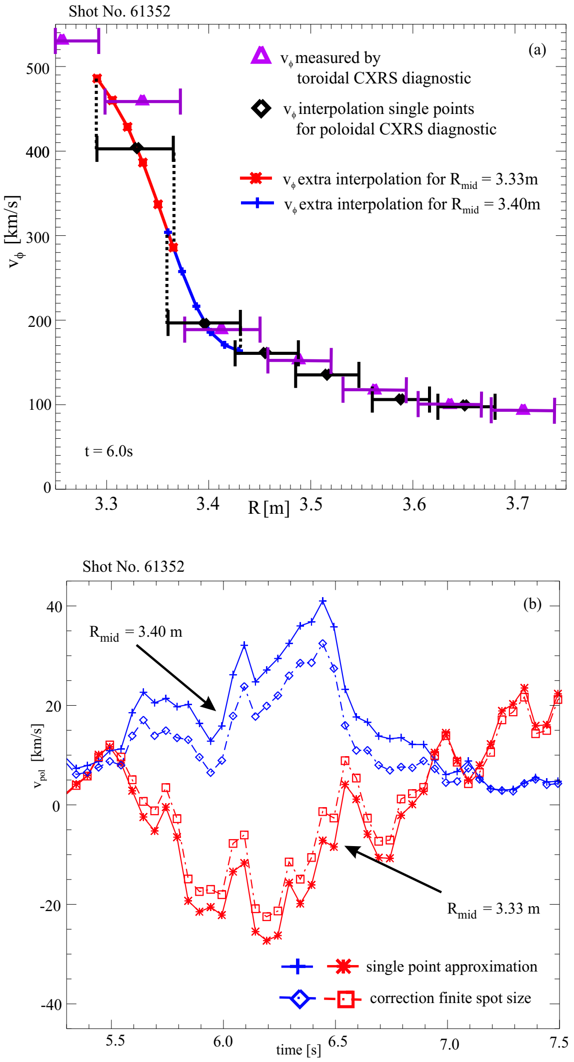

Figure 5.8: (a) The interpolation of the measured v_ϕ to the location of the poloidal v_θ chords. The horizontal error bars represent the radial extent of the collection spot including the $\sim$ 5 cm spot size and the finite spatial resolution due to line integration. Extra interpolated values in between the collection radii are calculated for the two innermost chords in the region with the strong gradient. (b) Values of v_θ for the two inner chords both using a single point approximation (solid line) and using a finite collection spot size and a weighting factor to account for the increasing impurity density towards the plasma centre (dotted lines).

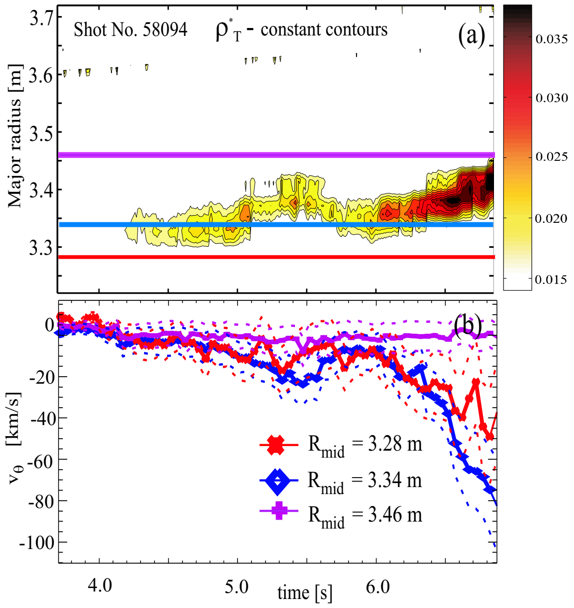

Figure 5.9: (a) The ITB criterion for shot no. 58094 and the locations of the CXRS channels for the v_θ measurement. (b) Time traces of v_θ measured at the three different radii shown in fig. 5.6(b).

lation of the average v_θ value a weight factor was introduced for the inner half of the collection spot, to account for the increasing impurity density towards the plasma centre. The excursions during the barrier are reduced by ~ 5-8 km/s, but are still clearly identifiable.

Measurements of v_θ are also presented for a third shot (no. 58094, $B_t/I_p = 3.4T/3.0MA$) in which more centrally viewing CXRS channels were used, as indicated in figure 5.6(b). In this plasma the central T_i was higher than in the previous example, with values up to 24 keV in the centre (figure 5.6(b)). The temporal and spatial evolution of the ITB along with the three v_θ channels covering the gradient region (from $R_{mid} = 3.28$m to $R_{mid} = 3.46$m) are shown in figures 5.9(a) and 5.9(b). The measurements show v_θ to increase strongly to -75 km/s for the channel at $R_{mid} = 3.34$m, when the central T_i reaches it highest values. This channel views the inner edge of the steep T_i gradient during this time. The innermost channel at $R_{mid} = 3.28$m is located in a less steep part of the T_i gradient and shows a smaller negative increase to -40km/s.

The channel at $\mathrm{R_{mid}} = 3.46$m, which views the foot of the barrier, does not show any significant change in v_θ.

These three examples demonstrate a clear link between the existence of an ITB and large, localised excursions in v_θ on JET. The relative increase in v_θ and its direction of rotation are both sensitive to the location of the viewing channel relative to the T_i profile location and gradient, and thus depend on the strength of the barrier. A limited spatial coverage of the core region for poloidal rotation measurements ($\mathrm{R_{mid}} = 3.30$m, mostly corresponding to $\rho = 0.3$) and the fact that the barrier is often formed more centrally than the innermost viewing chord, combined with a modest time resolution of 50 ms, means that it is not possible to resolve the question of causality between the ITB formation and v_θ excursions on JET. However it is clear that the increase in v_θ persists throughout the duration of the barrier, and in this respect differs from the poloidal rotation precursors observed on TFTR [Bell98, Stae01]. As shown in figure 5.7, after the ITB disappears ($t > 9.0$s) v_θ along the three inner chords relaxes back to pre-ITB values.

It is interesting to note that in some of the discharges studied a local modest spin up of the poloidal velocity could be measured, although no clear sign of a barrier appears in the contour plot at these locations. Disharge no. 62276 ($\mathrm{B_t/I_p} = 3.4\mathrm{T}/1.5\mathrm{MA}$)was taken as an example, for which the contour plot is shown in figure 5.10. A strong outer barrier exist during t = 3.9 s – 4.3 s, and this corresponds to an increase in v_θ along the chords at $\mathrm{R_{mid}} = 3.59$m and at $\mathrm{R_{mid}} = 3.65$m in positive direction from 5 to 25 km/s and from 10 to 20 km/s respectively (figure 5.11). At the location of the other four chords ($\mathrm{R_{mid}} = 3.36$ m – $\mathrm{R_{mid}} = 3.52$ m) no clear sign of a barrier appears in the contour plots in fig. 5.10. Nevertheless, during t = 3.9 s – 4.3 s a modest negative increase can be seen on the time traces of the chords at $\mathrm{R_{mid}} = 3.41$m and at $\mathrm{R_{mid}} = 3.47$ m, whereas the $\mathrm{R_{mid}} = 3.36$ m and $\mathrm{R_{mid}} = 3.52$ m channels tend to increase in the opposite direction. The T_i profiles in fig. 5.12 show a steep gradient region around $\mathrm{R_{mid}} = 3.35$ m – $\mathrm{R_{mid}} = 3.45$ m, although the criterion for an ITB appears not to be fulfilled. This example possibly illustrates the existence of poloidal flows without the presence of a strong ITB. To study in more detail the causality between poloidal flows and ITBs, the diagnostic for poloidal rotation is being upgraded with a faster detection system.

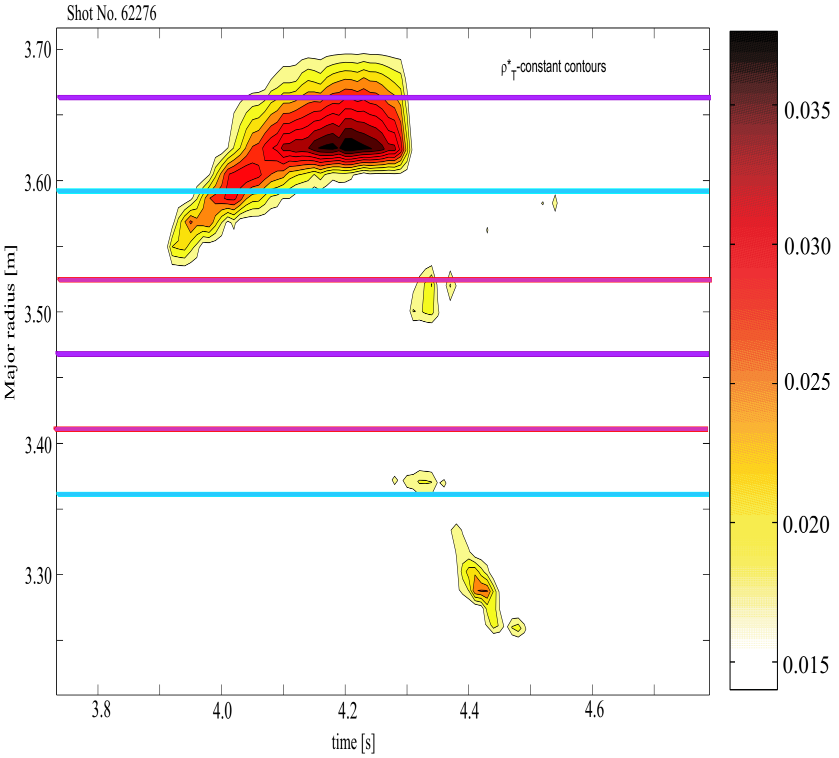

Figure 5.10: Discharge no. 62276 is an example of a plasma with a strong outer barrier, and indications of the formation of a weak inner ITB.

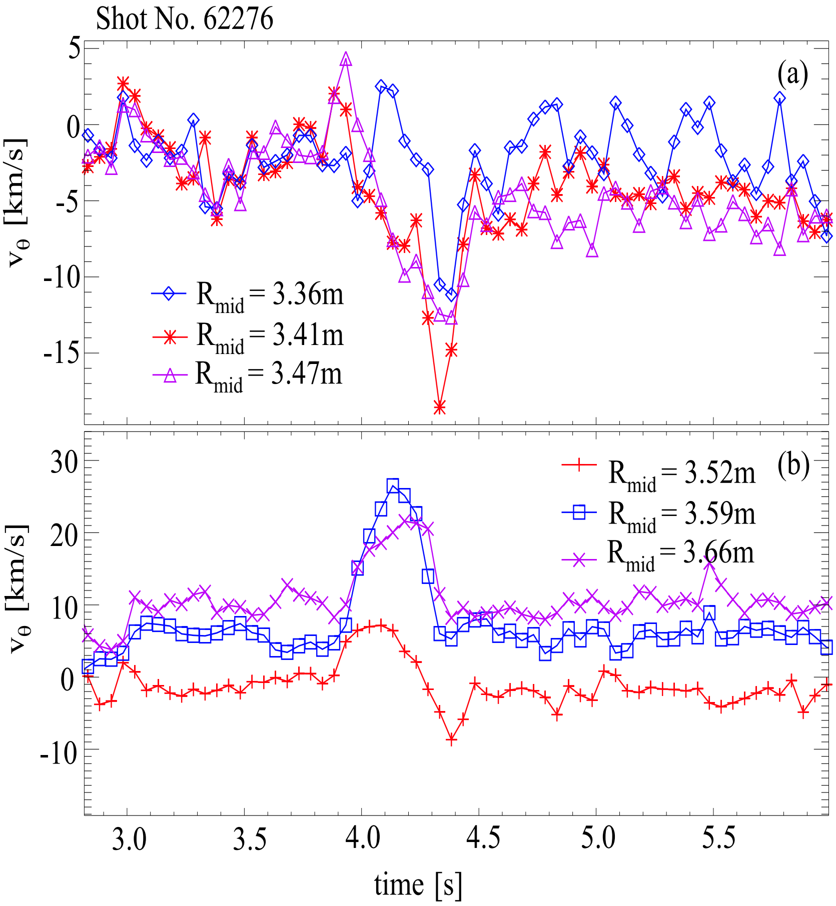

Figure 5.11: The v_θ time traces for shot no. 62276, (a) the inner chords where no clear ITB exists, and (b) the channels in the vicinity of the outer barrier.

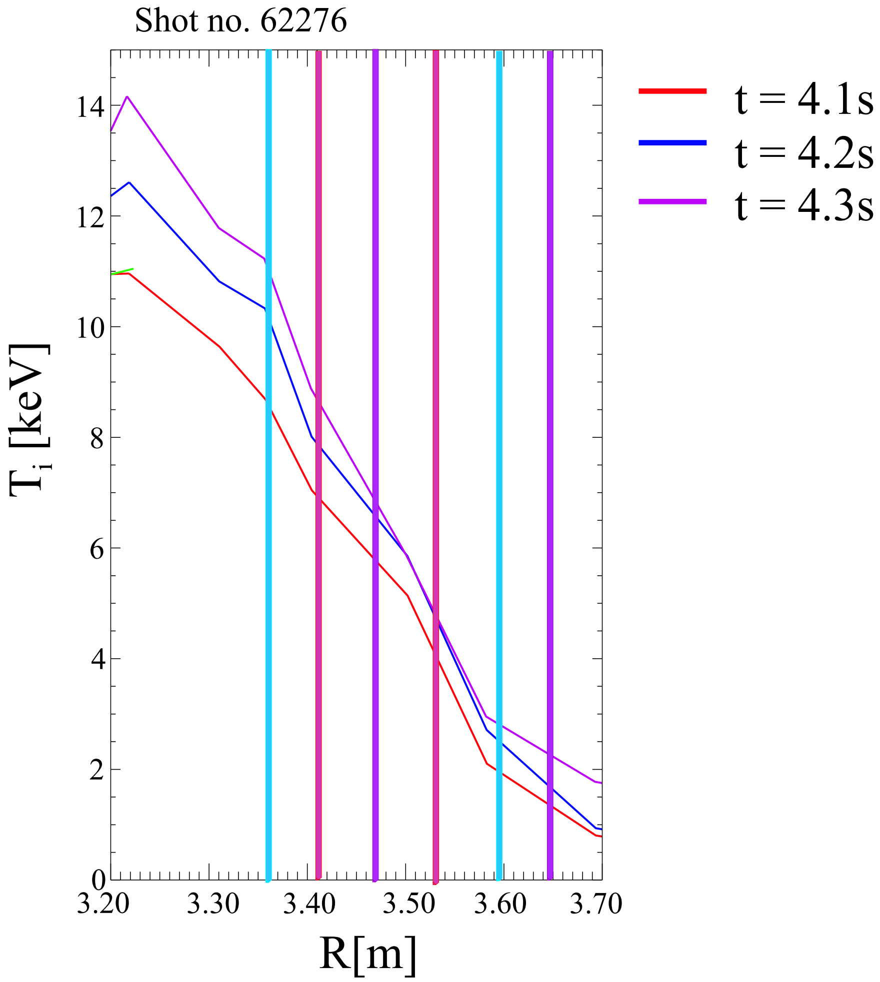

Figure 5.12: Ion temperature profiles for shot no. 62276 during the existence of a strong outer ITB around $R_{\mathrm{mid}} = 3.60$ m. The vertical lines correspond to the positions of the v_θ measurements. The profiles show also a steep T_i gradient in the region $R_{\mathrm{mid}} = 3.35$ m – $R_{\mathrm{mid}} = 3.45$ m, although the ITB criterion appears not to be fulfilled (fig. 5.10) here.

5.3 Diamagnetic and ExB components

The perpendicular velocity

$$\overline{v}_{\perp} = \frac{\overline{v} \times \overline{B}}{B}, \tag{5.1}$$

for which the radial component is given by

$$\overline{v}_{\perp,r} = v_{\theta}\frac{B_{\phi}}{B} - v_{\phi}\frac{B_{\theta}}{B} \tag{5.2}$$

but can approximately ($B \approx B_{\phi}$) be written as

$$\overline{v}_{\perp,r} = v_{\theta} - v_{\phi}\frac{B_{\theta}}{B_{\phi}}. \tag{5.3}$$

The equation for the radial electric field (eq.3.10) shows that $\overline{v}_{\perp,r}$ must be balanced by (i) a diamagnetic velocity ($\mathrm{v_{dia}}$), related to the pressure gradient, and (ii) an **E**x**B** velocity ($\mathrm{v}_{\mathbf{ExB}}$) as expressed by eq.(3.11). In figure 5.13 the different terms of eq.(3.11) are plotted for the examples shot no. 61352 and no. 58094. For shot no. 61352 the diamagnetic and toroidal components appear to cancel out, showing that the $\mathrm{v}_{\mathbf{ExB}}$ velocity profile roughly corresponds to the measured v_{θ} profile. A strong **E**x**B** shear exists in the barrier region. In the second example a very strong toroidal component, which does not completely cancel out the diamagnetic term, leads to an even larger shear in $\mathrm{v}_{\mathbf{ExB}}$ at the ITB location. These examples support the idea suggested in section 3.2.3 that a strong **E**x**B** velocity shear is responsible for the turbulent stabilisation and sustainment of the transport barrier.

5.4 Reflectometry measurements

Reflectometry measurements for a probing frequency (36.9 GHz) are shown in figure 5.14 for shot no. 58094. The radial position of the cut-off layer for the probing frequency (39.6 GHz) and two other close frequencies (38.1 and 41.1 GHz) are shown in figure 5.14(a). The spectrogram computed from a sliding FFT of the reflected signal and the spectrogram integrated over the whole frequency range are depicted in figure 5.14(b) and (c) respectively. A reduction in the fluctuation level during t = 5.0 - 5.6 s and after t = 6.0 s can be seen, corresponding to the two time intervals with large negative v_{θ} excursions in the vicinity

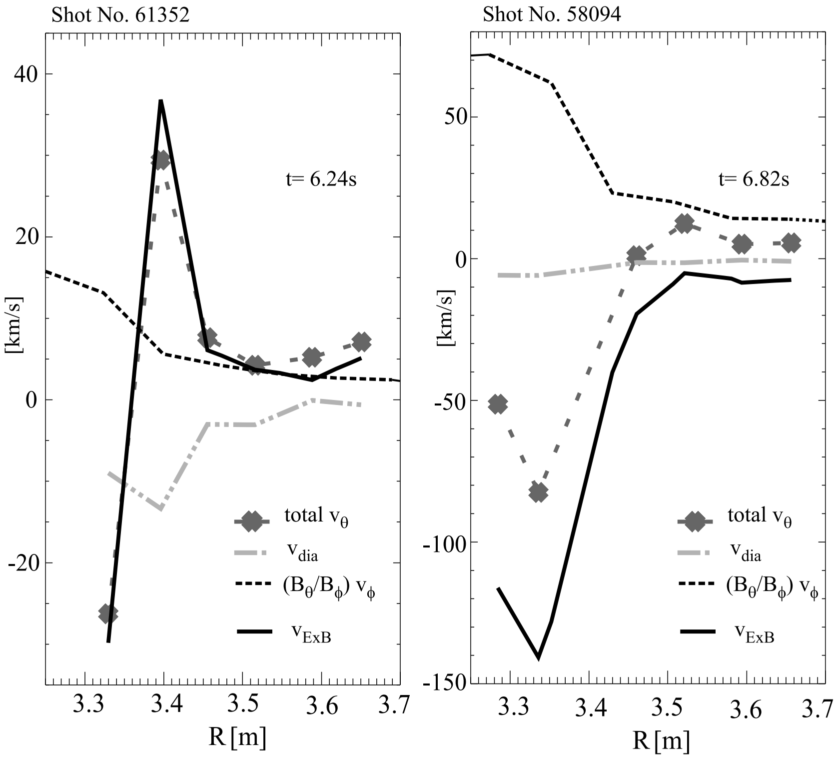

Figure 5.13: The diamagnetic and E x B contributions to the total v_θ. The E x B term is dominant in both cases.

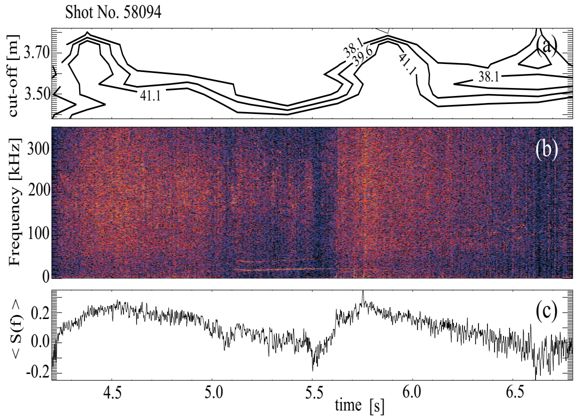

Figure 5.14: Reflectometry measurements showing a reduction of the turbulent fluctuations during t = 5.0 - 5.6 s and after t = 6.0 s, corresponding to the large negative excursions in v_θ .

of the reflecting layer (as shown in figure 5.9(b)). Since the reflecting layers for the three close frequencies remain almost parallel in this time window (except after 6.2s), the reduction in fluctuations is associated with a reduction in turbulence itself, rather than a changing density gradient. For the shot no. 61352, a reduction in the turbulent fluctuations was also observed during the increase in v_θ.

5.5 Comparison to NCLASS predictions

The CXRS measurements of v_θ are compared to the neoclassical predictions by NCLASS [Houl97] in figure 5.15. The transport code JETTO has been used to simulate the plasmas. The measured and neoclassical v_θ profiles for two of the shots described above, are compared at a single timeslice during the barrier in figure 5.15. At the location of the negative dip in the neoclassical predictions, around $R_{\text{mid}} = 3.35$m, the largest negative v_θ values are measured. There appears however to be a significant difference in absolute values of almost an order of magnitude. The positive increase for the channel around $R_{\text{mid}} = 3.40$m in discharge no. 61352, measures at the middle of the T_i gradient, is not reproduced by the NCLASS calculations. Comparison of the experimental profiles to the predictions for the main ion v_θ shows relatively good agreement in both negative direction and absolute value.

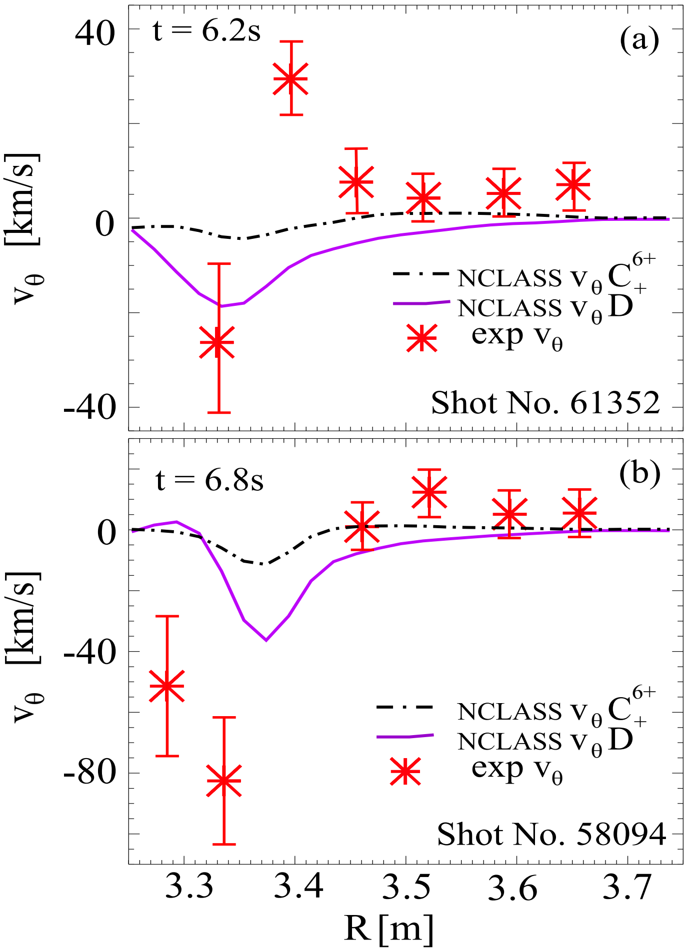

Figure 5.15: Comparison of measured v_θ profiles with neoclassical predictions by NCLASS for the two discharges during the ITB. The measured values are an order of magnitude higher than the predictions for the C^{6+} ions. The negative excursion is of a similar magnitude as the predicted main ion rotation velocity.

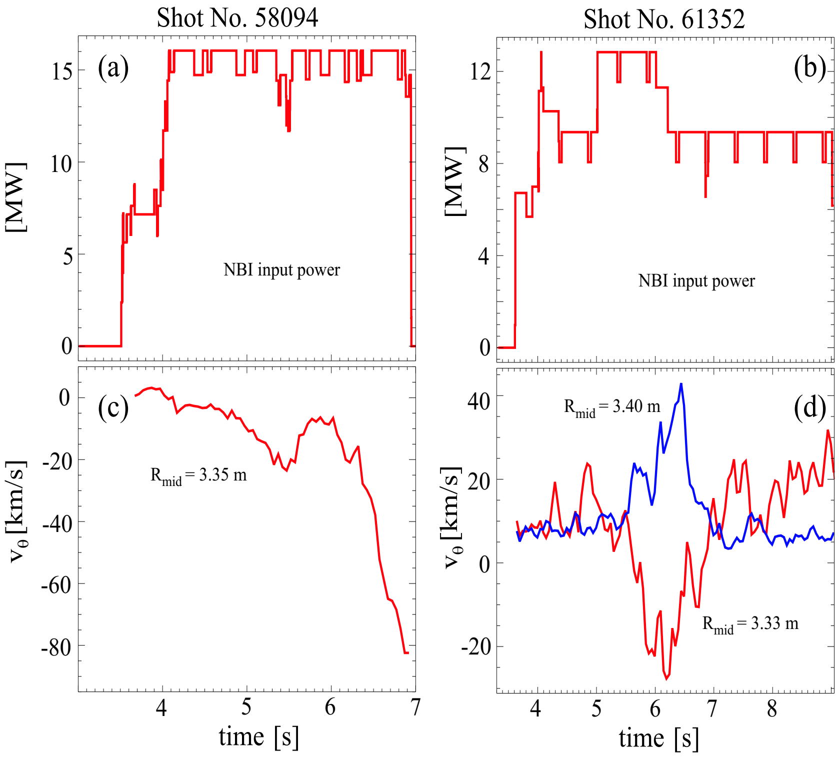

Figure 5.16: NBI input power for (a) shot no. 58094 and (b) no. 61352, and the (c) and (d) v_θ traces for chords in the ITB region.

The reason for the difference between measured and modelled values is at present unclear. The influence of the T_i and p_i gradients on v_θ has been tested in the simulations by modifying the shape of the input profiles for T_i, n_e and Z_{eff} in JETTO. These input profiles are normally taken from experimental measurements and thus intrinsically have an uncertainty that is reflected in the predicted output values for v_θ. However, the conclusion from the tests was that the desired modifications to the input profiles in order to obtain reasonable agreement between the NCLASS and experimental v_θ, were far too drastic to be explained by measurement errors alone.

Another possibility is that certain terms are not yet included in NCLASS that affect the poloidal rotation: one of them is the friction force between the main and impurity ions. Possibly the impurity ions are dragged by the main ion flow to increase their velocity to the main ion speed. It could explain why the order of magnitude of the measured v_θ corresponds to the predicted rotation velocity for the main ions rather than for the carbon ions, at least this holds for the negative peak around $\mathrm{R_{mid}} = 3.35$m, but does not explain the positive increase around $\mathrm{R_{mid}} = 3.40$m in shot no. 61352 for instance.

As discussed in chapter 3 the beam friction is not yet included, although an upgrade is in progress [Houl04]. The effect of beam injection is more difficult to understand. However, from the plasmas studied there doesn't seem to be a direct relationship between the NBI input power and the dynamics of v_θ in the ITB region. The time traces of the total beam power over the v_θ traces for the two examples shots, shot no. 58094 and no. 61352, are plotted in figure 5.16. For shot no. 58094 the beam power remained quite constant during t = 4.2 s – 6.8 s (a) (an interval with the presence of a clear barrier), while the v_θ chord at $\mathrm{R_{mid}} = 3.35$ m measured a large change from -5 to -80 km/s (c). The largest increases in poloidal velocity for the shot no. 61352 start at about 5.5 s (d), despite the earlier step in beam input power at 5.1 s (b). And, although the beam power deposition profile changes during the ITB evolution, it shows no clear correlation with the evolution of the v_θ measurements. From these observations, it is unlikely that the friction force between the fast ions from the beam and the bulk and impurity ions, could completely explain the discrepancy between measured and simulated poloidal velocity, but tests with the upgraded version of NCLASS have got to be performed to clarify the importance of an external poloidal momentum input.

5.6 Radial electric field

Using the experimental v_θ values instead of the neoclassical predictions in the calculations of the total radial electric field (from eq. 3.10), results in a significant difference in the region of the barrier, as is shown in the figure 5.17 for shot no. 58094(b) and no. 61352(a). The three contributions to the total $\mathrm{E_r}$ are plotted separately in figure 5.18: the pressure gradient ($\frac{1}{qn}\frac{dp}{dr}$) and the toroidal ($v_\phi B_\theta$) terms, and the poloidal contribution using both the experimental $(-v_\theta B_\phi)_{\mathrm{exp}}$ and NCLASS $(-v_\theta B_\phi)_{\mathrm{NCLASS}}$ poloidal rotation velocities. When the NCLASS predictions are used, the poloidal and the pressure gradient part are of the same order of magnitude and approximately cancel mutually, leaving the large toroidal contribution - which originates from unbalanced NBI injection - to dominate the total radial electric field profile. However, the high measured v_θ values in the barrier region, result in an experimental poloidal contribution that is significantly larger than $\frac{1}{qn}\frac{dp}{dr}$. The total $\mathrm{E_r}$ profile is no longer only dominated by the toroidal component, but is also influenced by the poloidal contribution. In fig. 5.17 it can be seen that outside the ITB ($\mathrm{R_{mid}} > 3.40$m) there is good agreement between the JETTO output and the fully experimental $\mathrm{E_r}$. In the region of the steep pressure gradient however, the shear in $\mathrm{E_r}$ is significantly larger when the experimental v_θ values are used instead of the NCLASS predictions, suggesting that the stabilising shear in the **E**x**B** flow is in fact stronger than the calculations predict.

In addition, the strong $\mathrm{E_r}$ in the ITB region could have an impact on the Motional Stark Effect (MSE) measurements of the q-profile [RC03]. There are indications of a change in the polarization angle consistent with the fully experimental $\mathrm{E_r}$. However the interpretation of the MSE data for the plasmas presented here was complicated by the presence of expanding current holes.

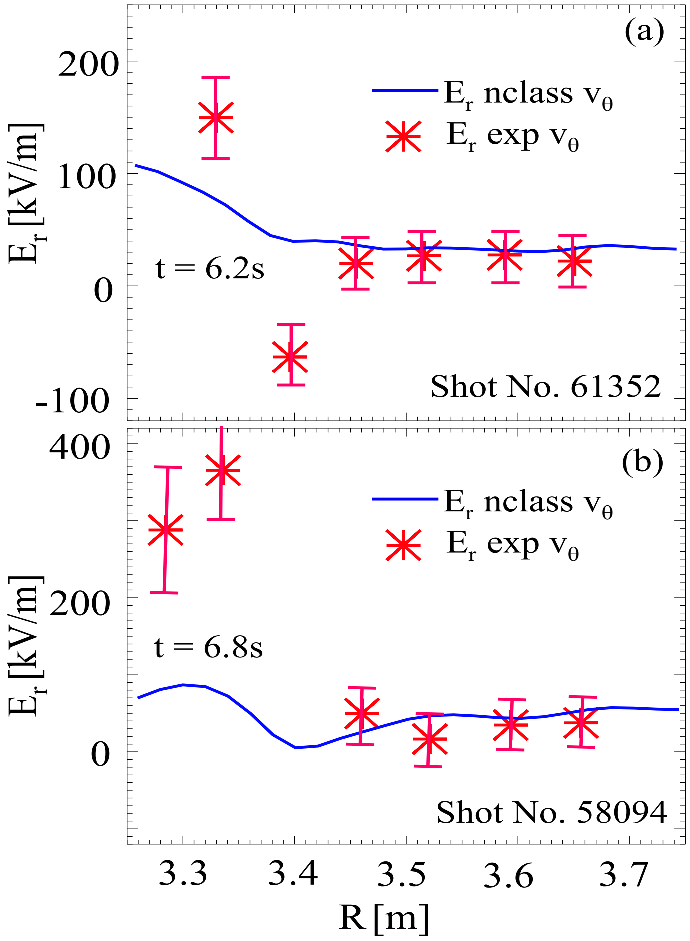

Figure 5.17: E_r profiles for the discharges no. 61352 and no. 58094 during each of the ITBs calculated using eq. 3.10, with the measured v_θ values (stars) and the NCLASS v_θ predictions (solid line) and measured toroidal and pressure gradient components.

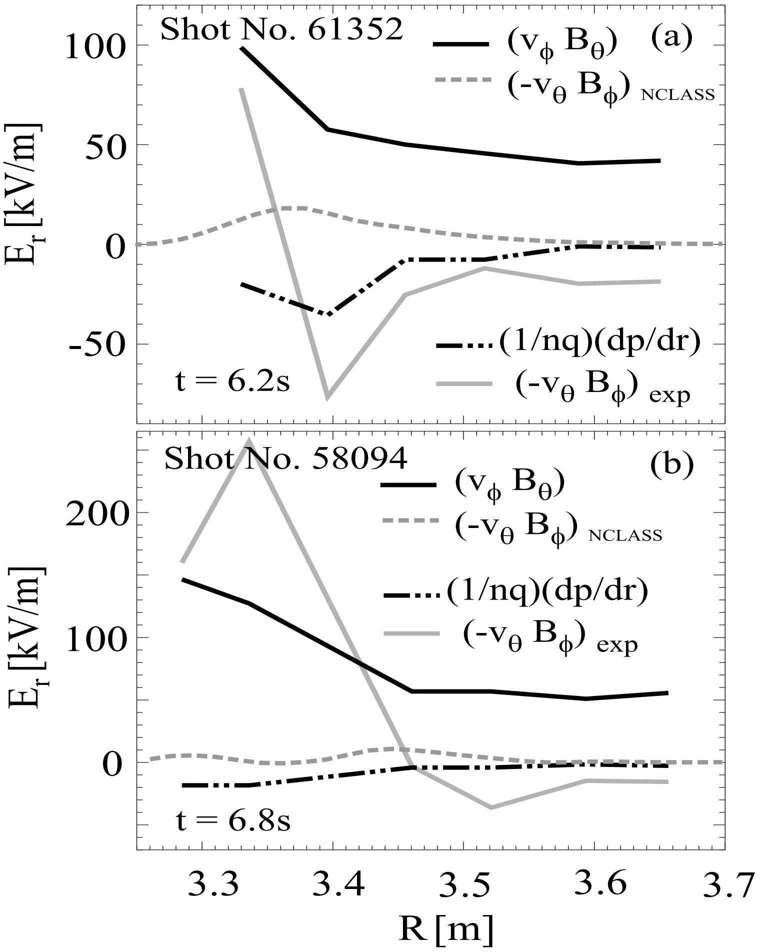

Figure 5.18: The different components of the total E_r plotted as a function of mid-plane radius: the experimental pressure gradient and the toroidal and poloidal terms, using both experimental and NCLASS calculated values of v_θ.

Chapter 6

Conclusions and future work

The measurement of the impurity ion poloidal rotation velocity (v_θ) using Charge eXchange Recombination Spectroscopy (CXRS) in the core region of JET plasmas has been improved in several ways:

- Two independent techniques are used to provide an accurate line calibration. The first method uses a Perkin-Elmer type 303-306 samarium hollow cathode discharge lamp, with a SmI line at 528.291 nm close to the C VI line at 529.1 nm. The second method uses the Be II at 527.06 nm and C III at 530.47 nm in the plasma spectrum as two marker lines on either side of the C VI line. As such the dispersion relation can be checked on a shot to shot basis, giving an accurate Doppler shift.
- The contribution of the toroidal rotation velocity that is picked up by the viewing chords of the core poloidal CX diagnostic, has been determined in dedicated experiments. It appeared to be 15% smaller than the calculations that take into account the original design parameters of the diagnostic and magnetic geometry of individual shots. The resulting difference for the poloidal rotation velocity is about 5 km/s.
- The CX spectra are distorted by temperature effects, originating from the energy dependence of the CX reaction rate and from the gyro-orbit motion during the finite lifetime of the excited state of the C^{5+} ions after charge exchange. The apparent velocities and temperatures have been estimated for the poloidal viewing chords of the CX diagnostic, and a correction to the spectra has been applied.

As a result the carbon poloidal rotation velocity and temperature in the region $\mathrm{R_{mid}} = 3.30\mathrm{m} - \mathrm{R_{mid}} = 3.65\mathrm{m}$ are now made routinely available on JET.

The improved measurement technique has been used to study poloidal rotation in plasmas with internal transport barriers (ITBs), which have a central region with improved confinement and the potential for long pulse duration, since a large part of the total current is driven non-inductively. Plasmas with an ITB are considered as the Advanced Tokamak Scenario for ITER [ITER01]. The physical mechanisms controlling the formation and sustainment of the barrier are not yet completely understood. Poloidal rotation is believed to play an important role as it contributes to the total radial electric field ($\mathrm{E_r}$).

For the first time on JET significant changes in v_θ linked to transport barriers have been identified. The excursions in velocity can be in the ion or electron diamagnetic direction, depending on the location of observation relative to the temperature profile. The time intervals with increased poloidal rotation correspond to intervals with a reduced level of turbulence, as confirmed by reflectometry measurements. Although the origin for the v_θ spin up has not yet been identified, it may be related to the ITB sustainment mechanisms, as the high velocities persist during the complete duration of the barrier. Compared to neoclassical NCLASS [Houl97] calculations, the measured v_θ is an order of magnitude higher. In addition, the $v_\theta B_\phi$ contribution to $\mathrm{E_r}$ in the barrier region, is of the same order as the large $v_\phi B_\theta$ component from unbalanced NBI injection, suggesting a larger stabilising $\omega_{\mathbf{E}\times\mathbf{B}}$ flow shear, than when the neoclassical predictions for v_θ are used. Possible reasons for the difference between measured and predicted v_θ values are turbulent effects, which are not included in the neoclassical code, the friction between impurity and main ions, the influence of unbalanced NBI heating, the presence of an additional E_r or distortions of the charge exchange spectra that are not yet included in the analysis.

To investigate whether or not the changes in poloidal rotation velocity trigger the barrier [Bell98, Stae01], and the possible influence of turbulence generated zonal flows [Lin99, Roge00, Hahm00], future work should consist of dedicated experiments with good control of the location of barrier formation and the propagation of the ITB in time and space with respect to the location of the v_θ measurement lines of sight. Additional chords will be added with higher time resolution (of the order of 1 ms) and more central viewing geometry for both v_θ and pressure profile measurements. By varying the q-profile, from weak to strongly reversed magnetic shear, and the additional heating scheme different theories on ITB dynamics can be further tested on JET.

Part II

Study of the influence of the dynamic ergodic divertor on carbon radiation and transport in the TEXTOR tokamak

Chapter 7

General aspects of the dynamic ergodic divertor

> Keine noch so große Zahl von Experimenten kann beweisen dass ich recht habe ; ein einziges Experiment kann beweisen dass ich unrecht habe
>
> Albert Einstein

The set-up of the Dynamic Ergodic Divertor (DED), installed in TEXTOR during the period March 2001 - May 2003, will be described, as well as the resulting novel edge magnetic configuration. Important beneficial effects of a stochastic boundary for plasma wall interaction were experimentally verified on the Tore Supra tokamak during its static ED operation, and a summary of the results is given in the review paper [Ghen96]. Since this work specifically adresses impurity radiation and transport, the main Tore Supra results related to radiation efficiency and core decontamination are repeated here to introduce the expected effect of the DED on impurities. At the end of this chapter the dynamic aspects of the ergodic divertor on TEXTOR are explained.

7.1 Set-up of the dynamic ergodic divertor in TEXTOR

At the inboard side of TEXTOR a set of sixteen helical coils are installed. Each of the coils produce a magnetic field in the plasma edge of

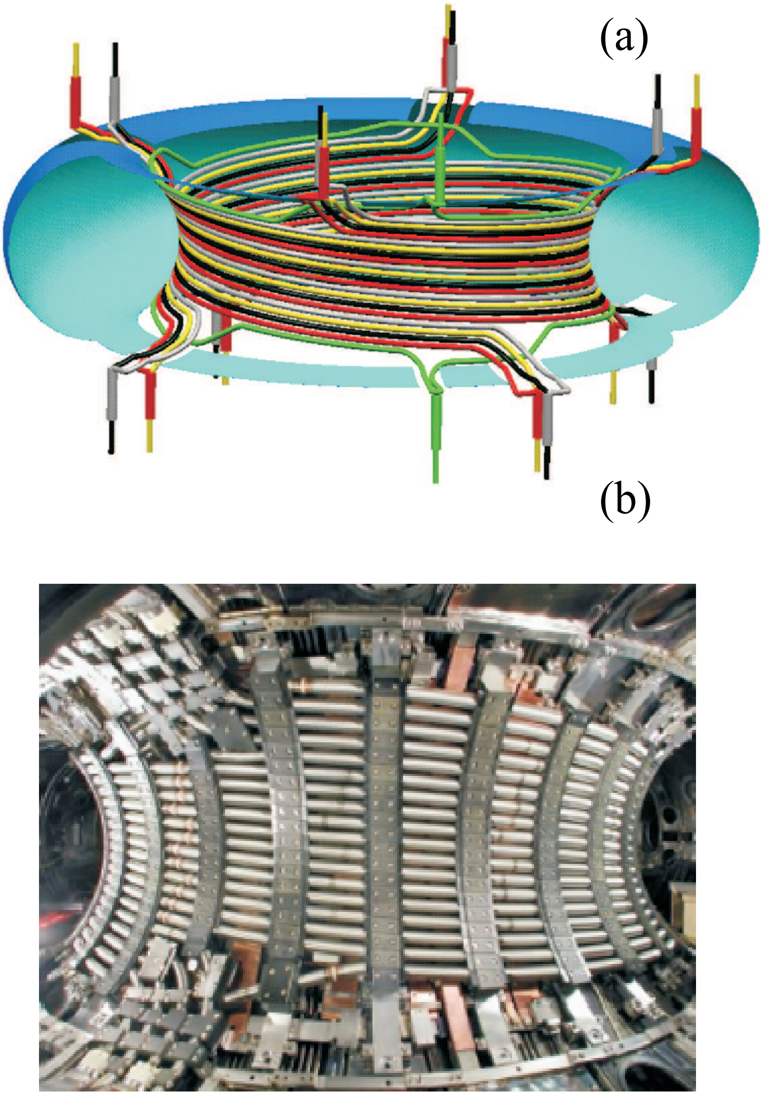

Figure 7.1: The DED coils at the inboard side of TEXTOR. (a) Schematic arrangement of the quadruple set of 4 helical conductors and 2 compensation coils (green). (b) Actual coil arrangement inside the vessel, before the installation of the graphite tiles.

the order of 10^{-3} to 10^{-1} T, comparable to the poloidal field B_θ in that region. The actual magnetic perturbation results from the superposition of these single components and is made resonant (i.e. has a very similar helical structure) to the $q = 3$ surface at the plasma edge. In this way it only locally perturbs the magnetic surfaces (around $q = 3$) and leaves the core plasma well confined. The coils are covered by graphite tiles that form the target plates of the divertor.

In figure 7.1 the schematic and practical coil arrangements are presented. The coils are aligned to the $q = 3$ surface (for $\beta_p = 1$). In the base configuration the phase of the current in subsequent coils differs by 90°: the currents in the black, yellow and grey coils have a phase difference of 90°, 180° and 270° respectively with respect to the current in the red one. The resulting magnetic perturbation field has a base mode $m/n = 12/4$ (where m is the poloidal and n the toroidal mode number, i.e. the number of periods in the poloidal respectively toroidal direction). By modifying the phasing of the currents in the coils other m/n compositions can be created as well: 3/1, 6/2, or combinations. The amplitude of the higher multipolarity modes decays faster with the distance from the perturbation coils. Therefore the 3/1 mode penetrates deeper into the core than 6/2, and 12/4 is only restricted to the edge [Fink98]. During the operation with 12/4 mode the plasma was shifted towards the inboard side to increase the perturbation level. In earlier designs of ergodic divertors the magnetic field perturbation was static. This leads to static load loss channels (via local 'ergodic fingers', as explained in section 7.2) and the formation of 'hot spots'. Rotating these strike points distributes the heat load over the wall and thus reduces the risk of local damage. This can effectively be done using AC currents in the coils and is the unique feature of the DED design in TEXTOR. The AC frequencies vary from a few Hz to 10 kHz.
It can be seen in figure 7.1 that the coil arrangement is not symmetric, the sixteen coils are bundled in four quadruplets, limiting the feed throughs for the coils to only four locations instead of sixteen for the symmetric configuration [Fink98]. However, this configuration could introduce non-desired perturbations to the plasma equilibrium and therefore two extra compensation coils (in green) were required [Abdu99].

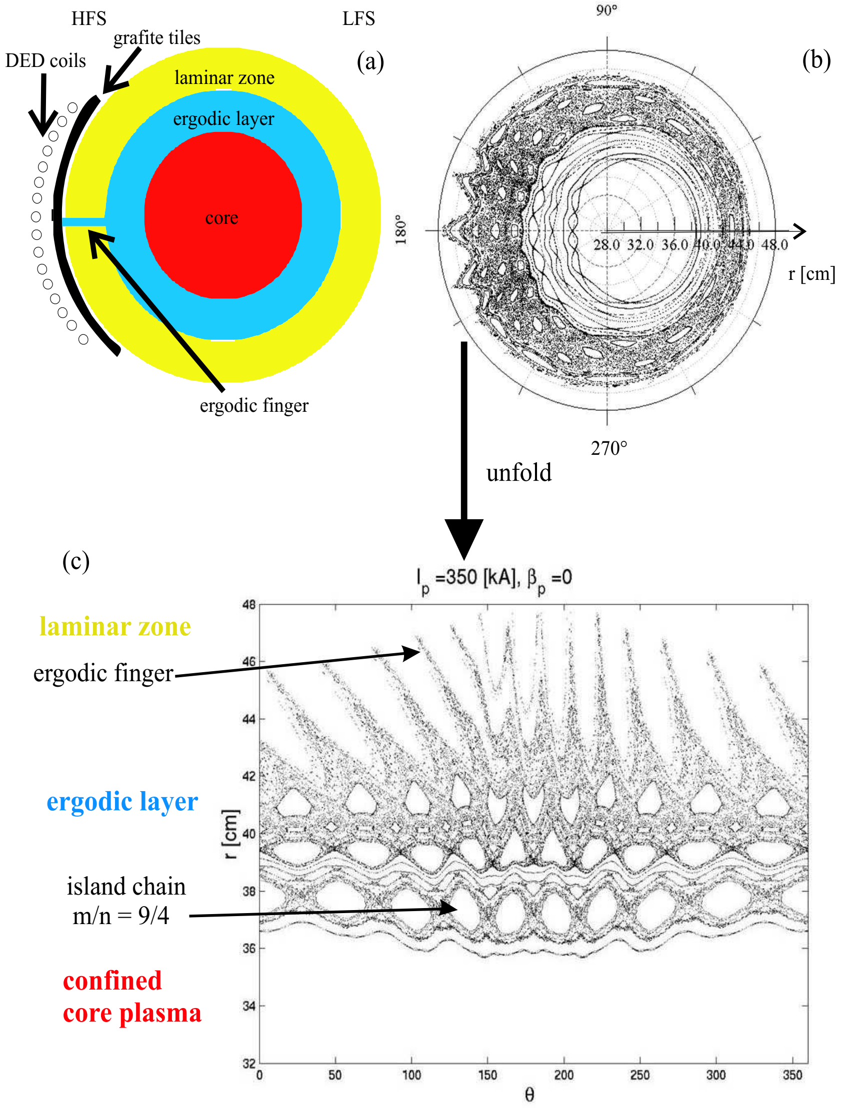

Figure 7.2: (a) Different magnetic structures in the plasma created by the perturbation field: the laminar zone, the ergodic layer and the unperturbed core plasma. An example of a Poincaré plot calculated from field line tracing, (b) presented in the poloidal circular cross-section and (c) the unfolded version, created by 'cutting' the poloidal plot at $\theta = 0$ and opening it up. The horizontal axis is now the poloidal angle and the vertical axis the plasma minor radius.

7.2 Magnetic field structure

The magnetic configuration resulting from the combined helical and perturbation field, can be divided into three zones as indicated in fig. 7.2a. The resonant magnetic perturbation creates chains of magnetic islands depending on its mode structure. For the base configuration a chain of islands will be created at the $q = 3$ surface with mode numbers $m/n = 12/4$, but also at $q = 3.25$ ($m/n = 13/4$), $q = 3.5$ ($m/n = 14/4$), ... and at $q = 2.75$ ($m/n = 11/4$), $q = 2.5$ ($m/n = 10/4$), ... and smaller islands in between (the secondary islands resulting from second order perturbations). The width of the islands depends on the strength of the perturbation field. With increasing perturbation field amplitude secondary islands start to overlap with the main islands creating an ergodic layer. If the perturbation is strong enough, the ergodic zone reaches the wall. These connections are called ergodic fingers from their particular shape in a Poincaré plot. The Poincaré mapping technique [Eich00, Jaku04, Fink98] is commonly used to visualise the behaviour of the field lines. The field lines are traced and each intersection with the poloidal plane at a specific toroidal location is indicated by one point on the poloidal cross-section (fig.7.2b and c). Ergodic field lines have a very high number of intersections with the poloidal plane at slightly different positions, shown by the filled (almost black) zones in fig. 7.2b. The non-overlapping island chains are also clearly visible. The unperturbed closed flux surfaces are not plotted in fig. 7.2b but would be represented by circles, or horizontal lines in the unfolded representation. The field lines closest to the divertor coils are radially displaced and diverted to the wall. This zone with open magnetic field lines can thus be seen as a multipolar helical divertor, with localised high heat and particle fluxes by the fast parallel transport along these open field lines, and is analogous to the open field lines in a classic axisymmetric poloidal divertor. The field lines in this laminar zone have a very short connection length (less than one toroidal turn), and therefore no points appear in the Poincaré plots.

The Poincaré plots also show that the perturbation is the strongest in the area around the perturbation coils (High Field Side (HFS)), but extends up to the Low Field Side (LFS). The radial extension of the laminar and ergodic regions is moreover determined by the strength of perturbation field, its mode structure, the q-profile and the plasma position. Typically, the ergodic zone is 2-5 cm in the 12/4 configuration (fig. 7.3) and substantially larger in the 3/1 configuration, where it can

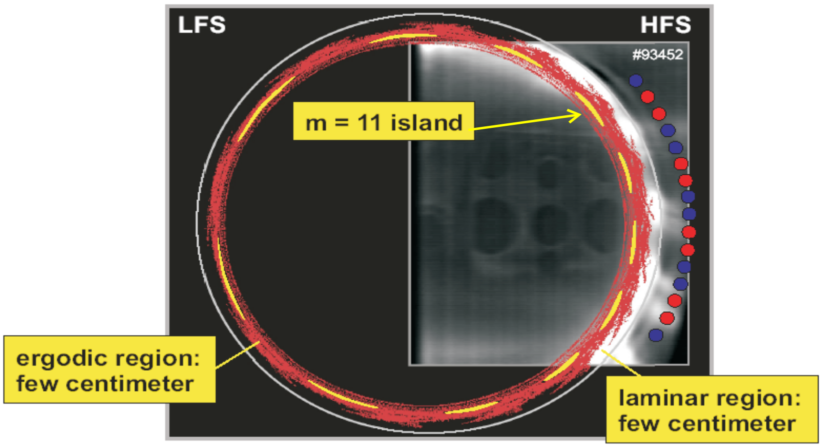

Figure 7.3: C III line radiation during 12/4 operation of the DED, and the corresponding Poincaré plot. The 11/4 island chain is clearly visible. For this mode composition the laminar and ergodic zone are both a few centimetres large [Lehn04].

reach upto the q=2 surface (fig. 2.10). In both cases the laminar zone is a few centimetres in radial dimension.

7.3 Effects on plasma parameters

The magnetic structure described in section 7.2 changes the energy and particle transport strongly. Because of the short connection lengths of the field lines in the Laminar zone ($L_{\text{wall}} \leq 2\pi q R$, for TEXTOR typically < 30 m) the particles are immediately directed (by fast parallel transport) to the wall, where they neutralise and are scattered back into the plasma.

In the ergodic layer the field lines have very long connection lengths. Diffusive transport dominates, but this is strongly enhanced because of the stochastic behaviour of the field lines. In [Toka97] Tore Supra ergodic divertor plasmas were modelled and it was found that both the electron heat diffusivity ($\chi_\perp^e$) and main ion particle diffusion coefficient ($D_\perp$) strongly increase in the stochastic layer, resulting in a colder and denser edge region than for the limiter configuration. Similar predictions were made in [Gerh04] for the TEXTOR plasmas. High n_e and low T_e in the ergodic layer have indeed been measured by Langmuir probes in

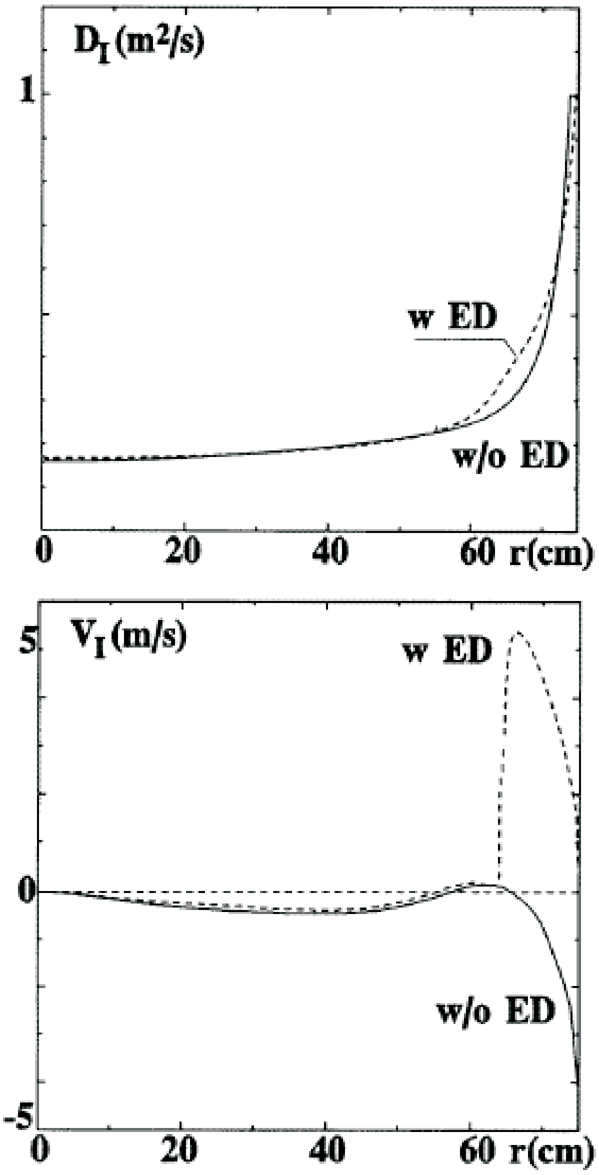

Figure 7.4: Calculated profiles of the carbon ion diffusivity D_I and convective velocity v_I for Tore Supra plasmas with (w ED) and without ergodic divertor (w/o ED) operation [Toka97].

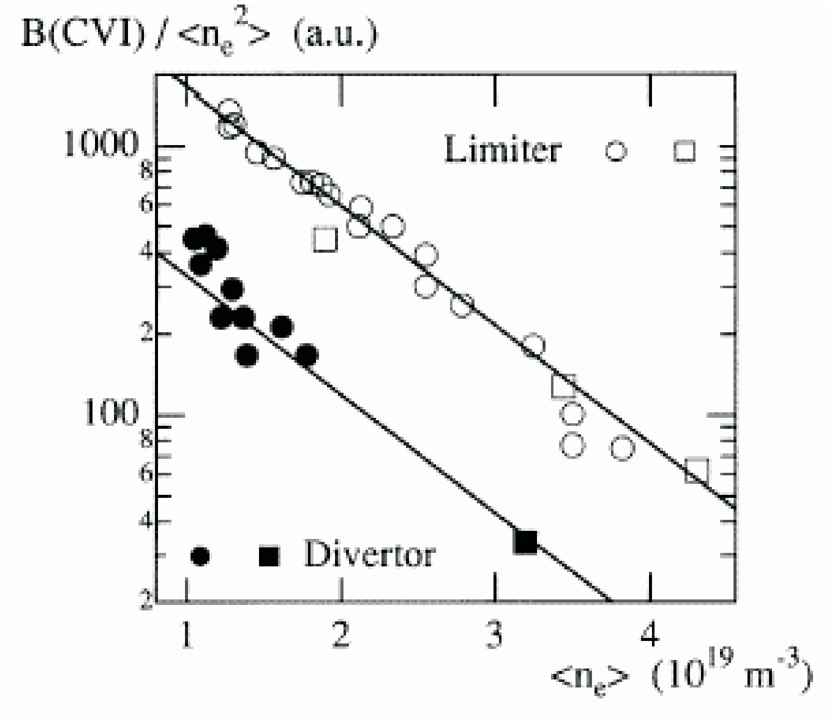

Figure 7.5: Normalised intensity of the C VI radiation as a function of the volume averaged electron density ($< n_e >$) in limiter and ergodic divertor plasmas on Tore Supra. B(CVI)/ $< n_e^2 >$ is representative for the carbon content of the bulk plasma [Ghen96]. In the ED plasmas the carbon core contamination is reduced as compared to the limiter configuration.

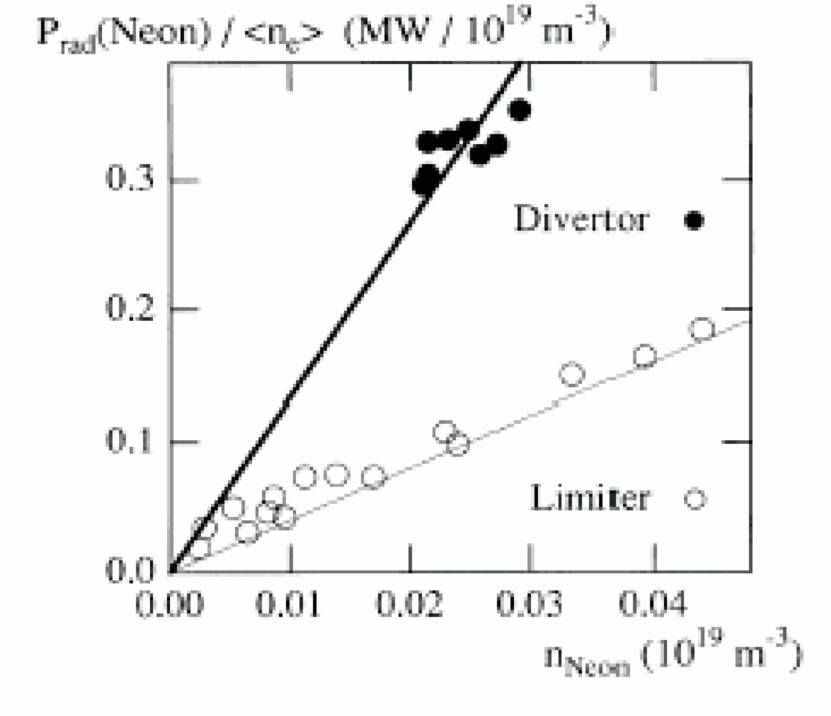

Figure 7.6: The neon radiated power normalised to the volume average density ($< n_e >$) as a function of the total neon density. For a fixed neon density $P_{rad}/ < n_e >$ is higher for divertor than for limiter plasmas, showing that the radiation efficiency is enhanced by the ED configuration [Ghen96].

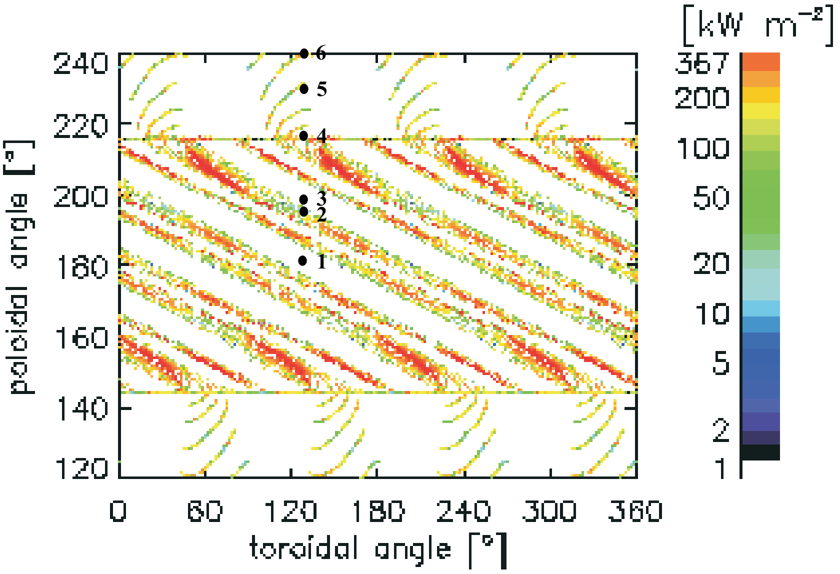

Figure 7.7: Predicted power load on the divertor target plates [Eich00] at the inner wall of TEXTOR. The black spots are the locations of six of the viewing chords of the carbon diagnostic (chapter 8).

the divertor area [Lehn05].

In [Toka97, Gerh04] the impurity transport in the stochastic layer was also modelled and the main conclusions were that the impurity diffusivity (D_I) does not change significantly, while the convective velocity (v_I) is positive in the edge region, directing impurities towards the wall. This is illustrated in fig. 7.4. In [Toka97] the carbon diffusion coefficient is calculated as the sum of the diffusion of the different charge states, defined as :

$$D_I \frac{dn_I}{dr} = \sum_z D_r^{z,\mathrm{eff}} \frac{\delta n_z}{\delta r}, \tag{7.1}$$

where $D_r^{z,\mathrm{eff}}$ depends on the level of stochastisation and the thermal velocity of the impurity ($\sqrt{T_i/m_z}$) and n_I is the total carbon density given by $n_I = \sum_z n_z$.

The convective velocity is defined as :

$$v_I n_I = \sum_z (v_r^{z,neo} + v_r^{z,st}) n_z, \tag{7.2}$$

where $v_r^{z,neo}$ is the neoclassical pinch velocity and $v_r^{z,st}$ is the velocity resulting from the stochastisation. This last term is positive, since it is

govered by the friction with the main ions and the parallel electric field, which are directed towards the regions with low plasma pressure, hence towards the plasma edge. Furthermore $v_r^{z,st}$ depend on the charge state and the mass of the impurity. Highly ionised impurities are preferentially dragged outwards by the friction with the main ions.
The outward directed flow results in high levels of impurity recycling, which increases the radiation, and at the same time a transport barrier for impurities is created preventing their core penetration (also called impurity screening [Bret91]). This effect combined with a reduction of the impurity production due to the lower edge temperatures is responsible for the general lower impurity content in the core of ED plasmas, although the core penetration probability strongly depends on the impurity species [MG01, Ghen96]. The screening effect for carbon is illustrated in figure 7.5 taken from experimental results on Tore Supra [Ghen96], showing that the carbon content of the bulk plasma in ED plasmas is considerably lower than for limiter plasmas. At the same time the lower temperatures and higher electron density at the edge enhance the impurity line radiation, resulting in a higher radiation efficiency. Figure 7.6 illustrates the increased radiation at a given injected neon density for both the ED and the limiter configuration. In chapter 9 the effects of the DED on the carbon radiation and core penetration in TEXTOR are studied.

Modelling of the power load on the TEXTOR wall (fig. 7.7 [Eich00]) predicts strike zones that are aligned to the DED coils. The predictions have been confirmed by IR temperature measurements [Jaku04]. By rotating the perturbation field at low frequencies, these strike points can move over the target plates and spread the heat over a larger area, avoiding the creation of 'hot spots'. The moving strike points can also be followed by observing the local carbon radiation (chapter 9).
Furthermore, a dynamic ED might induce a sheared plasma rotation and perhaps improve the confinement (by destroying the turbulent cells, as in the case of H-mode or ITB plasmas (Part I)). Calculations show that the torque exerted on the plasma by a fast rotating perturbation field would be sufficient to induce a plasma rotation [Fink99], which has indeed been observed [Fink05].

Chapter 8

A spectroscopic diagnostic for the detection of carbon ions

A multichord diagnostic for the detection of line radiation emitted by C^{2+} and C^{4+} impurity ions in the plasma has been designed [Crom02] and is installed on TEXTOR. Data are routinely recorded during plasma operation. In this chapter the diagnostic set-up and the choice of different components is described and motivated by the intended study of carbon screening. Issues related to the calibration are discussed, and examples of C^{2+} and C^{4+} emissivities are shown in the two operational modes of the system.

8.1 Diagnostic set-up

(a) Orientation of the lines of sight

The DED coils are located at the High Field Side (HFS) of the tokamak and the perturbation of the edge magnetic field is the strongest close to these coils. The main plasma wall interaction also occurs at the graphite tiles covering the DED coils. Therefore the enhancement of carbon radiation under the influence of the ergodic divertor can best be evaluated in this region. The diagnostic consists of a set of nine chords, oriented towards the HFS, that covers a viewing angle of about 120° (fig. 8.1). The intended orientation of the chords is indicated in black in the figure. However, during construction this turned out to be impossible since the viewing lines of the two uppermost channels (numbers 1 and 2) were cut off. It was decided to turn the complete set of chords to the red

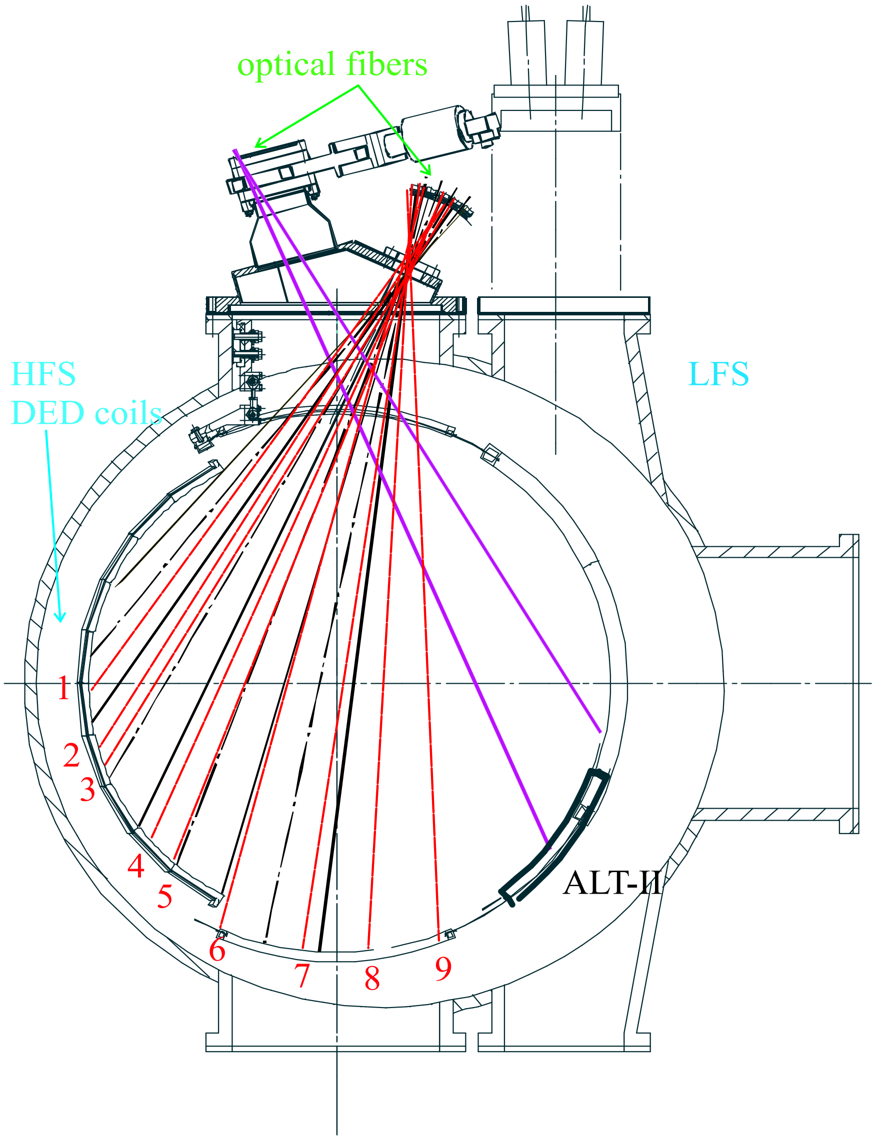

Figure 8.1: Schematic plot of the lines of sight (LOS) of the carbon diagnostic in a poloidal cross-section of TEXTOR. In black the original design, and in red the actual LOS after the necessary re-orientation. The two chords installed at the LFS are also indicated.

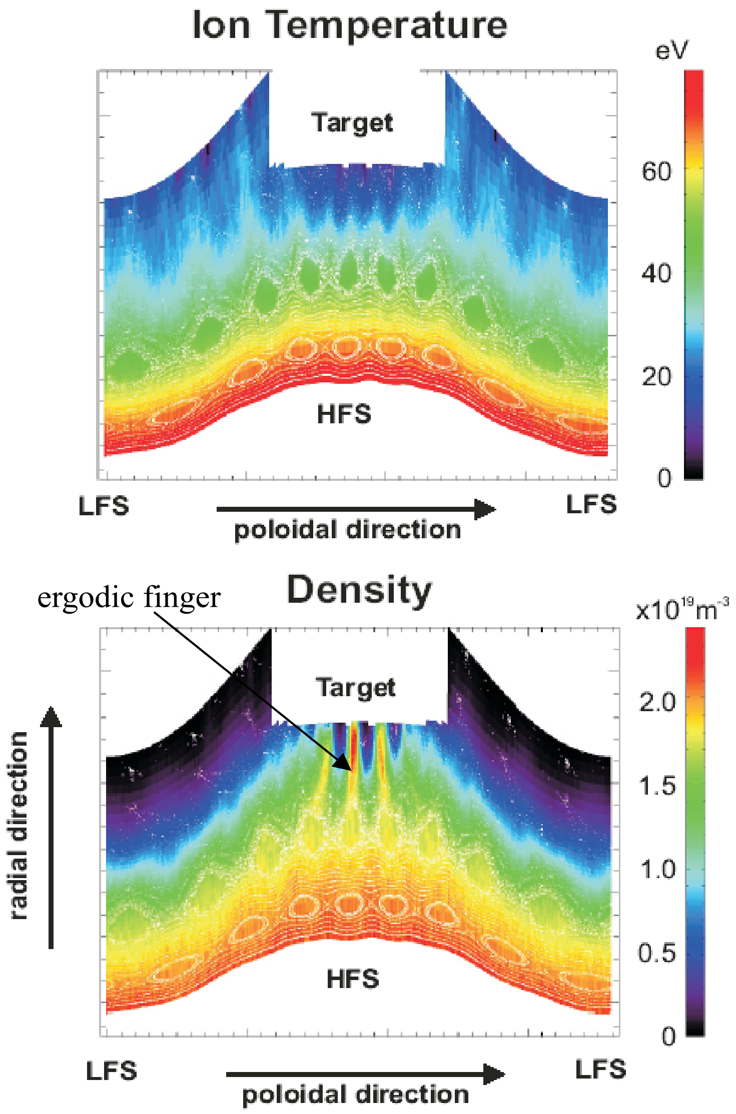

Figure 8.2: Prediction of T_i and n_e in the edge region of TEXTOR DED plasmas made by the Monte Carlo code EMC3-EIRENE for 12/4 configuration with maximal perturbation amplitude. A cold and dense edge region is created. Ergodic fingers connect the ergodic layer to the divertor target plates [Lehn04].

Table 8.1: Carbon ions ionisation potential

ion	ionisation potential (eV)
C^0	11
C^{1+}	24
C^{2+}	48
C^{3+}	65
C^{4+}	392
C^{5+}	490

orientation, which was the optimal technically feasible solution keeping the largest possible coverage of the DED coils (numbers 1-5 are on the graphite tiles, while 6-9 are outside). The first channel still required a separate adjustment and some modifications to the mounting head. Therefore the experimental results presented in chapter 9 were measured with only eight channels (numbers 2-9), during the first months of DED operation. In the meantime all nine channels have become operational.

For a more complete observation of the poloidal distribution of the carbon ions, two channels on the LFS have been added (fig. 8.1), one on the ALT-II limiter (fig. 2.7) and one outside.

(b) Carbon spectral lines

The objective was to study the screening of carbon, which is the main intrinsic impurity, and thus a comparison between its edge radiation and core contamination is required. For that reason spectral lines of C^{2+} and C^{4+} ions are chosen with wavelengths $\lambda_{C^{2+}} = 229.6$ nm (C III line) and $\lambda_{C^{4+}} = 227.1$ nm (C V line) respectively. The radial distributions of the radiated power from different carbon ions in TEXTOR conditions are shown in fig. 8.3. A 1-D transport code was used for these calculations. The lower charge states occur in the outer (cooler) parts of the plasma, while the higher charge states radiate in a radially more inward located zone. The larger radial spread of the emission of the He-like (C^{4+}) and H-like (C^{5+}) ions as compared to the lower charge states is caused by the higher ionisation potentials for the He- and H-like ions, given in table 8.1. The ionisation potential of the He-like carbon ions is 392 eV, significantly larger than the 65 eV for the Li-like (C^{3+}) and the

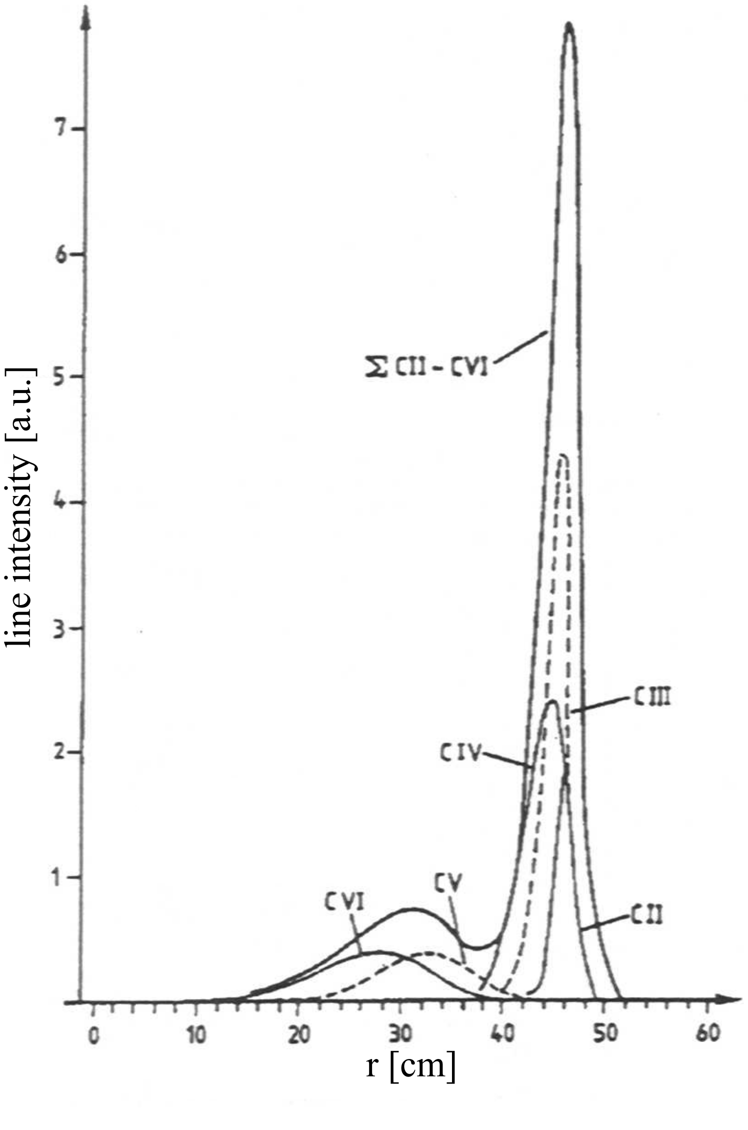

Figure 8.3: Distribution of the radiated power from carbon ions calculated with a 1D-transport code for TEXTOR conditions [Samm02] as a function of mid-plane radius.

48 eV for the Be-like (C^{2+}) ions. As a consequence the ionisation length for the C^{4+} ions is significantly larger than for the lower charge states, allowing more parallel and perpendicular transport, and spreading out the ions (and their radiation) over a larger poloidal and radial region. As only a 1D-transport code was used in the calculations in fig. 8.3 only the difference in radial distribution between the different states is given. The situation is similar for the distribution in poloidal direction, the C^{2+} ions will be more restricted to the vicinity of the carbon sources (for example around the ALT-II limiter or the strike points of the DED), while the C^{4+} ions will radiate from an approximately circular shell. From EMC3-EIRENE predictions (fig. 8.2) of T_i it can be seen that C^{2+} ions (with an ionisation potential of 48 eV) will mainly exist in the perturbed zone, and C^{4+} ions (ionisation potential 392 eV) will be located inside the $q = 3$ surfaces, i.e. in the confined core plasma (not calculated by the simulation). For the desired screening study, the C^{4+} radiation can be considered as a measure for the carbon contamination of the confined plasma.

The C^{2+} emission, on the other hand, is a good reference for the total carbon radiation, which originates mainly from the Be-like and Li-like ions as illustrated in fig 8.3. The lower charge states contribute a factor 2-4 more to the total carbon radiation than the He- and H-like ions. This is due to the relative difference between the ionisation and excitation energies, which is significantly larger for the Li- and Be-like ions, leading to more excitations per ionisation, and thus a higher radiated power [Samm02, Tele94, Tele00]. A high C^{2+} emission is expected in the vicinity of the ergodic fingers (indicated in fig. 8.2), since the total line radiation increases with the electron density and the C^{2+} emission is localised to the regions with plasma wall interactions.

The ratio of C^{2+} to C^{4+} emission can thus be considered as a figure of merit for the screening efficiency, the higher the ratio the better the carbon screening.

The small difference in wavelengths of the chosen C III and C V spectral lines (2.5 nm) permits the use of one single spectrometer equipped with a high resolution grating. The dispersion at the exit is 0.4 nm/mm, and the two lines appear at a distance of 6.25 mm, the arrangement is shown in fig. 8.4.

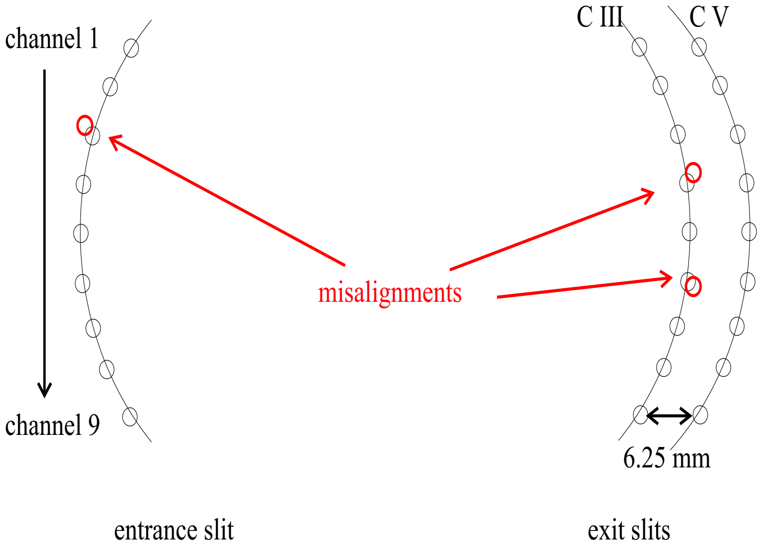

Figure 8.4: Arrangement of the sets of nine optical fibres at the entrance and exit slits of the spectrometer. The nine optical fibres are positioned on top of each other. The C III and C V lines appear at the exit at 6.25 mm distance. Small misalignments in the orientation of the exit fibres with respect to the entrance positions cause difficulties for the relative calibration of the chords (section 8.2).

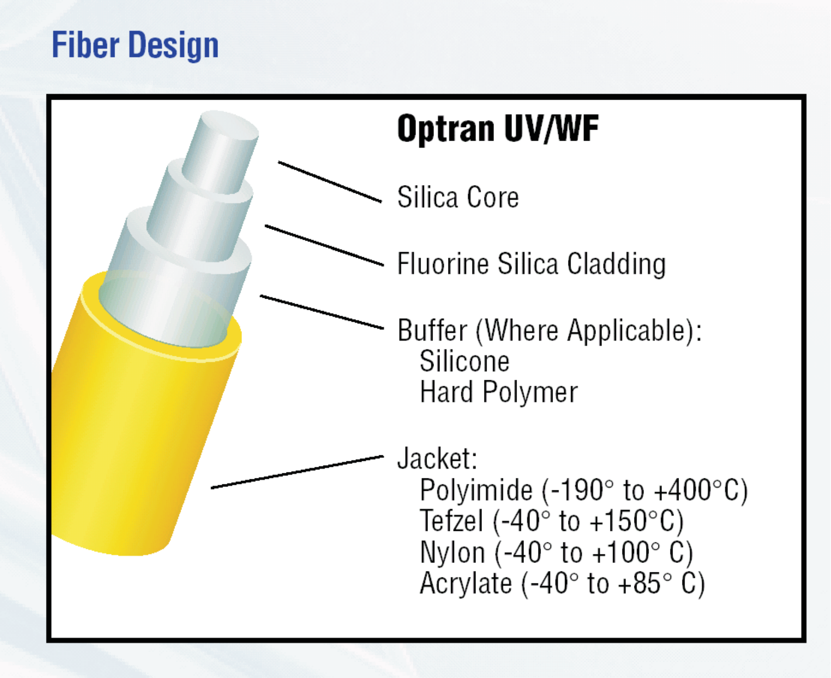

Figure 8.5: The optical fibres that are used have a silica core and a fluorine silica cladding and are suitable for UV transmission.

(c) Optical fibres and detection system

The light from the plasma is transferred to the entrance of a Czerny-Turner spectrometer by an ordered set of nine optical fibres. In addition, a second ordered set of 2×9 fibres connect the exit to the detection system[1]. The chosen spectral lines of C^{2+} and C^{4+} are emitted in the near UV and therefore special silica fibres had to be used, suitable for transmission in this wavelength region (fig. 8.5). The attenuation is relatively high for these short wavelengths, and therefore the spectrometer was placed close to the tokamak, on top of a wooden roof of the tokamak hall, straight above the viewing port, limiting the length of the light guides to about 6 m. The attenuation of the used optical fibres is plotted in fig. 8.6 and is about 200 dB/km around 225 nm, which corresponds to 0.2 dB/m. The ratio of input/output power (P_{in}/P_{out})

---

[1] The two channels at the LFS are connected to a separate spectrometer and a C III line in the visible wavelength range is detected at 465 nm.

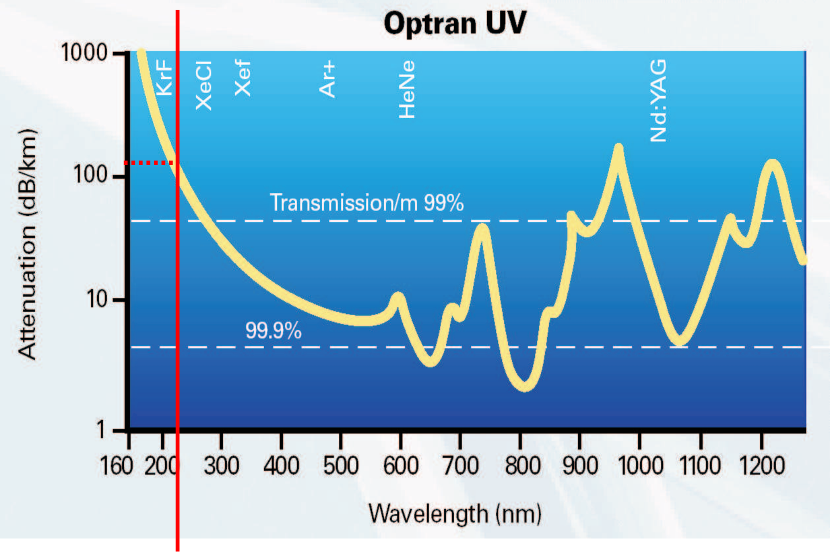

~200 dB/km @ 225 nm

Figure 8.6: The attenuation of the optical fibres as a function of wavelength. At the wavelenghts used in the diagnostic it is about 200 dB/km.

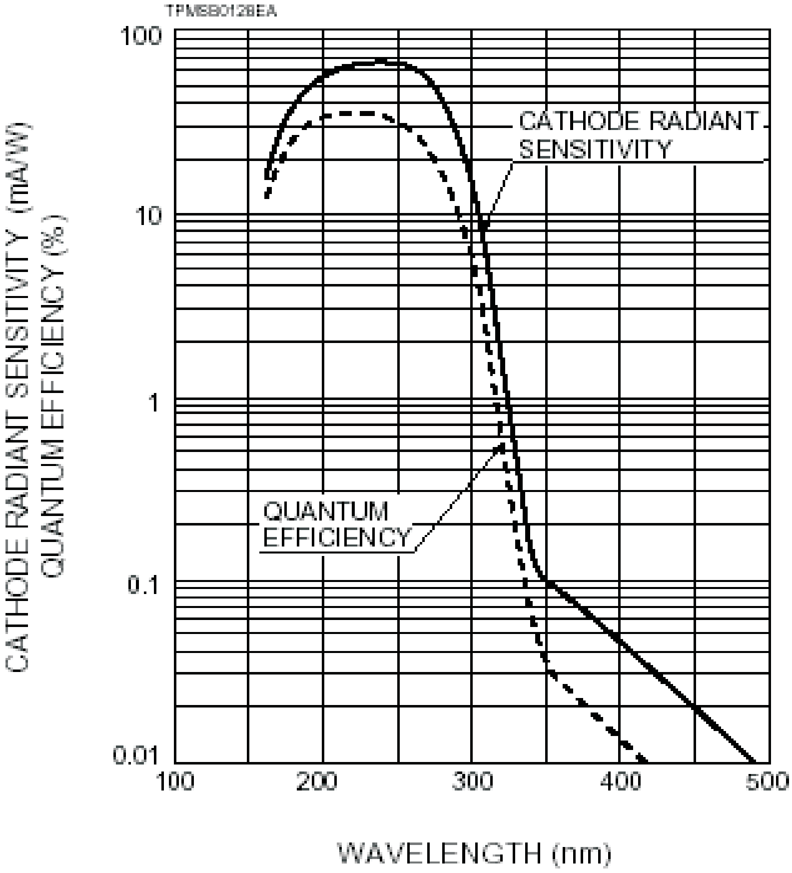

Figure 8.7: The quantum efficiency of the photomultipliers as a function of wavelength. The maximum is around 230 nm, in the vicinity of the carbon lines. The efficiency strongly decreases in the visible wavelength range.

Table 8.2: Calibration factors for different wavelengths for the left exit slit (detection of the CIII line).

channel	$\lambda = 253.55$ (nm)	$\lambda = 253.65$ (nm)	$\lambda = 253.75$ (nm)
1	0.57	0.75	0.94
2	0.48	0.54	0.63
3	0.57	0.63	0.63
4	0.87	0.83	0.69
5	1.00	1.00	1.00
6	0.83	0.92	0.94
7	0.65	0.67	0.75
8	1.00	1.00	0.94
9	0.43	0.46	0.31

per metre is thus given by the relation:

$$0.2\text{dB} = 10 \log \left(\frac{P_{in}}{P_{out}} \right). \tag{8.1}$$

The corresponding transmission (P_{out}/P_{in}) is then

$$\frac{P_{out}}{P_{in}} = 10^{-0.2/10} = 0.95, \tag{8.2}$$

which gives 74% ($(0.95)^6 = 0.74$) for the 6 m fibres.

At the two exit slits, the same type of optical fibres (with a slightly larger core diameter) are used to transfer the light to two photomultipliers (PMs) with one at each exit slit. The different chords are scanned (one after the other, with a maximum time resolution of about 100 ms for the complete set of nine channels – section 8.3). The PMs are inside a magnetic shielding case to prevent deflection of the electrons in the tubes from their trajectories. To avoid disturbance of stray light in the output signal of the PMs the quantum efficiency is such that the maximum is around 225-230 nm, and strongly decreases towards the visible range of the spectrum (fig. 8.7).

8.2 Relative calibration

In order to calibrate the different input channels relative to each other, a Hg(Ar) calibration lamp was used that has an intense mercury line

Table 8.3: Calibration factors for different wavelengths for the right exit slit (CV line).

channel	$\lambda = 253.55$ (nm)	$\lambda = 253.65$ (nm)	$\lambda = 253.75$ (nm)
1	0.50	0.50	0.45
2	0.39	0.38	0.40
3	0.44	0.50	0.50
4	0.58	0.63	0.60
5	0.67	0.83	0.85
6	0.78	0.79	0.80
7	0.67	0.67	0.70
8	1.00	1.00	1.00
9	0.44	0.46	0.45

in its spectrum at 253.65 nm, relatively close to the carbon lines. In a first test the maximum of this line (at $\lambda = 253.65$ nm) was put in the left (and right, by moving the grating) exit slit (fig. 8.4), and the output voltage of the PMs was measured for each of the nine chords separately. The calibration factors, after normalizing to the chord with the maximal output value, are in the tables 8.2 and 8.3. These factors take into account the differences in input and output fibres, as well as the losses inside the spectrometer.

As a second test the complete Hg line was scanned, by moving the grating of the spectrometer in small steps (of 0.10 or 0.05 nm). For each of the steps the output voltage of both PMs was measured and for each of the nine chords. The calibration factors for $\lambda = 253.55$ nm and $\lambda = 253.75$ nm, calculated as before for the central wavelength, are in the same tables. It can be seen that, especially for the exit slit of C III, they are quite different from the $\lambda = 253.65$ nm values. This is a severe problem for the relative calibration. Another way to visualise the difference is given in fig. 8.8, where the spectral line shape is reconstructed using the data of a few steps of the scan. Here the voltages are normalised for each of the channels to the output at the central wavelength of 253.65 nm. The resulting line shape strongly depends on the chosen channel. Thus, assuming that the Hg line shape did not change during the tests, the reason for these errors must lie in the alignment of the entrance and exit slits. As a consequence of small misalignments at the entrance slit in between the nine channels (fig. 8.4), the spectral lines may not appear exactly at the expected curve at the exit slit, but are slightly displaced left or right from the exit slit. Moreover misalignments at the exit may aggravate the situation. The dispersion of 0.4 nm/mm, combined with alignment errors at the entrance and the exit of the order of 0.1 mm, result in 0.05 nm at the level of the spectral line, which is already a significant factor.

Thus the relative calibration of the system as it was done in the tables 8.2 and 8.3 is only valid at one position of the spectral line. Even if the grating could be put such that the maxima of both carbon lines is exactly in the two exit slits (then the $\lambda = 253.65$ nm calibration factors could be assumed to be a good estimate), Doppler shifts might bring the lines out of their normal position, making it quasi impossible to accurately calibrate the system. Improvements to overcome this problem are being made and are described in chapter 10.

8.3 Operational modes

The system has two modes of operation :

- A scan of the nine chords one after the other at a repetition time of about 100 ms (for the complete set). An example of the detected C III and C V signals is shown in fig. 8.9, showing a few scans of the eight channels (numbers 2 to 9). In order to convert these data into the time evolutions of the C III and C V emissivities along each of the eight lines of sight, a deconvolution programme has been written and the output for the C V emissivities is shown in fig. 8.10.
- Alternatively a single chord can be selected for fast detection ($<$ 1 ms) to study transient phenomena at a fixed location. A scan of different chords can in this situation only be made with a set of identical discharges. An example of the C III and C V emission for chord number 4 is shown in fig. 8.11.

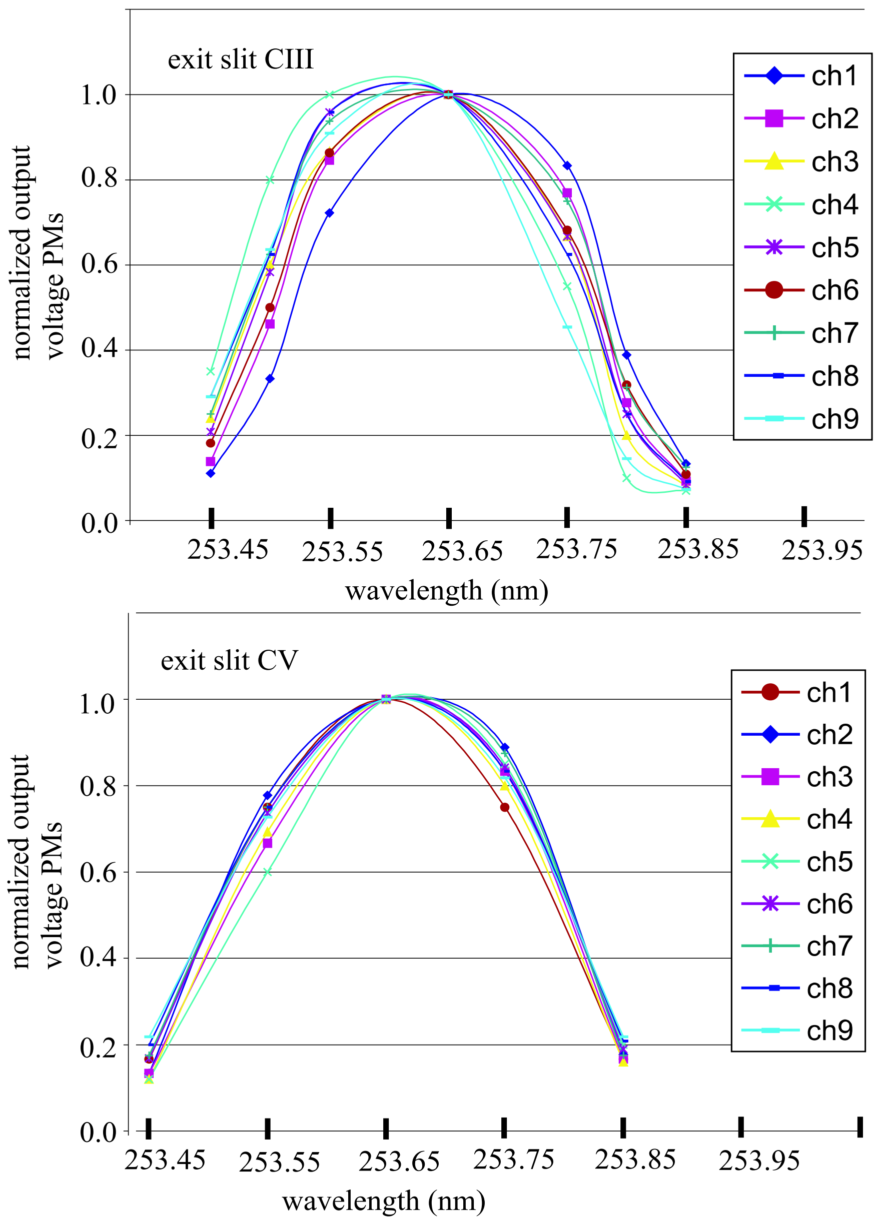

Figure 8.8: Scan of the complete spectral Hg-line (at 253.65 nm) in steps of 0.05 nm, and normalised response of the nine channels. The line shape is different for the different chords due to alignment errors of the fibres in the entrance and/or exit slits.

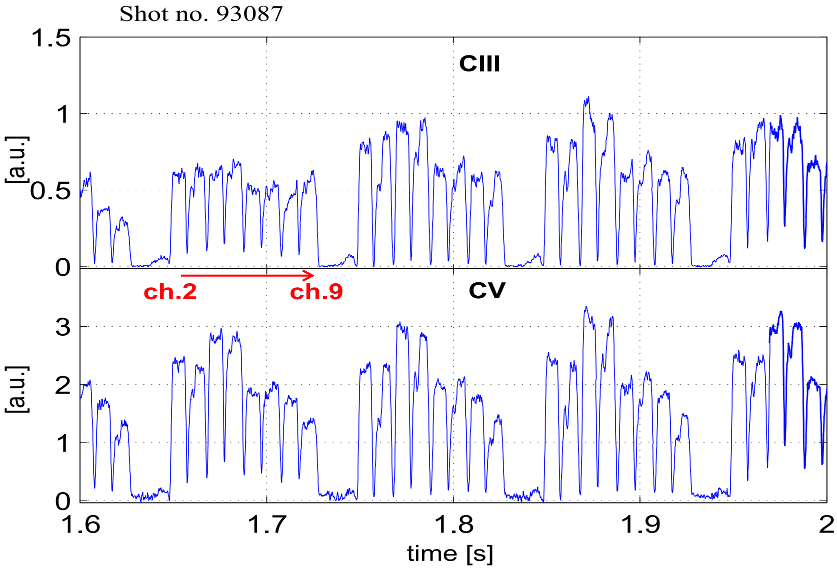

Figure 8.9: Scan of the eight channels, numbers 2 to 9, at a repetition rate of about 100 ms for the complete set. Every single chord is selected for about 10 ms. Both C III and C V emissivities are detected at the exit of the spectrometer. In this shot the plasma current was $I_p = 380\text{kA}$ and the toroidal magnetic field $B_t = 1.9\text{T}$.

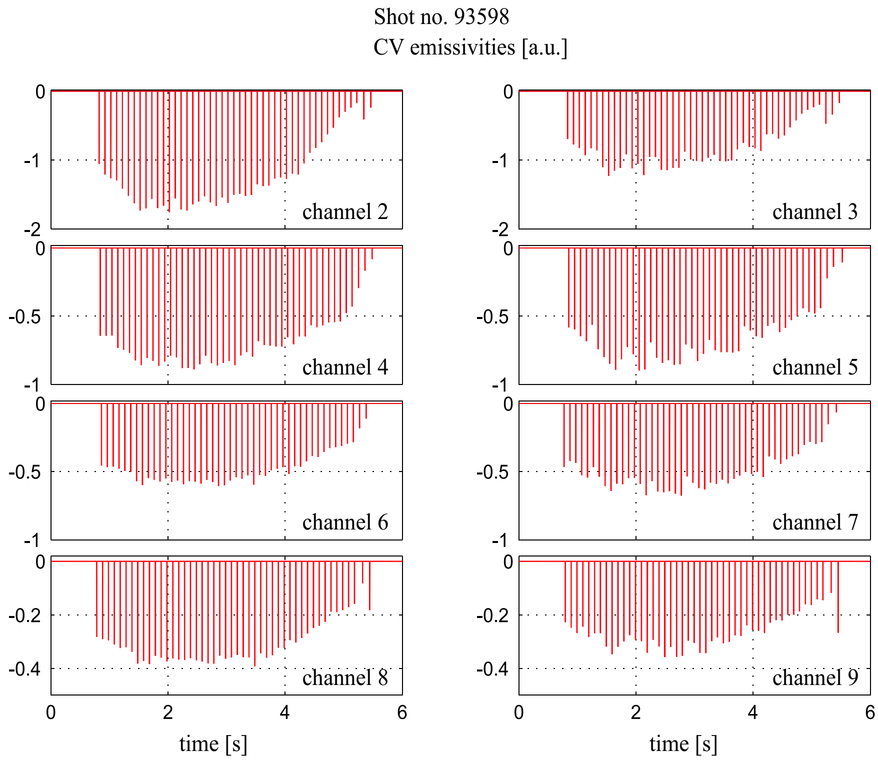

Figure 8.10: C V emission in the eight separate channels for shot no. 93598 with $I_p = 450$kA and $B_t = 1.9$T. The DED was operating in 12/4 mode with a current in the DED coils $I_{DED} = 7$kA, activated during t = 2.0 s - 3.5 s. The separation of the channels allows to determine the temporal evolution of the emissivities along the different channels with a time resolution of about 100 ms.

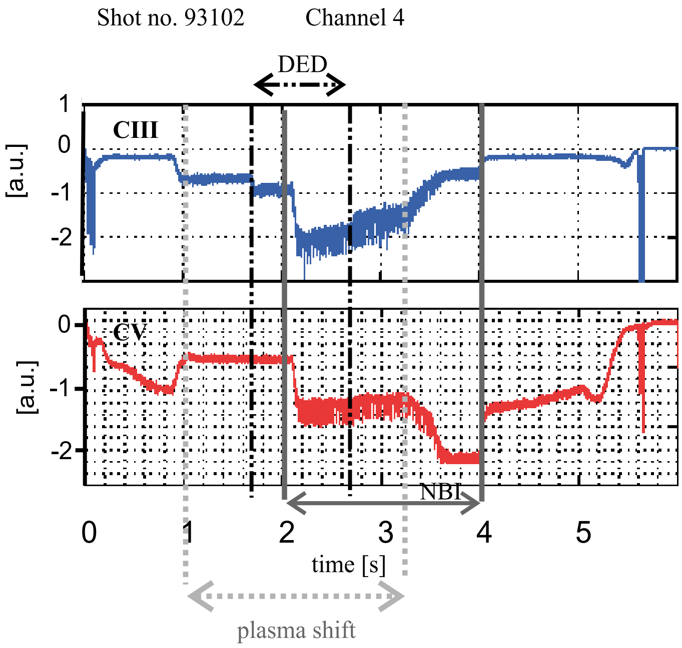

Figure 8.11: C III and C V emission recorded by the UV diagnostic during the single chord operational mode. $I_p = 380$kA and $B_t = 1.9$T, the DED is in 12/4 configuration with $I_{DED} = 4$kA, and is activated during t = 1.7 s - 2.7 s. A small increase (values are negative) in C III emission with the DED can be observed, there is no effect on the C V signal. The neutral beam was active during t = 2.0 s - 4.0 s, and both C III and C V increase with the NBI. The plasma was shifted towards the DED coils during t = 1.0 s - 3.5 s.

Chapter 9

Carbon screening by the dynamic ergodic divertor

Experimental data measured with the diagnostic described in chapter 8 have been used to study the response of intrinsic carbon to the new magnetic configuration created by the DED coils [Tele05a]. So far, the 12/4 and 3/1 configuration of the perturbation field have been tested. Examples will be shown both with static and rotating error fields.

9.1 DED operation in 3/1 mode

In the 3/1 mode a positive current is flowing in 8 of the 16 perturbation coils and a negative current in the others. The maximum value in each coil is 3.75 kA in this configuration.

9.1.1 Static perturbation field

In the first example, shot no. 94454 ($\mathrm{B_t/I_p}$ = 2.25T/300kA, fig. 9.1) the DC current in the perturbation coils was ramped up to an amplitude of 2 kA. At about 1 kA (t = 1.8 s) a 2/1 tearing mode in the plasma is excited and locks to the error field, resulting in a decrease of the toroidal rotation [Lian04, Fink05], an increased plasma wall interaction and loss of energy and particles. From fig. 9.1 can be seen that the total radiated power increases, and the line average central density drops. The density however, recovers relatively quickly to the value before the mode locking, due to the action of the feedback system. The carbon

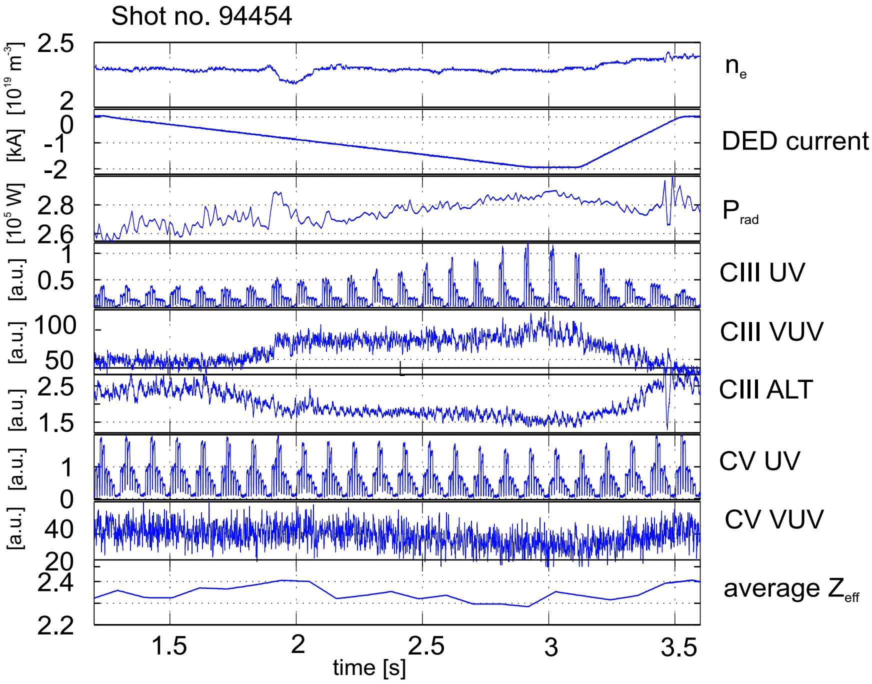

Figure 9.1: Effect of the static ergodic divertor in 3/1 mode (with a current ramp up) on the plasma density (n_e), the total radiation (P_{rad}) and core contamination (Z_{eff}), and on the emissivity of C III and C V lines. The discharge had $I_p = 300$kA and $B_t = 2.25$T.

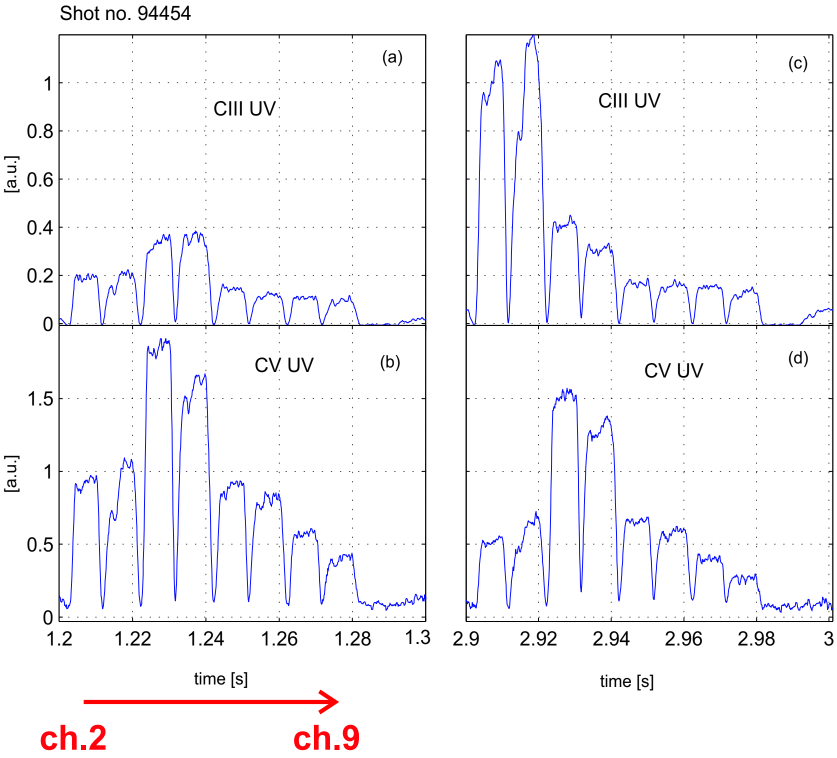

Figure 9.2: A zoom from fig. 9.1 of the eight channels of the carbon UV diagnostic. (a) C III emission without DED, (b) C V emission without DED, (c) C III with DED and (d) C V with DED. The C III emission increases by about a factor of 5 in the first two channels (numbers 2 and 3) when the DED is activated, while the other channels show only a modest increase. Similar behaviour can be observed for the decrease of C V emission : a factor of 2 for the channels 2 and 3, and about 20 % for the other channels.

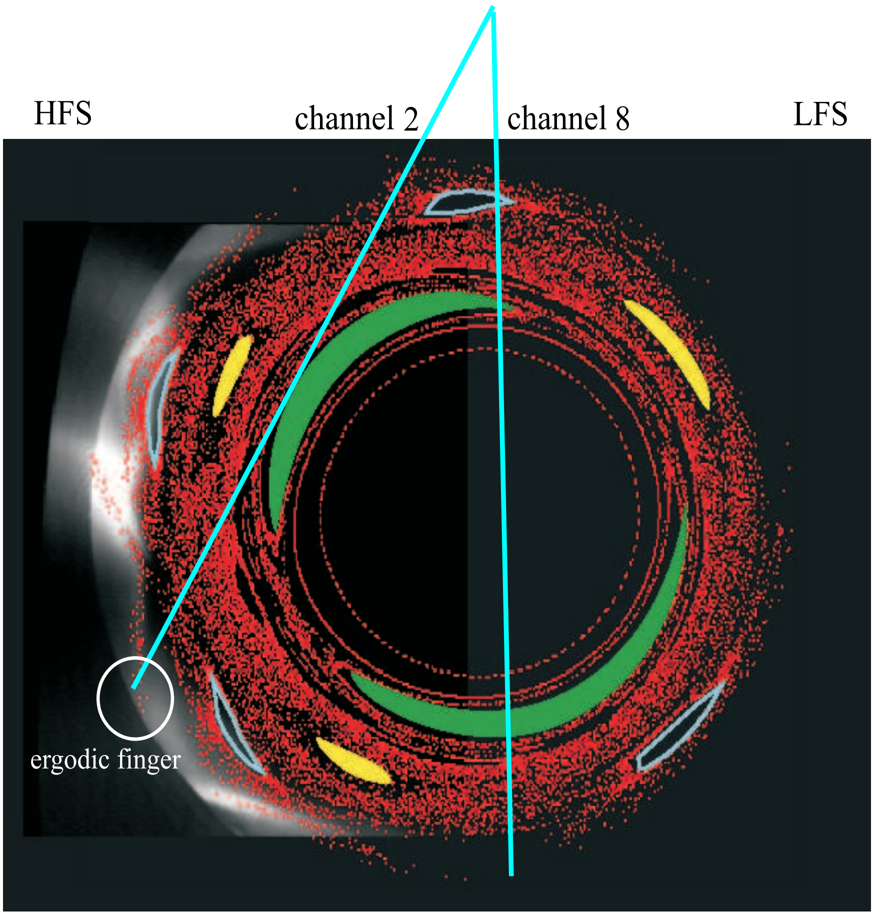

Figure 9.3: Orientation of two of the channels superposed on a Poincaré plot of the magnetic field structure. Channel 2 intersects an ergodic finger, which is a local phenomenon, while the radiation in channel 8 represents the global plasma response.

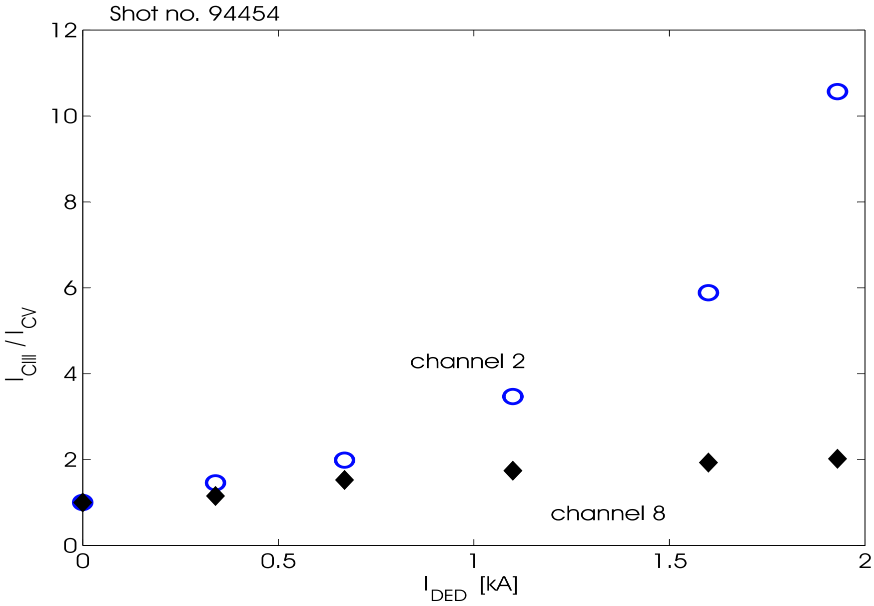

Figure 9.4: The intensity ratio of the C III and C V spectral lines for the channels 2 and 8 as a function of the current in the DED coils.

signal names of the new diagnostic are CIII UV and CV UV, recorded here as a continous scan of the eight operational channels (numbers 2 to 9 in fig. 8.1) one after the other. The signal CIII ALT is from the chord at the ALT-II limiter at the low field side (fig. 8.1). These carbon signals are compared to line emission in the VUV of C^{2+} and C^{4+} ions. The VUV diagnostic has one central viewing chord looking approximately horizontally through the plasma from the LFS towards the HFS at the midplane. It is located at a different toroidal angle as the UV diagnostic, and therefore the C III and C V signals of both diagnostics are not correlated, due to the 3 dimensional structure of the DED magnetic field.

The temporal evolution of the carbon signals shows that the C III and C V emission remains at a constant level until the mode locking occurs at about t = 1.8 s. From that moment on the C III signals from both the VUV and UV diagnostics increase while the C V signals decrease as well as the average Z_{eff}. At the ALT-II a decrease in C III emission can be observed. The zoom of figure 9.2 shows a quite different response depending on the poloidal orientation of the viewing chords.

The C III emission in the first two channels (numbers 2 and 3) increases by a factor of 5 while in the other chords the increase is limited to about 10 %. A similar decrease is observed in the C V emission: a factor of 2 for channels 2 and 3 and a modest 10 % - 20 % for the other chords. The reason for this difference in behaviour can be understood from fig.9.3 where the viewing geometry of the channels 2 and 8 are plotted on a Poincaré reconstruction of the magnetic field lines. Channel 2 is looking exactly at the location of a strike point (an ergodic finger connecting the ergodic layer with the wall), and there is a local very strong increase of the ratio C III / C V (up to a factor 10). The large difference in the ratio of C III / C V emission depending on the viewing orientation is also shown in fig. 9.4. Channels 2 and 3 represent the local behaviour in the vicinity of a strike point, while the other channels (numbers 4 to 9) and the VUV diagnostic measure the global plasma response. The decrease in C V emission is an indication for a decrease in the core carbon content, because the electron density and temperature in the unperturbed zone of the plasma are quite similar without or with DED activation, and because a decrease in C^{6+} concentration (measured by Charge eXchange Recombination Spectroscopy) and Z_{eff} is observed as well in these plasmas when the DED is active.

In general, the increase of the ratio C III / C V under DED operation could be explained by (i) the creation of a cold and dense edge layer and an increase in the level of impurity recycling and (ii) at the same time a decontamination of the core; the large deuterium flows towards the wall drag impurities out of the plasma through friction forces. These friction forces are charge dependent and so preferentially the highly charged impurity ions are expelled, resulting in a decontamination of the core plasma, consistent with the decrease in Z_{eff} and C^{6+} concentration.

9.1.2 Strike point sweep

During the 3/1 mode operation the strike points were also swept at a rotation velocity of about 1 Hz by adjusting the current distribution in the different DED coils as shown in fig. 9.5. The current in the DED coils is ramped up and down from 0 to 3.75 kA and back in about 1 second to realise the slowly rotating perturbation field. At 1 kA the onset of the 2/1 mode appears and is accompanied by a drop in n_e around t = 1.4 s. In the figure the current in two of the coils is plotted, during the ramp down of the current in coil number 1, the current in coil number 13 is increased (in this one the current is flowing in negative direction) such

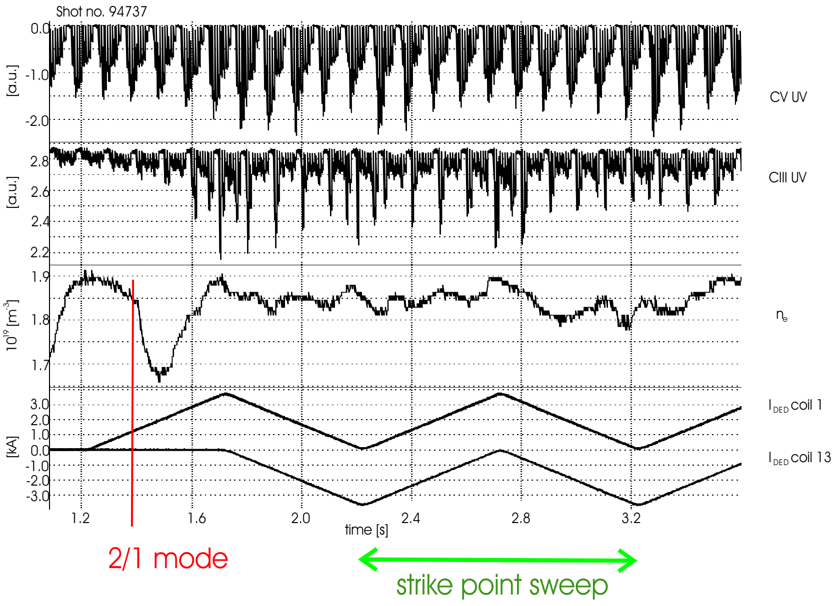

Figure 9.5: Example of a discharge with a slowly rotating perturbation ($I_p = 300$kA, $B_t = 2.25$T). From top to bottom are shown the C V and C III emission, the line averaged central density and the current in two of the DED coils.

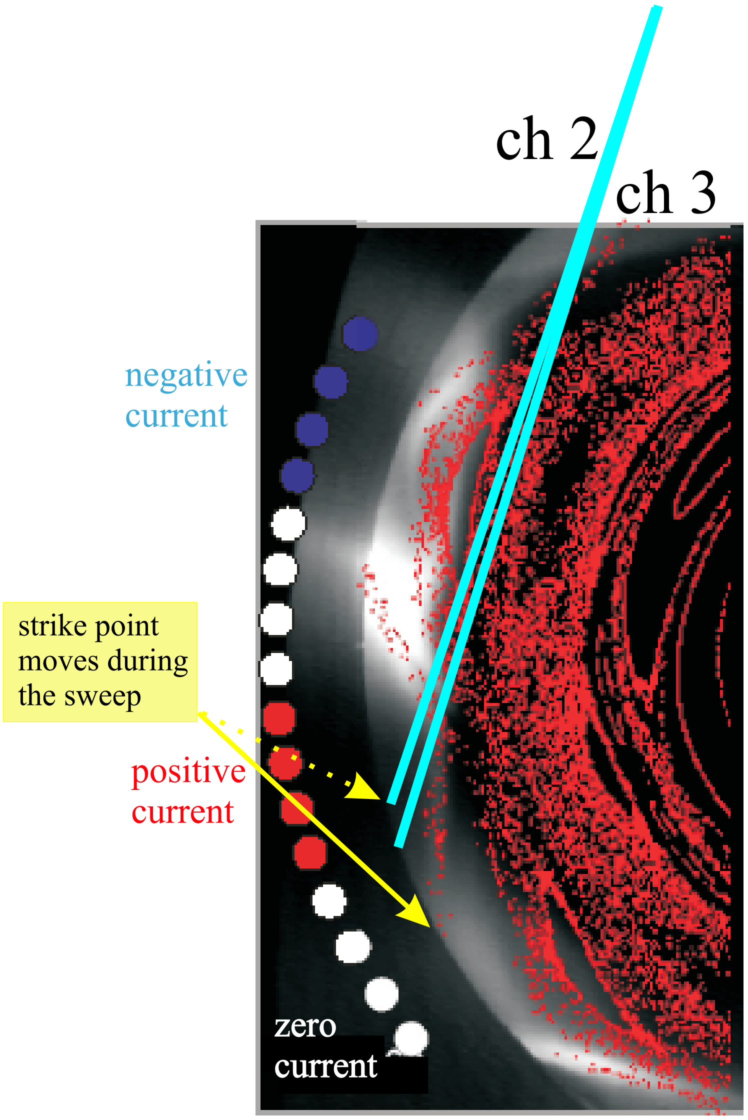

Figure 9.6: Plot of the viewing direction of channels 2 and 3 superposed on a Poincaré plot for a 3/1 mode in a $I_p = 300$kA, $B_t = 2.25$T plasma. During the slow rotation of the DED field, the ergodic finger moves in and out the viewing chords 2 and 3.

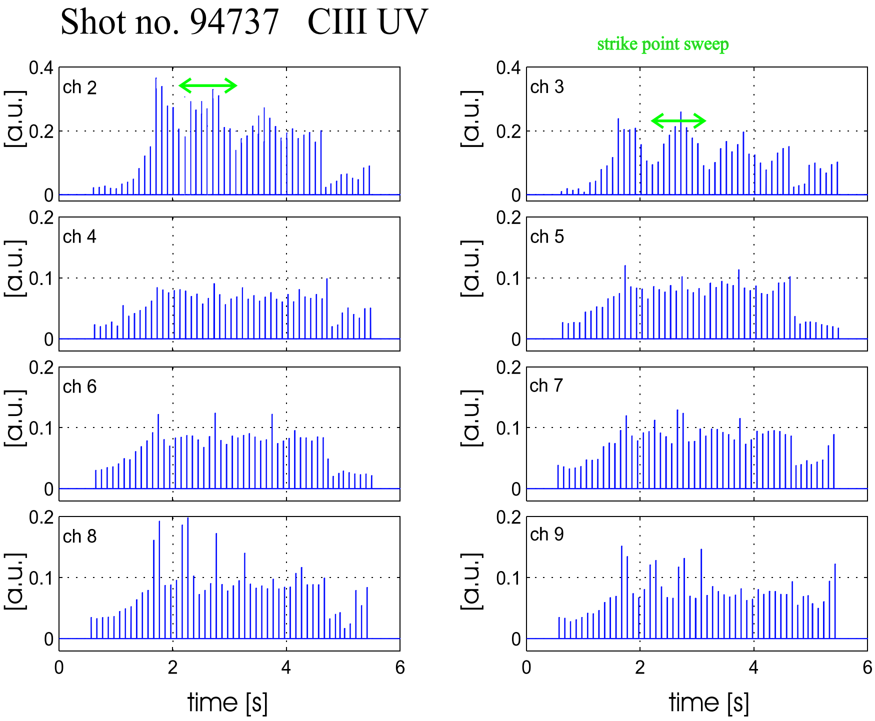

Figure 9.7: Time evolution of the C III emission in the eight separate channels of shot no. 94737 ($B_t/I_p = 2.25T/300kA$) from fig. 9.5, a discharge with a slow rotation of the DED field.

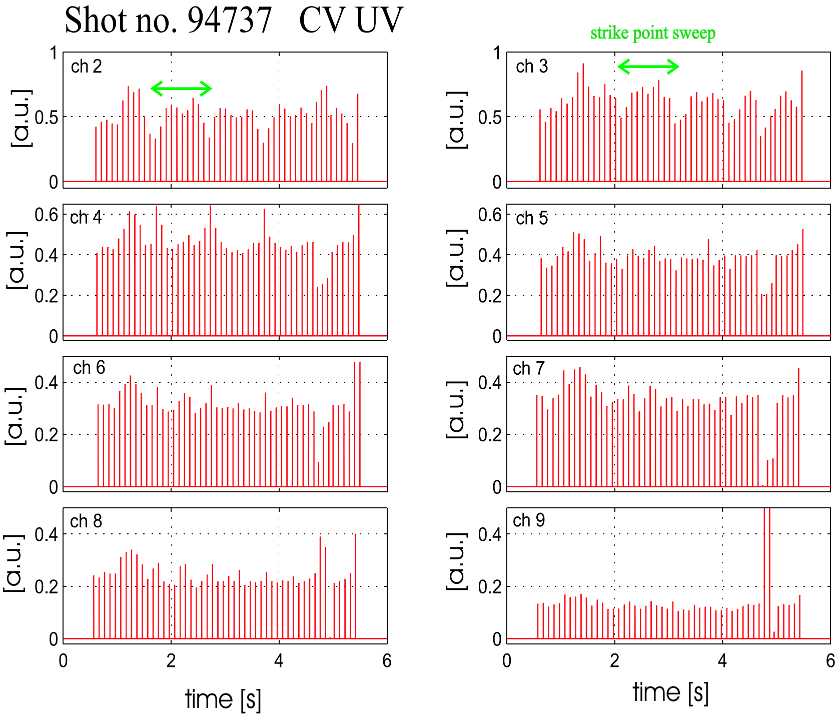

Figure 9.8: Time evolution of the C V emission in the eight separate channels of shot no. 94737 (fig. 9.5).

that the total perturbation amplitude remains at the same level. For this kind of discharge the location of the strike points can be followed with the carbon emission detected by the UV diagnostic, this is because the strike point moves in and out the view of the lines of sight, as illustrated in figure 9.6. The C III and C V emissions of the seperate channels are shown in the figures 9.7 and 9.8 respectively. The slow rotation of the perturbation field can be observed as a temporal increase and decrease in the C III and C V emission, mainly observed in the channels 2 and 3 (fig. 9.6).

9.1.3 Fast rotating DED field

The fast rotating perturbation field appears to influence the plasma rotation [Fink05]. An example of the carbon emission during a discharge with a rotating perturbation at 1 kHz is shown in figure 9.9. The C III and C V signals are modulated at a frequency of 1 kHz (fig. 9.10). This can be detected with the fast response of the photomultipliers and the high sampling rate of the memory modules. The scanning time for one channel is about 10 ms, and during this time the variation in C III and C V emissions is recorded with a time resolution of < 1 ms. The C III emission at the ALT-II is also modulated at 1 kHz. The modulation frequency is not influenced by the 2/1 mode locking nor by the rotation direction (co or counter with respect to the plasma current), as is the case for the plasma rotation [Lian04, dB04]. For a complete study of the carbon emission in plasmas with fast rotating DED fields, the time resolution of the detection system should be increased to < 1 ms for all channels simultaneously (chapter 10).

9.2 DED operation in 12/4 mode

The data presented here were taken during the first DED campaign with 12/4 operation, during which the current in the DED coils was, for technical reasons, limited to about 50 % of the maximum value. As the perturbation in this configuration is restricted to the very edge region, the plasma is intentionally shifted a few centimetres towards the HFS before the onset of the DED.

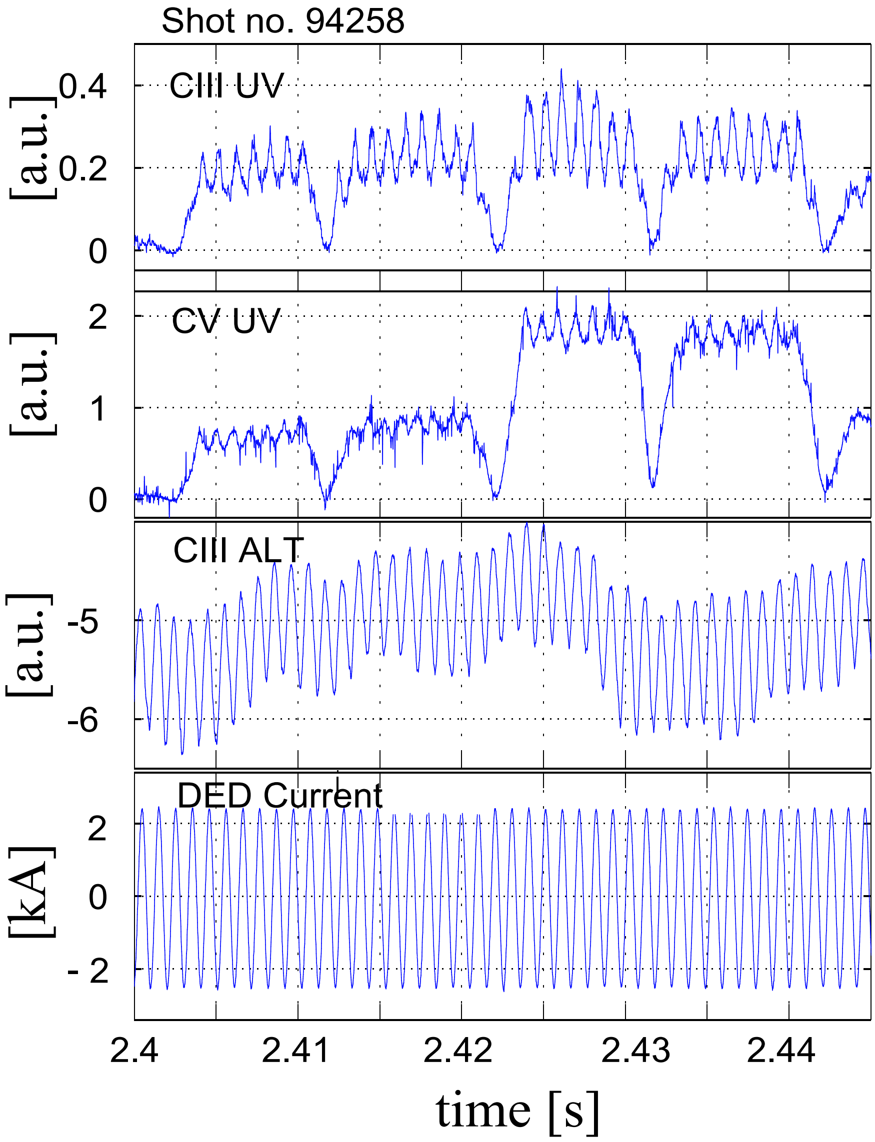

Figure 9.9: C III and C V emission and the DED current evolution for a discharge with 1 kHz rotation of the perturbation field. The plasma current was 300 kA and $B_t = 2.25T$.

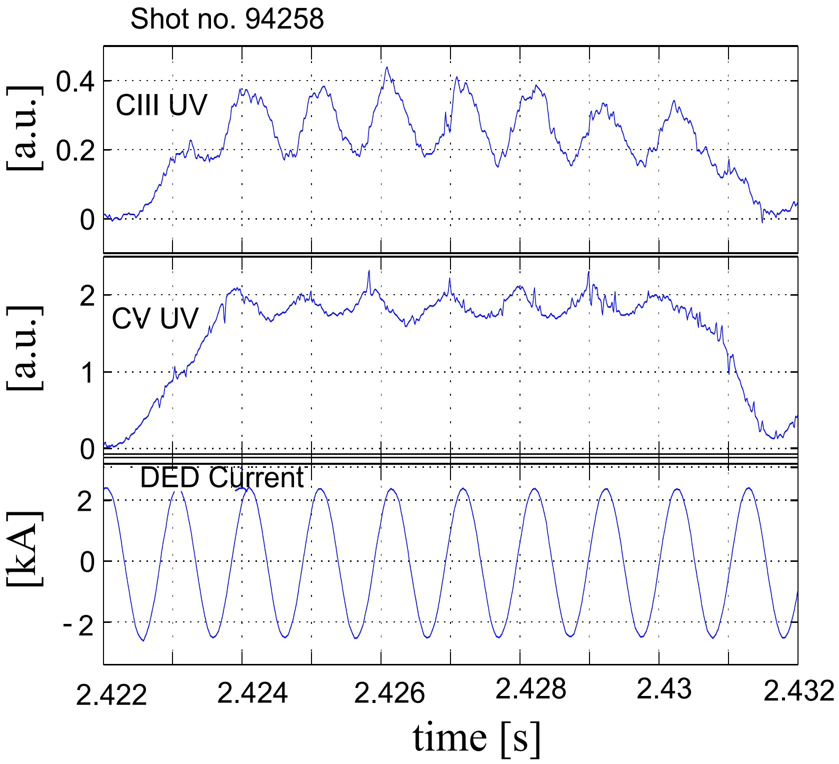

Figure 9.10: Zoom on one of the channels of fig. 9.9. During the scan of the eight channels, every single chord is exposed to the photomultipliers for about 10 ms. During this interval the time resolution is determined by the response of the photomultiplier and the sampling rate of the memory and is $\ll 1$ ms. The C III and C V emission is modulated at the same frequency as the DED current.

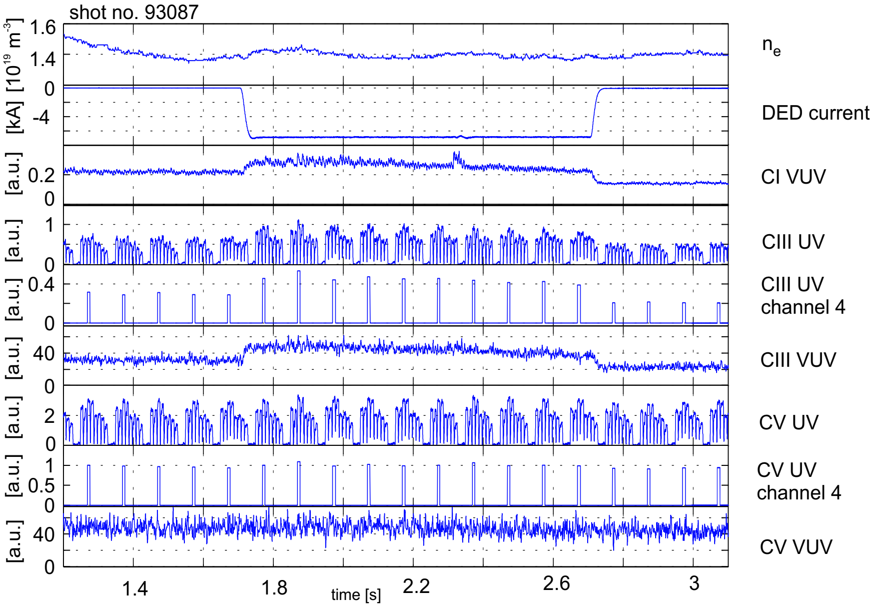

Figure 9.11: Central density and DED current in the static 12/4 mode operation ($I_p = 380$kA, $B_t = 1.9$T). Carbon emission from the VUV and UV diagnostics shows a weak increase for low ionisation states (C I and C III), but no change in the C V emission can be observed.

9.2.1 Static perturbation field

Figure 9.11 is an example with a static DED at a current amplitude of 7 kA. It can be seen that the C I and C III emissions increase by about 30 % with the DED. The behaviour of one single channel (number 4) of the UV diagnostic is also presented. The C V emission on the other hand, does not change under the influence of the DED (and also generally in the 12/4 operational mode, the Z_{eff} does not decrease, although the signal was not available for all discharges). Therefore, unlike for the 3/1 case, no clear plasma decontamination is observed in the 12/4 operation. From bolometric measurements it is calculated that the total radiation only increases slightly in these discharges. The reason is that despite the 30 % increase in the C III signals at the DED side, at the onset of the DED the plasma wall interaction and radiation at the ALT-II limiter strongly decrease. Although the viewing chord of the UV diagnostic at the LFS was not available for this discharge, mostly for the 12/4 operation the decrease of the C III signal at the ALT-II line of sight, is of the same level as the increase at the HFS. If one considers the total divertor area at the HFS to be about twice the ALT-II limiter surface, then this corresponds to an average increase in C III emission of only 15 %, and a weak enhancement of P_{rad}. The ratio C III / C V in the 12/4 configuration is thus only weakly influenced by the DED operation; therefore a screening of the carbon ions cannot clearly be identified, possibly because of the limited perturbation amplitude and/or the low penetration of the 12/4 mode.

9.2.2 Slow rotation

During a series of DED discharges which also had a 7 kA perturbation and slow rotation of the perturbation field, the UV diagnostic was fixed to one channel. The time evolution of the DED current in different coils, the central density and C III and C V emission are plotted in fig. 9.12. The UV C III emission increases by more than 50 % around t = 2.0 s while the UV C V signals decreases. The VUV diagnostic also shows an increase of C III (but by only 30 %), and no change in C V emission. An explanation for this difference in response is that during the rotation one of the strike points intersects the viewing channel 4 of the UV diagnostic. This behaviour is similar to the strong increase of the C III / C V ratio in the channels 2 and 3 during 3/1 mode operation (section 9.1.1), the emission in channel 4 in this case represents a local behaviour around a

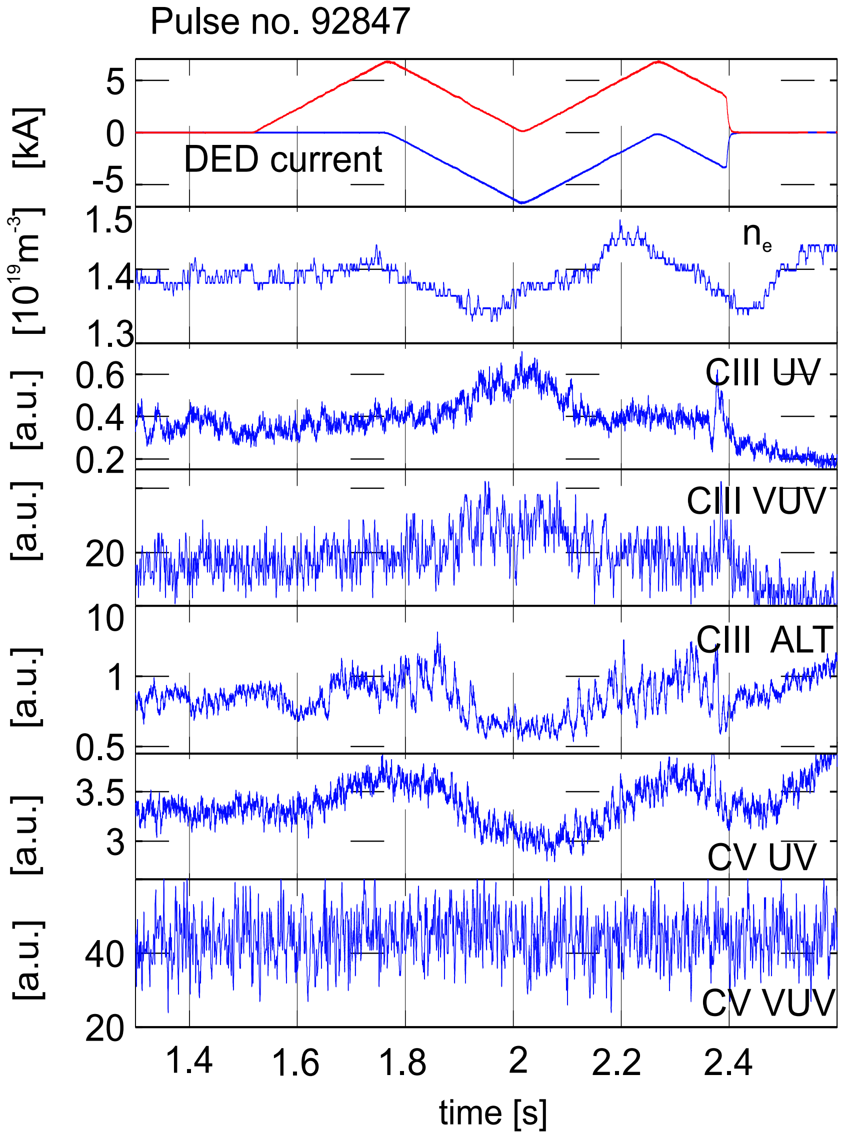

Figure 9.12: Time evolution of the DED current, line averaged central electron density and C III and C V emission in 12/4 mode with a slow rotation of the perturbation field ($I_p = 380$kA, $B_t = 2.0$T).

strike point, which differs from the global plasma response, as measured by the VUV chord.

Chapter 10

Conclusions and future plans

Efficient power exhaust in a reactor is one of the key issues in fusion research; an ergodic divertor could be a good option as it enhances the edge radiation without disturbing the confined plasma core or increasing the core impurity content. The diagnostic that has been designed and installed on TEXTOR contributes to the study of this predicted screening effect through the simultaneous detection of different ionisation states of the carbon impurity, which are located at different radial positions in the plasma.

So far on TEXTOR the m/n=12/4 and 3/1 operational modes of the dynamic ergodic divertor have been tested with a static and rotating DED field.

During 3/1 operation, the line ratios measured by the new diagnostic, show a clear increase in the carbon radiation from the lower charged carbon ions, while the density of the highly charged states in the confined plasma decreases. This is in agreement with the decrease in core plasma Z_{eff} and a strong outward plasma flow dragging the impurities through friction forces. The observations are consistent with the screening effect for impurities that is explained in [Toka97] by a positive convective velocity (towards the wall) mainly caused by the friction forces between impurities and main ions. The diffusion coefficient of the main ions is strongly enhanced due to the stochastisation, resulting in a strong outward plasma flow. Since the friction force depends on the charge state of the impurities, the highly charged impurity ions are preferentially expelled from the plasma, reducing also Z_{eff}. At the same time the low temperature and high density at the edge in ergodic divertor plasmas enhance the radiation of the low charge states, as well as the increase level of impurity recycling.

No such screening effect for carbon ions is observed during the 12/4 operation, only a modest increase in carbon radiation, this may be due to the low perturbation amplitude (the current in the DED coils was limited in these discharges to 50 % of its maximum value) and/or to the short penetration depth of the perturbation field in this configuration. Further analysis during 12/4 operation with the full current is being made and is reported in [Tele05b]. Later on also the m/n=6/2 operation of the DED will be tested.

The slow rotation of the perturbation field moves the position of the strike points of the divertor and this can be followed on the time evolution of the carbon signals.

Concerning the diagnostic itself, the experience during the construction process and the results from the DED operation so far, have initiated some improvements to the system:

- In view of a good relative calibration of the different chords (section 8.2) new entrance and exit slits are installed, made with a higher precision. The entrance slit has a variable width ; up to now the width of the entrance light beam was determined by the full core diameter of the entrance fibres (600 μm) and their numerical aperture (0.22). It was found that, despite the relatively large losses in the 6 m optical fibres between plasma and spectrometer, the actual number of photons arriving at the PMs allows the use of a narrower entrance slit, which increases the resolution. Secondly, at the exit slit of the spectrometer the optical fibres are being substituted by new light guides that have a larger core diameter (1000 μm instead of 800 μm). In this way a larger part of the spectral line will be detected by the photomultipliers (the signals are integrated line intensities), making the system less sensitive for alignment errors.

- To increase the time resolution, the present detection system of 2 PMs with a repetitive scan of the 9 channels at about 100 ms, will be replaced by 2×9 photomultipliers. Using these separate PMs the time resolution will be < 1 ms, which is particularly important to study transient phenomena during high frequency rotation (in the kHz range) of the perturbation field.

- An additional set of four spectrometers for the detection of carbon fluxes (via the C^{1+} ions) has also been recently installed along the same lines of sight as in fig 8.1. On a shot to shot basis four chords out of the nine can be selected for the additional simultaneous measurement of C^{1+} ions, which will allow more complete transport studies.

Bibliography

[Abdu99] S. Abdullaev, K. Finken, and S. Spatschek. Asymptotical and mapping methods in study of ergodic divertor magnetic field in a toroidal system. Phys. Plasmas, 6(1):153, 1999.

[Anto96] T. Antonsen, J. Drake, P. Guzdar, A. Hassam, Y. Lau, C. Liu, and S. Novakovskii. Physical mechanism of enhanced stability from negative shear in tokamaks: implication for edge transport and the L-H transition. Phys. Plasmas, 3(6):2221, 1996.

[Balea] R. Balescu. Transport processes in plasmas, Vol. 1, Classical transport. North-Holland.

[Baleb] R. Balescu. Transport processes in plasmas, Vol. 2, Neoclassical transport. North-Holland.

[Bara04] Y. Baranov, X. Garbet, N. Hawkes, B. Alper, R. Barnsley, C. Challis, C. Giroud, E. Joffrin, M. Mantsinen, F. Orsitto, V. Parail, and S. Shaparov. On the link between q-profile and internal transport barriers. Plasma Phys. Control. Fusion, 46(8):1181, 2004.

[Beer97] M. Beer, G. Hammett, G. Rewoldt, E. Synakowski, M. Zarnstorff, and W. Dorland. Gyrofluid simulations of turbulence suppression in reversed-shear experiments on the Tokamak Fusion Test Reactor. Phys. Plasmas, 4(5):1792, 1997.

[Bell98] R. Bell, F. Levinton, S. Batha, E. Synakowski, and M. Zarnstorff. Poloidal rotation in TFTR reversed shear plasmas. Phys. Rev. Lett., 81(7):1429, 1998.

[Bell00] R. Bell and E. Synakowski. New understanding of poloidal rotation measurements in a tokamak plasma. AIP Conference Proceedings, 547:39, 2000.

[Bigl90] H. Biglari, P. Diamond, and P. Terry. Influence of sheared poloidal rotation on edge turbulence. Phys. Fluids B, 2:1, 1990.

[Bour03] C. Bourdelle, W. Dorland, X. Garbet, P. Gohil, G. Hoang, and C. Roach. Impact of α on the microstability of internal transport barriers. Proceedings of the 30th EPS Conference on Contr. Fusion and Plasma Physics, St.-Petersburg, 7-11 July 2003, ECA, 27A:P.1–89, 2003.

[Bret91] C. Breton, C. DeMichelis, M. Mattioli, P. Monier-Garbet, E. Agostini, T. Fall, W. Hess, J. Lasalle, T. Evans, A. Grosman, P. Ghendrih, A. Pecquet, L. Poutchy, A. Samain, and J. Vallet. Plasma decontamination during preliminary ergodic divertor experiments in Tore Supra. Nucl. Fusion, 31(9):1774, 1991.

[Burr97] K. Burrell, M. Austin, C. Greenfield, L. Lao, B. Rice, G. Staebler, and B. Stallard. Effects of ExB velocity shear and magnetic shear in the formation of core transport barriers in the DIII-D tokamak. Phys. Plasmas, 4(5):1499, 1997.

[Chal01] C. Challis, Y. Baranov, G. Conway, C. Gormezano, C. Gowers, N. Hawkes, T. Hender, E. Joffrin, J. Mailloux, D. Mazon, S. Podda, R. Prentice, F. Rimini, S. Shaparov, A. Sips, B. Stratton, D. Testa, and K.-D. Zastrow. Effect of the q-profile modification by LHCD on internal transport barriers in JET. Plasma Phys. Control. Fusion, 43:861, 2001.

[Chal02] C. Challis, X. Litaudon, G. Tresset, Y. Baranov, A. Becoulet, C. Giroud, N. Hawkes, D. Howell, E. Joffrin, P. Lomas, J. Mailloux, M. Mantsinen, B. Stratton, D. Ward, and K.-D. Zastrow. Influence of the q-profile shape on plasma performance in JET. Plasma Phys. Control. Fusion, 44:1031, 2002.

[Conn04] J. Connor, T. Fukuda, X. Garbet, C. Gormezano, V. Mukhovatov, and M. Wakatani. A review of Internal transport barrier physics for steady state operation of tokamaks. Nucl. Fusion, 44:R1, 2004.

[Copp67] B. Coppi, M. Rosenbluth, and R. Sagdeev. Instabilities due to temperature gradients in complex magnetic field configurations. Phys. Fluids, 10:582, 1967.

[Crom02] K. Crombé, G. Telesca, G. Van Oost, and G. Van Den Berge. Transport, radiation and rotation properties of carbon on TEXTOR under the influence of the Dynamic Ergodic Divertor - Physical issues and design of a new diagnostic. Proceedings of the 29th EPS Conference on Contr. Fusion and Plasma Physics, Montreux, 17-21 June 2002, ECA, 26B:P–2.056, 2002.

[Crom03] K. Crombé, Y. Andrew, I. Coffey, P. de Vries, C. Giroud, N. Hawkes, E. Joffrin, D. McDonald, A. Murari, J. Ongena, F. Sattin, M. Valisa, and K.-D. Zastrow. Improvement measurements of impurity ion poloidal rotation velocities in JET. Proceedings of the 30th EPS Conference on Contr. Fusion and Plasma Physics, St.-Petersburg, 7-11 July 2003, ECA, 27A:P–1.55, 2003.

[Crom04] K. Crombé, Y. Andrew, C. Giroud, N. Hawkes, A. Murari, M. Valisa, G. Van Oost, and K.-D. Zastrow. Calibration of the charge exchange recombination spectroscopy diagnostic for core poloidal rotation velocity measurements on JET. Rev. Sci. Instrum., 75(10):3452, 2004.

[dB04] M. de Bock, R. Jaspers, M. von Hellermann, K. Finken, and A. Rogister. Plasma rotation during operation of the dynamic ergodic divertor in TEXTOR. Proceedings of the 31st EPS Conference on Contr. Fusion and Plasma Physics, London, 28 June - 2 July 2004, ECA, 28G:P–1.117, 2004.

[Diam94] P. Diamond, Y. Liang, B. Carreras, and P. Terry. Self-generating shear flow turbulence : a paradigm for the L to H transition. Phys. Rev. Lett., 72(16):2565, 1994.

[Eich00] T. Eich, D. Reiser, and K. Finken. Two dimensional modelling approach to transport properties in the TEXTOR-DED laminar zone. Nucl. Fusion, 40(10):1757, 2000.

[Erns04] D. Ernst, P. Bonoli, P. Catto, W. Dorland, C. Fiore, R. Granetz, M. Greenwald, A. Porkolab, M. Redi, J. Rice, and K. Zhurovich. Role of trapped electron mode turbulence in internal transport barrier control in the Alcator C-mod tokamak. Phys. Plasmas, 11(5):2637, 2004.

[Fink98] K. Finken, T. Eich, and A. Kaleck. First modelling of the TEXTOR DED near field divertor. Nucl. Fusion, 38(4):515, 1998.

[Fink99] K. Finken. Perturbation field penetration into the TEXTOR tokamak and the resulting torque. Nucl. Fusion, 39(6):707, 1999.

[Fink05] K. Finken, S. Abdullaev, M. de Bock, M. von Hellermann, M. Jakubowski, R. Jaspers, H. Koslowski, A. Kraemer-Flecken, M. Lehnen, Y. Liang, A. Nicolai, R. Wolf, O. Zimmermann, M. de Baar, G. Bertschinger, W. Biel, S. Brezinsek, C. Busch, A. Donne, H. Esser, E. Farshi, H. Gerhauser, B. Giesen, D. Harting, J. Hoeckzema, G. Hogeweij, P. Huettemann, S. Jachmich, K. Jakubowska, D. Kalupin, F. Kelly, Y. Kikuchi, A. Kirschner, R. Koch, M. Korten, A. Kreter, J. Krom, U. Kruezi, A. Lazaros, A. Litnovsky, X. Loozen, N. Cordozo, A. Lyssoivan, O. Marchuk, G. Matsunaga, P. Mertens, A. Messiaen, O. Neubauer, N. Noda, V. Philipps, A. Pospieszczyk, D. Reiser, D. Reiter, A. Rogister, M. Sakamoto, A. Svatchkov, U. Samm, O. Schmitz, R. Schorn, B. Schweer, F. Schueller, G. Sergienko, K. Spatschek, G. Telesca, M. Tokar, R. Uhlemann, B. Unterberg, G. Van Oost, T. Van Rompuy, G. Van Wassenhove, E. Westerhof, R. Weynants, S. Wiesen, and Y. Xu. Toroidal plasma rotation induced by the dynamic ergodic divertor in the TEXTOR tokamak. Phys. Rev. Lett., 94:015003, 2005.

[Frig03] D. Frigione, C. Challis, M. de Baar, C. Bourdelle, F. Crisanti, R. de Angelis, P. de Vries, B. Esposito, L. Garzotti, E. Giovannozzi, and N. Hawkes. Pellet fueled high density ITBs at JET. Proceedings of the 30th EPS Conference on Contr. Fusion and Plasma Physics, St.-Petersburg, 7-11 July 2003, ECA, 27A:P–2.91, 2003.

[Garb03] X. Garbet, Y. Baranov, G. Bateman, S. Benkadda, P. Beyer, R. Budny, F. Crisanti, B. Esposito, C. Figarella, C. Fourment, P. Ghendrih, F. Imbeaux, E. Joffrin, J. Kinsey, A. Kritz, X. Litaudon, P. Maget, P. Mantica, D. Moreau, Y. Sarazin, A. Pankin, V. Parail, A. Peeters, T. Tala, G. Tardini, A. Thyagaraja, I. Voitsekhovitch, J. Weiland, and R. Wolf. Micro-stability and transport modelling of internal transport barriers on JET. Nucl. Fusion, 43:975, 2003.

[Gena88] G. Genacchi and A. Taroni. JETTO: a free boundary plasma transport code (Basic Version). Rep. ENEA RT/TIB, p. 5, 1988.

[Gerh04] H. Gerhauser and R. Zagorski. Preliminary results of modelling changes of edge plasma transport due to the presence of TEXTOR-DED. Contr. Plasma Physics, 44(Issue 1-3):70, 2004.

[Ghen96] P. Ghendrih, A. Grosman, and H. Capes. Theoretical and experimental investigations of stochastic boundaries in tokamaks. Plasma Phys. Control. Fusion, 38:1653, 1996.

[Gohi99] P. Gohil, K. Burrell, R. Groebner, K. Holtrop, D. Kaplan, and P. Monier-Garbet. Wavelength calibration of the charge exchange recombination spectroscopy system on the DIII-D tokamak. Rev. Sci. Instrum., 70(1):878, 1999.

[Guen00] S. Guenter, S. Schade, M. Maraschek, S. Pinches, E. Strumberger, R. Wolf, and Q. Yu. MHD phenomena in reversed shear discharges on ASDEX Upgrade. Nucl. Fusion, 40(8):1541, 2000.

[Hahm95] T. Hahm and K. Burrell. Flow shear induced fluctuation suppression in finite aspect ratio shaped tokamak plasma. Phys. Plasmas, 2:1648, 1995.

[Hahm00] T. Hahm, K. Burrell, Z. Lin, R. Nazikian, and E. Synakowski. Zonal flows measurements concept I. Plasma Phys. Control. Fusion, 42:A205, 2000.

[Hawk95] N. Hawkes. Experimental Studies of Ion Pressure, Impurity Flows and their Influence on Transport in the JET tokamak. PhD Thesis, Imperial College London, 1995.

[Hawk97] N. Hawkes. Comparison of a charged coupled device and a microchannel plate detector for Doppler spectroscopy. Rev. Sci. Instrum., 68:2051, 1997.

[Hawk01] N. Hawkes, B. Stratton, T. Tala, C. Challis, G. Conway, R. DeAngelis, C. Giroud, J. Hobrik, E. Joffrin, P. Lomas, P. Lotte, J. Mailloux, D. Mazon, E. Rachlew, S. Reyes-Cortes, E. Solano, and K.-D. Zastrow. Observation of zero current density in the core of JET discharges with lower hybrid heating and current drive. Phys. Rev. Lett., 87(11):115001, 2001.

[Hawk02] N. Hawkes, Y. Andrew, C. Challis, R. DeAngelis, V. Drozdov, J. Hobrik, E. Joffrin, P. Lotte, D. Mazon, E. Rachlew, S. Reyes-Cortes, F. Sattin, E. Solano, B. Stratton, T. Tala, and M. Valisa. The formation and evolution of extreme shear reversal in JET and its influence on local thermal transport. Plasma Phys. Control. Fusion, 44:1105, 2002.

[Hirs81] S. Hirshman and D. Sigmar. Neoclassical transport of impurities in tokamak plasmas. Nucl. Fusion, 21:1079, 1981.

[Houl97] W. Houlberg, K. Shaing, S. Hirshman, and M. Zarnstorff. Bootstrap current and neoclassical transport in tokamaks of abritrary collisionality and aspect ratio. Phys. Plasmas, 4(9):3230, 1997.

[Houl01] W. Houlberg, V. Parail, G. Corrigan, and D. Heading. The NCLASS module in the JETTO analysis code, 2001.

[Houl04] W. Houlberg and S. Hirshman. Accurate calculation for the shielding factor for high energy beam currents. 46th APS Conference, Savannah, Georgia, USA, p. PP1.090, 2004.

[Ide00] S. Ide. Latest progress in steady state plasma research on the Japan Atomic Energy Research Institute Tokamak JT-60 Upgrade. Phys. Plasmas, 7(5):1927, 2000.

[ITER01] ITER. Summary of the ITER Final Design Report - presented by the ITER Director. July 2001.

[Jaku04] M. Jakubowski, S. Abdullaev, and K. Finken. Modelling of the magnetic field structures and first measurements of heat fluxes for TEXTOR DED operation. Nucl. Fusion, 44(S1), 2004.

[Kim91] Y. Kim, P. Diamond, and R. Groebner. Neoclassical poloidal and toroidal rotation in tokamaks. Phys. Fluids, B3(8):2050, 1991.

[Koid94] Y. Koide, M. Kikuchi, M. Mori, S. Tsuji, S. Ishida, N. Asakura, Y. Kamada, T. Nishitani, Y. Kawano, T. Hatae, T. Fujita, T. Fukuda, A. Sakasai, T. Kondoh, R. Yoshino, and Y. Neyatani. Internal transport barrier on q=3 and poloidal plasma spin-up in JT-60U high-β_p discharges. Phys. Rev. Lett., 72:3662, 1994.

[Koid01] Y. Koide, A. Sakasai, Y. Sakamoto, H. Kubo, and T. Sugie. Multichord charge exchange recombination spectroscopy on the JT-60U tokamak. Rev. Sci. Instrum., 72(1):119, 2001.

[Laws57] J. Lawson. Some criteria for a power producing thermonuclear reactor. Proc. Phys. Soc. B, 70:6, 1957.

[Lehn04] M. Lehnen and the TEXTOR-team. First results from the dynamic ergodic divertor at TEXTOR. Oral presentation at the 16th International Conference on Plasma Surface Interactions in Controlled Fusion Devices (Portland Maine, USA), 24-28 May 2004.

[Lehn05] M. Lehnen, S. Abdullaev, W. Biel, S. Brezinsek, K. Finken, D. Harting, M. von Hellermann, M. Jakubowski, R. Jaspers, M. Kobayashi, H. Koslowski, A. Kraemer-Flecken, G. Matsunaga, A. Pospieszczyk, D. Reiter, T. Van Rompuy, U. Samm, O. Schmitz, G. Sergienko, B. Unterberg, R. Wolf, and O. Zimmermann. First results from the dynamic ergodic divertor at TEXTOR. Journal of Nucl. Mater., 337-339:171, 2005.

[Levi95] F. Levinton, M. Zarnstorff, S. Batha, M. Bell, R. Bell, R. Budny, C. Bush, Z. Chang, E. Fredrickson, A. Janos, J. Manickam, A. Ramsey, S. Sabbagh, G. Schmidt, E. Synakowski, and G. Taylor. Improved confinement with Reversed Magnetic Shear in TFTR. Phys. Rev. Lett., 75:4417, 1995.

[Lian04] Y. Liang, H. Koslowski, A. Kraemer-Flecken, O. Zimmermann, G. Bertschinger, M. von Hellermann, M. de Bock, K. Finken, G. Fuchs, E. Westerhof, R. Jaspers, and R. Wolf. Observation of mode structure and mode locking using the Dynamic Ergodic Divertor on TEXTOR. Proceedings of the 31st EPS Conference on Contr. Fusion and Plasma Physics, London, 28 June - 2 July 2004, ECA, 28G:P–1.126, 2004.

[Lin99] Z. Lin, T. Hahm, W. Lee, W. Tang, and P. Diamond. Effects of collisional zonal flow damping on turbulent transport. Phys. Rev. Lett., 83(18):3645, 1999.

[Mail02] J. Mailloux, B. Alper, Y. Baranov, A. Becoulet, A. Cardinali, C. Castaldo, R. Cesario, G. Conway, C. Challis, F. Crisanti, M. de Baar, P. de Vries, A. Ekedahl, K. Erents, C. Gowers, N. Hawkes, G. Hogeweij, F. Imbeaux, E. Joffrin, X. Litaudon, P. Lomas, G. Matthews, D. Mazon, V. Pericoli, R. Prentice, F. Rimini, Y. Sarazin, B. Stratton, A. Tuccillo, T. Tala, and K.-D. Zastrow. Progress in internal transport barrier plasmas with lower hybrid current drive and heating in JET. Phys. Plasmas, 9(5):2156, 2002.

[Mail04] J. Mailloux, C. Challis, K.-D. Zastrow, J. Adams, B. Alper, Y. Baranov, P. Belo, L. Bertalot, P. Beaumont, R. Buttery, S. Conroy, E. la Luna, P. de Vries, C. Giroud, N. Hawkes, E. Joffrin, P. Lomas, D. McDonald, S. Pinches, S. Shaparov, and I. Voitsekhovitch. Tritium fuelling of JET plasmas with internal transport barriers. Proceedings of the 31st EPS Conference on Contr. Fusion and Plasma Physics, London, 28 June - 2 July 2004, ECA, 28G:P–1.148, 2004.

[Meis01] H. Meister, A. Kallenbach, A. Peeters, A. Kendl, J. Hobirk, and S. Pinches. Measurements of poloidal flow, radial electric field and ExB shearing rates at ASDEX-Upgrade. Nucl. Fusion, 41(11):1633, 2001.

[Mess96] A. Messiaen, J. Ongena, U. Samm, B. Unterberg, G. Van Wassenhove, F. Durodie, R. Jaspers, M. Tokar, P. Vandenplas, G. Van Oost, J. Winter, G. Wolf, G. Bertschinger, G. Bonheure, P. Dumortier, H. Euringer, K. Finken, G. Fuchs, B. Giesen, R. Koch, L. Koenen, C. Koenigs, H. Koslowski, A. Kraemer-Flecken, A. Lyssoivan, G. Mank, J. Rapp, N.

Schoon, G. Telesca, R. Uhlemann, M. Vervier, G. Waidmann, and R. Weynants. High confinement and high density with stationary plasma energy and strong edge radiation in the TEXTOR-94 tokamak. Phys. Rev. Lett., 77(12):2487, 1996.

[MG01] P. Monier-Garbet, C. DeMichelis, P. Ghendrih, C. Grisolia, A. Grosman, R. Guirlet, J. Gunn, T. Loarer, C. Bush, C. Clement, Y. Corre, L. Costanzo, B. Schunke, and J. Vallet. High radiation from intrinsic and injected impurities in Tore Supra ergodic divertor plasmas. Journal of Nucl. Mater., 290-293:925, 2001.

[MG04] P. Monier-Garbet, P. Andrew, P. Belo, G. Bonheure, Y. Corre, K. Crombé, P. Dumortier, T. Eich, R. Felton, J. Harling, J. Hogan, A. Huber, S. Jachmich, E. Joffrin, H. Koslowski, A. Kreter, G. Maddison, G. Matthews, A. Messiaen, M. Nave, J. Ongena, V. Parail, M. Puiatti, J. Rapp, R. Sartori, J. Stober, M. Tokar, B. Unterberg, M. Valisa, I. Voitsekhovitch, and M. von Hellermann. Impurity-seeded ELMy H-modes in JET, with high density and sustainable heat load. Proceedings of the 20th IAEA Fusion Energy Conference, Vilamoura, 1-6 November 2004, IAEA-CN-116:EX/P1–2, 2004.

[Onge01] J. Ongena, R. Budny, P. Dumortier, G. Jackson, H. Kubo, A. Messiaen, M. Murakami, J. Strachan, R. Sydora, M. Tokar, B. Unterberg, U. Samm, P. Vandenplas, R. Weynants, N. Brix, M. Charlet, I. Coffey, G. Cordey, S. Erents, G. Fuchs, M. von Hellermann, D. Hillis, J. Hogan, L. Horton, L. Ingesson, K. Itami, S. Jachmich, A. Kallenbach, H. Koslowski, A. Kraemer-Flecken, K. Lawson, A. Loarte, G. Maddison, G. Mank, G. Mckee, A. Meigs, F. Milani, P. Monier-Garbet, M. Nave, M. Puiatti, V. Parail, J. Rapp, S. Sakurai, S. Sharapov, F. Sartori, M. Stamp, H. Tamai, G. Telesca, M. Valisa, G. Van Wassenhove, B. Weysson, and K.-D. Zastrow. Recent progress toward high performance above the Greenwald density limit in impurity seeded discharges in limiter and divertor tokamaks. Phys. Plasmas, 8(5):2188, 2001.

[Onge02] J. Ongena and G. Van Oost. Energy for future centuries. Will fusion be an inexhaustable, safe and clean energy source? Fifth Carolus Magnus Euro-Summer School on Plasma and Fusion Energy Physics, Bad Honnef (Germany) - 10/21 September 2001. Transactions of fusion science and technology., 41(2T):3, 2002.

[Para99] V. Parail, Y. Baranov, C. Challis, G. Cottrell, B. Fisher, C. Gormezano, G. Huysmans, X. Litaudon, A. Sips, F. Soldner, E. Springmann, A. Taroni, and D. Ward. Predictive modelling of JET optimized shear discharges. Nucl. Fusion, 39(3):429, 1999.

[RC03] S. Reyes-Cortes, N. Hawkes, P. Lotte, C. Fenzi, B. Stratton, J. Hobrik, R. Angelis, F. Orsitto, and C. Varandas. Measurement of plasma radial electric field by the motional Stark effect diagnostic on JET plasmas. Rev. Sci. Instrum., 74(3):1596, 2003.

[Roge00] B. Rogers, W. Dorland, and M. Kotschenreuther. Generation and stability of zonal flows in Ion-Temperature Gradient Mode turbulence. Phys. Rev. Lett., 85(25):5336, 2000.

[Rozh97] V. Rozhansky and M. Tendler. Plasma rotation in tokamaks. Reviews of Plasma Physics, 19:Consultants Bureau, New York, p.147–256, 1997.

[Samm02] U. Samm. Radiation cooling experiments and reactor application. Fifth Carolus Magnus Euro-Summer School on Plasma and Fusion Energy Physics, Bad Honnef (Germany) - 10/21 September 2001. Transactions of fusion science and technology., 41(2T):352, 2002.

[Satt01] F. Sattin, Y. Andrew, C. Giroud, N. Hawkes, M. Valisa, K.-D. Zastrow, and contributors to the EFDA-JET workprogramme. First core poloidal flow measurements in JET. Proceedings of the 28th EPS Conference on Contr. Fusion and Plasma Physics, Funchal, 18-22 June 2001, ECA, 25A:373, 2001.

[Solo04a] W. Solomon, K. Burrell, L. Baylor, R. Fonck, P. Gohil, D. Gupta, R. Groebner, G. Kramer, G. McKee, and R. Nazikian. Experimental test of neoclassical theory of poloidal rotation in tokamaks. Proceedings of the 20th IAEA Fusion Energy Conference, Vilamoura, 1-6 November 2004, IAEA-CN-116:EX/P4–10, 2004.

[Solo04b] W. Solomon, K. Burrell, L. Baylor, P. Gohil, and R. Groebner. Extraction of poloidal velocity from charge exchange recombination spectroscopy measurements. Rev. Sci. Instrum., 75(10):3481, 2004.

[Stae99] G. Staebler. Density gradient bifurcation in tokamaks. Nucl. Fusion, 39(6):815, 1999.

[Stae01] G. Staebler, R. Waltz, J. Kinsey, G. Bateman, A. Kritz, T. Onjun, A. Pankin, P. Zhu, and W. Horton. Drift wave based modelling of the poloidal spin-up precursor and stepwise expansion of transport barriers. Nucl. Fusion, 41(7):891, 2001.

[Stra95] E. Strait, L. Lao, M. Mauel, B. Rice, T. Taylor, K. Burrell, M. Chu, E. Lazarus, T. Osborne, S. Thompson, and A. Turnbull. Enhanced Confinement and Stability in DIII-D Discharges with Reversed Magnetic Shear. Phys. Rev. Lett., 75:4421, 1995.

[Tala01] T. Tala, J. Heikkinen, V. Parail, Y. Baranov, and S. Karttunen. ITB formation in terms of ω_{ExB} flow shear and magnetic shear s on JET. Plasma Phys. Control. Fusion, 43:507, 2001.

[Tala02a] T. Tala, V. Parail, A. Becoulet, C. Challis, G. Corrigan, N. Hawkes, D. Heading, M. Mantsinen, and S. Nowak. Impact of different heating and current drive methods on the early q-profile evolution in JET. Plasma Phys. Control. Fusion, 44:1181, 2002.

[Tala02b] T. Tala, V. Parail, A. Becoulet, G. Corrigan, D. Heading, M. Mantsinen, and P. Strand. Comparison of theory-based and semi-empirical transport modelling in JET plasmas with ITBs. Plasma Phys. Control. Fusion, 44:A495, 2002.

[Tala04] T. Tala, F. Imbeaux, V. Parail, C. Bourdelle, G. Corrigan, X. Garbet, D. Heading, X. Litaudon, P. Strand, and J. Weiland. Fully predictive transport simulations of ITB Plasmas in JET, JT-60U and DIII-D. Submitted to Nucl. Fusion, 2004.

[Tala05] T. Tala, Y. Andrew, G. Corrigan, K. Crombé, D. Heading, F. Imbeaux, V. Parail, P. Strand, and J. Weiland. Progress in predictive transport modelling of ITBs in JET. To be presented at 32nd EPS Conference on Contr. Fusion and Plasma Physics, Tarragona, 27 June - 1 July 2005, 2005.

[Tele94] G. Telesca, H. Claassen, A. Pospieszczyk, R. Koch, and D. Van Eester. Study of plasma contamination during ICRF heating under boronized wall conditions in TEXTOR. Nucl. Fusion, 34(5):625, 1994.

[Tele00] G. Telesca, B. Unterberg, R. Jaspers, A. Messiaen, J. Ongena, J. Rapp, U. Samm, N. Schoon, M.Lehnen, M. Tokar, G. Van Oost, and R. Zagorski. Neon radiation efficiency for different confinement regimes in TEXTOR-94. Nucl. Fusion, 40(11):1845, 2000.

[Tele05a] G. Telesca, K. Crombé, M. Tokar, B. Unterberg, G. Verdoolaege, R. Zagorski, and G. Van Oost. Preliminary study of the influence of the DED on carbon radiation and transport in the TEXTOR tokamak. Journal of Nucl. Mater., 337-339:361, 2005.

[Tele05b] G. Telesca, G. Verdoolaege, K. Crombé, M. Lehnen, A. Pospieszcyk, B. Unterberg, and G. Van Oost. Screening and radiation efficiency of carbon with Dynamic Ergodic Divertor on TEXTOR. To be presented at 32nd EPS Conference on Contr. Fusion and Plasma Physics, Tarragona, 27 June - 1 July 2005, 2005.

[Toka97] M. Tokar, H. Lazaar, W. Mandl, W. Hess, and C. DeMichelis. Modelling of plasma and impurity behaviour in a tokamak with a stochastic layer. Plasma Phys. Control. Fusion, 39:569, 1997.

[Tres02] G. Tresset, X. Litaudon, D. Moreau, and X. Garbet. A dimensionless criterion for characterizing internal transport barriers in JET. Nucl. Fusion, 42:520, 2002.

[vH90] M. von Hellermann, W. Mandl, H. Summers, H. Weisen, A. Boileau, P. Morgan, H. Morsi, R. Koenig, M. Stamp, and R.

Wolf. Visible charge exchange spectroscopy at JET. Rev. Sci. Instrum., 61(11):3479, 1990.

[vH95] M. von Hellermann, P. Breger, J. Frieling, R. Konig, W. Mandl, A. Maas, and H. Summers. Analytical approximation of cross-section effects on charge exchange spectra observed in hot fusion plasmas. Plasma Phys. Control. Fusion, 37:71, 1995.

[Wagn82] F. Wagner, G. Becker, K. Behringer, D. Campbell, A. Eberhagen, W. Engelhardt, G. Fussmann, O. Gehre, J. Gernhardt, G. v. Gierke, G. Haas, M. Huang, F. Karger, M. Keilhacker, O. Klueber, M. Kornherr, K. Lackner, G. Lisitano, G. Lister, H. Mayer, D. Meisel, E. Mueller, H. Murmann, H. Niedermeyer, W. Poschenrieder, H. Rapp, H. Roehr, F. Schneider, G. Siller, E. Speth, A. Staebler, K. Steuer, G. Venus, O. Vollmer, and Z. Yu. Regime of improved confinement and high beta in neutral beam heated divertor discharges of the ASDEX tokamak. Phys. Rev. Lett., 49:1408, 1982.

[Walt95] R. Waltz, G. Kerbel, J. Milowich, and G. Hammet. Advances in the simulation of toroidal gyro-Landau fluid model turbulence. Phys. Plasmas, 2:2408, 1995.

[Wolf03] R. Wolf. Internal transport barriers in tokamak plasmas. Plasma Phys. Control. Fusion, 45:R1, 2003.

[Xu00] Y. Xu, C. Yu, J. Luo, J. Mao, B. Liu, J. Li, B. Wan, and Y. Wan. Role of Reynolds-stress induced poloidal flow in triggering the transition to improved Ohmic confinement on the HT-6M tokamak. Phys. Rev. Lett., 84(17):3867, 2000.

[Yu00] C. Yu, Y. Xu, J. Luo, J. Mao, B. Liu, J. Li, B. Wan, and Y. Wan. Demonstration of the role of turbulence-driven poloidal flow generation in the L-H transition. Plasma Phys. Control. Fusion, 42:A217, 2000.

[Zast04] K. Zastrow, J. Adams, Y. Baranov, P. Belo, L. Bertalot, J. Brzozowski, C. Challis, S. Conroy, M. de Baar, P. de Vries, P. Dumortier, J. Ferreira, L. Garzotti, T. Hender, E. Joffrin, V. Kiptily, J. Mailloux, D. McDonald, R. Neu, M. O'Mullane, M. Nave, J. Ongena, S. Popovichev, M. Stamp,

J. Stober, D. Stork, I. Voitsekhovitch, M. Valovic, H. Weisen, A. Whiteford, and A. Zabalotsky. Tritium transport experiments on the JET tokamak. Plasma Phys. Control. Fusion, 46(12B):B255, 2004.

[Zhu99] P. Zhu, W. Horton, and H. Sugama. The radial electric field in a tokamak with reversed magnetic shear. Phys. Plasmas, 6(6):2503, 1999.